Cell adhesion and cell mechanics during zebrafish development

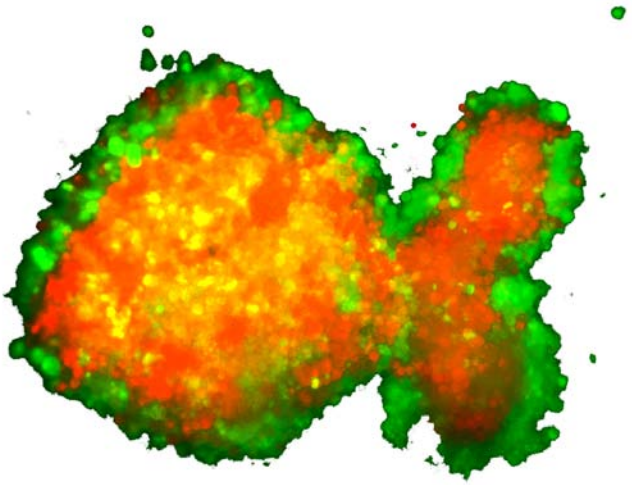

DISSERTATION

vorgelegt von Dipl. Biol. Michael Krieg am 02.10.2009

zur Erlangung des akademischen Grades Dr. rer. nat.

der Fakultät für Naturwissenschaften

der Technischen Universität Dresden

Tag der mündlichen Verteidigung: 07.12.2009

Consultant 1
Prof. Dr. Daniel J. Müller
Biotec / TU-Dresden

Consultant 2
Prof. Dr. Carl-Philipp Heisenberg
MPI-CBG Dresden

Consultant 1

Prof. Dr. Daniel J. Müller
Department of Cellular Machines
Biotec / TU-Dresden

Consultant 2

Prof. Dr. Carl-Philipp Heisenberg
MPI-CBG Dresden

... to my family ...
... my parents and my sisters ...

Wenn ich ein Problem lösen will, dann darf durch die Lösung kein Bestandteil des Problems verschwinden Albert Camus.

Contents

Preface 1

1 Motivation and Summary 3

2 Introduction 9

2.1 Zebrafish gastrulation . . . 9
2.1.1 Time course of development . . . 9
2.1.2 Nodal signaling . . . 14
2.1.3 Germ layer formation and epithelial mesenchymal transition 15
2.2 Adhesion and mechanics in development . . . 19
2.2.1 Mechanical forces during tissue formation . . . 20
2.2.2 Shaping cells . . . 31
2.3 Cell adhesion molecules . . . 34
2.3.1 Integrins . . . 35
2.3.2 Cadherins . . . 36
2.4 Cell adhesion techniques . . . 42
2.4.1 Image-based techniques to characterize cell adhesion . . . 43
2.4.2 Techniques to measure cell adhesion forces . . . 46
2.5 AFM – an all-in-one toolbox for cell mechanics . . . 51
2.5.1 Single cell adhesion force spectroscopy . . . 51
2.5.2 Single cell elastography . . . 56

3 Experimental Section 63

3.1 Techniques . . . 63
3.1.1 AFM and SCFS . . . 63
3.1.2 Cell elasticity . . . 67
3.1.3 Fluorescence recovery after photobleaching . . . 70
3.2 Methods . . . 71
3.2.1 mRNA preparation . . . 71

3.2.2 Single cell microinjection . . . 73
3.2.3 Cell culture . . . 74
3.2.4 Hanging drop experiments . . . 75
3.2.5 *In-vitro* biotinylation . . . 76
3.2.6 Western blotting . . . 78
3.2.7 The AFM setup . . . 79
3.2.8 Adhesion measurements . . . 79
3.2.9 Cell-cortex tension measurements . . . 81
3.2.10 Tether extraction using AFM . . . 84
3.2.11 FRAP Protocol . . . 85
3.2.12 Non-covalent surface modifications . . . 86
3.2.13 Covalent surface modification . . . 87
3.2.14 Statistical data processing . . . 88
3.2.15 Single cell transplantations . . . 88
3.2.16 Laser scanning confocal microscopy . . . 89
3.2.17 Image processing . . . 89
3.3 Materials . . . 91
3.3.1 Cell culture . . . 91
3.3.2 Western blotting . . . 93
3.3.3 Atomic force microscopy . . . 94

4 Cell sorting and surface mechanics 95
4.1 Introduction . . . 95
4.2 Results and Discussion . . . 96
4.2.1 Adhesion . . . 96
4.2.2 Cortex Tension . . . 101
4.2.3 Cell sorting . . . 103

5 Cell cohesion and migration 119
5.1 Introduction . . . 119
5.2 Results and Discussion . . . 120
5.2.1 Collective cell migration . . . 120
5.2.2 Migration in crowded and abandoned environment . . . 122
5.2.3 Modulation of cell adhesion properties . . . 123
5.2.4 Cell migration and cell-cell adhesion . . . 125
5.2.5 Summary of adhesion force measurements . . . 130

6 Membrane tension influences cell behavior **131**
6.1 Introduction . . . 131
6.1.1 Cell membrane architecture . . . 131
6.1.2 Cell membrane mechanics . . . 132
6.1.3 Biophysics of membrane-nanotube extrusion . . . 137
6.1.4 Molecular strategy of membrane-cytoskeleton adhesion . . . 141
6.2 Results . . . 145
6.2.1 Activation of Ezrin by Nodal signaling . . . 145
6.2.2 Ezrin and plasma-membrane blebbing . . . 146
6.2.3 Cortex mechanics . . . 149
6.2.4 Membrane mechanics . . . 149

7 Membrane tethers and kinetics **161**
7.1 Introduction . . . 161
7.2 Results . . . 164

8 Final observations **171**

Acknowledgments **175**

Appendix **I**
List of Figures . . . V
List of Tables . . . VII
Movie legends . . . VIII
Curriculum vitae . . . X
List of Publications . . . XIII
Versicherung . . . XIV

Index **XIV**
Glossary . . . XIV
Bibliography . . . XIX

Preface

During my work on the first project, how cell adhesion and cell cortex tension influence the sorting of primary zebrafish germ layer cells, I encountered an interesting sorting pattern. Mixing ectodermal and mesodermal progenitor cells in a hanging drop, the two cell types normally form a sphere within a sphere configuration — ectoderm is surrounded by mesoderm. This configuration is preceded by a compaction of the mixed cells and a fusion of already formed clusters in close vicinity. One day, three clusters fused and formed an aggregate which strikingly resembled a fish. The cover for "Nature Cell Biology", curiously published on the 1st of April, was born.

To motivate the reader browse through my thesis, I encourage the reader to follow zebrafish germ layer formation in real time. From the fertilization of the zebrafish egg until the end of gastrulation 8 - 10 hours elapse. The same amount of time is anticipated to finish reading this manuscript. In the life of a zebrafish, this is a very short time, but for the life of the reader it might feel endless. Therefore, the reader can enjoy a small movie on the lower right side of each odd page to relax the hard facts of this thesis*. The same movie is provided as a supplementary movie file on the compact disc.

*The movie is processed and originally provided by [1]

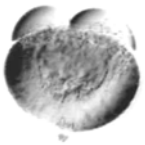

1. Motivation and Summary

Development of vertebrate organisms out of a single oocyte is a phenomenal achievement of evolution. After fertilization, a series of cell divisions gives rise to a vast number of cells which subsequently have to share specialized tasks and build complex structures such as eyes, heart or brain (see Fig. 1.1). But how can cells that originate from a single ancestor control all these processes? Surely, an important aspect are differences in gene expression among the emergent cell types [2]. At the end, however, it is not sufficient to know which genes are expressed at what stage. We also want to know about how cells do their job physically and how genetics influence behavior. To build up an organism, the behavior of single cells has to be coordinated on the tissue scale and should not lose the ability to remodel different compartments individually [3]. One of the fundamental questions here is, how does the difference in gene expression influence the behavior of the cells and determine tissue architecture.

In an undifferentiated organism, all cells have the same specification and behave similarly in respect to their morphological properties and their gene expression pattern. As a consequence, all cells occupy identical environments and share related duties. Strikingly, as soon as differentiation starts, the constituting cells change their properties and as a result eventually separate from each other, ending up in different compartments to perform specific functions. Such positional changes normally take place by cell migration and by cell sorting. Sorting can happen passively governed by cell surface properties [4]. In general, sorting will occur, if the constituent entities have differential properties, such as particle size [5], surface tension [6, 7], a differential chemotaxis [8] or motility [9], normally realized as a faster migration within an organism. Mostly, such passive position changes are accelerated by active cell migration from one point to another, guided by extracellular cues. Among those cues are signalling molecules [10] or interaction with the adhesive environment [11].

In early zebrafish development, cells of the embryo proper differentiate into three germ layers and form the endoderm, mesoderm – usually termed

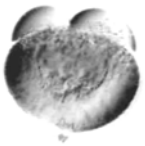

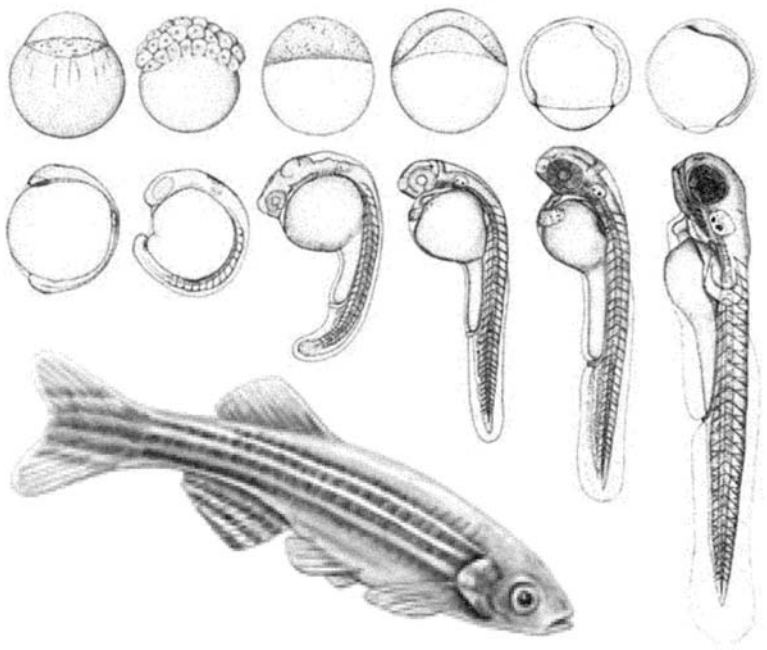

Fig. 1.1 Vertebrate development

Schematic representation of characteristic stages during zebrafish development. A fertilized egg starts to divide and give rise to a number of cells which, in the course of further ontogenesis, start to populate the developing embryo. Different organs arise upon the interplay of various cell types until a complete organism is formed at the end of the ontogenesis. Image after [12].

mesendoderm – and ectoderm. During the course of gastrulation, the mesendoderm originates and begins to populate the interior of the embryo [12] while staying separated from other germ layers. Many studies have been dedicated to elucidating the genetic cascade which triggers the advent of the mesendoderm [2] and the associated morphological changes during specification [13, 14]. In contrast, much less is known about the cell-mechanical conversions taking place when one cell type transforms into another. One of the most prevalent hypotheses in the field, the *Differential Adhesion Hypothesis (DAH)* proposes that sorting events *in-vitro* and germ layer morphogenesis *in-vivo* are directed by the surface tension of the involved cell assemblies [15, 16]. Moreover it is hypothesized that sorting be a direct consequence of differential adhesive properties among the constituent cell types resembling the behavior of immiscible liquids [17] with distinct surface tensions. Germ layer morphogenesis of the frog [18] and zebrafish [19] or the positioning of the oocyte during *Drosophila* oogenesis was explained on the basis of the DAH assumptions. Apart from the surprising analogy between tissues and liquids, the validity of the DAH was challenged, and questions arose whether cell-adhesion-governed surface tension

alone can indeed explain all aspects of germ layer morphogenesis [20, 21, 22]. During zebrafish gastrulation, differential-adhesion-governed cell sorting was argued to be a major determinant of tissue positioning [19] while the contribution of cell adhesion to active cell motility is still under hearty discussion [23, 14]. This thesis is separated into three parts and is committed to accumulating knowledge about how mechanical properties on a tissue (Chapter 4), cellular (Chapter 5) and molecular (Chapter 6) scale influence germ layer morphogenesis (see also Fig. 1.2).

Firstly, surface tension or surface energy density as a physical property needs to be explained in a cell biological context. In other words, what is the cell biological origin for tissue surface tension. Years ago, Steinberg postulated that the surface tension of a tissue type is solely manifested in its adhesive properties [16]. Later, Harris suggested that not only adhesion, but rather a combination of adhesion and acto-myosin contraction gives rise to complex cellular re-arrangements as they occur during gastrulation [20]. Surprisingly, despite the long-lasting debate, no quantitative measurements on single cells have been made to solve this potential controversy. The work of this thesis tries to present quantitative data acquired with an *Atomic Force Microscope (AFM)* on cell mechanical properties such as cell adhesion and myosin dependent cortex tension to relate it to tissue formation *in-vitro* and *in-vivo*. To accomplish this task, cell-cell separation assay was established and for the first time in the lab, an assay to measure cell cortex tension was developed and applied. With these tools at hand, I could show that cell-cell adhesion is necessary but alone not sufficient to facilitate correct tissue positioning. Rather, cell sorting and germ layer formation is a combination of cell cortex contractions, cell adhesion and possibly cell migration. The experimental findings for tissue positioning have been reproduced *in-silico* using a *Cellular Potts Model* employing quantified measurements for adhesion and contraction made with an AFM.

Secondly, active cell migration seems to play an important role during tissue formation *in-vivo*, but the role of cell-cell adhesion guiding migration in a 3D environment is not yet completely understood. Years ago, it was suggested that motility is strictly scaled by the cell's adhesive potential [24]. Recently, this view has been challenged and it was argued that migration in 3D is largely different and relies on a mechanism that is distinct from migration on flat substrates [23, 25]. During zebrafish gastrulation, cells move in collectives on top of other cells [26, 14] rather than as single cells on deposited extracellu-

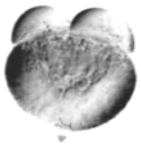

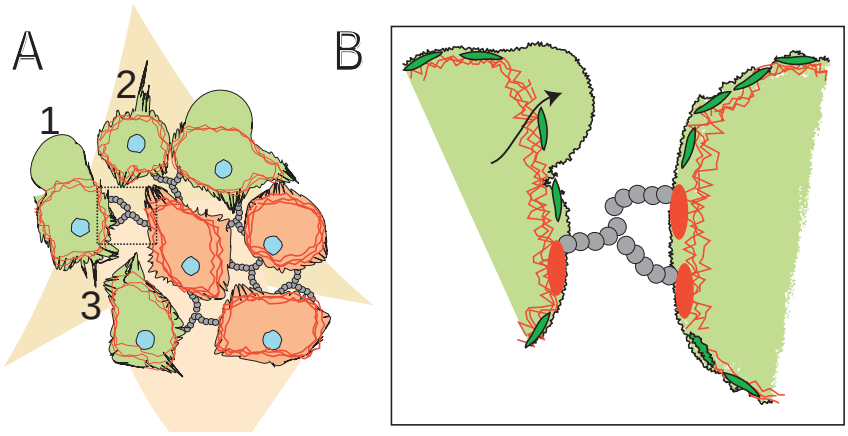

Fig. 1.2 Cell adhesion, cortex tension and membrane mechanics influence cell behavior

A: Schematic representation and summary of the cell mechanical problems studied during this thesis. Cells adhere via cell adhesion molecules (grey) and separate according to their adhesion strength and cortical actin distribution (red + red, green + green). The adhesion among the cells is necessary to physically couple them together, enabling them to coordinate their collective migration within the embryos as a coherent tissue sheet. Migration per se is dependent not only on adhesion but also on the ability to send out protrusion. A variety of 'cell-feet' have been characterized such as 1. plasma-membrane blebs, 2. filopodia and 3. lamelipodia. **B:** Close view on the interface between two cells that adhere via homophilic adhesion molecules (e.g. Cadherins, grey). The latter are coupled via linker molecules (red particle) to the cortical actin cytoskeleton (csk, red wires), which determines the mechanics of the cell interface. The plasma - membrane is linked to the cytoskeleton by specific proteins (e.g. members of the Ezrin, Radixin, Moesin family, green) that either couple directly to positively charged lipids or integral membrane proteins. Cell shape is largely determined by the mechanics of this system. If adhesion of the membrane to the cytoskeleton fails, hydrostatic pressure inside the cell forces the membrane off and leads to extensive plasma-membrane blebbing. At the end, adhesion, migration and integrity of the cell cortex mechanical system are necessary to perform efficient germ layer morphogenesis.

---

lar matrix structures [27]. Therefore, the question remains, how intercellular interactions influence collective cell migration *in-vivo* [28]. Here, co-workers and I studied cell migration of germ layer progenitors with reduced cell-cell adhesion in living zebrafish embryos. In addition to that, we complemented these results by studying cell migration in embryos that have no neighboring cells — reducing collective to single cell migration. We could observe that the directionality of collective cell migration is strongly dependent on cell-cell adhesion and if reduced, directionality is partially lost. Interestingly, cell-cell adhesion is only important when cells move in coherent clusters and is not important when cells move without neighbors. These findings propose a new role of cell-cell adhesion in regulating collective cell migration. Furthermore, during this thesis work, new image-processing-tools to analyze 3D motility

data were implemented in this lab.

Lastly, a question remains as to the intracellular machinery modulating migration of embryonic cells *in-vivo*. To move, a cell has to change shape. Cell shape changes generally depend on a controlled association of the membrane with the actin cytoskeleton. It was suggested that a tightly regulated adhesion of the plasma-membrane to the underlying cortex is necessary for correct protrusion formation [29, 30] and hence movement of the cells. Not surprisingly, the same molecule maintaining this interaction, called Ezrin2, is expressed during zebrafish gastrulation in the mesendodermal tissue. Ezrin2 is activated upon Nodal/TGFβ signaling at the onset of gastrulation [31]. A loss-of-function of Ezrin in the mesendodermal cell layer leads to increased plasma-membrane blebbing *in-vitro* and *in-vivo*. Furthermore, embryonic development is perturbed, indicating a crucial role of the ERM function in morphogenesis. Biophysical characterization of the membrane properties, overall the association energy density [32, 33] and the number of the membrane cortex interactions [34] are measured with AFM [35, 36] of mesendodermal cells with and without Ezrin. Reducing the expression of Ezrin molecules in the cells leads to both a reduction in adhesion energy and molecular cross-linker density. These experiments shed light into a novel role of Nodal signaling in controlling the morphogenesis of germ layers by regulating the plasma-membrane properties of individual cells.

Across the board, we aim to contribute knowledge on how adhesion, cortex and membrane tension — mechanical properties as such — influence cell behavior during tissue separation and collective migration at the single cell level using the model system of zebrafish germ layer morphogenesis.

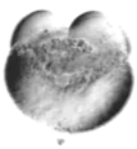

2. Introduction

2.1. Zebrafish germ layer formation

The use of zebrafish as a model organism for genetic and developmental studies was introduced by George Streisinger in the early 1980s [37] and became one of the most important model systems for studying vertebrate development. Zebrafish have several advantages over other vertebrates like mice or *Xenopus*. Zebrafish embryos develop fast, *ex-utero* and are transparent, making them a perfect subject to be studied with optical microscopy such as confocal laser scanning microscopy and differential interference contrast (DIC) microscopy. Furthermore, unlike any other model organism, the zebrafish is particularly suited for single cell transplantation experiments that allow the properties of modified cells to be monitored in their natural, embryonic environment. In the past, transplantation studies have unraveled the contribution of cell autonomous and non-autonomous effects during morphogenesis [38]. On top of that, the zebrafish is diploid in contrast to tetraploid *Xenopus*, making mendelian analysis and reverse genetics, such as TILLING, applicable to study gene function [39]. Although no permanent cell line has been established, the zebrafish offers an excellent opportunity to create primary cell cultures as a model system to study the properties of single cells individually [13, 40]. Taken together, working with zebrafish offers superior opportunities to characterize how physical properties influence embryonic development.

Zebrafish is an excellent model system for developmental genetics and embryogenesis. Individual cells can be labeled and followed during the course of development.

2.1.1. Time course of development

Development of a zebrafish starts, like any other *obligatory* multicellular organism*, with the fertilization of the oocyte. Entry of the sperm triggers calcium waves which in turn activate filament contractions in the egg leading

*Emphasis is put on obligatory, because *Dictyostelium* does 'develop' into multicellular structures under certain circumstances but usually lives as a solitary amoebae.

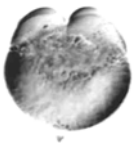

to a separation of the embryonic cytoplasm from the yolk cytoplasm [41]. The embryo proper then exists as a *blastodisc* on the animal pole of the embryo (see Fig. 2.1 A and Ref. [12]). The segregation of embryonic and extra-embryonic cytoplasm continues throughout the first cell divisions. This is the so-called *cleavage period* (see Fig. 2.1 B). The first cleavages of the blastodisc are incomplete, creating daughter cells that are still connected to the yolk cell via cytoplasmic bridges. Important for development is that, up to this stage, yolk and cellular proteins can be exchanged freely by diffusion. Furthermore, during the cleavage period the volume of the embryo does not increase, leading to a larger number of smaller cells [2]. Within the next three hours, rapid and synchronous divisions give rise to a cell cluster sitting on the animal pole of the embryo, namely the *blastoderm* (see Fig. 2.1 C). This is a compact cell sheet which lays on top of the yolk cell — in contrast to a *blastula* which is a hollow sphere delimited by an epithelium like in sea urchin (see Fig. 2.3). Cells of the blastoderm are not yet determined to a specific developmental fate in these early stages. Rather than that the progenies of the blastoderm contribute to all tissues of the forming embryo. Just at the beginning of gastrulation, specification starts and the fate of the cells becomes restricted at the tissue level [42].

2.5 hours post fertilization (hpf) transcription of zygotic genes starts and marks the so-called *mid-blastula transition* (MBT). Concomitantly, cell divisions become asynchronous and cell cycles lengthen [12]. At this time the *yolk-syncytial layer* (YSL, [43]) is formed. Collapse and fusion of the cells at the blastoderm margin into the yolk creates a thin, multinuclear layer directly underlying the blastoderm. The YSL adopts a crucial function in the induction of the germ layer at the onset of gastrulation when it secretes the primary signal for mesendoderm specification [2]. In the course of gastrulation, the YSL remains transcriptionally active and is thought to pattern the dorsoventral axis of the gastrula [44]. Besides its signaling function, the behavior of the YSL reflects certain aspects of the overlying germ layer progenitors. For example, the YSL nuclei are not statically anchored within the cortex of the yolk cell, but follow the movement of the hypoblast, specifically the mesoderm, as development proceeds through gastrulation* [43].

Like the YSL in the interior of the embryo, another extra-embryonic tissue type is formed on the outer side. Between the 32 and 128 cell stage the

*A proposed mechanism is a cortical flow within the YSL induced by the migration of the mesendoderm.

enveloping layer (EVL) is formed after the first horizontal (in the plane of the embryo) cell division*. The EVL is an epithelial sheet that forms *tight-junctions* to the blastodermal cells directly underneath and probably protects the embryo proper from the environment. It also is tightly connected to the yolk cell and was proposed to be a major motor of epiboly [45, 46] in *Fundulus* and zebrafish† [14, 47]. Apart from that, EVL cells contribute to the formation of the Kupffer's vesicle, the organ of laterality responsible for left-right patterning during later stages of development [48].

At 4 hpf the blastoderm begins to move around the yolk in a process called *epiboly* and covers the entire yolk cell at the end of *gastrulation*. Epiboly and gastrulation are the processes during which the three germ layers are formed and the axis of the embryo is created with anterior-posterior as well as dorso-ventral polarity. Gastrulation in zebrafish starts at 50 % epiboly (∼ 5 hpf), when cells of the blastoderm internalize at the dorsal side of the embryo (see Fig. 2.1 D,F). A local thickening known as the germ ring margin appears in the marginal region of the embryo due to a transient arrest of epiboly [12]. This thickening is formed by an accumulation of cells. As a consequence of convergence of blastodermal cells to the dorsal side of the germ ring, the shield is formed [49]. The shield constitutes a central part of the early embryo because it is known to induce differentiation into different germ layer progenitors. Therefore, the name 'organizer', originally denoted by Mangold and Spemann for chick gastrulation, is also used for zebrafish to describe this region of the embryo [12]. Here, single cells lose contact with the blastoderm and migrate away from the organizer to populate the *hypoblast*. More specifically, internalizing cells migrate in the opposite direction than the non-internalizing blastoderm. The latter is now separated into two distinct structures — the already mentioned hypoblast and the *epiblast*. At this stage, 50-60 % epiboly has been reached, but the whole yolk cell still needs to be covered by the embryo proper. Throughout gastrulation and epiboly, the epiblast feeds cells into the hypoblast, which then differentiates into the mesoderm and the endoderm. Both can already be distinguished on the basis of their behavior. Initially, endodermal cells show random movements [9], but soon migrate persitently and converge towards the dorsal side of the gastrula after this initial lag phase. Mesodermal cells, in contrast to endodermal cells, converge directly after internalization towards the animal pole and participate in axis formation.

Gastrulation means "*formation of the gut*" and leads to the morphogenesis of the ectoderm, mesoderm and endoderm.

*Up to the 32 cell stage, division occurs only vertically (see Fig. 2.1)

†Contractile elements in the YSL pull the EVL around the yolk like a hat over a head.

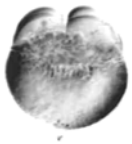

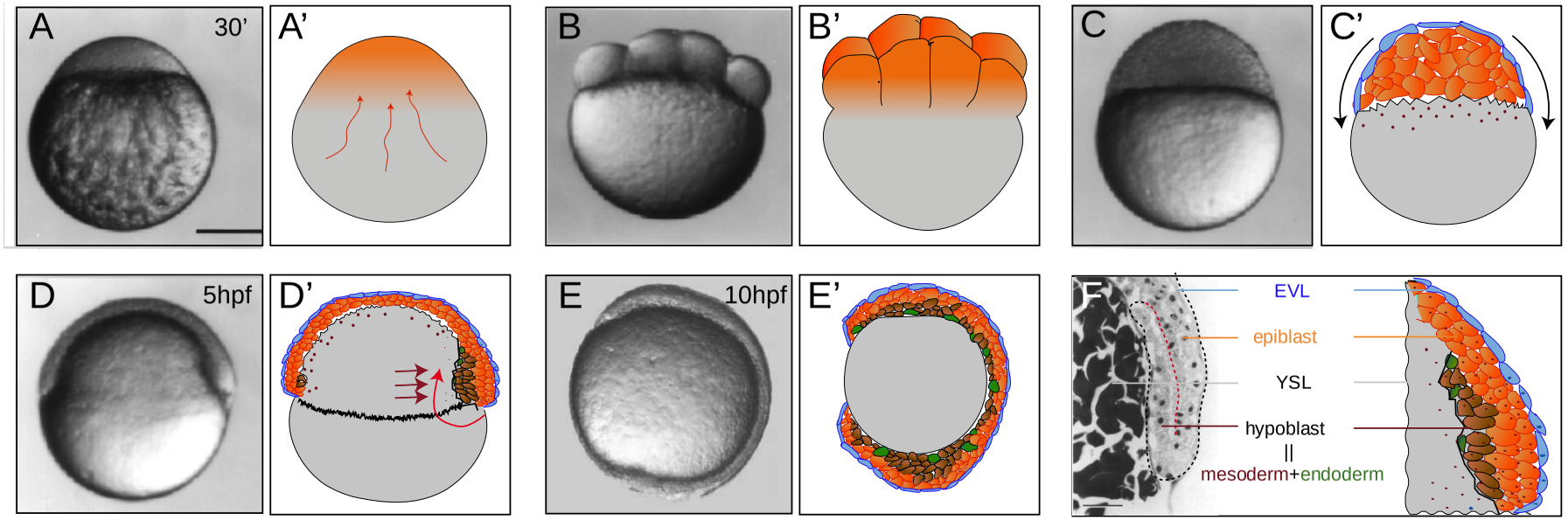

Fig. 2.1 Early zebrafish development

Light microscopic [12] and schematic representations of key stages during the first ten hours of development. **A:** One cell emerges after separation of embryo from yolk cytoplasm. **B:** Subsequent cell divisions lead to a blastodermal cap on top of the big yolk cell. Up to the 32 cell stage, the cells are connected to the yolk. **C:** Four hours post fertilization, the blastoderm moves around the yolk cell in a process called epiboly. Cells at the blastoderm margin collapse into the yolk cell and form the yolk syncytial layer (YSL). The extraembryonic enveloping layer (EVL, blue) forms and covers the blastoderm. **D:** At 50 % epiboly, signals from the yolk cell (brown arrows) induce invagination of the blastoderm at the dorsal side of the embryo. A local thickening marks the ingression of the cells that subsequently turn direction and migrate to the anterior pole. This is the formation of the hypoblast and develops into mesoderm and endodermal structures later on. **E:** At the end of gastrulation, in the tailbud stage, the body axis is apparent and the head and the tail anlage have formed. **F:** Electron micrograph [49] and schematic diagram of the situation at the shield stage (5 hpf). Throughout the figure, undifferentiated or epiblast tissue is colored orange, mesoderm in brown, endoderm in green and the EVL in blue.

The convergence of cells to the dorsal side leads to a narrowing of the embryo and, together with radial intercalations and epiboly [50], causes a lengthening of the body axis (see Fig. 2.1 E). The extension of the embryo is a direct result of medio-lateral intercalations during which cells 'squeeze' between each other [26]. Convergent extension can also be seen in the epiblast, which also undergoes radial intercalations, causing a thinning of the embryo. Radial intercalations are, next to microfilament contractions in the yolk, a major driving force of epiboly. Cells move from deep to more superficial layers, thereby creating a pushing force that contributes to the spreading of cells around the yolk [49]. At the tailbud stage (8 - 10 hpf), marking the end of gastrulation, the epiblast forms the outer germ layer, the *ectoderm*, and the hypoblast forms the two inner germ layers, the *endoderm* and the *mesoderm*. At the stage, the mesodederm has already differentiated into sub-populations which can be easily distinguished on the basis of their gene expression pattern*, as well as on the basis of their collective behavior [52]. Whereas leading (anterior axial) mesodermal cells move in a cohesive group and build up the pre-chordal plate and their derived structures†, paraxial cells move more independently as a loosely associated collective. The epiblast, giving rise to the ectoderm, can be characterized as a pseudo-epithelial germ layer, whereby neighbor-changes among the cells is observed less frequently.

Internalizing cells that form the mesoderm dramatically change their adhesive and mechanical properties on the basis of an altered gene expression.

An intriguing feature of tissue formation is that the emerging cell types obtain spatial information and populate new environments within the embryo. The same is true for zebrafish germ layer morphogenesis when epiblast and hypoblast separate and occupy different compartments in the embryo. In other words, both mesendoderm and ectoderm stay separated by the Brachet's cleft [53], and do not mix again but migrate in opposite directions on top of each other [12]. The genetic cascade, inducing the mesoderm and endoderm from an undifferentiated blastoderm, has been deciphered in great detail. It is a concerted action of Nodal/TGFβ signaling molecules that induces mesendoderm cell fate from an undifferentiated precursor. Nevertheless, which mechanisms keep them separated is still a matter of unproven, ambiguous hypotheses.

*Paraxial mesoderm expresses high levels of *notail* whereas axial mesoderm expresses *goosecoid* ([2, 51]).

†prechordal plate gives rise to hatching gland [12]

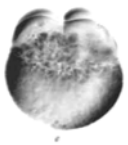

2.1.2. Mesendoderm formation and Nodal signaling

Nodal signals are members of the transforming growth factor β super family and constitute a key component of mesoderm and endoderm generators in vertebrate development. Initially discovered in mice, Nodals have been found in various vertebrate animals, such as *Xenopus* and zebrafish. In mice, Nodals are not only required to induce but also to pattern the mesoderm. The expression of Nodal molecules is induced by VegT early during *Xenopus* development. In zebrafish, dorsal organizer formation and probably Nodal expression is regulated by *eomesodermin*, but its mode of action is still not completely understood. The molecular picture of Nodal-induced mesendoderm induction, in contrast, is explained very well.

Nodal signaling is responsible for the induction of the mesodermal germ layer in zebrafish.

Nodal signals, such as *squint* (*sqt*), are expressed and secreted by the yolk cell and marginal cells of the embryo, whereas *cyclops* (*cyc*) is expressed by the future mesendoderm only [2]. High levels of both signals will induce anterior mesoderm marked by expression of *goosecoid*, whereas low concentration will induce primarily posterior structures marked by expression of *no tail*. *Cyc* and *sqt* are functionally redundant and can compensate for each other. Mutations will only result in a severe defect if both genes are depleted [54]. Such embryos develop no mesodermal and endodermal structures and do not form a hypoblast, highlighting their role in controlling the involution of cells during germ layer development. Nevertheless, there seems to be small functional variation between *sqt* and *cyc*: whereas *sqt* can activate genes in cells distant from its source, gene activation through *cyc* is locally restricted to proximal cells only. The effects of the double mutant are phenocopied by an over-expression of *lefty*, presumably by blocking the interaction of the ligands with their receptors [55].

These secreted Nodal signals are received by cells that express the inherent receptor *taram-a* [56], an *activin-like-kinase* (*ALK1*) as well as its co-receptor *one-eyed-pinhead* (*oep*). Mutations in *oep* lead to a severe loss of mesendoderm structures [57] and are therefore strictly required for proper germ layer formation. Interestingly, *oep* mutation can be rescued completely by the expression of a Nodal-related molecule called *activin*. It was shown that Activin can bind to TaramA independently from the co-receptor oep [55, 58]. Receptor binding of Cyc/Oep or Activin results in autophosphorylation and binding of Smad2/3 transcription factors (see Fig. 2.2 and Ref. [2]). The latter get phosphorylated and associate with Smad4 to translocate into the nucleus, where they induce

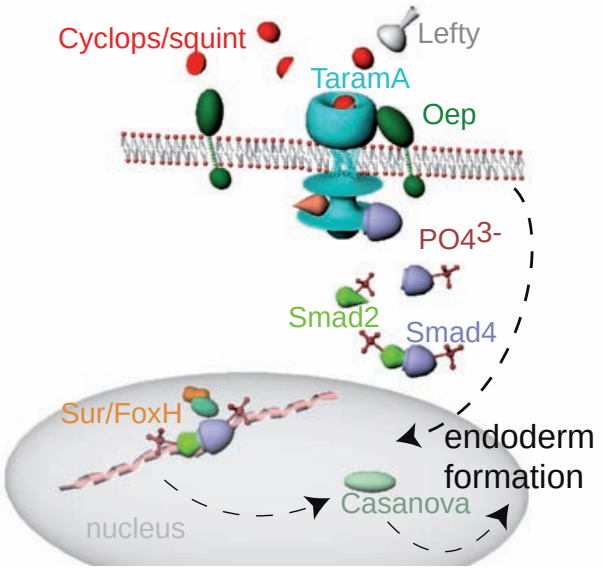

Fig. 2.2 Nodal-TGFβ signaling

Nodal signals such as Squint or Cyclops bind to their respective cognate receptor Taram-A with Oep as a co-receptor. Interaction with lefty inhibits Nodal signaling. This leads to the activation of the kinase function of Taram-A and a phosphorylation of Smad2 and Smad4. Smad4 shuttles Smad2 into the nucleus where it activates the transcription together with Schmalspur and Bonny & Clyde of target genes such as *casanova*.

transcription of mesendoderm target genes in concert with other factors. Some of these genes, e.g. *goosecoid* or *floating head*, mark the formation of mesodermal structures [59]. Direct targets of the Nodal signaling machinery involved in endoderm induction are the genes *casanova* and *bonny & clyde* [60]. *Casanova* (*cas*) is the central player in endoderm formation (see Fig. 2.2) and can induce endodermal markers even in absence of Nodal signaling, if expressed ectopically [61]. Once the gene transcription cascade is switched on, cells change not only their identity but also their physical properties [14, 9]. The direct correlation of physical or mechanical properties with behavior of the germ layer progenitor cells and how these maintain tissue boundaries is still missing. Especially, a link between signaling activity such as Nodal signaling and a change in the physical properties such as adhesion and elasticity, which leads to a change in cell behavior, is of particular interest. In general, the mechanism by which tissue boundaries are maintained is thought to involve a difference in the cell and tissue surface properties such as intercellular adhesion [19], cell-cell repulsion [62], acto-myosin contraction [63] and migration [9].

A complex signaling cascade selectively induces mesodermal or endodermal fate in germ layer progenitor cells.

2.1.3. Germ layer formation and epithelial mesenchymal transition

In zebrafish the three germ layers arise during gastrulation and at its end, build up a stratified tissue architecture (see Fig. 2.1). Later in development, the ectoderm, as the germ layer at the very top, will form skin, eyes and nerves. The inner layer, the endoderm will contribute to the development of

the lungs and thyroid and gut-derived structures. In between the ectoderm and the endoderm, the anlage of the mesoderm will generate blood, bones and muscles [64]. We have seen that Nodal signaling induces the formation of the germ layers and now we want to introduce cellular mechanisms which lead to a separation of one tissue type from another.

Epithelial mesenchymal transition is a process where cells become highly motile and invasive. It typically takes place during multicellular development and metastatic cancer progression.

Epithelial-mesenchymal transition (EMT) is known as the process when cells of an epithelial structure lose their adhesion to neighboring cells and invade the surrounding tissue. This is accompanied by a morphological transformation during which the columnar epithelial cells change into a amoeboid shape, indicative of a highly motile cell [65]. Several examples have been reported where EMT takes place during development, such as the migration of neural crest cells from an neuro-epithelium [66] or the ingression of endodermal cells during sea urchin gastrulation [67]. The latter example was long seen as the archetype of epithelial-mesenchymal transition when primary mesenchymal cells (PMC) lose contact from the ectoderm and move into the blastocoel to build up the future archenteron (see Fig. 2.3 A). Most obviously, ingressing cells decrease their cell-cell adhesion before internalization [67]. For this reason, adhesive switches and EMT are two concepts that are now as good as synonymous for one another [68].

EMT involves downregulation of adhesion molecules and activation of small GTPases to modulate cytoskeletal organization.

In general, the molecular pathway leading to an EMT is well conserved among different species and shows more or less similar characteristics. Because of its abundance all over the animal kingdom and its relation to many diseases such as cancer, a comprehensive description has been worked out. According to Shook and Keller [69], an EMT can be subdivided in the following events (see also Fig. 2.3 C), whereas not all but the majority of theses steps have to be taken:

1. Specification to a mesenchymal phenotype by alteration in gene expression
2. Disruption of the basal lamina so that the cells can invade the surrounding tissue
3. Changes in cell shape by an alteration of the acto-myosin function
4. De-epithelization and disruption of adherent contacts
5. Ingression and locomotion into the deep tissue layers
6. Maintenance of epithelial integrity after the transformed cells left the original site within the epithelium

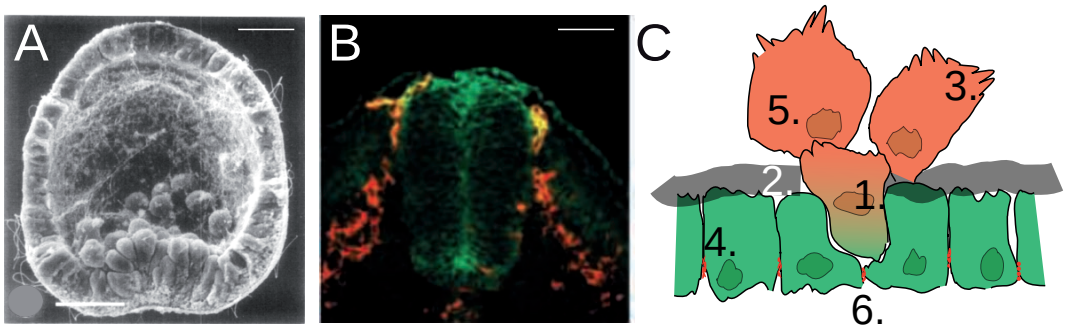

Fig. 2.3 Epithelial mesenchymal transition in development

A: Sea urchin gastrulation with ingression of single primary mesenchymal cells. Epithelial cells are columnar, whereas endodermal cells are round and loosely associated [67]. **B:** Neural crest cell (red) delaminate from the neural tube (green) during neuralation in the chick embryo. NCC migrate as single cells whereas the neural tube forms a columnar epithelium [66]. **C:** Schematic diagram of a classical EMT. Epithelial cells (green) adhere to a basal lamina (grey) and are connected with adherens junctions (red dots) and transform into a mesenchymal phenotype upon a change of gene expression pattern (indicated by red-green shading). Breakdown of adherens junctions and disruption of the basal lamina liberates cells which are about to transform into a mesenchymal phenotype, depicted as a amoeboid cells with numerous cell protrusions (orange). Notably, during transformation, epithelial integrity is maintained. Numbering indicates the steps described below.

The mentioned events are not necessarily restricted to fate changes in development but also take place during malignant transformation and cancer progression. A central role in the process of EMT is played by the cell adhesion molecule E-cadherin [65] and its regulator Snail [70]. E-cadherin is suggested to be differentially regulated in the forming germ layers [71] during zebrafish gastrulation. But what about the other points? Are the events during zebrafish gastrulation which lead to the three primary germ layers indeed best described as an EMT?

Recent published data explain zebrafish hypoblast formation on the basis of a change of the adhesive properties of the constituent cells [71]. Cells at the blastoderm margin lose their contact from epiblast and ingress as single cells. To achieve this, cells down-regulate their cell-cell adhesion molecules, or in parts, switch to alternative adhesion systems. Activation of Stat3* by the canonical Wnt/β-catenin pathway leads to a repression of E-cadherin [71]. This is realized by activating the transcription of Snail [72], a negative regulator of E-cadherin expression and an indicator of EMT [70], at the germ ring margin. Gastrulation of the sea urchin [67] and germ layer formation in

*Signal transducer and activator of transcription

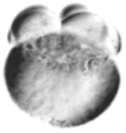

mice [73] are also suggested to involve a reduction in the adhesive properties of the invading endodermal cells. Besides a down-regulation of cell-cell adhesion molecules during EMT, the activation of small GTPases leads to a massive remodeling of the cytoskeletal system [74]. As a consequence, mesenchymal cells lose contact from their original tissue type, become invasive and are not tightly associated with a collective tissue but touch neighboring cells only transiently [75]. In contrast, epithelial cells form a tight cell layer and, if motile, migrate only within the epithelium. An example of this is medio-lateral intercalation during chick gastrulation, where two epithelial sheets move towards each other and cells change their neighbors concomitantly [76].

Although some of the features that are discussed above are true for zebrafish gastrulation, germ layer development cannot be explained as a classical EMT. Indeed, cytoskeletal changes have been described and mesendodermal cells become more motile [77]. Nevertheless, many differences exist compared to the exemplified description. Neither does the precursor epiblast represent an epithelium with *adherens junctions* between the cells, nor does the developing mesoderm maintain mesenchymal character [27]. During ingression of the cells to form the hypoblast, no basal laminae or other extracellular matrix structures have to be disrupted. Furthermore, the expression pattern of *THE* molecular landmark of a classical EMT, Snail, that is detected at the beginning of gastrulation around the germ ring margin by *in-situ* hybridisation (ISH, [72]), ceases shortly after hypoblast invagination in the axial mesoderm*. While the initial stages of mesodermal ingression are accompanied by a down-regulation of E-cadherin†, immediately after hypoblast formation, the same cells upregulate again their cell-cell adhesion molecules [78, 79, 27] leaving the contribution of adhesion in this process unclear.

Zebrafish gastrulation cannot be characterized by a classical EMT

Perhaps zebrafish gastrulation can be called a *transient* EMT occurring in the organizer, but the scenarios leading to a separation cannot explain why the germ layers stay separated after they have formed. The cells not only change their adhesive properties during EMT, but also modify their mechanical properties which determine their resistance to external forces. Mesenchymal cells for example are often very soft compared to epithelial cells, permitting an efficient migration through 3D extracellular structures [80, 23]. Such changes are often induced by an alteration of actin organization regulated by small GTPases such as Rho, Rac and Cdc42. That mechanical forces can induce

*Paraxial mesodermal cells still express Snail until the end of gastrulation [72]

†E-cadherin is transcriptionally controlled by Snail, resulting in a negative feedback

and alter gene expression pattern has been shown several times [81, 82]. Surprisingly, the reverse effect, how cell fate transformation alters the mechanics of a cell, is not entirely understood during development. By using AFM to measure piconewton forces and the convenience of zebrafish as a vertebrate model system, we unite these advantages to unearth these yet hidden answers. But where do we stand now in our knowledge of how physical properties of cells influence their behavior to act on tissue formation?

2.2. Physical properties of cells during multicellular development

The differentiation of an organism relies on an unambiguous communication of the constituting cells by secreted signal molecules and growth factors. However, that is not everything. Development is determined by many different cues from the environment, e.g. extracellular matrix stiffness [83], gravity or bodily contacts [84]. It is clear that cells in all types of tissues are subjected to forces, the magnitude depends on the location of the cells in the organism. Epithelia *per se* experience large forces, because they generally shield the internal tissues of an organism from the external environment. These forces result in deformations within the plane of the epithelium (stretching) and out-of-plane deformations (bending). Large forces for example occur in teeth, cartilage and bone tissue [85] of multicellular animals because they have to bear the weight of the whole individuum. It is clear that under such large loads, tissues and cells deform from their 'equilibrium' shape*. Therefore, these tissues have evolved to bear large stresses and minimize the strain, and it is not surprising that teeth and bones are very stiff structures. Yet even much smaller forces have a great influence on cell behavior on the minute scale. Several studies have indicated that stretching or compression of a cell can activate load-dependent ion channels which in turn generate an action potential [86], gene expression [81] or lead to phosphorylation of proteins which remodel the cytoskeleton [87].

Much is known about how mechanical properties of tissue culture cells or extracellular matrix (ECM) structures influence cell behavior [83, 88, 89, 90, 91, 92, 93, 94]. Up to now, a lot of systems have been analyzed where cells

Mechanical properties of cellular environment influences cell fate and behavior in certain cell culture lines.

*quotation marks indicate that not a physical, but rather a conceptual cell state is meant - in biology, a state of chemical equilibrium would lead unavoidably to the death of the organism. Specifically here, it is indicated that no external forces other than gravitation acts on the cell.

are capable of sensing and interpreting mechanical forces from their environment. These systems range from stretch-activated ion channels [86], mechanosensitive release of neurotransmitters [95] to tensile stresses in arteries imposed by the blood flow [96]. Recently, elasticity of the extracellular matrix was shown to influence the differentiation of a mesenchymal stem cell line into different cell types [83]. Soft ECM induced a neurogenic fate, whereas stiff substrates were myogenic and even stiffer matrices induced the formation of bone-derived structures. It could be shown that differentiation of the stem cells strongly depends on processes involving non-muscle myosins such as myosin II. But not only elasticity of the extracellular matrix was shown to determine the fate of undifferentiated cells. Also different cell shapes modulate differentiation of human mesenchymal stem cells: If allowed to flatten on adhesive substrates, cells differentiated into osteogenic precursors, whereas non-spread round cells were committed to a adipocytic cell fate [94]. Here again, acto-myosin contractility was necessary to induce differentiation. Despite the understanding of how cells sense and interpret mechanical forces, less knowledge is available on how the generation of forces alters tissue dynamics.

2.2.1. Mechanical forces during tissue formation

A lot of work has been dedicated to elucidating environmental cues in the specification of undifferentiated tissue culture cells. Much less, however, is known about how physical forces modulate morphogenesis of an organism. Next to the determination of cell fate within a tissue, the relative positioning of two tissues is driven by physical forces. A likely scenario for this can be the following: A cell alters its mechanical properties and gets softer while differentiating. Therefore it cannot integrate in the existing tissue, is expelled and able to form a new progenitor tissue. Although many studies have suggested that a change of cell behavior in the organism is associated with a change in their mechanical properties, a quantitative description of physical forces and cell behavior during development of an organism is still lacking. In general, many concepts exist of how physical forces act on cells and their interfaces to drive tissue repositioning. The following section summarizes three concepts how mechanical cell properties influence separation and patterning of two tissues.

Many scenarios explain morphogenesis on the basis of mechanical cell properties but remain to be proven experimentally.

Cell sorting and tissue self-assembly

One of the first examinations of this problem by Roux more than 100 years ago, traced back tissue formation to 'some' kinetic properties of the cells [97]. He dissociated tissues and recorded the movement of individual cells to propose that cells produce diffusible substances that attract or repel certain cell types during the re-aggregation process. The substances were not known back then. While other studies could not confirm those findings [98], more elaborate investigations were encouraged. Johannes Holtfreter and his student Philipp L. Townes [15] performed a series of re-aggregation experiments on chemically dissociated tissues in different combinations. The dissociated cell mixtures recombine *in-vitro* according to their *in-vivo* origin and form structures resembling a natural configuration. Co-culturing randomly arranged cells from amphibian medullary plate (neural tissue), epidermis and axial mesoderm sort out and formed centrally located neural tissue surrounded by mesenchyme and epidermis on the very surface. Townes and Holtfreter also provided a mechanistic explanation for these phenomena. They suggest that the participating cells perform the same kind of 'inherent' movement *in-vitro* as they would do *in-vivo*. These cell inherent migratory tendencies or directed movements lead to a sorting and the stratification into the normal germ layer configurations. Further tissue segregation then becomes complete and is maintained not only by directed movement but also by the emergence of selective cell adhesion [15]. These observations later led to one of the biggest dogmas in developmental biology.

Cell sorting and tissue reorganization is dependent on selective affinity and directed migration, according to Townes and Holtfreter [15].

The same problem was caught up not much later by Malcolm Steinberg in the early '60s [16, 99]. Steinberg suggested that cells have a preference of interacting with like cells over unlike cells. Performing cell sorting experiments, in which he mixed disaggregated cells of two tissue types of different origin, he could find that one tissue is always surrounded by another, adopting a central position within an heterotypic aggregate (see Fig. 2.5 A). In contrast to Townes and Holtfreter [15], he argued that directed migration cannot account for the occurrence of sorting, leaving 'the preferential cohesion of the internally segregating cells when they encounter one another through their random movements' as the more likely explanation for the sorting process.

The *Differential Adhesion Hypothesis* proposed morphogenesis on the basis of surface energetic properties of the constituent tissue types which behave like ordinary liquids.

His experiments led him to formulate the *Differential Adhesion Hypothesis (DAH)*. Keypoints herein are [100, 16, 101]:

1. the system is comprised of discrete units of two types

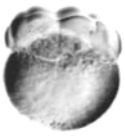

2. the units are mobile and not spatially fixed

3. the units adhere and cohere with different strength to reduce the interfacial free energy

According to this definition, the analogy of cells in tissues to molecules in liquids becomes apparent (see Fig. 2.4). Water molecules are discrete entities. So are cells. Water molecules in a drop are mobile. Cells, either in a tissue or an re-aggregate, are mobile too. Water molecules attract each other with intermolecular hydrogen bonds. Cells adhere with specific cell-adhesion molecules.

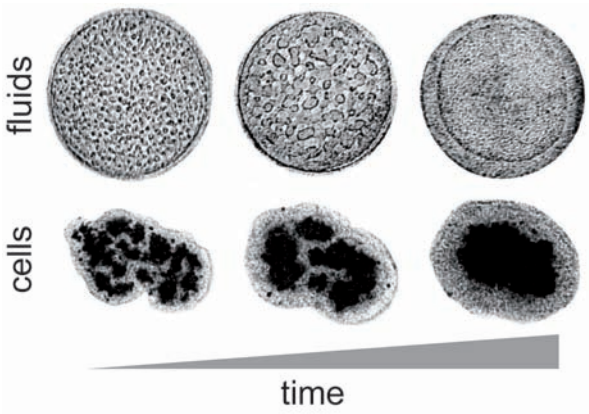

Fig. 2.4 Fluid phase separation and cell sorting

Phase separation of immiscible fluids resembles sorting of two heterologous tissue types [17]. **Upper panel:** Gas and liquid phase ordering in SF6 under reduced gravity. **Lower panel:** Sorting out of chicken embryonic pigmented epithelial cells (dark) from chicken embryonic neural retinal cells (light).

If not subjected to external forces, a drop of water will always adopt a spherical shape. Similarly, an irregular cluster of cells will always round up and form a sphere when placed in culture medium. Steinberg suggested that the force produced during rounding can be best explained by the concept of surface tension* [17, 99]. The molecules on the surface of the water droplet experience a resultant force towards the center of the drop due to its surface tension [102]. Therefore, the boundary contracts and reduces its area. Equally, cells at the surface of an aggregate experience a net force towards the center. He realized that cell-sorting movements in explanted tissue masses are analogous to rounding-up, droplet coalescence and the break-up of emulsions into homogeneous phases in immiscible liquids (see Fig. 2.4) Steinberg himself pointed out in his seminal series of publications that "*one might expect many features of these cellular systems to imitate comparable features of oil-and-water systems. The very process of sorting out of two kinds of cells*

Sorting of a heterologous cell mixtures is analog to phase separation of two immiscible liquids due to differences in surface tension.

*The surface tension is defined as the amount of energy that is required to increase the surface of a material by one unit area.

to produce an external tissue and ... an internal tissue is a perfect imitation of the breaking of a dispersion of one liquid in another immiscible liquid of similar density.".

When an emulsion of liquids separates and forms a sphere-within-a-sphere, the outer phase has the least attraction among its molecules and can be measured as a surface tension. When two tissues separate, just like liquids, the external mass was argued to be the one with the lower cohesion among its cells [99]. The cohesion of the cells within an aggregate can be quantified and expressed as tissue surface tension [103]. Therefore, the DAH has predictive power. Assuming that a certain tissue type minimizes its surface free energy proportional to the cell adhesion strength one would predict that the stronger adherent cell type will always end up in the center of an heterotypic aggregate. This implies that a hierarchy of sorting corresponds to a hierarchy in cellular cohesiveness, meaning that cohesiveness is a transitive property [104]. In other words, when tissue A has a higher adhesion than tissue B, and tissue B a stronger adhesion than tissue C, tissue A will always sort internally when combined with tissues B and C [101, 105]. The conditions for the sorting of a heterologous tissue mixture on the basis of their surface energetic properties yields the following relations:

$$\text{separation:} \quad W_A \geq W_B > W_{AB} \tag{Eq. 2.1}$$

$$\text{spreading:} \quad W_{AB} < \frac{W_A + W_B}{2} \quad \text{with} \quad W_{AB} \geq W_B \tag{Eq. 2.2}$$

$$\text{mixing:} \quad W_{AB} \geq \frac{W_A + W_B}{2} \tag{Eq. 2.3}$$

In Eq. 2.1, complete separation or incomplete spreading of one tissue over another takes place, because the units maximize (homophilic) contacts among themselves rather than between each other and reduce the contact area of heterologous interactions (red arrows in Fig. 2.5 B). Complete spreading will occur when Eq. 2.2 is fulfilled. Herein, the adhesion of celltype A is maximized, whereas the heterologous adhesion is intermediate between cell type A and B. An extreme case can be observed when the adhesion between the different cell types is largest, e.g. when the heterotypic contacts are preferred. Then, Eq. 2.3 leads to complete mixing and is called checkerboard pattern because of the alternate occurrence of the different cell types in a sorting configuration (red arrows in Fig. 2.5 A and Ref. [106]).

In most of the cases during animal development, tissues do not disintegrate

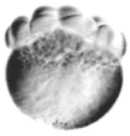

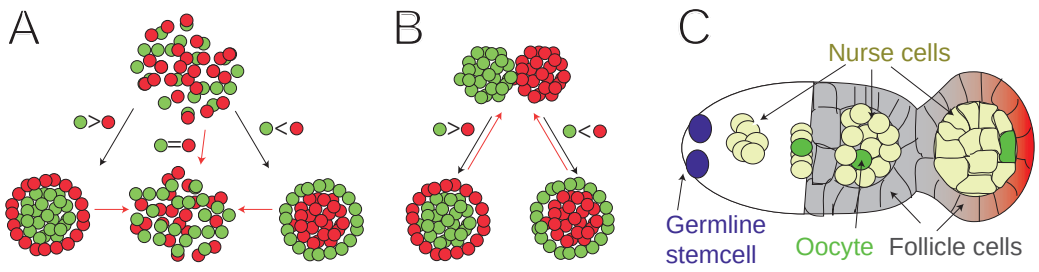

Fig. 2.5 Differential adhesion determines tissue positioning

A: Cell sorting of an initially intermixed heterotypic cell suspension. Cells can either separate or stay intermixed. According to the DAH, from left to right the red cells have a lower, equal and higher adhesion compared to the green cells [107]. The black arrow leads to tissue envelopment (Eq. 2.2) while the red arrow indicates mixing according to Eq. 2.3. **B:** Similar tissue configuration can be achieved when two tissue aggregates are juxtaposed. The tissue with the lower adhesion molecule expression and surface tension will flow around the other with the higher expression (red arrow, Eq. 2.1). **C:** Drosophila oocyte (green) is guided and positioned by differential expression of E-cadherin in the neighboring follicle cells (grey) [108]. Red shaded cells depict increased expression of E-cadherin.

and have to sort out again. This problem was also recognized by Steinberg and he could show that the same patterns of tissue boundaries are achieved when two different tissue balls are placed next to each other (see Fig. 2.5 B and Ref. [16]). Then, one aggregate with the lower surface tension and perhaps adhesion will spread around the other aggregate, creating a sphere-within-a-sphere as if the two tissues have been completely intermixed.

Nevertheless, real sorting of cells on the basis of differentially expressed adhesion molecules was observed during oogenesis in *Drososphila* oocytes [108]. The positioning of the oocyte in this system is mediated by E-cadherin, whose highest concentration could be found at the interface between the oocyte and the most posterior follicle cell (see Fig. 2.5 A). The oocyte attaches itself selectively to the follicle cell expressing E-cadherin (shown as red shading in Fig. 4.2 C) and competes with its sister cells, which do not express high amounts of E-cadherin. Positioning fails if E-cadherin in the posterior follicle cell is deleted, showing that cell adhesion is sufficient to guide proper cell sorting [108].

Positioning of *Drosophila* oocyte can be explained by differential adhesion among the constiutent cells.

Despite the efforts that have been made to provide unambiguous proof for the DAH, surprisingly little evidence is presented on how adhesion-governed tissue surface tension directs morphogenesis *in-vivo*.

First doubts Tissue sorting and tissue surface tension have been hypothesized to originate in the cell's adhesive properties [16]. The first doubts that cell adhesion alone can direct sorting behavior *in-vitro* and germ layer formation *in-vivo* arose with several studies in the early '70s [109, 110, 111, 112]. Showing that cytochalasin B, a potent actin depolymerizing agent, inhibits cell sorting and tissue spreading reversibly, demonstrated that the disruption of the contractile apparatus prevents cell sorting [109]. 14 years after the formulation of the DAH, the authors stated "*that the specific sorting of cells may result from different mechanisms than from those involved in the initial formation of aggregates*". Although experimental evidence has been communicated that cell sorting is indeed facilitated by a differential adhesion-governed hierarchy of tissue surface energies [113], it is very likely that other cell properties influence the patterning of a tissue *in-vivo* [112, 114, 115].

'Surface tension' is a physical equilibrium property that is described purely on the basis of the attraction of the constituting units and the surface energy of the system. In biology it is difficult to reduce a system or an event to only one component, and the question remains which properties of individual cells determine the effective surface tension of a tissue [116]. Therefore, we have to look for a proper definition and for properties that influence the surface tension, meaning the tendency to minimize the surface area of the tissue of interest. Among them, adhesion [16] has been extensively studied, but up to now only few examples have been observed *in-vivo* where a differential expression of cell adhesion molecules influences tissue behavior [108, 117]. Cell cortex tension [118] has been proposed* but there are many more cell properties which influence the tissue geometry.

During his classical sorting and enveloping experiments, Steinberg used cells from different germ layers, namely the ectoderm, mesoderm and the endoderm of *Rana pipiens* and found the ectoderm enveloped by the mesoderm [18]. This is in contrast to the situation *in-vivo*, which was also the main criticism of his DAH that aimed to explain the behavior of tissue not only *in-vitro* but also *in-vivo*. Furthermore, surface tension driven processes cause an aggregate to minimize the surface area which always lead to spherical aggregates *in-vitro*, whereas *in-vivo* tissues are hardly spherical but reside in complex shapes [119]. Furthermore, surface tension as a physical property defines the free energy change associated with an area change of a substance in vacuum. Tissues usually do not exist in a vacuum and can only be characterized by an

Surface tension determines the shape of tissues *in-vitro* [19] and partially *in-vivo* [119] but does not explain all phenomena [120].

*and will be analyzed in detail in this work

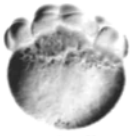

interfacial tension*. This energy change, therefore, strongly depends on the surrounding environment. Similarly, experiments conducted *in-vitro* do not necessarily match the situation *in-vivo*. Explanted mesenchymal aggregates round up *in-vitro* whereas *in-vivo* these aggregates are elongated when ectoderm are present. When such mesenchymal aggregates are now surrounded by an epithelial layer *in-vitro*, they keep their elongated shape and do not round-up. Experiments could show that the adjacent ectoderm has a surface tension relieving effect and influences the shape of the mesenchymal tissues in its vicinity [119]. This 'coating' effect is linked to an adhesive interaction [119] between the two tissues. Therefore, the surface tension of an isolated aggregate alone cannot predict morphogenesis *per se* because it could be modified by the existence of other tissue types.

Alternative explanations for tissue self-assembly An alternative explanation for tissue positioning and cell sorting was proposed by Harris [20] and much later by Lecuit [22]. Just by enumerating the difference between cell aggregates and liquid droplets, he came up with a new interpretation, now known as *Differential Surface Contraction Hypothesis (DSC)*. Harris proposed that the same outcomes of the DAH can be reached by assuming a differential contraction among the constituent cell types and is not necessarily a pure consequence of a differential adhesion between the cells. But he also pointed out that adhesion in general is still important and not negligible. To explain tissue self assembly on the basis of differential contractions, Harris had to make the following assumptions:

Differential contraction can have the same consequences on tissue positioning and cell sorting as differential adhesion among the constituent cell types.

- the cells show a uniform contraction of the cell cortex when they face the external medium
- the contractions are relieved when the cells contact a cell of another histotype leading to a 'relaxed' interface
- the contractions are relieved even stronger when the cells contact a cell of the same histotype
- the two cell types involved have differential contractile properties

Importantly, there exists a hierarchy among cell contractions, and the contractions in the cell are even more reduced when it is in contact with a cell of the

*The free energy change associated with an area expansion in a certain medium.

same histotype. Therefore, the more contractile a given cell type is over its exposed surface*, the more internally it should sort out relative to other, less contractile, cell types. Harris' formulation of cell sorting is not as elegant as the DAH, because it assumes that the endogenous differences in contraction are dependent on the cell environment†, but it is probably more correct.

First hints that medium-induced contraction can cause aggregate rounding came from a study using explanted neural plates [121, 122]. When put into culture, bundles of microfilaments were induced to form at the basal surfaces and the whole explant was forced to round up. This idea inspired Lecuit to contemplate about Echinoid (Ed) driven cell sorting in *Drosophila* epithelia [22]. He assumed that Ed plays a role during cell sorting in that it supports the assembly of a contractile acto-myosin ring at *adherens junctions* leading to apical constriction and subsequent cell sorting by exerting tension along the interface. He refined this idea and communicated that in general acto-myosin based cortex tension is a fundamental property of cells which determines the positioning of tissues by modulating their adhesive interactions [118, 123]. If there is indeed a differential cortex tension in these cells or if acto-myosin contractions are able to drive cell sorting in general remains to be elucidated (see Sec. 4).

Cell packing

Cell packing has gained interest in recent years, because it serves as a 'playground' to combine mathematical modeling with developmental biology. Many geometric considerations have been transferred to classical biological problems. As an example, cell divisions in epithelia influence the geometry of the tissue structure, especially the packing order of the cell in the *Drosophila* wing disc epithelium [124]. Optimization of cell packing to control form and shapes of embryos can be achieved by various means. Local tissue growth in an restricted environment can modify a tissue and has been shown on cultured endothelial cells [125] with implication for tumor growth and morphogenesis [126].

Another peculiar example is the patterning of cone cells in the *Drosophila* retina [127]. The retina normally consists of four cone cells which are surrounded by two primary pigment cells (see Fig. 2.6). When the cone cells assemble in the ommatidium, they always adopt the same topology. It has

Cell packing is analog to the packing of soap bubbles but not solely determined by area minimization principles [120].

*Actually it is the gradient of the loss of contractions when the cell changes its interface from medium to a cell of the same origin.

†A characteristic of an interfacial tension as described above.

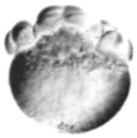

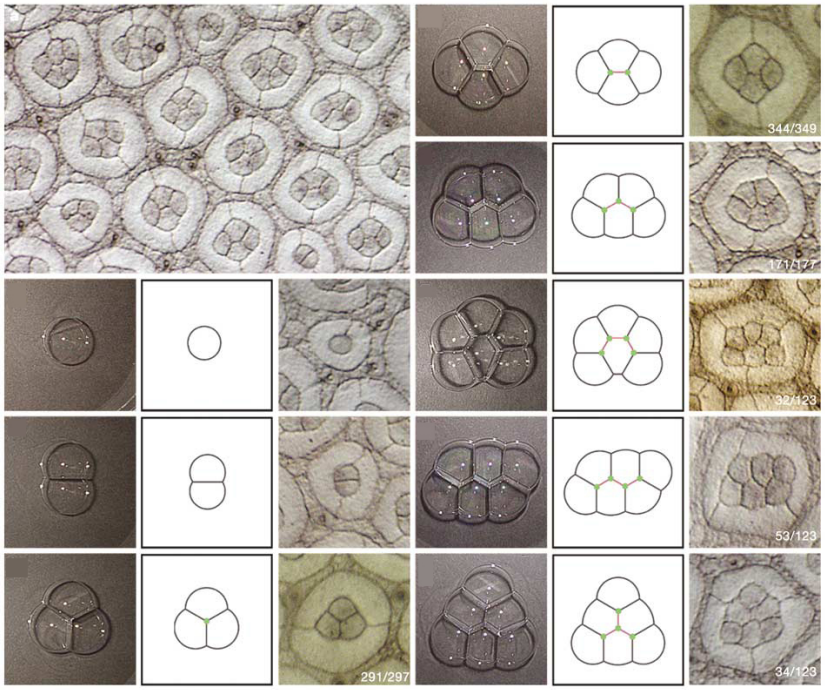

Fig. 2.6 Cell surface mechanics in development

The *Drosophila* retina is a prototypical example of how cell surface mechanics mediate patterning during development. In wildtype animals four cone cells are surrounded by two pigment cells. In *roi* mutants the number of cells is ill-defined but nevertheless they still pack together like an analogous configuration of soap bubbles [127].

already been recognized that surface mechanical properties such as surface tension dictates the shape of simple systems like bubbles, which only allows three interfaces to meet at one point [128]. Anything else is energetically not favored. Although cells are not soap bubbles, they show similar topologies. Interestingly, *Drosophila* mutants which show a number of cone cells deviating from four, showed the same packing as an equivocal number of soap bubbles would show (see Fig. 2.6), but still could only adopt the shape dictated by Plateau's rule. In other words, no more than three cone cells meet at one point in any type of configuration even if five or more cells were involved (see Fig. 2.6 and Ref. [127, 129]). Furthermore, it was shown that *Drosophila* N-cadherin (DN-cad) localizes at the junction between two cone cells but not between a cone cell and a pigment cell, where only *Drosophila* E-cadherin (DE-cad) was detected. Knocking down DN-cad or over-expressing it in the neighboring pigment cells leads to a severe failure of retina patterning, but not to an over-expression of DE-cad, highlighting a process driven by differential adhesion among neighboring cells. On the basis of these experiments, it has

been proposed that a regulated distribution of different Cadherins mediates the area minimization of the cone cells to obey Plateau's rule [127]. This work shows for the first time how surface mechanics influence the patterning of cells into complex structures and how basic, simple physical principles govern the packing of cells into tissues. But nevertheless, it is clear that cells are more complex than soap bubbles and that their shapes are not governed by equilibrium properties such as surface tension. Computer simulations have shown that active processes such as actomyosin contractions have to be considered to explain the patterning of the retina [120]. In general, myosin contractions are needed to perform complex shape changes in single cells [130] and tissues [63, 131].

Apical constriction

Apical constriction (AC) is one of the most intensively studied mechanisms regarding how acto-myosin activity changes the shape of a tissue [132, 131, 75, 76, 133]. It is a process where an flat epithelial tissue is forced into a highly curved arrangement (see Fig. 2.7). Neurulation, where the neural tube forms out of a flat neural plate (see Fig. 2.7 B), has long been attributed to arise from differential adhesion between cells of the prospective tube and the neighboring ectodermal epithelium [134]. The latter was shown to express E-cadherin, while the tube cell additionally expresses N-cadherin. This was thought to be sufficient to explain tissue separation. In addition to this differential adhesion-driven process, contraction of an apical located acto-myosin belt helps to force the neural tube into its new shape and to separate it from the neighboring tissue [132]. Next to neurulation, gastrulation in *Drosophila* [131] and *Xenopus* [133] is an example in which constriction of apical cells leads to invagination and the formation of a new tissue (see Fig. 2.7 A, C). A lot of knowledge on how mechanical properties of cells influence tissue shape has been derived from studies on *Xenopus* gastrulation [133]. Unfortunately, no measurements of the physical forces involved in this process have been presented so far.

Apical constriction is a way to separate two tissues from a common ancestor. It is driven by a highly controlled myosin activity.

Apical constriction is clearly a tissue phenomenon, and the question remains how mechanical properties of single cells can influence, if not drive such events. Keller et al. [133] described apical constriction as "*an isotropic force-generating process that acts in a mechanically anisotropic environment, which channels its effect towards displacing the outer epithelium inwards*". This means that cells elongate when they constrict apically, whereas this elongation makes tissue bending ineffective (see Fig. 2.7 C). The less a cell elongates, the

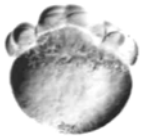

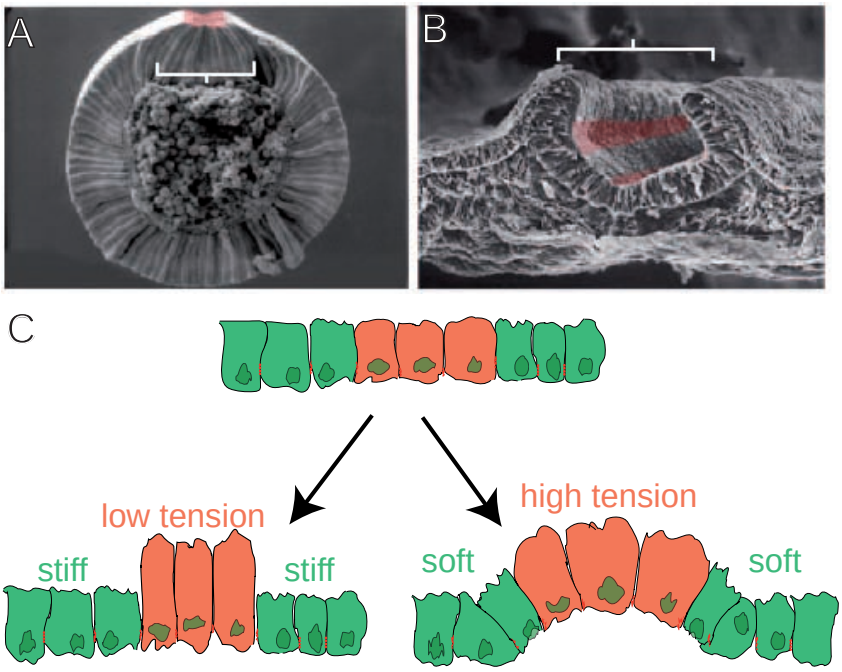

Fig. 2.7 Apical constriction and cortex tension

A: Electron micrograph of a gastrulating *Drosophila* embryo with invaginating mesodermal cells that undergo apical constriction. **B:** Neurulation of the chick embryo results from apical constriction (shaded in pink) and tissue bending. (A and B taken from [118]) **C:** Schematic representation of how tissue bending is influenced by single cell mechanics. The cortical tension of the red, invaginating cells reduces elongation, thus bending of the tissue. Simultaneously, if the surrounding epithelial cells are too stiff, they cannot bend and reduce the effect of constriction leading to an elongated rather a bottle cell shape.

more effective it is in bending the tissue. This behavior suggests that resistance to apical-basal elongation is important in bending a cell sheet by apical constriction. There are now several factors reducing elongation of the invaginating cells. One could be an external force, e.g existence of other cells on the basal side of the epithelium that are stiff enough to be not deformed by the constricting invagination zone. Another mechanism could be a *cell cortical tension** reducing apical-basal deformation. Basolateral cortical tension would resist apical-basal elongation, with higher tension driving the cell toward the spherical shape and severe bending of the tissue. A specialized apical-basal reinforcement of the cytoskeleton could also resist elongation, either by an active contraction or an increased elastic resistance to stretching in this dimension. Taken together, AC is a proto-typical example of how two tissues separate from

*The concept and cellular origin of cortex tension will be introduced in Sec. 2.2.2 and 2.5.2.

each other on the basis of differential mechanical properties of the constituent cells.

2.2.2. Shaping cells

Unlike in mathematics, the whole in biology is usually more than the sum of its single parts. This famous saying surely is true but sometimes the shape and the formation of tissues cannot only be expressed by the ensemble property of the respective cell type. Especially when new tissues are formed during gastrulation, mechanical properties of a small group of cells can change and be decisive for the development of the whole organism. Forces are beginning to be considered important for this process [135]. The cell property responsible for scaling the strain to an external or internal stress is elasticity or tension within the cell.

A variety of cellular processes that require a physical interaction of the cell with the surrounding environment are controlled by cell cortex tension. These include cell migration [136, 137, 130, 138], protrusion formation such as cell surface blebbing [139], phagocytosis [140], tissue deformation like apical constriction [133, 131] and adhesion in general [118]. The origin for a cellular cortex tension is an interplay between an outward-directed hydrostatic pressure [141, 142, 143] and a net inward-directed myosin contractile force [136]. More specialized functions are aided by other molecules. During cytokinesis for example, tissue culture cells undergo dramatic cell shape changes and, while rounding up, produce significant forces. These forces are partially coordinated by the actin binding protein Moesin [144], an ERM member which couples the cortical cytoskeleton to the plasma membrane (see Sec. 6.2). Cell shape changes in general require generation of an intracellular force, which is then transmitted to the environment. At this interface, a dominant actin-cortex is assembled and resides in a pre-stressed state of higher potential energy which allows the cell to react quickly in response to intracellular regulation as well as extracellular signals. Such signals can be chemokines like SDF-1 which have been shown to induce extensive plasma-membrane blebbing upon modulation of the actin cytoskeleton [130] during migration of zebrafish germ cells.

Cortex tension drives many cell processes that include an interaction with the environment, such as migration, endocytosis and adhesion.

Cortex tension has a great influence on the shape of an interface of two or more adhering cells [120, 127, 118]. Homophilic Cadherin adhesion tends to globally flatten an interface between two adhering cells, thus creating a lower local curvature in the adhering parts (see Fig. 2.8 A). Concomitantly it locally increases the contact area [120]. This is consistent with the idea that adhe-

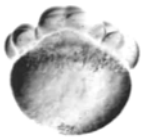

sion reduces intercellular interfacial tension [118].The Cadherin-mediated contacts are stabilized intracellularly by α- and β-catenin which interact indirectly with actin cytoskeleton. On top of that, it has been shown that E-cadherin coordinates the assembly of different actin structures, such as belts and networks in the contact zone [145]. Therefore, adhesive interactions presumably also modulate cortex tension of the interface by coordinating actin assemblies. Such assemblies, on the other hand, have been shown to modulate adhesion [146, 147], presumably creating a feedback loop between adhesion and cortex tension. Depending on the type of cell, different scenarios can happen (see Fig. 2.8).

Cortex tension is believed to counteract adhesion, e.g. a high tension impedes high adhesion and could result in repulsion [148]

1. When two cells adhere and a contractile acto-myosin network remains at the cell-cell boundary, it increases the cortical tension which reduces the contact surface. A higher tension impedes adhesion simply by forcing the shapes into a sphere.

2. When adhesion overcomes the tension of the cortical network, the interface flattens and increases. Alternatively, engagement can cause the network to disassemble, therefore allowing an increase of the contact zone.

In other words, adhesion and cortex tension have opposite effects on the contact size between two cells and hence interfacial tension, because adhesion tends to maximize the contact, while cortex tension tries to minimize it (see Fig. 2.8 A,B). The minimization effect can be easily explained by a maximization of curvature, which would lead to point contact with infinite cortex tension. Similarly, with infinite adhesion, the two contacting bodies would collapse into a straight line, maximizing the interfacial contact between each other. Therefore, adhesion leads to a cell-cell contact increase which has to be balanced by cell cortex contractions. This scenario is well-explained in a recent model [120] that describes the packing of cone cells in the *Drosophila* retina [127]. Simulations showed that when the interfacial tension of this system is only determined by adhesion, incorrect topologies are obtained. If the interfacial tension is modeled as a combination of adhesion and cortex tension, correct topologies and geometries are obtained which correctly explains the situation *in-vivo*.

Next to cell contact formation, cortex tension is one of the main driving forces for plasma-membrane blebbing*. Because the cortex is under isomet-

*Next to cortex tension, osmotic pressure is proposed to create plasma-membrane bleb-

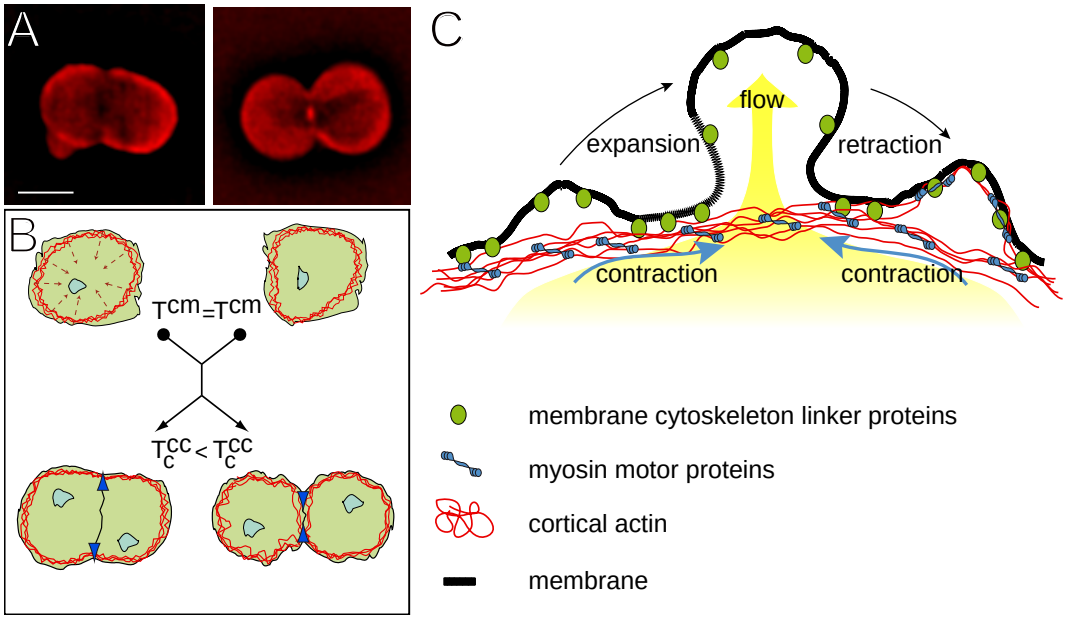

Fig. 2.8 Cortex tension in the cell

A: Fluorescence micrograph of two cells injected with Alexa-546 coupled actin monomers. The actin-localization at the cell-cell interface determines the cortex tension at this boundary and together with adhesion the length of the contact zone. **B:** Cells in solution have a homogenous actin localization around the cortex. The acto-myosin cortex contracts leading to an inward-directed net force. When they come into contact, actin distribution at the cell-cell interface determines the cortex tension and the shape of the doublet. A lower T_c^{cc} will lead to a larger contact length with the same adhesion between the cells [118]. Blue arrows indicate the preferred boundary behavior – expansion or retraction. **C:** Cell cortex tension influences blebbing activity. An isometric contraction of the cortex leads to an pressurized cytosol. Local cracks in the cortex or de-coupling of the membrane from the csk leads to a flow of cytosol into the spherical protrusion. Subsequent actin re-polymerization in the bleb and myosin contraction will re-incorporate the bleb into the cell body (after [149]).

ric contraction, the cytoplasm is believed to be under pressure (see Fig. 2.8 A and Ref. [142, 143]). Once a critical hole size is reached due to breakage of the cortical layer*, cytoplasm flows into the region, creating a bulge which is called membrane bleb. Without cortical tension, no protrusive activity would be detectable [151], resulting in a complete retraction of cell surface blebs. However, a tight regulation of cortex tension leads to localized blebbing activity [25] and can be used by the cell to break symmetry and to polarize [152] in one direction. Such local changes of the tension in the cortical actin network can be achieved by either reducing the thickness of the acto-myosin belt, mod-

bing [150].

*Either by locally increased contractility or decreased thickness of the cortex. Both can be triggered externally by signalling cascades such as PIP_2.

ulating the activity of contractile elements or the degree of cross-linking [152]. It has been shown that tumor cells use this mechanism to migrate efficiently in 3D environment possibly without the use of specific cell surface adhesions. Herein, an increased activity of the Rho pathway resulted in a higher myosin contraction and therefore multiple bleb nucleations [25]. Interestingly, the cortex is in a state close to its critical tension and it has been calculated that a stress-increase of only 10% in the cortex leads to acto-myosin network damage [152]. Therefore, cortex breakage seems to be an 'easy' way to polarize a completely symmetric, round cell. How this is achieved *in-vivo* is still unclear. A possible scenario would be a locally increased contraction after ligand binding to a certain cell receptor. Good candidates are G-protein coupled receptors which cause a liberation of PIP_2 to enhance myosin activity [153].

Plasma-membrane blebbing is the outward ballooning of the membrane as its cytoskeletal attachments are weakened. The balloon is infiltrated by cytosol whose flow is powered by a isometric contraction of the cell cortex.

Cortical myosins have also been shown to guide protrusion formation in endothelial cell. During angiogenic sprouting, endothelial cells branch from existing vessels to invade the surrounding environment. This protrusion formation is preceded by a local depletion of myosin that promotes formation to initiate angiogenesis [154]. Such a regulation of cortical stability suggests a further function of myosin in maintaining cortex tension as an actin-filament cross-linker.

Despite the emphasis put on acto-myosin driven processes during development, it is important to note that cell adhesion is a fundamental property of all multicellular organisms and that no individual development would be possible without it. Cells need to adhere to form a tissue, and tissues build up the whole organism. Therefore a lot of developmental processes have been shown to be governed by adhesion [16, 155, 19]. This is further underlined by the appearance of approximately 5000 publications in the PubMed library when the term "`cell + adhesion + morphogenesis`" is applied. But what is cell adhesion and how is it maintained?

2.3. Cell adhesion molecules

Cell adhesion is the process by which cells physically interact with their environment. This environment includes other cells in multicellular organisms or extracellular matrices (ECM). ECM in general is defined as a proteinous material which is deposited by cells between different organs or cells [153], but can also be anorganic, e.g. in bone or teeth. It has mainly structural roles, but also has signaling functions and serves as a guidance cue or trail for cell

migration. ECM can be as diverse as bone, tendon, connective tissues and also hair. These tissues are all made up of different molecules, such as Collagens and adhesion glycoproteins such as Fibronectin, Laminin and Vitronectin*. All of the mentioned proteins are ligands for a huge family of ECM receptors, the Integrins. There are also other ECM receptor apart of the Integrins. Integrins, however, are the most important ones. Before we go on to speak about the molecules that are typically involved in cell-cell-adhesion, for the sake of completeness, we will have a short look at the family of Integrin receptors†.

2.3.1. Integrins

Integrins are a huge family of heterodimeric ECM adhesion receptors consisting of one α and one β sub-unit. In all, there are 18 α and 8 β sub-units which form 24 different combinations [157]. Although most Integrins bind to more than one ECM protein, genetic studies have revealed that there are Integrins that have unique and irreplaceable functions [157]. The most abundant ligands are RGD (arginine, glycine, aspartate) containing peptides. The RGD motive is found in many proteins including Fibronectin, Vitronectin, Collagen, Laminin and many more [158]. This sequence is bound by a variety, probably 12 of the known 24 different Integrin heterodimers. Both α and β sub-units are involved in ligand binding, whereas ligand binding is possible only after activation of the Integrin, which results in a conformational change. This so-called *inside-out* signaling is primed by binding of the intracellular adaptor molecule Talin to the β sub-unit. This interactions straightens the molecules, forcing it from its inactive bent structure to an open, high-affinity conformation (see Fig. 2.9). Binding of both ligand and cytoplasmic proteins initiates focal complex formation, which eventually develop into stable focal adhesions [159]. These huge complexes consist of more than 50 proteins and are used by the cell to adhere to extracellular matrix components and to migrate on flat substrates [160, 161].

Integrins are heterodimeric adhesion receptors that bind extracellular ligands such ass collagen, laminin or fibronectin.

During development, Integrins have an important role. The classical example of Integrin-mediated tissue formation is gastrulation of *Xenopus*. Strong localized deposition of Fibronectin on the blastocoel roof is necessary for proper migration of mesodermal cells and formation of lamellipodia [164]. In line

*Hair is composed of Keratins, a special type of intermediate filaments which usually are found intracellularly [156] and are not considered further.

†Certain Integrins also participate in cell-cell adhesion, e.g. LFA-1 during the immune response.

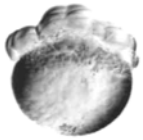

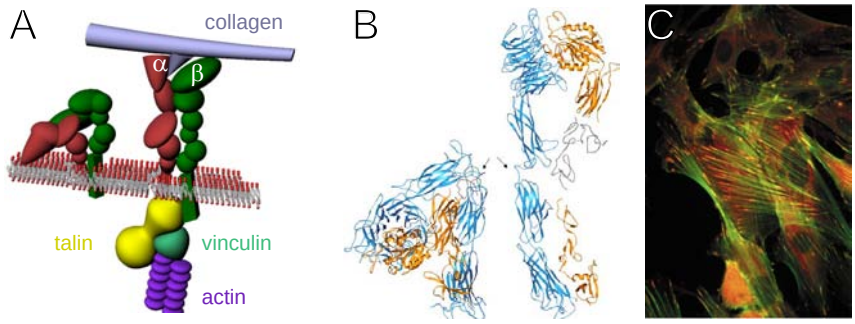

Fig. 2.9 Integrins structure and function

A: Schematic diagram of inactive and activated $\alpha\beta$ heterodimer. Upon ligand binding (collagen) and cytoplasmic association to adaptor molecules like talin, integrin adhesion receptor switch to a high affinity state. **B:** Crystal structure of the inactive and activated heterodimer [162]. **C:** Activation eventually leads to formation of focal complexes, depicted in red. Spatial overlap with actin (green) is visible and essential for focal adhesion function. Image after [163].

with the abundance and diversity, Integrins and their ligands have many more functions apart from their adhesive capacity. For example, the Integrin ligand Fibronectin is supposed to provide a guidance cue by binding chemotactic signals that influence migratory mesoderm. Furthermore, a change of one type of Integrin to another was shown to be a mechanism to regulate cell migration and cell fate. During morphogenesis of muscle cells, switching the expression between $\alpha 5$ and $\alpha 6$ Integrin subunit triggered differentiation of myoblasts to multinucleated muscle cells [165]. Integrins have also been implicated in boundary formation of different compartments in the brain. Variations of spatial and temporal expression of different kinds of Integrins control the spatial organization of cerebral cortex, and if perturbed, lead to severe disorganizations of the brain. Similar boundary maintenance of opposing tissue have been attributed to Cadherins [3], especially at the time of rhombomere formation during development.

2.3.2. Cadherins

Cadherin is a superfamily of Ca^{+}-dependent, homophilic adhesion molecules involved in cell-cell adhesion. Non-classical family members also have regulatory roles in mechanotransduction.

Cadherins are a huge family of calcium-dependent cell adhesion molecules [166] that generally interact with molecules of the same kind. They are composed of several Ig-like extracellular aminoterminal domains, comprising 110 aminoacids each [167]. The diversity among the Cadherins is enormous and they can be classified in proto- or atypical and classical Cadherins.

Protocadherins are expressed during various stages of vertebrate development and have been extensively studied in the formation of the nervous system [168]. Although Protocadherins have a weak adhesive purpose [169], they often have a signaling or regulatory function. Many protocadherins can induce cell sorting *in-vitro* [170] which is not due to their adhesion function. For example, Paraxial Protocadherin (PAPC) negatively regulates adhesion activity of classical Cadherins (C-cadherin) during *Xenopus* gastrulation [171]. Apart from homophilic interactions, protocadherins are also known to undergo heterophilic interactions. Protocadherin 15 for example interacts with Cadherin 23 in the mouse ear to establish tip-links between individual sensory hair-cells [86]. This is an example of Cadherins in mechanotransduction, where a mechanical signal - in this case sound waves - is converted into a biochemical signal by opening a stretch sensitive ion channel. Another interesting molecule is Protocadherin (Pcdh)-α. It carries a RGD motif and can facilitate interactions with Integrins *in-vitro*. Intracellularly it binds the actin bundling protein Fascin in neurofilaments and has been associated with higher brain functions such as long term potentiation [172]. In general, intracellular binding partners of non-classical Cadherins are diverse. They range from intermediate filaments for desmosomal associated molecules over tyrosine kinases known for protocadherins to the classical Cadherin-Catenin interactions [153].

Protocadherins have mainly signaling or regulatory functions such as Flamingo or PAPC.

Many Protocadherins are mainly involved in signal transduction during development and are called *atypical* Cadherins because their structure is largely different than the consensus architecture. Flamingo (Fmi), Fat and Dachsous (Ds) form central part in the planar cell polarity (PCP) pathway which was initially discovered during *Drosophila* wing morphogenesis [173, 174]. In zebrafish for example, Fmi was proposed to have a dual function to guide cell migration, one by signaling and another by mediating cell cohesion [175].

Structurally, the group of atypical Cadherins is much less conserved than other groups of Cadherins. The number of extracellular Ig-repeats can range from four (μ-Protocadherin, [176]) to 34 (Fat, [173]). Plasma membrane anchoring of the atypical Cadherins can be established via a 7 trans-membrane domain as in the case of Flamingo, or by a GPI anchorage [177]. Atypical members do not seem to have a major adhesive role [173], but are involved in addition to the signaling function, in regulating actin assembly by activating VASP complexes as has been shown for Fat1 [178]. Therefore, it appears that Ds, Fat, and Fmi mediate cell-cell interactions in signaling pathways which propagate polarity cues and regulate tissue size, and, however, are not just

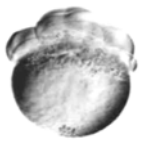

responsible for mechanical adhesion between cells.

Classical Cadherins exhibit five extracellular Cadherin repeats, named EC1-EC5 from the most distal part as shown in Fig. 2.10 A. Each domain of the extracellular part folds into characteristic Ig - like Cadherin domains, composed of a stacked array of six beta-sheets [179]. The interdomain boundaries are involved in binding three Ca^{2+} ions. Conserved residues like aspartic and glutamic acid bind the metal ion with different affinities, and are involved in straightening and stiffening of the protein [180]. This straight conformation is crucial to set up the molecule in its rod-like active form and is thought to be involved in the proper functionality of the molecules (see Fig. 2.10). Only if all three calcium binding sites are occupied in the interdomain boundary 1-2 (see domains in Fig. 2.11), is proper structure and hence stable adhesion ensured [180].

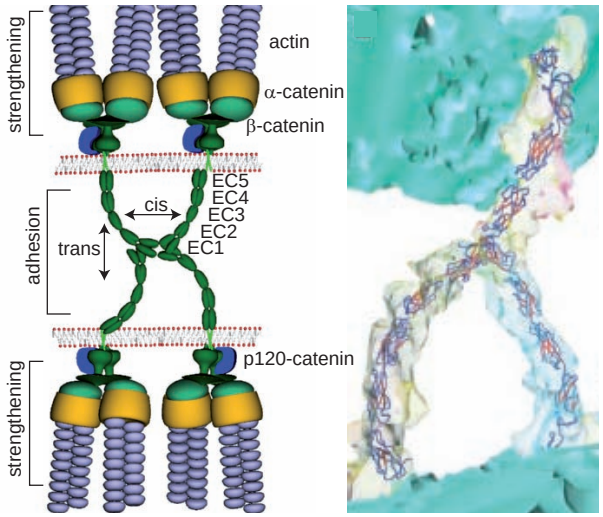

Fig. 2.10 Overall architecture of classical Cadherins

Left: Schematics of a Cadherin *cis* (on one cell) - trans (on opposing cells) dimer and binding its intracellular partners α-, β- and p120-catenin. Cadherin homophilic interaction occurs at its distal EC1 domain [181, 182]. How actin couples to the Cadherin-Catenin complex i not exactly known [145]. **Right:** Three Cadherin molecules modeled into a desmosomal knot [183] forming tip-to-tip adhesive complexes.

The five extracellular repeats are linked to the intracellular side by the means of a single pass transmembrane segment. The transmembrane segments (TMS) and cytoplasmic tails of classical Cadherins exhibit the highest homology among different family members [184]. E-cadherin TMS, for example, include heptad repeats of leucine residues, which are thought to promote lateral aggregation (dimerization) as it is known for various coiled coil motives [184].

The classical family of calcium-dependent adhesion molecules can be further separated into two distinct classes, type I and type II Cadherins. The main difference between both is the existence of an additional tryptophane residue at position four (Trp4) in type II Cadherins, in addition to the tryp-

tophane at position two (Trp2) [177, 168]. Specificity of classical Cadherins is still a matter of debate and is discussed controversially in the literature. Earlier experimental assays showed that type I Cadherins preferentially bind molecules of the same type [185, 186, 187]. More recent biophysical data on isolated adhesion molecules showed no kinetic preference of homophilicity over heterotypic binding [188, 189, 182, 190].

The aminoterminal tryptophane at position two (Trp2) is thought to play a crucial role in Cadherin function. It acts as a ligand for a highly conserved acceptor pocket composed of three residues (histidine, alanine, valine; HAV), in a second Cadherin molecule *on an opposing or on the same* cell. Figure 2.11 presents a 3D crystal structure of the EC1 domain with the Trp2 pointing into the HAV containing pocket. Mutation of either one of these residues results in strong reduction of adhesion [191]. Alternatively, occupation of the acceptor site by a tryptophane analog or a binding competitor, such as indole acetic acid, leads to a diminished Cadherin-Cadherin interaction [192, 193, 194]. The same tryptophan analogue was recently used to inhibit the binding of living cells to E-cadherin decorated surfaces [155]. Because certain tryptophane analogues were communicated to be cyto-toxic [195], an alternative competitor is widely used to switch-off the Cadherin function specifically. Similarly, HAV-containing peptides have been used extensively to reduce Cadherin mediated binding efficiently in cell culture studies [196].

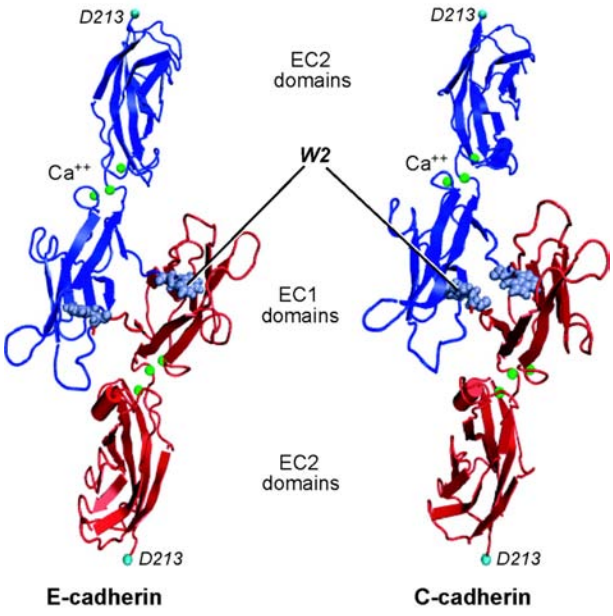

Fig. 2.11 Molecular basis of Cadherin adhesion

Crystal structure of the E-cadherin and C-cadherin homophilic interface. Calcium ions are needed to stabilize the inter-domain boundaries (green dots). The conserved tryptophane residue W2 sticks out and points into a conserved pocket consisting of histidine, alanin and valin (HAV). Picture taken from [197].

The link to the actin cytoskeleton is established by the means of adaptor molecules from the Catenin family (see Fig. 2.10 A). α, β and p120-catenins

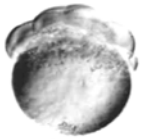

are the most prominent members of this family. Catenins not only establish a structural link, but can also take part in transducing signals from the plasma-membrane to the nucleus, and altering transcription of specific target genes. Herein, β-catenin has a major function and plays crucial roles during development [198]. As part of the canonical Wnt-pathway it travels forth and back to the nucleus and acts as a transcriptional regulator of various target genes as a response to growth-factors such as Wnt and Wingless. It was also shown to act as an inducer of dorsal mesoderm in *Xenopus* [199]. Therefore, over-expression of classical Cadherins could deplete the intracellular pool of β-catenin available for transcription activation.

In contrast to β-catenin, the role of α-catenin is not established in detail. It is supposed to participate in structural linkage between the Cadherin molecules and the actin cytoskeleton. For a long time it was thought that α-catenin directly cross-links intracellular Cadherin domains with the actin cytoskeleton (see Fig. 2.10 and Ref. [153]), but recent data suggest that this interaction is indirect [145]. An allosteric switch in α-catenin may mediate actin cytoskeleton reorganization [146]. Destruction of the actin cytoskeleton results in a complete loss of cell adhesion and is, therefore, strongly required for proper cell-cell contact [200].

Cadherins bind to the actin cytoskeleton on the intracellular side which is needed for efficient re-enforcement of the adhesion site.

The Catenin p120 has versatile functions. It regulates adhesion in several different ways, including the transport, stability, and function of Cadherins [201] and also binds to microtubules [202, 203]. Furthermore, p120-catenin participates in signaling pathways and was found to shuttle in and out of the nucleus to interact with *kaiso*, a transcriptional regulator of the zinc finger family [204].

Best known members of classical type I Cadherin family are N-cadherin*, C-cadherin†, R-cadherin‡ and E-cadherin§, which all primarily bind homophilically to molecules on opposing cells. E-cadherin has important roles during morphogenesis [3] and is the first adhesion molecule expressed in the beginning of a new lifeform [205]. It consists of about 800 amino-acids, and a total mass of 120 kDa after glycosylation [177]. During co-translational export into the endoplasmic reticulum, the molecule inserts with its N-terminus into the lumen of the extracellular side and gets further processed. Post-translational modifications include glycosylation as well as N-terminal trimming of the first

*Neuronal Cadherin found in mesenchymal cell or synapses
†Cleavage Cadherin found in *Xenopus* early development
‡Retinal Cadherin originally found in mouse retina
§Epithelial Cadherin is the flagship of all classical Cadherins

80 nucleotides in the late secretory pathway by specific convertases such as Furin [206, 207]. This is necessary to prevent the delivery of inactive precursor molecules, which would not be able to mediate cell adhesion, to the plasma membrane. Moreover, cleavage of the precursor also brings the crucial tryptophane residue, which is thought to be strongly involved in adhesion mechanism [182], to the 2nd position of the aminoterminal end.

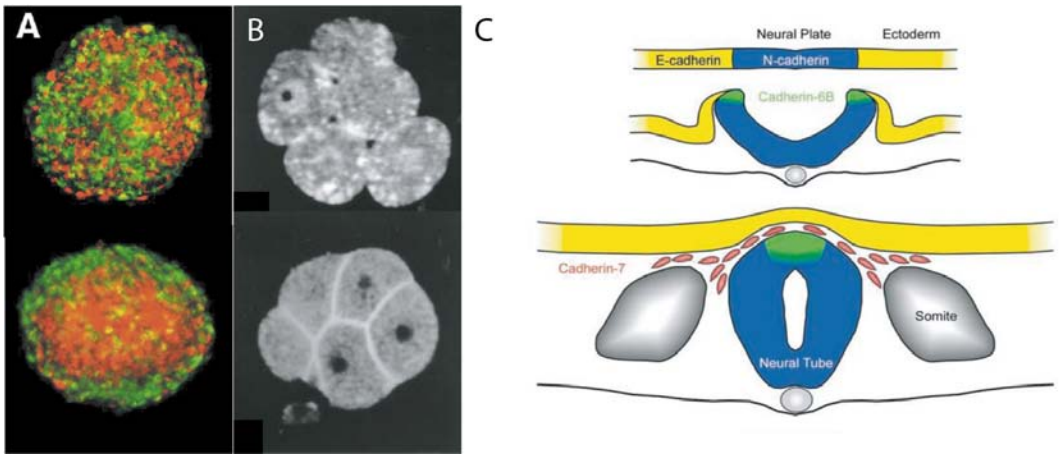

Fig. 2.12 Cadherins in development

A: Sorting of cells from two different tissue types expressing different amounts of Cadherins. The type with a higher amount sorts into the inside of the aggregate (red, [113]). **B:** Compaction of the mouse morula is correlated with a re-localization of E-cadherin to the cell-cell boundaries (white staining, [208]). A failure in E-cadherin function will lead to implantation defects of the embryo. **C:** Infolding of the neural fold is not only a consequence of a differential contraction in presumptive neural plate cells, but also due to an expression of different Cadherins among the neighboring tissue types. E-cadherin is expressed in the ectoderm, while N-cadherin is expressed by cells of the neural plate which in turn lose the expression of E-cadherin. Cadherin-6b (green) is present at the neural fold and marks the emergence of neural crest cells. During neural tube closure, neural crest cells start to migrate and undergo EMT, which depends on the expression of Cadherin 7 [209].

Many different Cadherins are expressed in different cell types and have diverse roles during multicellular development.

Many Cadherins are differently expressed in time and space during the development of an organism (see Fig. 2.12). This differential expression of tissue-specific adhesion molecules is a key factor in building body parts, where cells sort out from a common precursor and end up in different compartments due to a switch in their differentiation pathway [16, 209]. Many publications have addressed the different aspects of adhesion in animal development, which ranges from the compaction of the mouse morula upon expression of Uvomurolin (E-cadherin, [208]), or the migration of neural crest cells [209] to formation of rhombomere boundaries in the developing brain [210]. In zebrafish,

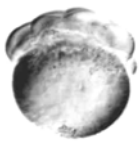

it has been shown that E-cadherin has crucial roles during germ layer formation in the course of gastrulation [19, 71]. Whether adhesion alone can drive this sorting process or how important adhesion is to the migratory behavior of cells in an embryo is of fundamental interest. Most likely, many other cellular properties such as cortex and membrane tension influence cell migration and germ layer positioning during zebrafish morphogenesis. The contribution of adhesion and myosin generated cortex tension in coordinating these processes has not been resolved due to the lack of appropriate tools to measure them [211].

Cell adhesion is a fundamental property for multicellular organisms and a broad spectrum of biological processes require a controlled adhesion. If it fails, it unavoidably leads to severe diseases, perturbed development or the death of the individuum. Among the processes which require controlled cell adhesion that are worth mentioning are embryonic development [14, 78], assembly of tissues and the nervous system [212, 3], cellular communication [213, 86], inflammation and wound healing [214], tumor metastasis [215], cell culturing, and viral and bacterial infection. Although much is known about cell adhesion, many questions remain unanswered bound to its populous prospects, collective complexity [216] and the difficulty to measure it. Therefore, the need for sensitive methods to characterize cell adhesion is still not satisfied.

2.4. Methods to characterize cell adhesive and mechanical properties

Various molecules evolved to couple cells together or to their environment and have a function in many different contexts all over the animal kingdom. Over the years, researchers undertook a lot of effort to characterize the contribution of different cell adhesion molecules to cell behavior under various conditions, using many different model systems or cell culture models. With time, many techniques have been developed to examine cell adhesion. Thereby, cell adhesion can be characterized on the tissue level, cell level and on the single molecules level. In the following, the advantages and pitfalls of several methods are given, regarding how cell adhesion in general can be characterized or measured.

Many different techniques were developed to quantify adhesion properties of single cells or cells in a tissue.

2.4.1. Image-based techniques to characterize cell adhesion

Cell aggregation

One of the easiest ways to characterize cell adhesion is to perform so-called aggregation assays. A defined number of cells is left to aggregate either on a two-dimensional substrate, in an agitated culture or in a hanging drop. The aggregation on an non-adhesive substrate has the advantage that the process of clustering can be followed by timelapse microscopy [27]. Aggregation is then plotted as aggregate size versus time and can be modeled using Smoluchowski's collision theory [217] to extract the rates of aggregation. Differences in the aggregation kinetics can deliver information about motility and adhesion. If the substrate is non-adhesive, cells are unlikely to propel forward actively and motility is due to random brownian motion solely* [217, 218]. The most likely property influencing aggregation of single cells into clusters is adhesion†. The trend in aggregation rate should then be correlated to the expression of cell adhesion molecules in the cluster.

Although very easy to perform and applied manyfold [27, 219] to characterize adhesive properties of cells, this assay provides little information about the adhesive event as such. Neither forces are recorded, nor can the cells be followed directly during the adhesion event. Furthermore, motility can not be ruled out to augment kinetics and the number of cells strongly influences the aggregation steps.

Cell sorting and Tissue Surface Tensiometry

In a cell sorting experiment, two populations of cells are first dissociated and then mixed and their re-aggregation behavior is recorded (see Fig. 2.5 and Fig. 4.8). According to the DAH, the two cell types will separate from each other, if the adhesive properties are different (see Eq. 2.2). On the contrary, the cell types stay intermixed, if the difference in adhesion is too low to allow sorting to occur [99]. Therefore, just by eyeballing assisted with quantitative image processing, a qualitative comparison of different tissues can be undertaken [19]. Despite relying on many assumptions made in the DAH, this assay was used to deduce qualitative difference in adhesion among different cell types [220, 175, 40].

*Meaning that aggregation is NOT transport limited.
†Meaning that aggregations is reaction controlled.

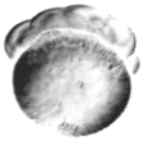

The sorting process is driven by tissue surface tension σ which was proposed to be governed by intercellular adhesion [221]. Hence, measurement of tissue surface tension could provide a quantitative value for cell-cell adhesion. With the sessile drop method, by which an initially round tissue fragment is subjected to a gravitational force in a centrifuge, comparative surface tension measurements can be acquired [103, 222]. The gravitational field causes the aggregate to flatten and hence increase the surface area. Since σ tries to minimize the surface area, the rounder an aggregate resumes after centrifugation the higher is the σ and hence the intercellular adhesiveness of the tissue mass [119]. The geometry of the aggregate after flattening can yield quantitative values for σ, a method called axisymmetrical drop shape analysis (ADSA, [223]). Herein, the contour of the aggregate is detected and fit to a theoretical profile calculated with a computer program [224]. The deviation between the experimental and theoretical contour is minimized in successive steps until the calculated contour best fits the experimental data. With this method, σ was measured for aggregates of cells expressing cytoplasmically truncated EP/C-cadherin, and was proven to be approximately half as large compared to wild type aggregates [224].

Tissue surface tension can be measured by compression of an aggregate or by contour analysis of an aggregate after centrifugation.

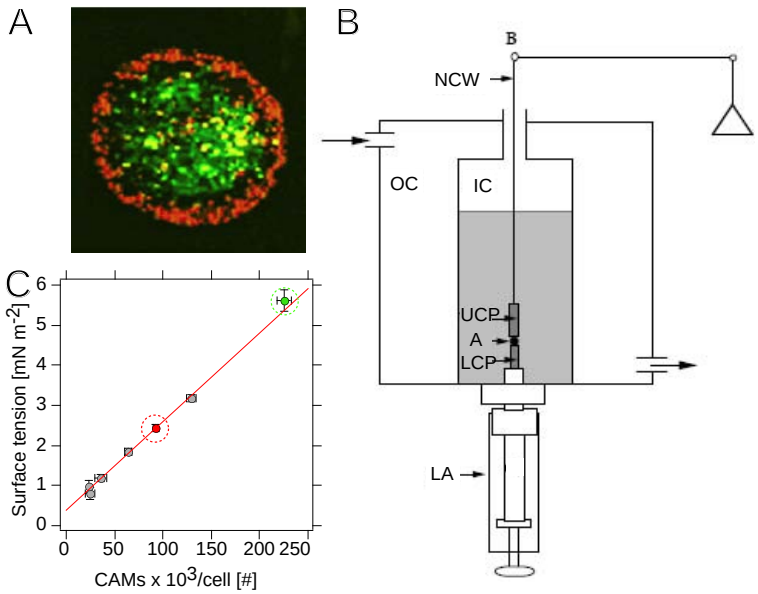

Fig. 2.13 Tissue surface tensiometry

A: Sorting of two cell lines expressing different amounts of Cadherins [113] **B:** Parallel plate compression apparatus ([105]) to measure aggregate surface tension. **C:** Linear correlation between aggregate surface tension and CAM expression in a L929 cell line [113].

Surface tension can also be measured by compressing an aggregate between two parallel plates (see Fig. 2.13 B). According to Laplace Law, the equilibrium geometry of the aggregate is defined by the pressure P inside the aggregate [225, 7, 113, 17, 18, 19, 105] and is proportional to σ. When a tissue mass is compressed between two parallel plates (upper [UCP] & lower [LCP] com-

pression plates; [see Fig. 2.13 C])*, the pressure inside the aggregate balances the external forces [224]. Analyzing the geometry of the aggregate under the external force yields σ:

$$\sigma = \frac{f}{\pi R_{contact}^2} \left(\frac{1}{R_{equat}} + \frac{1}{R_{height}} \right)^{-1} \qquad \text{(Eq. 2.4)}$$

The force f can be easily measured by the deflection of the spring or the weight on a electrobalance (NCW, [see Fig. 2.13 C]), and the contact radius ($R_{contact}$) as well as equatorial radius (R_{equat}) and height R_{height} of the aggregate are accessible by light microscopy.

The advantage of this assay is that it can estimate the forces governing tissue shape. The main disadvantage is that the interpretation is strongly dependent on the assumptions made in the DAH and will not only be due to adhesion in certain tissue combinations and conditions [111, 226]. In line with that, the sorting process *per se* does not tell anything about adhesive interactions, nor does it reveal the forces of adhesion.

Washing assay

One of the first assays to quantify adhesive properties was the classical washing assay [227]. A number of cells is seeded on a substrate decorated with the molecules of interest or other cells and left to adhere for a given time. Thereafter, unbound and weakly attached cells are washed off by rinsing the substrate with cell culture medium using a pipette flow and the remaining bound cells are counted. The percentage of adhering wildtype or control cells is then compared to the experimentally mutated or perturbed conditions [228]. This assay has the big advantage that it offers a high throughput by analyzing a huge number of cells, but is rather uncontrolled regarding the flow condition and irreproducible due to the application of unknown and uneven detachment forces. The washing assay is also restricted in the range of the applied forces and differences among certain cell types can not be resolved after a certain contact time. In addition to that, it is certainly dependent on cell shape and the ability of the cells to spread on the substrate.

*The plates are immersed in cell culture medium (IC) which is thermally equilibrated in an outer chamber (OC).

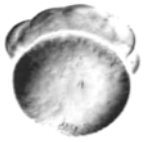

2.4.2. Techniques to measure interaction forces of single cells

Flow chamber

A flow chamber measures the lifetime of an adhesive interaction under a constant force applied in a laminar flow-flied

A more sophisticated assay used to estimate the adhesion force is to subject the cells to a constant laminar flow [229]. In a so-called flow chamber, a controlled number of cells is immersed in a reservoir and the flow pushes them along an adhesive substrate that can be monitored with an optical microscope (see Fig. 2.14 A and Ref. [230]). The cells adhere transiently to the substrate, which is visualized by stop-and-go events, whose frequency and duration depends on the adhesive interaction and the flow rate. The important feature of this assay is that the force and the loading rate is controlled and can be adjusted by the flow-velocity and the viscosity of the surrounding medium. The read-out of the experiment is the lifetime of the specific interaction under such an externally (controlled by the flow) applied load. Estimation of interaction specificity is made easy, because inhibitors of the adhesion molecule (EDTA or mAb*) can be directly immersed in the cell culture medium. Often micro-spheres coated with adhesion molecules or leukocytes have been used to measure single molecule interactions. Thereby the catch bond behavior of L-selectin/P-selectin glycoprotein ligand-1 interaction (PSGL-1, see Chap. 7 and Ref. [230]) could be revealed. Because a torque is generated due to binding of the molecule to the surface, the flow leads to a rolling of the beads over the substrate. Therefore, the flow chamber assay became a useful assay, because it nicely simulates the rolling behavior of leukocytes in arteries [214]. Moreover, the correlation between E-cadherin mediated adhesion and tumor cell invasiveness has been investigated [231]. Although this method is sensitive enough to study the kinetics of single receptor-ligand bonds [232, 193], the main disadvantage with this assay is that it can hardly measure adhesive events above the single molecule level. Hence it is restricted for immediate adhesion events but not for long term adhesion.

Centrifugal force assay

To measure the adhesion forces of cells as a function of the time contact time, a centrifugal assay was developed [235, 233, 234]. Here, cells are grown on a disk, which is rotated in a chamber filled with medium with a certain viscosity (see Fig. 2.14 C). The rotation of the disk imposes a flow and hence a drag force

*Ethylenediaminetetraacetic acid or mono-clonal antibody

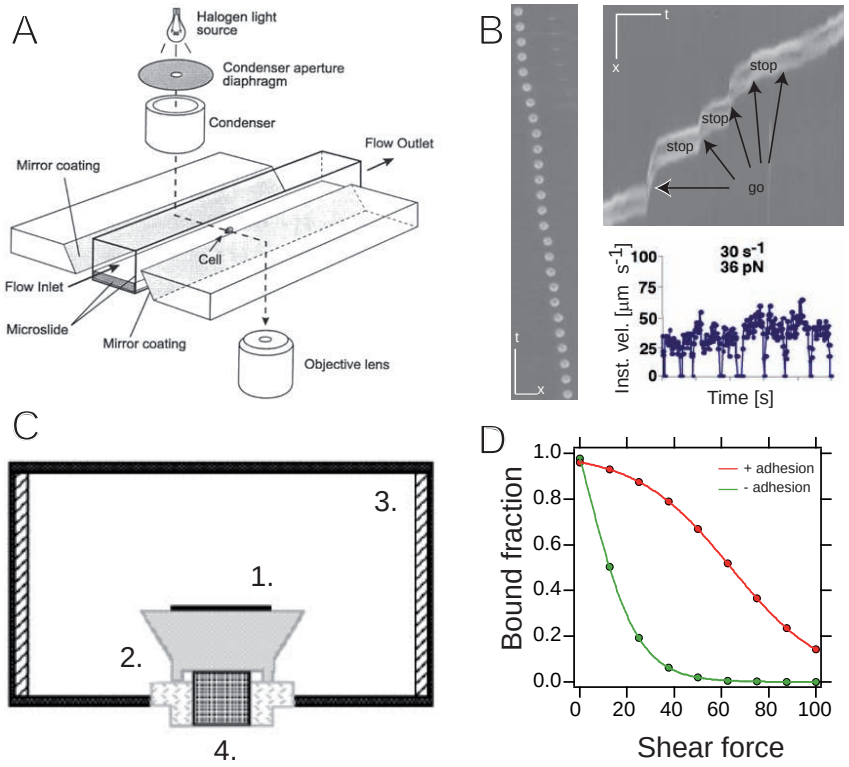

Fig. 2.14 Flow chamber devices to measure cell adhesion

A: General set-up of a flow chamber to measure single cell adhesion events. The fluid including the cells are given into the chamber and monitored with an optical microscope. Taken from [230] **B:** Raw data of a flow chamber experiment. The left picture shows snapshots of a timelapse movie with a cell running from left to right (time on the vertical, distance on the horizontal axis). The kymograph (top right) of a cell shows stop and go events marked by black arrows. The graph below shows the instantaneous velocity of the cell as a function of the time. Several stop events are visible when the velocity drops to zero [230]. **C:** General assembly of a spinning disc device [233] with the 1. glass cover slip, 2. spinning disc, 3. temperature controlled fluid chamber and the shaft to exert the torque on the disc. **D:** Characteristic detachment profile of a spinning disc experiment. The number of bound cells after spinning reduces with increasing radius due to a larger radial velocity, hence shear force (adapted from [234]).

---

is exerted on the cell. At a constant spinning velocity ω, the cells experience a higher shear stress ϕ, the further away they are from the center of the disc. Cells that adhere close to the center of rotation usually do not detach, because the force is too low, while cells at the edge of the disc R are subjected to the highest shear stress (see Fig. 2.14). Hence, each cell experiences a certain shear stress (force) according to the distance R_d it adheres from the center of rotation:

$$\phi = 0.8 R_d \sqrt{\rho \eta \omega^3} \qquad \text{(Eq. 2.5)}$$

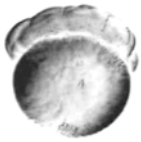

The viscosity η and density ρ of the surrounding medium can be adjusted to scale the force on the adherent cells. After spinning, the cells are fixed and counted, and the number of bound cells N_c is plotted as a function of the distance. Usually, due to the force profile, a sigmoidal detachment profile is obtained (see Fig. 2.14 D).

$$N_c(\phi) = \frac{1}{1 + \exp b(\phi - \phi_{50})} \qquad \text{(Eq. 2.6)}$$

This method proved handy even for the measurements of cells which adhered on the disk for many days. Nevertheless, it does not offer any detailed information on the de-adhesion process, since the cells are monitored before and after the spinning process. Furthermore, forces are only estimated since the detachment process depends on the cell shape.

Micropipette aspiration

MPA measures the adhesive capacities of two contacting cells.

One of the first single cell manipulation techniques with the ability to apply and measure forces was the micropipette aspiration (MPA, [187, 236]). Herein, one cell is aspirated into a pipette and brought into contact with another cell, then aspirated in a second pipette with a controlled pressure. After a certain contact time, the second pipette is retracted. If the pressure in the pipette is not high enough, the cells will stay together (see Fig. 2.15 A-F). Now, this is repeated with increased pressure in the second pipette until it is sufficient to separate both cells. The values recorded for each of the last two cycles in the series ($n-1$ and n) were used to calculate the suction force f for each doublet using the equation:

$$f = \pi \left(\frac{d_p}{2}\right)^2 \cdot \frac{(P_{n-1} + P_n)}{2} \qquad \text{(Eq. 2.7)}$$

where d_p is the inner diameter of the aspirating micropipette and P_n is the last pressure needed to separate the two cells.

The advantage of this method is that it offers the ability to manipulate single cells and can exert force up to the micronewton range just by increasing the suction pressure in the pipettes. On the other hand, the force resolution is low and short contact times between cells can hardly be measured reliably.

Magnetic and optical tweezers

The magnetic tweezers (MT) technique uses an external magnetic field to apply force to one or more super-paramagnetic microparticles. The force f applied

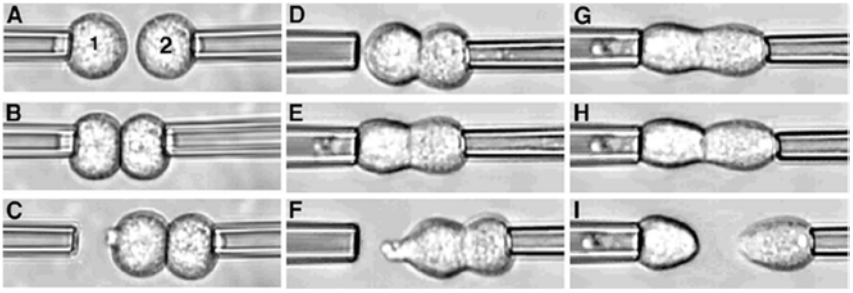

Fig. 2.15 Micropipette aspiration

A-I: Two cells are held by a micropipette and torn apart. If adhesion is stronger between the cells, the cells will slip out of the pipette. Thereafter, the suction pressure is increased and the displacement cycle is repeated. The cells will be separated if the pressure in the pipette exceeds the adhesion of the cells [187].

---

to such a particle in a high magnetic field is:

$$\vec{f} = MV\nabla\vec{H} \qquad \text{(Eq. 2.8)}$$

where M is the saturation magnetization of the microparticle per unit volume, V is the volume of the magnetic particle, and $\nabla\vec{H}$ is the external magnetic field. Therefore, the magnetic particle experiences a directed force in direction of the magnetic field gradient (see Fig. 2.16). MT have been extensively used to characterize visco-elastic behavior of specific cell regions [237] and to probe the local environment of cell adhesion receptors [238, 239]. Thereby, beads coated with extracellular matric molecules such as FN are left to adhere to a cell and are pulled away subsequently. The resistance to force is an indication of the strength of the intracellular coupling and the micro-environment, e.g. lateral separation of single Integrin receptors [238]. One of the advantages is that MTs can exert torque on a particle, offering unique opportunities to study supercoiling of macromolecules or measuring rate dependent visco-elastic properties (magnetic twisting cytometry [240]). The main disadvantage of MT is that it can only exert negative forces (pulling) but no positive forces (pushing). Furthermore, it is incapable of resolving forces in the nanonewton range and is restricted to single molecule analysis.

Optical tweezers (OT) in cell biology are still exotic, though the construction of optical tweezers is conceptually simple. In an OT experiment, a dielectric particle is trapped in a focussed laser beam (see Fig. 2.16). The change of momentum T with time t of the laser light results in a force f which is directed towards the point of highest intensity (intensity=power/area;

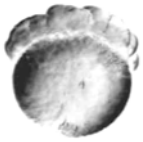

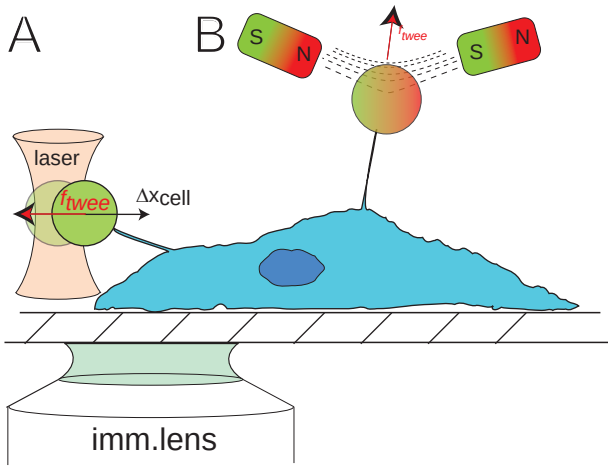

Fig. 2.16 Optical tweezers

A: Schematic working principle of an optical and a magnetic tweezer. A bead (green) is focussed with a laser beam (reddish) and brought into contact with a cell (blue). An interaction displaces the bead from the center which experiences a restoring force. **B:** The magnetic field gradient generated by a pair of magnets imposes a constant vertical force on the micron-sized magnetic bead. A restoring force acts on the bead when displaced by external forces, e.g. from a cell.

$I = W/A$):

$$\frac{\mathrm{d}T}{\mathrm{d}t} = f = N_A \frac{W}{c} \qquad \text{(Eq. 2.9)}$$

In other words, a change in the momentum with time causes a force that is proportional to the laser power W and the numerical aperture N_A of the microscope lens with the speed of light c as a constant. Therefore, in the vicinity of the focus, an 'optical trap' behaves like linear spring [241] and the force is proportional to the displacement of the bead from the center of the beam. Despite this simple relation, exact measurement of forces is not simple and the 'optical trap' has to be calibrated with elaborate procedures [242].

Optical tweezers have an excellent force resolution and can measure forces in three dimensions.

Like in a magnetic tweezer experiment, the bead is usually coated with the molecules of interest and used to exert the force onto the specimen. To do so, it is brought into contact and the adhesive or tensile properties are tested [243, 244]. However, the bead not only serves as handles but is also used to infer the motion, a technique referred to as backfocal plane interferometry. Nowadays, OT pulling experiments are also carried out to probe the lipid bilayer mechanical properties by extruding lipidic nano-tubes from the plasma-membrane. As we will see later, the force needed to do so is a read-out for the plasma-membrane cytoskeleton adhesion energy [36]. The advantage of an OT set-up is its unbeatable force resolution and the ability to measure forces in three dimensions. Unfortunately, without the use of specially coated beads [245] the forces that can be resolved are typically below 200 piconewton. Another pitfall of optical tweezers is the heating of the sample with larger laserpowers [246, 247].

Cell adhesion force spectroscopy

To characterize the adhesion of a cell to a certain ligand type, a technique was invented to 'scrape' the cell off a substrate with a flexible cantilever spring*. Therefore, this method can be characterized as a cell scraper. It is particularly useful to analyze a time-course of adhesion and investigate single cell behavior rather than single molecules or tissues. Similar to an AFM, the cantilever deflection is perceived with a laser beam and recorded with a photo-diode. The deflection of the cantilever during the removal of the cell is used to characterize the adhesive interaction. In the course of an experiment, cells are left to adhere for different time periods and the adhesion force is recorded. The $f(t)$ data can then provide information about maximal adhesion force f_{max} and ⅂, the characteristic time for adhesion of a bond and a measure of how quickly the cell reaches the saturation force:

$$f(t) = f_{max}\left[1 - \exp\left(\frac{-t - t_0}{⅂}\right)\right] \qquad \text{(Eq. 2.10)}$$

with t_0 as the time from when the cells are seeded to when attachment forces are large enough to be measured [248, 249]. This point already describes the disadvantage of the technique, because it is insensitive to measuring low forces.

2.5. AFM – one tool to beat them all

2.5.1. Single cell adhesion force spectroscopy

SCFS allows quantification of single molecules unbinding forces as well as adhesion of whole cells which could exceed many tens of nanonewtons.

The ability of AFM to measure small forces and spatial stability allows us to measure cell adhesion ranging from many hundreds of nanonewtons down to the forces required to deform liquid crystals such as cell membranes [250]. In *Single Cell Force Spectroscopy* a cell is attached to an AFM cantilever which is used in a force distance (see Fig. 2.17) cycle as a probe to perceive interactive events with a given target†. This can be a bio-compatible material, a ligand bearing surface or another cell. The cell is usually coupled to the cantilever non-covalently by different strategies. It can be done either with non-specific interactions using CellTak [251] or lectins [252, 253, 254], antibodies or the coupling of a biotinylated cell to a streptavidin coated cantilever [186].

*Actually the instrument is a modified AFM with an tilted cantilever and a modified measurement chamber.

†A detailed introduction to AFM and the underlying principle is presented in Sec. 3.1.1

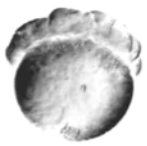

Sometimes cell adhesion molecules such as fibronectin or collagen are used [255].

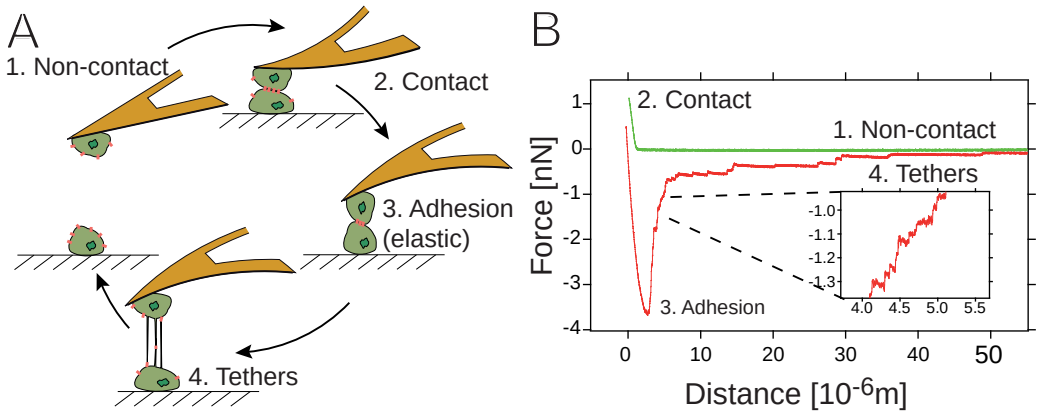

Fig. 2.17 Single cell force spectroscopy

A: A cell is coupled to the cantilever and approached to a surface or another cell resting on the substrate (1). (2) Once in contact, adhesion molecules (red) will diffuse into the contact zone. (3) After a predefined contact time, the cell is retracted and the cantilever bends because of the adhesive strength between the two cells. (4) Further retraction of the cantilever causes molecules to unbind from each other or from the cytoskeleton. Unbinding from the cytoskeleton causes extrusion of lipid nanotubes called tethers. **B:** SCFS data showing a typical separation spectrum. The green curve represents the approach and contact regime of the force-distance-cycle in (A). Separation of the cells is visible as a sharp de-adhesion peak, where the bonds are elastically coupled to the cell body. After a certain separation distance, remaining bonds unbind from the cytoskeleton and form tethers - bonds that are connected to the cell body by thin membrane tubes. The inset shows elastically coupled interactions, which are characterized by a negative slope before the actual unbinding event.

The first experiments were done less than ten years ago by the Gaub group, who attached single *Dictyostelium* cells with wheat germ agglutinin (WGA) to the cantilever [254, 256]. Using such cells offers the advantage that only one type of adhesion molecule (csA) is expressed during the aggregation state of the amoebae*, which can be deleted easily by homologous recombination. Subsequent force measurements for the first time revealed the adhesion strength between two individual cells down to single-molecule resolution. Strikingly, information about the unbinding event is obtained. The adhesion does not fail immediately but with discrete interactions or small unbinding events, visible as force steps in the spectrum (see Fig. 2.17 B). Such discrete unbinding events can either describe the rupture force of a receptor-ligand pair, or the

**Dictyostelium* normally is a single-celled organism, but when starved aggregates to multicellular organism [257].

force that is required to form a lipidic membrane tether. The force steps disappeared when csA was knocked out but did not change when the tethering of the adhesion molecules was changed from a lipid anchor to a transmembrane domain [254]. This shows that the interaction indeed failed between two csA molecules rather than an extraction of the protein from the membrane, which would yield a different unbinding pattern. Furthermore they showed that growing *Dictyostelium* cells which do not adhere normally, have an increased adhesion when the csA adhesion molecule is ectopically inserted and properly expressed. Adhesion measurements in general are very sensitive to the starting conditions, e.g. the initial size of the contact area [256, 258]. The contact area itself, however, is a function of the contact force between two cells and if uncontrolled leads to irreproduceable measurements. SCFS now offers the possibility to control the force by bringing two cells into contact, eliminating big variations originating from changes in the size of the initial contact area. Like any other technique, AFM has its disadvantages: Normally the optical axis is parallel to the direction of the force exertion, making it difficult to observe cell deformation occuring during the unbinding event with an optical microscope. Only with elaborate modifications it is possible to incorporate the optical axis perpendicular to the direction of the pulling [259]. Nevertheless, AFM-SCFS offers the possibility to measure cell-cell adhesion with single molecule resolution [211].

The most convincing advantage of using a cell as a probe, compared to an isolated receptor, is its functional state. An isolated molecule taken out of the cell is not subject to intracellular regulation. In the cell, every interaction is well-coordinated and is controlled by signaling pathways, which turn it on and off. Therefore, the cell-controlled and modulated state of a certain receptor - ligand pair cannot be studied by *Single Molecule Force Spectroscopy (SMFS)* and is restricted to a 'frozen' state. On the other hand, the interaction is well defined and can be studied under the influence of potential binding partners [260] or inhibitors [261]. In contrast to experiments using isolated single molecules, it can be much more complex to probe a specific interaction using living cells. The reason for this is the multitude of possible specific and unspecific cell-surface interactions that naturally occur on the cell surface. Therefore, rigorous control experiments have to be designed to nail down the measured adhesion force to a specific set of proteins embedded in the cell membrane and presented to the ligand bearing matrix. Several strategies have already been communicated in the field. The most confidence inspires to eliminate the

SMFS is an AFM-based method to probe inter- or intramolecular forces. It is widely used to unfold transmembrane proteins [262] and to determine receptor-ligand kinetics [263, 264].

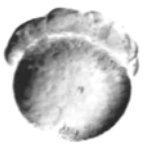

suspected molecule by knock-out strategies [155, 213, 265] but also calcium chelators [253, 155], antibodies [228, 266] or competitive inhibitors [267, 155] are frequently used.

Using a combination of knock-out and blocking strategies it was possible to quantify the cell-mediated enhancement of Integrin mediated adhesion to collagen [253] matrices. In this study, Chinese Hamster Ovary cells were left to adhere to a collagen coated mica for short and long contact times. Whereas only a weak adhesion force of $100 \sim 700$ pN could be measured for short contact times (5 seconds), the adhesion increased manifold up to 20 nN when the cell was left to adhere for several minutes (see Fig. 2.18 A). The strengthening in adhesion was interpreted by the formation of Integrin clusters. The establishment of strong adhesion was furthermore due to activation of Rho-pathway, and an inhibition of Rho kinase led to an almost complete reduction in adhesive forces (see Fig. 2.18 A). These results could be confirmed using MDCK cells on Laminin or Collagen matrices [265].

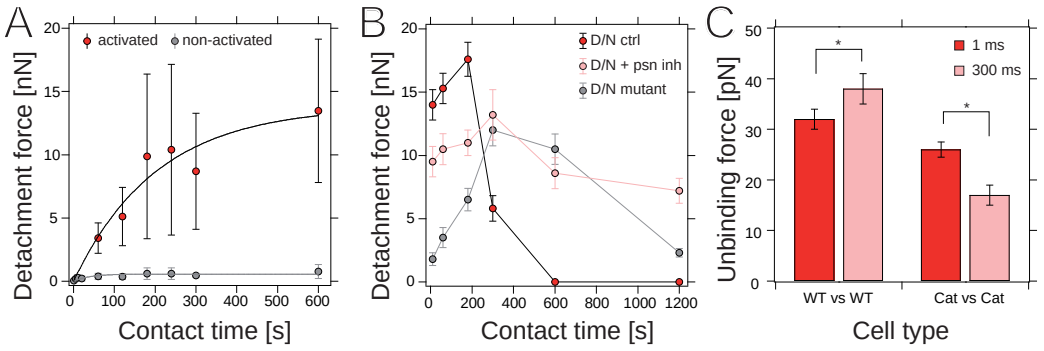

Fig. 2.18 Cell adhesion strengthening with time

Two examples of how adhesion strength could develop with increasing contact time. **A:** Adhesion forces normally increased during the first 200 seconds and stayed constant after that. 'Activated' cells show adhesion strengthening after 1 min contact time, whereas non-activated cells do not show such an effect and stay non-adhesive. A conformational change in the Integrin structure is supposed to be responsible for this switch [253]. Force-time data was fit to Eq. 2.10 and yielded a maximum adhesion force of ∼13 nN. **B:** Adhesion force versus contact time of Notch/Delta expressing *Drosophila* S2 cells. After a rapid increase in adhesion force similar to (A) in the first 200 s, a rapid drop is seen until the force reaches zero, presumably due to a intracellular cleavage of notch by presenelin protease. The drop is inhibited by mutant proteins as well as an inhibitor for presenelin [213]. **C:** Single molecule interaction strength of cells in contact for very short time (1 ms) and longer interaction time (300 ms). α-catenin knock-out cells fail to strengthen the interaction compared to wildtype counterparts [268].

A conceptually interesting study was presented by the group of Cedric Wesley on the model system of the Delta-Notch interaction pair. The interaction

SCFS allows to monitor how the cell modulates the adhesive contact. Adhesion strength could increase or decrease during the time two cells are in contact [253, 213].

of both molecules induces a signaling cascade which establishes boundaries between two different tissue types. Here, the contribution of adhesion strength to signaling activity of the Notch-Delta pathway was of particular interest [213]. *Drosophila* S2 cells expressing Notch receptor were brought into contact with S2 cells expressing Delta and the adhesion strength was recorded. From earlier studies it was known that next to its signaling activity, the Delta-Notch pair is able to induce a clustering of cells that do not express any other adhesion molecules, therefore most likely having a function in cell-cell adhesion [269]. Inasmuch it was of particular interest how the signaling rate is linked with the adhesion strength between the two molecules. It was shown that adhesion is completely lost when the Notch receptor is cleaved by the action of the Presenelin protease in the cells (see Fig. 2.18 B and Ref. [213]). Interestingly, the adhesion force decreased with contact time between the cells, due to the cleavage of the receptor and a subsequent failure to strengthen the adhesive interaction. Rigorous control experiments were designed to underline this hypothesis. For example, different mutants of the receptor and the ligand were used, or proteins involved in post-translational modification of Notch such as o-focusyltransferase were knocked down using RNAi. Furthermore, treatment of the cells with an inhibitor of the Presenelin protease which cleaves the Notch receptor kept a high adhesion force even after very long contact times (see Fig. 2.18 B).

Another example of how the cell actively modifies the adhesive interaction was demonstrated on the Cadherin-Catenin interaction [268]. In a series of simple experiments, it was shown that α-catenin is necessary for rapid initial adhesion strengthening on the single molecules level (see Fig. 2.18 C). For contact times as short as 300 ms a strengthening of a single Cadherin-Cadherin interaction already occurred compared to a contact time of 1 ms. This strengthening was not seen when α-catenin loss-of-function cells were used. Furthermore, the existence of α-catenin induced the formation of several bonds at a 300 ms contact time.

All the data reviewed above is just an example of how cells modulate their adhesion during contact. There are more contributions to this field, in which AFM was used to follow how a cell modifies molecular interactions or mechanics, but these will not be reviewed in detail here [270, 271]. A lot more understanding is needed to fully appreciate the complexity of how mechanics influence signaling and vice versa.

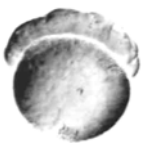

2.5.2. Single cell elastography

Zebrafish as a model system is becoming more and more important to study cell behavior such as migration and social intercourse during morphogenesis. Especially during gastrulation, the formation of the three different germ layers, emerging cells change their gene expression pattern. Concomitantly, their adhesive and actin-myosin activity changes dramatically. How this change affects the mechanical properties of the cells and how they feed back to morphogenesis is not completely understood [133, 116] due to the lack of appropriate techniques. The analysis of the cell mechanical properties by *Single cell elastography, (SCE)* is possible without prior knowledge of the cytoskeletal state and invasive staining techniques to visualize macromolecular assemblies. For this reason, SCE could be used to complement classical techniques such as *in-situ* hybridization, and fluorescence and optical microscopy to study changes in cell mechanics during gastrulation.

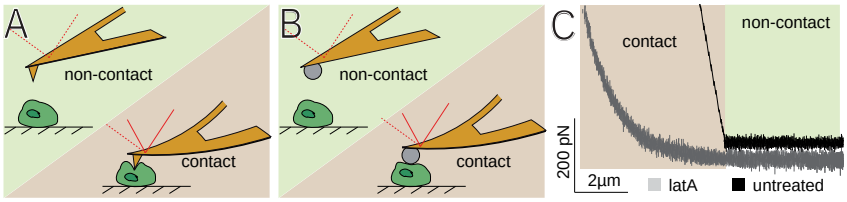

Fig. 2.19 Single cell elastography using AFM

A-B: Schematic representation of the measurement principle. An AFM cantilever TIP is brought into contact with a cell to probe *local* mechanical properties (A). The stress induces a deformation proportional to the force and the contact geometry as well as the stiffness of the tested region. Depicted in (B) is a BEAD-coupled cantilever that is used to deform a cell adherent to a substrate using a predefined contact force. Deflection of the force probe measures the stiffness of the *whole* cell. **C:** Two example indentation curves of a zebrafish cell in presence and in absence of the actin-depolymerizing agent Latrunculin A. Note, in absence of a cortex, the cell deforms dramatically already under very low forces. Curves are aligned at the contact point. Shading represents regimes before and after contact.

Single cell elastography, (SCE) is a method that has been implemented in the lab during this work to monitor the load-effected deformations of a cell. In general, well-controlled forces are applied to the cell either cyclically [272] or linearly [273] and the deformation is recorded (see Fig. 2.19). From such contact experiments, mechanical parameters such as a Young's modulus (see Sec. 3.1.2) or cortex tension (see below) are extracted and compared to different cell states or conditions applied to the cell (such as cytoskeletal inhibitors [274]). To determine the elastic properties of a cell, either a sharp tip (see Fig.

2.19 A), or a micrometer-sized bead can be used (see Fig. 2.19 B). The former has the advantage of a high spatial resolution, but is restricted in the amount of force that can be applied [275]. With a bead as an indenter, the contact geometry is smooth and well-defined and distributes the load over a larger area. Therefore, the strain is reduced and larger forces can be applied without damaging the cell. Using a tip as an indenter can reveal subtle heterogeneities of the cell surface mechanical properties and of the subsurface (cortical) layers at the nano-scale. When analyzing such heterogeneities by AFM it has been possible to resolve the cellular structure of certain regions within a single cell based on its mechanical properties [276]. To do so, many force curves are taken at various positions in x, y to create an image where the contrast of each pixel is defined by a local elasticity value. The resulting image is called 'force-map' [277, 278] and allows identification of intracellular components. Several subcellular compartments were identified with SCE, such as actin filaments [276], nuclei [279], mitochondria [280] or microtubuli [281].

SCE measure the local or global resistance to deformation upon an external force. Changes in mechanical properties due to malignant transformation can be followed.

Changes of cell mechanical properties have been implicated in a variety of diseases and are enthusiastically used as a marker for transformed malignant cells [282, 283, 284]. A recent comparative study on invasive cancer and healthy cells from the same donor showed that the transformed cell types had a 70% lower resistance to force [283]. A change in the strain resistance reflects a change of the intracellular architecture. Alterations in cytoskeletal composition or assembly is thought to be the main contribution to this effect. One likely possibility is the lack of actin cross-linkers such as α-Actinin or myosin or mis-expression of actin de-stabilizers like Cofilin or Gelsolin. Another possibility is that actin polymerization *per se* is affected and cannot build up an organized, force-bearing network. As one can see in the spectrum of Fig. 2.19 C the resistance to deformation decreases manifold when the actin cytoskeleton is perturbed by drugs.

Up to now, SCE has been applied to different cells using various techniques. Micromanipulation techniques such as magnetic or optical tweezers have been used to measure the local elasticity of cellular sub-compartments. Atomic force microscopy has been used extensively, as well as micropipette aspiration of single cells to measure the visco-elastic properties of the whole cell. Taken together, the main advantage of AFM-SCE is that it can exert force in the piconewton and nanonewton range which offers the possibility to probe different subsurface layers of the cell just by adjusting the contact force. Thereby, it is not only restricted to the nanoscale by the use of a sharp tip as

an indenter (see Sec. 3.1.2), but is also able to extract global mechanical cell properties.

Liquid-droplet model and cortex tension

Most of the SCE data taken with AFM has been analyzed using the Hertz-model to extract the Young's modulus E (see Sec. 3.1.2). The Hertz-model assumes a linear isotropic elastic material, like rubber or steel. This fits some of the indentation experiments with adherent cells, but not necessarily under all experimental conditions and for non-adherent cells. An alternative model is the *liquid-droplet model*. This model assumes a fluid-filled bag surrounded by a perpetual cortical tension. It was first introduced by Evans and co-workers to explain deformations of leukocytes into micropipettes (see Fig. 2.20 and Ref. [285]). Cells aspirated into a pipette will project a hemispherical protrusion (also called tongue) into the pipette when the pressure in the pipette is equal or higher than the critical pressure P_{crit} inside the cell. The higher the pressure in the micropipette, the faster is the flow of the cell. The cell could completely flow into the pipette if the pressure is not reduced. Release of the pressure results in a complete recovery of the cell shape into its spherical form, indicating a liquid-like response. The driving force for this recovery was supposed to be a potential energy stored in the cell cortex, specifically termed cortical tension T_c. T_c in general is seen as the driving force for the cell shape recovery (passive) after large deformations (e.g. in micropipettes, [286]) and (active) cell shape changes under zero external loads [143]. The time scale for these processes is sized by the viscosity of the interior cytoplasm [285]. The tension originates from and is maintained by a cortical layer adjacent to the cell plasma-membrane and includes the contractile apparatus which is formed by polymerization of actin filaments and is cross-linked by actin binding proteins in association with myosin molecules.

The liquid droplet model assumes a viscous fluid filled 'bag' with a persistent tension around the cell cortex. This is typically realized by a circumferential, contractile acto-myosin belt.

The contraction of myosin is likely to be the cause for the persistent cortical tension [287, 136, 285]. The first experimental evidence for this came from studies with *Dictyostelium*. Herein, it could be evidenced that an increase in cortical tension after treatment of the cells with Concanavalin A (Con A) was reversed when the cells lacked myosin heavy chain. In wildtype conditions, cell stiffness increased more than twofold directly after the addition of Con A*. *Dictyostelium* cells lacking the myosin contractile apparatus have a reduced

*Con A is supposed to cross-link cell surface receptors to induce an activation of intracellular signal transduction, e.g. phosphoinositide cascade and myosin phosphorylation

resting cortical tension and failed to stiffen after the treatment with Con A. These findings were underlined when cells were treated with an ATP depleting agent NaN_3 which causes a rigor contraction of myosins and a subsequent manifold increase in cortical tension. Collectively, those observations indicate that the cell behaves like a viscous liquid, surrounded by a persistent cortical tension.

Measurements of cortex tension

Cortical tension has been measured using a variety of different techniques. Overall, micropipette manipulation (MPM) is one of the major methods. As already mentioned, aspiration of a small part of the cell with a radius R_c into the pipette with a radius $R_p < R_c$ with a pressure P larger than the critical pressure P_{crit} is used to calculate the cortical tension T_c of the cell:

$$P_{crit} = 2 \cdot T_c \left(\frac{1}{R_p} - \frac{1}{R_c} \right) \qquad \text{(Eq. 2.11)}$$

The analogy to the Laplace law becomes apparent and was already introduced in Eq. 2.4. Similar to the surface tension, the cortex tension results in an isometric contraction which acts to minimize the surface area of a cell and is supposed to be the driving force for cell rounding in solution [286]. But it is not the cell surface itself, which is responsible for the rounding up of cells in solution, but rather intracellular actively contractile elements (see below).

Cortex tension is widely measured using micropipette aspiration as well as indentation experiments, such as AFM or cell poker.

Another method to estimate T_c is the use of tapered micropipettes. Here, cells are pushed through conical closing pipettes with a defined external pressure and their area expansion is monitored [288]. The cells continuously flow into the pipette while their area increases until the cortex tension balances the external pressure and the cell comes to rest. The cortex tension is calculated from the pressure difference across the cell and the principle radii of curvature of the leading and the trailing cell edge in the pipette (see Fig. 2.20). Different pressures result in different area expansions which yields the cell cortex tension.

Lomakina et al. used spherical bead indentation experiments with micropipettes to extract values of T_c [289]. A bead clamped with a micropipette is gently brought into contact with a cell in another pipette (see Fig. 2.20) while the equilibrium contact radius R_{con} is measured and related to the force

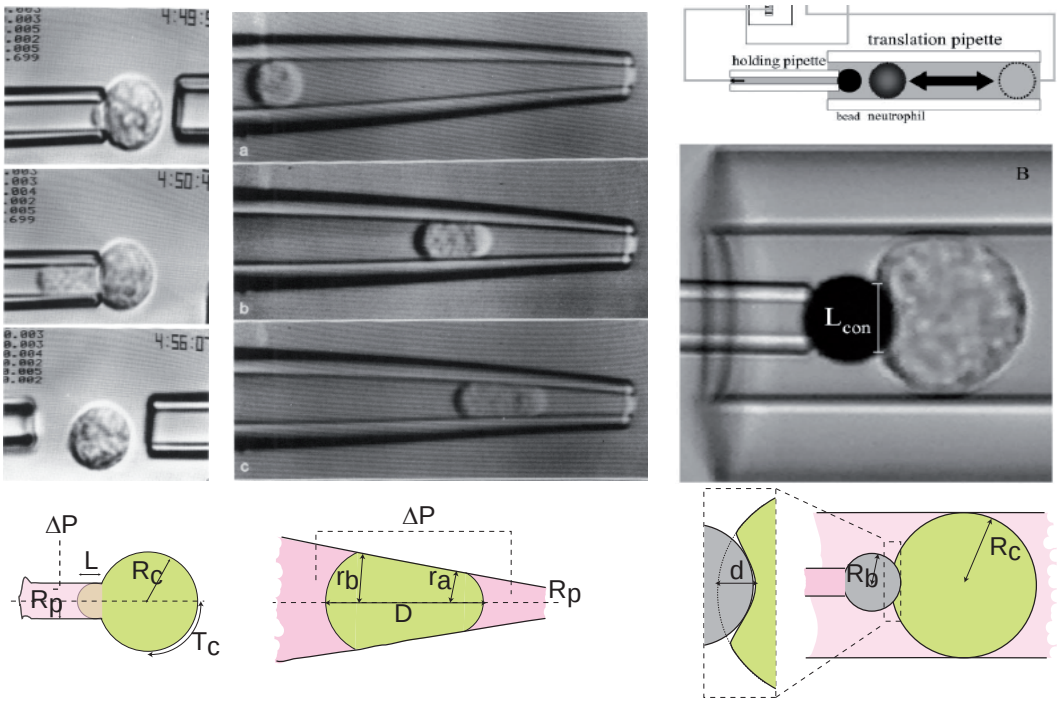

Fig. 2.20 Micropipettes to measure T_c

Left: Micropipette aspiration of a blood granulocyte [285]. In the upper panel the pressure is set to the critical pressure, where the length of the aspirated part $L = R_p$. The middle panel shows an example where $\Delta P > P_{crit}$ and a flow into the pipette occurs. The lower panel shows complete recovery into its spherical shape after release of the pressure. **Middle:** Micropipette manipulation [288]. A cell is squeezed through a tapered pipette and the geometry, namely the radii of curvature at the leading and trailing cell edge are used to extract the cortex tension. **Right:** Indentation experiments using micropipettes [289]. A bead is held by a pipette while another cell is railed into the bead floating in another pipette, accelerated by an external pressure.

---

according to:

$$f = 2\pi R_{con}^2 T_c \left(\frac{1}{R_b} + \frac{1}{R_c}\right) \qquad \text{(Eq. 2.12)}$$

This method was adapted to AFM indentation experiments were a conical indenter or a bead-coupled cantilever is used to deform the surface of the cell [292]. The force-indentation ($f - \delta$) relation is then modified and can be described by [292, 289]:

$$f = \left[2T_c \left(\frac{1}{R_c} + \frac{1}{R_b}\right) \cdot 2\pi R_b\right] \cdot \delta \qquad \text{(Eq. 2.13)}$$

in which f is the contact force, δ is the indentation (force induced deformation of the cell), R_c is the cell radius and R_b is the bead radius. The model can be

Cell type	T_c	Technique	Ref.
Granulocyte	$35\,\mu\mathrm{N}\cdot\mathrm{m}^{-1}$	MPA	[285]
Dictyostelium	k=4 $\mathrm{mN}\cdot\mathrm{m}^{-1}$	Cell Poker	[287]
Lymphocytes	k=1.4 $\mathrm{mN}\cdot\mathrm{m}^{-1}$	Cell Poker	[290]
Dictyostelium	$15\,\mathrm{mN}\cdot\mathrm{m}^{-1}$	MPA	[136]
Neutrophils	$33\,\mu\mathrm{N}\cdot\mathrm{m}^{-1}$	MPA	[140]
Neutrophils	$23.2\,\mu\mathrm{N}\cdot\mathrm{m}^{-1}$	MPM	[289]
Neutrophils	$24\,\mu\mathrm{N}\cdot\mathrm{m}^{-1}$	MPM	[288]
Fibroblasts	$391\,\mu\mathrm{N}\cdot\mathrm{m}^{-1}$	MPA	[291]
Myeloid (HL60)	$155\,\mu\mathrm{N}\cdot\mathrm{m}^{-1}$	AFM	[292]
Lymphoid (Jurkat)	$21\,\mu\mathrm{N}\cdot\mathrm{m}^{-1}$	AFM	[292]
Macrophage	$140\,\mu\mathrm{N}\cdot\mathrm{m}^{-1}$	MPA	[293]
Macrophage	$100\,\mu\mathrm{N}\cdot\mathrm{m}^{-1}$	RICM	[148]
Zebrafish ectoderm	$77.7\,\mu\mathrm{N}\cdot\mathrm{m}^{-1*}$	AFM	this study

Table 2.1 Literature values for T_c

Published values for cortex tension of various cells using different techniques. When indicated, an elasticity constant was communicated. * The cell elasticity of these cells is k=1.2 $\mathrm{mN}\cdot\mathrm{m}^{-1}$ and therefore similar to Lymphocytes [290].
Abbreviations used in this table: MPA, Micropipette aspiration; MPM, Micropipette manipulation; AFM, Atomic Force Microscopy

used to extract indentation data acquired with AFM-SCE when indentations are small, the cells are roughly spherical, show a prominent actin cortex in the medium interface and have a low cytoplasm/nucleus-ratio. With this and many more techniques, values for T_c of many different cell types (see Table 2.1) were acquired.

Taken together, the cortical actin cytoskeleton is of great importance for all cell processes which include communication and physical interaction with the environment. An important feature has to be kept in mind: Without adhesion, neither multicellular assembly nor physical interaction would be possible. Although the concept of differential adhesion-driven tissue dynamics is challenged in many publications [294], the need for cell adhesion for morphogenesis is indisputable. The aim of this thesis, however, is to show thatmechanics of tissue formation are not to be reduced solely to the action

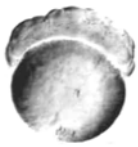

of adhesion but rather are a combination of a plethora of cell surface properties, such as membrane tension, cell cortex assemblies and of course adhesion [295, 21, 296, 297, 20, 127, 120, 115, 111, 15].

3. Experimental Section

3.1. Techniques

3.1.1. AFM and SCFS

Since the advent of Atomic Force Microscopy in 1986 [298] it has become a enormously versatile tool in biological and biophysical research. The power of AFM is based on the ability to measure a wide range of forces ranging from a few piconewton up to several micronewton. Initially developed as an imaging tool to raster-scan the topography of a sample, the main application of AFM in quantitative biology nowadays is as a force spectroscopy dynamometer.

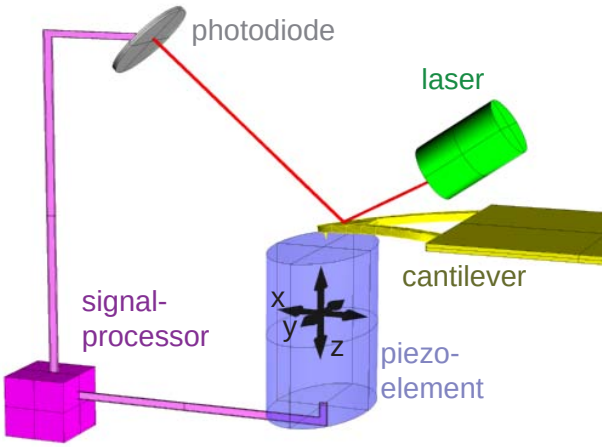

Fig. 3.1 Atomic force microscopy

A flexible force probe cantilever (yellow) with a small stylus is moved in respect to a sample specimen by the means of a piezo electric element (blue). The deflection of the cantilever due to attractive or repulsive surface forces is recorded by a laser (green), which is reflected onto a photodiode (grey). A deflection from the equilibrium position results in a potential difference on the photodiode which in turn generates a signal that is integrated into a feedback circuit (violet).

In force spectroscopy mode, an ultra-small stylus attached to a flexible cantilever is moved by the means of a piezo-electric ceramic along the z axis at a fixed x, y position (see Fig. 3.1). Such a piezo element usually consists of lead zirconate-titanate crystals which change dimensions depending on the applied voltage, ensuring a spatial accuracy of less then 0.1 Ångstrøm. This is a sensitive mean by which the cantilever probe can be positioned over the sample. When the probe is approached to the sample surface, the soft cantilever bends due to the surface force gradient that depends on the sample and the surrounding

environment. Before contact of the probe and sample, attracting *van der Waals* forces act on the probe. The forces diminish rapidly when probe and surface are separated due to a strong distance dependence. When both bodies are in contact, repulsive forces dominate over attractive forces due to steric interactions of the outer electron shells of sample and probe atoms [299]. The surface force leads to a deflection of the cantilever to (attraction) or away (repulsion) to the surface (see Fig. 3.2). In certain conditions, e.g. when both surfaces are charged, the force between the bodies are not attractive but repulsive [300]. In air strong meniscus forces result in a significant attraction between the probe and the sample due to a omnipresent water layer at ambient conditions. Weak forces are therefore masked, but can be overcome when measured in liquid environment [301].

Forces in the piconewton range are hard to resolve and there is a considerable effort to design sensitive force probes. Usually a beam shaped cantilever is used which is manufactured of silicon or silicon nitride. Most sensitive cantilevers have a low spring constant and a high resonant frequency to be less influenced by external mechanical vibrations. Low spring constants are achieved by longer cantilevers [302] whereas a higher frequency is achieved with shorter, thicker cantilevers. Another factor influencing the performance of a cantilever is 'drift'. Usually, AFM force probes are coated with a thin layer of chromium and gold on the backside to enhance reflectivity in liquid environment. Even if subjected to small temperature changes, this leads to a considerable surface stress bending the cantilever in one direction until the temperature of the environment is equilibrated. Such 'drift' leads to a unpredictable cantilever deflection, disturbing long term force measurements [300]. To minimize this effect, short cantilevers are widely used for AFM imaging or biological force measurements because experiments usually are in the order of many tens of seconds up to hours [303]. Moreover, small cantilevers are less prone to hydrodynamic drag effects that complicate analysis of force curves taken with higher velocities [304]. When the cantilever moves with high velocities through a viscous medium, it experiences a force in opposite direction and, hence, deflect from the equilibrium position. This effect depends on the distance to a surface and becomes larger when the medium is confined between the cantilever and a substrate.

Even for very soft cantilevers (spring constant k_c=10 mN $\cdot$ m^{-1}) a force of 10 pN leads to a deflection of only ≈1 nm. This subtle movement is translated into a larger movement by a laser beam that is reflected off the back of the cantilever onto a four quadrant photodiode. This detection method is widely known as a optical lever technique [300]. Upon a deflection of the cantilever z_c under a force f, the laser spot will shift on the photodiode (Δ_{PSD}) proportional to the distance between the tip and the detector, d and the length of the cantilever L_c :

$$\Delta_{PSD} = \frac{z3d}{L} \qquad \text{(Eq. 3.1)}$$

The shift on the detector then creates a potential difference ΔV , because the signal in the four quadrants (A, B, C, D) changes with the position of the laser on the diode:

$$\Delta V = \frac{(A+B)-(C+D)}{(A+B+C+D)} \qquad \text{(Eq. 3.2)}$$

This potential difference is converted into a force after measuring the sensitivity and the spring constant of the cantilever. Therefore, at the beginning of each force measurements,

the stiffness of the cantilever has to be measured. In principle k_c can be calculated by knowing the dimensions (w_c=width, t_c=thickness, L_c=length) and the Young's modulus (E) of the cantilever beam:

$$k_c = \frac{f}{z} = \frac{E w_c t_c^3}{4 L_c^3} \qquad \text{(Eq. 3.3)}$$

Usually, the exact values are unknown and vary quite a lot from cantilever to cantilever due to manufacturing processes [305]. For example, a small deviation in the thickness will result in huge errors for k_c. There are several ways to actually measure the spring constant, e.g. to add a mass at the cantilever tip and observe the change in resonance frequency or to use a reference cantilever whose spring constant is known. This is very tedious and adding a mass often leads often to a damage of the force probe and is irreversible. In commercial AFMs, cantilevers are calibrated by the so-called thermal noise method and allows to measure the k_c reliably and non destructive without the addition of an external mass. Herein the cantilever is modeled as a harmonic oscillator and deflects due to thermal fluctuations with $\langle \Delta z_c^2 \rangle$ as the mean squared deflection and $k_b T$ the Boltzmann term:

$$k_c = \frac{k_b T}{\langle \Delta z_c^2 \rangle} \qquad \text{(Eq. 3.4)}$$

For soft cantilevers the mean deflections are about 3 Å but can be significantly higher if other noise sources like mechanical vibrations are involved. Other noise sources add a background to this thermal response. As none of the other noise sources is likely to have a resonance at the resonant frequency of the cantilever, it is a simple matter to subtract this background [305]. The noise is typically recorded for several seconds and transformed into the frequency domain. For a harmonic oscillator, the energy transfer is highest at its resonant frequency and one obtains a sharp peak in the power-spectrum. The area below the remaining peak is then a measure of the power of the cantilever fluctuations and proportional to the spring constant of the cantilever.

The read out of a force spectroscopy experiment is a so-called force-distance curve (see Fig. 3.2), when the cantilever is vertically ramped towards the sample while the deflection of the tip is monitored. The direct read-out of this experiment is a photodiode current versus the position of the piezo-electric translator (D_{pzt}). After calibration, they are converted into a force (f) and a distance (δ). This curve is then corrected for the deflection (z_c) of the cantilever to obtain a force-displacement curve and is particularly important when analyzing the mechanics during the contacts of soft samples:

$$\delta = D_{pzt} - z_c \qquad \text{(Eq. 3.5)}$$

In general, three regimes of a force distance curve can be distinguished (see Fig. 3.2). In the non-contact regime, the force probe is far away from the surface and no forces except hydrodynamic friction act on the cantilever. This is proportional to the velocity of the AFM cantilever and the viscosity of the surrounding medium [304]. The non-contact part of a force curve defines the zero force line and is the reference value for all subsequent force measurements. Approaching the surface closer than a few micrometer or nanometer* the

*The exact distance depends on the ionic strength of the surrounding medium.

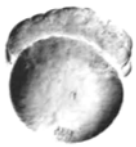

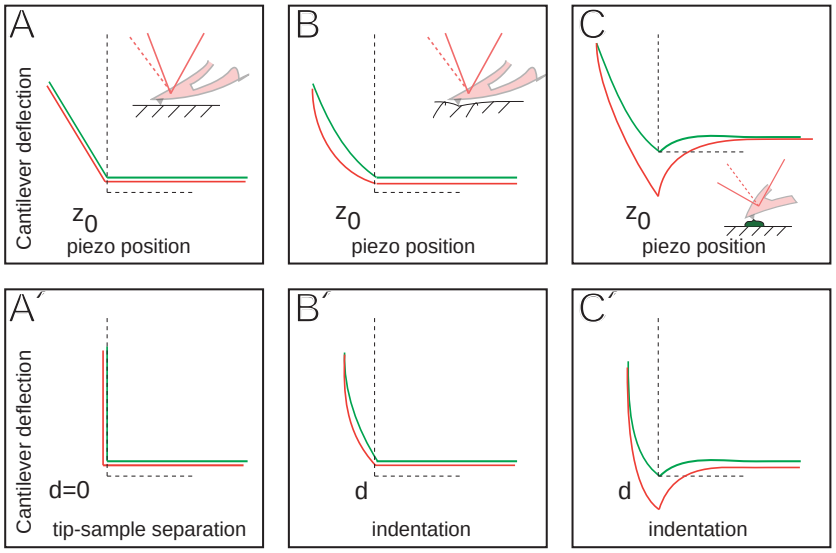

Fig. 3.2 Schematics of force curves taken on different surfaces

A: Force curve taken on an infinitely stiff substrate. Correction of the substraction of the cantilever deflection from the piezo movement yields the tip-sample separation (A'). The schematics show the situation during the contact. **B:** Force curve taken on an elastic substrate, which deforms under the load of the cantilever. Hysteresis between red and green curve indicates viscous dissipation which takes place during the contact. The inset shows the deformation of the substrate. **C:** In addition to the deformation of the substrate, adhesion between the tip and the sample can take place. This is depicted by negative forces and the cantilever bends downwards (see inset). Green, approach curve; red, retract curve; z_0, contact point; δ, indentation.

cantilever starts to bend according to a surface force gradient, which can be repulsive or attractive. Sometimes the attractive force gradient can be larger than the spring constant of the cantilever which leads to a so-called snap-in (see Fig. 3.2 C). Here, the cantilever suddenly jumps into contact. Are repulsive force dominating, the cantilever establishes contact as soon as the force is larger than the repulsive surface forces. Only then the slope is influenced by the stiffness of the sample and independent of the surface forces. For an infinitely stiff sample, the inverse of the slope of the contact region defines the deflection sensitivity s and defines how far the cantilever deflects to reach a certain potential difference on the photodiode*. Typically s is given in nm·V^{-1}. The contact region of soft samples is more complex and the contact point is usually ill-defined (green curve in Fig. 3.2, see also Sec. 3.1.2), especially if there is noise. This is due to the fact that at small cantilever deflections the sample is already significantly indented. If adhesion between the probe and the sample takes place, the deformation of the sample is not only caused by the spring force but also by the adhesion forces. Therefore, if the stiffness of a sample is of particular interest adhesion between the probe and the support has to be minimized.

Is the desired contact force reached, the piezo inverses its velocity vector and retraction starts. For viscoelastic samples there is a hysteresis between the contact region of the

*The deflection of the cantilever on a stiff substrate equals the piezo-movement.

approach and the retract curve, which can also shift the contact point to the left if no adhesion is involved. If adhesion is involved, the cantilever and the sample are much longer connected than the actual surface limit. Adhesion in general is visible as prominent force peak, but can also be a force plateau, as seen in the case of a tether extrusion experiment.

3.1.2. Cell elasticity

Rheology

Rheology is the science interested in the mechanical properties of soft matter. In a rheological measurement the relation between an imposed stress (Θ=Force/Area=F/A_c) and a resultant strain (ε=$\Delta L/L_0$) of a material is studied. In a simple solid elastic material the stress Θ is proportional to strain ε with the Young modulus as a constant:

$$\Theta = E \cdot \varepsilon \qquad \text{(Eq. 3.6)}$$

If an material is mainly viscous, the stress depends on the rate of strain application or how fast the material is deformed, which is most typical for newtonian liquids with strong intermolecular attraction. For most bio-molecules, cells and tissues, the response to force is neither purely elastic nor viscous but shows signature of both, solid and liquid properties. Both properties can be decoupled and this was technically first achieved by oscillating an AFM cantilever up and down when in contact with a the sample [277].

Working with cells has several pitfalls next to viscoelasticity and if elastic properties are wished to be determined reproducibly, the force curves have to recorded spatially controlled. For example, several studies indicated that the cell structures alter their mechanical properties. Stem-cell nuclei not only are the stiffest compartment in a cell [306, 279] but change during differentiation. Furthermore, actin cables in an adherent cell have a higher resistance to load than the cytoplasm in-between these cables and only a deviation of a few nanometers can induce a large error on the measurement [307]. By the use of AFM, one can control space and force very precisely and therefore offers an excellent tool to study cell elastic properties [308].

Cell elasticity

Cell elasticity generally means the reversible deformation of the sample cell under an externally imposed load. Many different devices have been used to deform cells with forces ranging from a few piconewton to micronewton. Instruments use different force vectors to probe parts of or whole cells and one can distinguish between inward directed forces, like cell poker [309, 310] (global cell property) or AFM (local & global cell property, [277, 308, 311, 312, 313, 273, 274, 314, 292, 315]) and outward directed forces such as optical or magnetic tweezers (local, [316, 142, 237, 317]) and micro-glass needles (global, [318, 319]).

Among these methods, AFM is the most popular and versatile. Initially, cell elasticity was probed using atomic force microscopy to indent a cell strongly adherent to a surface with a conical indenter - the sharp AFM tip [320, 277]. To do so, cells are grown on a culture dish and a force curve is taken on the surface of the cell. The loading force will cause the

sample to deform and deflect the AFM-cantilever. Relating the force f to the deformation δ of the sample yields the stiffness k of the cell according to the Hooke's law:

$$f = k \cdot \delta \tag{Eq. 3.7}$$

Here, stiffness is simply explained as the slope of the resulting force displacement ($f - \delta$) curve, without considering tip-sample contact geometry. A more serious description of AFM indentation experiments is the Hertz model, which was first introduced by Radmacher in the field of cell elastography [277]:

$$f(\delta) = \frac{2E}{\pi(1-\nu_p)^2} \cdot \tan\alpha_c \delta^2 \tag{Eq. 3.8}$$

with E as the Young's modulus, ν_p is the Poisson ratio and usually considered to be 0.5 for any incompressible material and α_c as the opening angle of the AFM tip. δ is the indentation of the sample (see Eq. 3.5). Originally developed by Heinrich Hertz for the contact problem of two solid bodies, the model describes the relationship between the contact radius and the applied load for homogenous and isotropically linear elastic bodies.

The application of the Hertz model to the analysis of single cell elastography experiments attributed a material property to the probed sample. For the first time, a cell became comparable in terms of numbers to well known elastic substances like rubber or steel. Because the mechanical properties are likely to vary across their surface, it is not clear how useful a quantity of an elastic modulus of a living cell is. Next to the assumptions in the Hertz model, some technical difficulties have to be solved when analyzing SCE data, which also have to be considered when cortex tension measurements are of interest. These are independent from the model used to analyze SCE data but are bound to the principle of indentation experiments. Among the problems are:

1. probe and sample do not adhere during contact
2. strains are to be minimized
    - sample deformations are purely elastic and do not deform plastically
3. cells are linear, isotropic and homogenous materials
4. the contact point between cell and probe is explicitly known

All of the these problems are hardly to clarify but several strategies are known to become clear of them. Firstly, to reduce non-specific interaction during a contact experiment, the indenter is passivated with either long-chain poly-ethylen-glycol (PEG, F127) or heat inactivated serum albumin (hiBSA). Secondly, sample deformations are minimized by increasing the contact area during the contact. For this reason, AFM probes have been used that carry a bead instead of a sharp tip at the front of the cantilever to indent the soft sample. Other than that, it was shown that tip radii of 100 nm* already lead to strains that invalidate assumptions made for the Hertz model at forces as small as few piconewtons [275]. For example, the use of a bead with a radius of 5 µm reduces sample strains even at higher forces yielding meaningful values for the Young's modulus. This already reduces the impact

*which can be considered as a blunt tip

of the third point, because cells of course are not an isotropic or homogenous material, but contain many different substructures with differing mechanical properties. Large errors on the quantitative description of a cell as a continuum is included. Therefore a sufficiently large bead 'averages' over a certain area and yields an 'ensemble' elastic modulus. The Hertz formula for a spherical indenter re-writes as follows with R_b as the radius of the indenting bead:

$$f(\delta) = \frac{4E}{3(1-\nu)^2} \cdot \sqrt{R_b} d\delta^{\frac{3}{2}} \qquad \text{(Eq. 3.9)}$$

The fourth and last point is by far the most difficult to circumvent and many strategies have been proposed to eliminate it. Indenting an infinitely stiff substrate, the contact point is easily accessible, but for soft samples determination becomes deleterious especially when noise is involved [321]. Unless the cantilever is soft, the relation between cell deformation and cantilever deflection is no longer linear, and the softer the material, the less tip deflection will be, at the worst, hidden in the noise of the probe.

Force integration to equal limits (FIEL) was applied to generate elasticity maps of madine darby canine kidney cell (MDCK) to show changes in elastic properties of the same sample [273]. Instead fitting the force distance data to Eq. 3.8, the work needed to deform the sample, calculated as the area underneath the contact region of the indentation curve was compared. This analytical approach has several important features. It is independent of the probe size as long as the same probe is used in both measurements. It is also independent of the sample topography and the sample drift, and does not require absolute height measurements. Finally, and most importantly, it is essentially independent of the tip-sample contact point, because a small error in the lower integration limit will change the work only very little [273]. This method provides, however, only relative comparisons between different samples and does not specifically quantify properties of a given material.

Anther approach finds the contact point by fitting the non-contact regime of the force curve independently to the contact regime [321]. The contact point of the deflection curve is found by assuming that the pre-contact regime is linear with a slope close to zero, depending on the thermal drift of the cantilever. After contact, the slope changes either to an approximately quadratic or linear deflection-indentation relation, depending on the material used. Consequently, both regimes are fitted to linear and quadratic functions. The intersection of both trends was used in a second fitting procedure as the contact point and lower fitting limit [321]. This approach was followed during this thesis to estimate the contact point of SCE data.

The effect of misidentifying the contact point is especially severe when indentations are very small. When specific substructure of a cell are analyzed, such as a lamellipodium, indentation can be rather small. As indentation depth increases, the effect gets smaller and smaller and can be neglected for deformation larger than few hundreds of nanometers.

Several modifications of the Hertz model have been proposed in the literature. Among them only a few have been applied successfully to biological cells. The Sneddon modified Hertz model was used to identify differences between elastic properties of stable and dynamic cell protrusions [322]. At low loads, the contact area (A_c) does not fit the predictions of the Hertz model, because adhesion significantly increases A_c. Of course these small attractive contact forces (in the order of a few tens of piconewton) have only little influence when large forces (e.g. nanonewtons) are externally applied. Another modification is the Johnson-

Kendall-Roberts theory which can be used to determine adhesion energy and elasticity from a measurement. This model was applied in cell-cell separation experiments using micropipette aspiration. Adhesion energy and elastic modulus of cells was determined simultaneously [323] only if the cells had an intact actin meshwork. If latter was destroyed in presence of Latrunculin B, a drug inhibiting polymerization, the elastic response to force was lost and the cell behavior could not be modeled with the JKR theory anymore. Similar scenarios are likely to happen for other situations as well and will be discussed again in Sec. 6.2.

Next to the Hertz-model, liquid droplet model has been proposed to analyze force-deformation data acquired with AFM. Whereas the basic introduction was in Sec. 2.5.2, experimental details together with liquid-droplet model assumptions are explained below.

3.1.3. Fluorescence recovery after photobleaching

Fluorescence recovery after photobleaching (FRAP) is a widely used technique to measure protein dynamics in living cells [324]. In the course of a typical FRAP experiment a small spot of known size and geometry of a fluorescent sample is bleached using a high intensive laser beam. Recovery of the fluorescence in the bleached area takes place immediately by diffusion and partial exchange of molecules from unbleached regions of the sample and is recorded at low laser powers. The sample usually has a GFP tagged protein of interest, and its mobility is investigated. FRAP experiments provide information on two different parameter:

1. the time scale of recovery which is related to the diffusion of the tagged protein
2. the mobile fraction of the fluorophore

. The recovery time can be slowed down, if the tagged specimen interacts specifically with intracellular binding partners [325]. Secondly, the mobile fraction of the fluorophore is obtained and yield information how many molecules are exchanged at the end of the recovery. Typically, recovery is never hundred percent, due to trapped, confined or specifically bound molecules. Especially in membranes, the molecule of interest can be confined by membrane barriers or by microdomains which both affect the mobility of the fluorophore [326]. The proteins in the immobile fraction do not diffuse. The mobile fraction M_f is defined according to:

$$M_f = \frac{I_{\text{inf}} - I_0}{I_i - I_0} \qquad \text{(Eq. 3.10)}$$

with I_{inf} as the fluorescence intensity after full recovery, I_0 as the intensity directly after bleaching and I_i as the initial fluorescence before the bleach pulse. Before each analysis, the region of interests have to be background corrected and corrected for bleaching during the recovery process. Therefore, the pre-bleach intensity is defined as 100 %. Without correcting for the loss of total fluorescence during the recovery process, the region of interest (ROI) intensity can never recover to 100 %.

Usually more important is the diffusion analysis of the mobile fluorophore, because they provide information about the viscosity of the surrounding medium and potential interactions with presumptive ligands in the cell. The diffusion coefficient, D (usually $\text{m}^2 \cdot \text{s}^{-1}$ or $\text{cm}^2 \cdot \text{s}^{-1}$), reflects the mean-square displacement that a protein explores through a random walk (i.e. Brownian motion) over time. It is important to recognize that D is not a linear

rate. That is, the time required to cover increasing distances will not increase in a linear fashion. Such a random walk is characterized by the fact that with time the molecule covers the square root of the distance. The half-life $t_{1/2}$ of the recovery time can be calculated by fitting the intensity-time $I(t)$ curve as shown in Fig. 6.11 with a simple exponential:

$$I(t) = M_f(1 - \exp[\tau t]) \qquad \text{with} \qquad t_{1/2} = \frac{\ln 0.5}{\tau} \qquad \text{(Eq. 3.11)}$$

The half-life of the recovery can be used then to calculate the diffusion coefficient $D = \frac{zw}{t_{1/2}}$ with z as the depth and w as the width of the bleaching spot. If no directed flow or drift is present, recovery of the bleached region is solely by diffusion. Unrestricted diffusion of a particle in a free volume is described by the Einstein-Stokes relation and correlates the diffusion with the viscosity, η, and the size of the labeled species, R_H, of interest:

$$D = \frac{k_b T}{6\pi\eta R_H} \qquad \text{(Eq. 3.12)}$$

This relation describes well the mobility of soluble proteins in the cytoplasm but fails to describe the diffusion of membrane bound proteins. Biological membranes have a much higher viscosity so that the size of the soluble segment does not determine the mobility anymore, but the diffusion is only affected by the size of the membrane-inserted region [326]. Therefore, diffusion of membrane inserted proteins is best described by the Saffman-Delbrück approximation [327]. The Saffman-Delbrück equation considers a theoretical protein with a cylindrical transmembrane segment without interactions with the surrounding lipid bilayer. However, most membrane molecules diffuse more slowly than expected for random brownian motion in a lipid layer. This might be due to lipid-lipid-interactions, obstacles, and temporary binding sites in cell membranes. That is why it is very difficult to deduce quantitative values for viscosities from FRAP measurements. To date, no simple solution has been presented. The only information about cell membrane viscosities has come from single tether extraction experiments [35, 328, 329].

Up to now, FRAP has been used top measure the mobility of a myriad of different soluble and membrane bound proteins. It has been used to measure protein interaction, conformational changes of proteins, diffusion in subcellular compartments and was used to follow protein dynamics throughout different stages of the cell cycle. Because this thesis is mainly interested in studying the fluidity of cellular membranes, the next table summarized values for diffusion coefficients acquired with fluorescent lipid probes in living cells.

3.2. Methods

3.2.1. mRNA preparation

mRNA was prepared using a commercial transcription kit (Ambion mMessage). First, circular plasmids were cut at the 3' end of the gene-encoding region to linearize the vector. The coding region is initiated either by a SP6 or a T7 promotor. Linearization is necessary because the RNA polymerase will then fall off the template strand and only creates transcripts of the right length, ending with the coding region.

Cell type	D	Dye	Technique	Ref.
Cos-7	$1.1\,\mu m^2\,s^{-1}$	$DiIC_{16}$	FRAP	[330]
COS-7	$0.9\,\mu m^2\,s^{-1}$	GFP-GPI	FCS	[331]
Fibroblast	$1.0\text{-}1.4\,\mu m^2\,s^{-1}$	DHDIC	FRAP	[332]
NRK cells	$5.4\,\mu m^2\,s^{-1}$	DOPE	SPT	[333]

Table 3.1 Lipid bilayer diffusion coefficients

Published values for diffusion coefficients using different cells, labels and techniques. Abbreviations in this table: $DiIC_{16}$, 1,1'-diahexadecyl-3,3,3,3-tetramethylindocarbocyanine perchlorate; FRAP, Fluorescence Recovery After Photobleaching; GFP-GPI, Green-Fluorescent-Protein coupled Glycosyl-Phosphatidyl-Inositol; FCS, Fluorescence Correlation Spectroscopy; DHDIC, Dihexadodecylindocarbocyanin; DOPE, dioleoylphosphatidylethanolamine; SPT, Single Particle Tracking

---

1. Linearization

   - 10 µl plasmid ($1\,\mu g \cdot \mu l^{-1}$)
   - 5 µl BSA (delivered, depending on the enzyme used)
   - 5 µl Buffer according to the enzyme
   - 1 µl restriction enzyme
   - add water to 50 µl total reaction volume

The restriction reaction was incubated for 3 h at 37°C and purified afterwards using the Qiagen QiaQuick PCR Purification kit. The linearized plasmid was then used for mRNA transcription. The following protocol has been used and the reaction was placed for 3 h in a 37°C water bath:

2. Transcription

   - 5 µl linearized plasmid
   - 2 µl 10 × reaction buffer
   - 2 µl enzyme, depending on the promotor
   - 10 µl 2 × NTP/Cap for incorporating nucleosides and 5' cap
   - add RNAse-free water to 20 µl total reaction volume

At the end of the incubation time, the reaction was stopped upon addition of 1 µl DNase. To remove all un-incorporated nucleosides and enzymes, the reaction was processed using a Qiagen RNAeasy RNA purification kit. At the end, 1 µl of the purified RNA solution was mixed with 9 µl sample buffer and run on a 1 % agarose gel to check the quality of the transcription (see Fig. 3.3). In most of the cases, only one band was visible. To estimate the concentration, 0.7 µl of the concentrated RNA solution was diluted in 70 µl ultrapure water and the absorbance at 260 nm was measured.

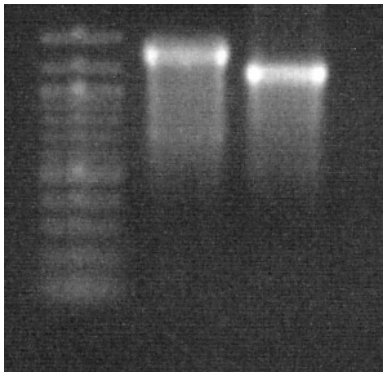

Fig. 3.3 mRNA transcription

cyclops and *dnEZR* mRNA separated on a 1 % agarose gel to check purity and integrity of the transcript. The marker is followed by dn*EZR* transcript and a transcript of the *cyclops* gene.

3.2.2. Single cell microinjection

In this thesis, the main subject is to characterize the biophysical properties of single cells and to relate them to the germ layer formation. At the stage of gastrulation, each vertebrate animal consists of at least three different germ layer cell types. To reduce the variability that come along with the different types of cells in the developing zebrafish, we need to modify the development of each embryo. Most easily, this is done by injecting mRNA which is known to specify embryonic cell fate into the freshly fertilized egg. For example, to induce endodermal cell fate, a transcription factor downstream of Nodal signaling, *casanova*, was over-expressed in the cells. For mesodermal cell fate a combination of *cyclops* to activate the Nodal signaling pathway and a casanova morpholino to block the activation of endoderm specification was used (see Sec. 2.1.2 and see Fig. 2.2).

For microinjection, needles were pulled using a Harvard Instruments needle puller. Needles were backfilled with the solution of interest, connected to a microinjecting device and built into a Narishige micromanipulator for fine positioning of the needle over the sample. The very tip of the needle was then broken with a clean forceps and the drop size was adjusted to 500 pl total volume. Adjustment of the drop volume was easy to achieve by regulating the time and the pressure on the microinjection device. As a guide for correct size, a microscale was used [334, 335] (see Fig. 3.4).

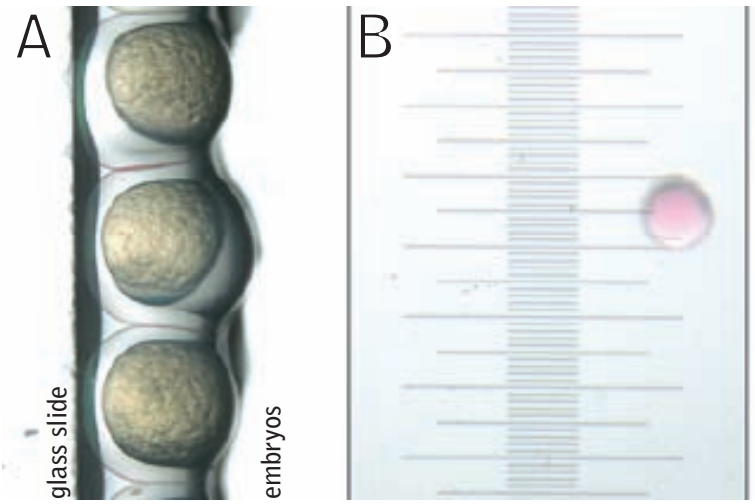

Fig. 3.4 Zebrafish egg microinjection

A: A collection of zebrafish eggs are aligned at the edge of a glass slide in a petri dish. **B:** A microscale is used to guide the adjustment of the correct volume of the drop (red). Picture taken from [334].

Freshly fertilized eggs were aligned on the edge of a glass slide put in a petri dish (see Fig. 3.4 A). Surface tension immobilized the embryos so that they do not move when the needle penetrated the chorion (see Fig. 3.4). When injecting into the yolk, a small cloud will appear. More sophisticated and way more faithful, the needle can be penetrated directly into the cell instead of the yolk, to ensure proper delivery of the mRNA into the embryo. If only the chorion was penetrated and not the embryo proper, the injected solution will diffuse rapidly and nothing will be visible. When injecting more than one mRNA or morpholino in different needles, attention has to be paid, that embryos do not develop past the two-cell stage because cytoplasmic streaming is not sufficient anymore to draw the mRNA into the embryo proper. Table 3.2 and Table 3.3 summarizes the different mRNAs and morpholinos which have been injected during the experimental work of this thesis.

After injection, embryos were stored at 31°C for $\approx$ 5 hours before cell culture until they reached dome/sphere stage transition, as indicated in Fig. 2.1 C. The exact stage was monitored with a binocular microscope (Zeiss).

mRNA	Mass	Function	Ref.
cyclops	100 pg	TGFβ activ.	[336]
casanova	50 pg	endoderm activ.	[61]
da*Taram-A*	25 pg	endoderm activ.	[56]
lefty	100 pg	TGFβ suppr.	[337]
dn*EZR*	300 pg	$\downarrow$ membr.-csk-interaction	[338]
da*EZR*	100,300 pg	$\uparrow$ membr.-csk-interaction	this study
mRFP	100 pg	GPI anchored RFP	
gap-GFP	100 pg	palmitoylated GFP	
lyn-YFP	100 pg	myristoylated YFP	[339]
lifeAct	50 pg	filamentous actin stain	[340]
dn*Rok2*	250 pg	$\downarrow$myosin activation	[77]
dn*MRLC2a*	250 pg	$\downarrow$myosin activation	

Table 3.2 mRNA injections

All mRNAs that were used to alter the cell fate of embryonic zebrafish cells, to modify their molecular composition or to fluorescently label specific molecules. For mRNA injections, in general 1 drop of 500 pl of a $0.2\,\mu g \cdot \mu l^{-1}$ solution has 100 pg.

3.2.3. Cell culture

Cells were taken from sphere stage embryos after washing and removal of the chorion. To ensure integrity of cell adhesion molecules for the subsequent measurements, enzyme free dissociation methods were used. In that stage of development, usually no adherence junctions have formed [27]. For the cell culture the following procedure was used:

- wash embryos in E3 medium

Morpholino	Mass	Function	Ref.
e-cadherin	0.5-8 ng	Cell adhesion	[78]
n-cadherin	6 ng	Cell adhesion	[341]
casanova	2 ng	endoderm suppr.	[342]
*ezrin*2	4 ng	↓ membr.-csk-interaction	[31]
radixin	4 ng	↓ membr.-csk-interaction	

Table 3.3 Antisense morpholino injections

- de-chorionate embryos for 8 min in 2 mg·ml^{-1} pronase (ROCHE) in a small petri dish (⊘=3.5cm)
- transfer into fresh petri dishes (⊘=6cm) and wash 3 times in E2 medium (see Sec. 3.3.1) using a glass Pasteur pipette (230 mm)
- transfer into an Eppendorf tube (2 ml) and add 1 ml of fresh dissociation buffer
- pipette up and down gently to disrupt the yolk sac; now the solution becomes turbid
- centrifuge at 500 g for 30 s and replace supernatant by fresh cell culture medium

recom. repeat last step to remove further yolk proteins especially for cell surface biotinylation procedures

Cells were left to recover for 20 minutes at room temperature before the actual experiment was started. Cells that were used for re-aggregation experiments were cultured in DMEM whereas cells for measurements under ambient conditions (no CO_2 supply) a carbonate-free DMEM/F12 1:1 mixture was used.

3.2.4. Hanging drop experiments

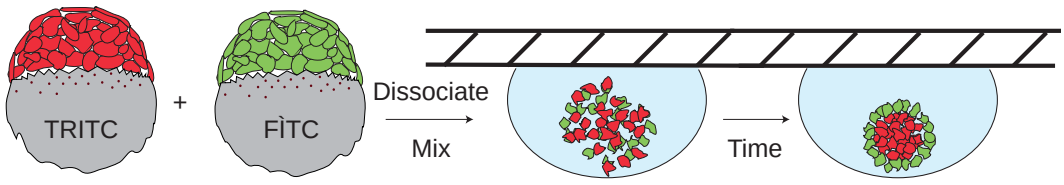

Fig. 3.5 Hanging drop culture

Embryos are injected with two different fluorescent dyes to distinguish the origin of the cells during the experiment. At sphere/dome stage, embryos were dissociated and single cells were mixed. A drop was seeded on a glass slide or petri-dish and inverted. This hanging drop was then observed with an epi-fluorescence microscope.

After blastoderm dissociation at 5 hpf, 1.5·10^6 cells/ml of two different germ layer progenitor cell types were allowed to aggregate in 25 µl or 50 µl hanging drops. The ratio of

Inhibitor	conc.	function	Company	Reference
EGTA	5 mM	Cell adhesion	SigmaAldrich	[155]
IAA	10 mM	E-cadherin	SigmaAldrich	[155]
Activin	100 ng·ml^{-1}	mesendoderm activ.	SigmaAldrich	[58]
(−) - Blebbistatin	50 µM	myosin inactiv.	SigmaAldrich	[343]
(+) - Blebbistatin	50 µM	myosin inactiv.	CalBioChem	[343]
BDM	10 mM	myosin inactiv.	CalBioChem	[344]
Latrunculin A	1 µM	actin depol.	SigmaAldrich	[345]
Cytchalasin D	10 mM	actin depol.	SigmaAldrich	[109]
Staurosporin	5 µM	Kinase inhibitor	SigmaAldrich	[338]
U-73122	1 µM	PLC inhibitor	SigmaAldrich	[29]
NPM	20 mM	Con A-Mannoside inhib.	SigmaAldrich	[346]

Table 3.4 List of used inhibitors

Abbreviations used in this table: EGTA, ethylene glycol tetraacetic acid; IAA, indole acetic acid; BDM, 2,3-butanedione monoxime; NPM, 4-Nitrophenyl α-D-mannopyranoside; PLC, phospho lipase C

co-cultured cells was set to 1:1 or 1:2 with the enveloping cell type at the higher concentration. Cultures were incubated for at least 17 h in a humidified chamber equilibrated with 5 % CO_2 at 27 °C. To reduce cortex tension, the cells were cultured in the presence of 50 µM (−) - Blebbistatin (CalBioChem), 10 mM Cytochalasin D (SigmaAldrich) or 20 mM 2,3- butanedionemonoxime (BDM, CalBioChem) as indicated. Control aggregates were cultured in the presence of 50 µM (+) - Blebbistatin (CalBioChem, see Fig. 4.10). Incubation in 5 mM EDTA did not lead to aggregation or sorting (see Fig. 4.8). To selectively inhibit cortex tension in ectoderm progenitors, MZ-*oep* embryos were injected with 350 pg *dnrok2* mRNA. Images were taken after 0, 4, 6, 8 and 17 h in culture with Metamorph (Digital Imaging) using an epi-fluorescence microscope (Zeiss Axiovert 200M equipped with EXFO X-cite 120, 5× lens, 470[40]BP/525[50]BP and 546[12]BP/575LP excitation/emission filters, Zeiss) and a CoolSnap CCD camera (Roper Scientific, 4.6×4.6 µm^2, 12 bit/pixel). Linear contrast adjustment was applied to the whole image using ImageJ. To analyze the sorting dynamics, 5000 cells of each type were cultured in a passivated micro-chamber. Sorting was followed with a rate of 4 frames/min and analyzed as described below. EDTA addition into the culture did not lead to any changes in cluster size (see Fig. 4.8 H).

3.2.5. In-vitro biotinylation

In-vitro biotinylation of membrane proteins is one of the prevalent methods to determine the plasma-membrane proteome of a cell type. Fluorescence activated cell sorting is only the methods of choice if a good monoclonal antibody recognizing extracellular epitopes is available. For zebrafish proteins, almost no monoclonal antibodies have been raised, although some conserved proteins are recognized due to cross-species reactivity of the antibodies, e.g.

Tubulin or Actin. In a typical biotinylation experiment, cells are biotinylated for ca 40 minutes on ice to prevent endo/exocytosis and hence internalization of the labeled proteins. After that, reaction is thoroughly stopped and cells are dissociated. The cell lysate is applied to a Streptavidin column which binds all of the biotin-labeled proteins. The flow-through ideally only contains the intracellular fraction. After washing, the extracellular column-bound fraction is eluted either with a high concentration of biotin, or, if the biotin is coupled via a S-S bond to the reactive group (protein), via a disulfide bond reducing agent, e.g. dithiothreitol (DTT). Both fractions can now be analyzed running a conventional western blot. In this work, the cell surface protein isolation kit from PIERCE BIOTECHNOLOGY was used which supplies a cross-linker which is coupled to the biotin with disulfide group. This offers the opportunity to remove the bound proteins easily from the biotin. The cross-linker is a amine-reactive NHS ester group, which target efficiently primary amino groups which are present on the surface of nearly all proteins. It is a nucleophile that is very reactive towards polar solvents and loses reactivity in aqueous environments.

In the following, a detailed procedure will be presented:

1. De-yolking
    - dechorionize at least 100 embryos per reaction, ideally 150
    - transfer embryos in 1.5 ml Eppendorf tube with 1 ml $\frac{1}{2}\times$ Ginzburg fish ringer without Ca^{2+} (55 mM NaCl, 1.8 mM KCl, 1.25 mM $NaHCO_3$)
    - pipet up and down to disrupt the yolk sac
    - 5 min shaking at 1100 rpm
    - centrifuge at 400 g for 30 seconds and discard supernatant
    - wash once again in Ginzburg fish ringer solution
2. biotinylation
    - centrifuge at 300 g for 30 s
    - add 200 µl of a 1 mg·ml^{-1} NHS-biotin solution
    - rock 30 min on ice
    - add 1.3 ml TBS buffer with 65 µl quench solution to each reaction
    - 5 min rocking
    - centrifuge 300 g
    - add 1.5 ml TBS and rock for 5min
    - centrifuge and add 200 µl lysis buffer+protease inhibitor (dissolve 1 tablet in 1 ml PBS and use 1 to 10)
    - incubate for 30 min on ice and sonicate every 10 min; alternatively, vortex
    - centrifuge cell lysate at 10.000 g for 2 min at 4°C and transfer supernatant into a new tube
3. Isolation of labeled proteins

- prepare a column with 250 µl streptavidin and wash 3× with the supplied washing buffer
- add whole cell lysate onto the column and incubate for 60 min at room temperature
- place tube in a 2 ml collection tube (provided) and centrifuge at 1000 g for 2 min; keep flow through since it contains intracellular proteins
- wash column 3 × with 500 µl of washing solution

4. Protein elution

- prepare a solution of 50 mM DTT in 1× SDS sample buffer by adding 23.7 µl 1M DTT (50 µl/tube, provided) in 450 µl SDS sample buffer
- add 200 µl SDS sample buffer to the column and incubate for 60 min at room temperature
- place column in a new reaction container and centrifuge at 1000 g for 2 min
- run a gel

3.2.6. Western blotting

Polyacrylamide gel

For western blotting, a standard protocols was used.

gel conc %	5	7.5	10	12.5	15	stacking gel
AA/bis in ml	2	3	4	5	6	0.8
Tris 1.5M/0.4% SDS pH 8.8 in ml	3	3	3	3	3	0.75
H_2O in ml	7	6	5	4	3	4.4
APS 10% in µl	80	80	80	80	80	40
TEMED in µl	8	8	8	8	8	4

Table 3.5 Recipes to prepare a SDS-PAGE gel

Electroblotting

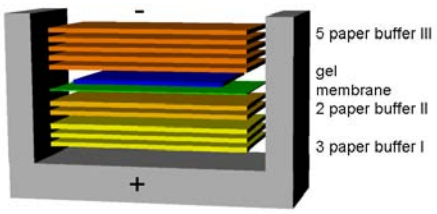

Fig. 3.6 Assembly of an electro-blot

Blot assembly to transfer proteins from a PAA gel to an nitrocellulose membrane

- prepare membrane: - 30 sec in methanol, - 2 min in ddH_2O, - 5 min in buffer II
- put blot together according Fig. 3.6
  - 3 Whatman paper [9×16 cm] drenched in buffer I [0.3 M Tris, 20% methanol, pH 10.4]
  - 2 paper soaked in buffer II [0.025 M Tris, 20 % methanol, pH 10.4]
  - 5 paper soaked in buffer III [0.04 M amino-n-caproic acid, 0.025 M Tris, 20% methanol, pH = 9.4]
- blot at 70 mA/gel
- stain 5 min in Poinceau
- scan membrane and mark bands with pencil
- block for 1 h with 5% milk powder in PBST (0.1 % Tween in PBS)
- primary antibody (rabbit anti E-cad 1:10.000 in blocking buffer) over night
- wash membrane 4×5 min and once 10 min in PBST
- apply 2^{nd} antibody for 1 h
- wash membrane 4×5 min and once 10 min in PBST
- develop for 5 min in 1:1 detection solution

3.2.7. The AFM setup

The set-up to perform cell-interaction experiments is shown in Fig. 3.7. It consists of several features specifically designed for efficient cell-cell separation experiments and is described in detail in [347]. Cells tend to stay in contact upon a forced separation by long membrane nanotubes. These can extend for several tens of micrometers making a long pulling distance unavoidable. Furthermore, single cell force spectroscopy measurements need an integration into a optical observation system to judge the state of a cell during the separation experiment and to place the probe in respect to the sample cell. Equipment with a fluorescent lamp is useful if two different cell types have to be tested. Hence, the two cell types can be labeled differentially and identified according to their fluorescent color. This is particularly useful when transgenic lines are used which show a great cell-to-cell variability in the expression of the desired transgene. Using a GFP reporter then can be useful to choose the most efficiently transfected/injected cell.

3.2.8. Adhesion measurements

Cantilever preparation

Plasma-activated cantilevers (Veeco MLCT, nominal spring constant $k_c = 30\,\mathrm{mN \cdot m^{-1}}$) were incubated with Concanavalin A (Con A, $2.5\,\mathrm{mg \cdot ml^{-1}}$, Sigma) overnight at 4°C and carefully rinsed in PBS before use.

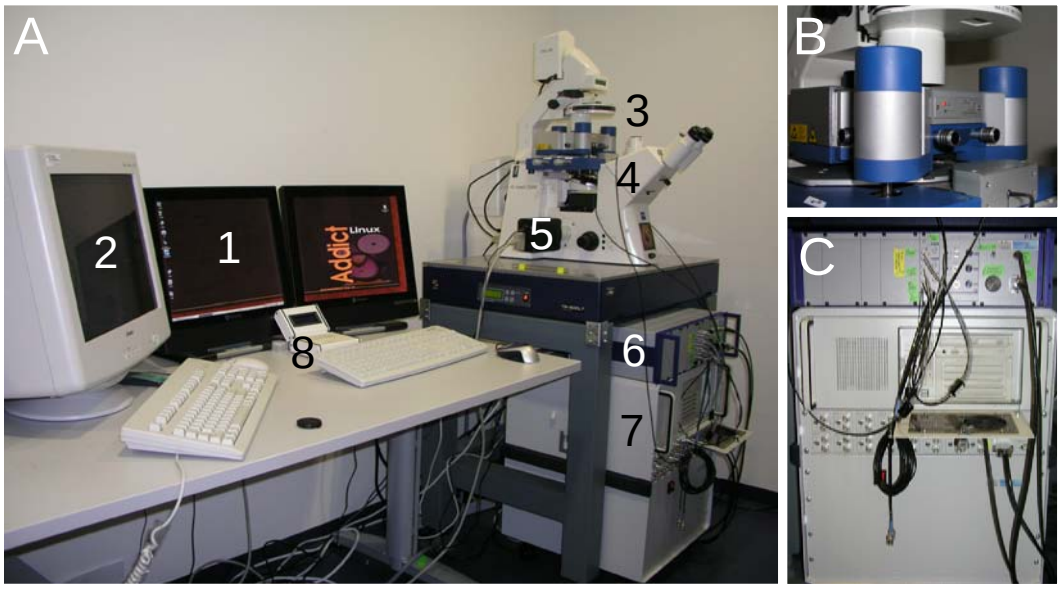

Fig. 3.7 AFM - set-up for single cell force spectroscopy measurements

A: General set-up of the AFM instrument. Monitors for AFM software controlling (1) and optical microscopy (2). AFM head with piezo, laser, photodiode (3) is placed on top of a Zeiss Axiovert 200 (4) equipped with a camera (5) for life cell imaging during the force spectroscopy experiment. The head is controlled by a feedback controller (6) and equipped with a $100\,\mu m$ piezo for cell-cell separation experiments (7). **B:** Close-up of the AFM head mounted on a x, y stage. $100\,\mu m$ piezos are built in to the stage. **C:** Front view of the controller.

Substrate preparation

Plasma-activated microscope slides (GoldSeal) were prepared using a two-well coating mask (home-built) to obtain an adhesive and non-adhesive substrate. One well was filled with $50\,\mu l$ heat-inactivated fetal calf serum (Invitrogen), ensuring passivation of the surface (non-adhesive substrate), whereas the other was filled with $50\,\mu l$ Con A ($2.5\,mg \cdot ml^{-1}$; adhesive substrate). Before the experiment, substrates were gently rinsed with the cell culture medium (see Sec. 3.3.1) used to perform the adhesion tests. Diluted cell suspensions were then seeded onto the substrate.

AFM experiments

All experiments were carried out at 25°C. For homotypic adhesion experiments, cells were selected using phase-contrast microscopy. For heterotypic adhesion experiments, one-cell-stage embryos were injected with both mRNA (see above) and either FITC- or TRITC-coupled dextran (Molecular Probes). Cells were identified using fluorescence microscopy. A given 'probe'-cell (see Fig. 4.1) was selected from the non-adhesive side of the substrate with a Con A-coated cantilever by gently pressing on it with a controlled force of 1 nN for typically 1 s. The cell was raised from the surface for 2-10 min to firmly attach to the cantilever. The probe-cell was then moved above a 'target'-cell that was firmly attached to the adhesive Con A-coated part of the substrate. Adhesion experiments ('force-distance cycles',

see Fig. 4.1) were performed using a 1 nN contact force, 10 $\mu m \cdot s^{-1}$ approach and retract velocities, and contact times ranging from 1-60 s. Contact time was varied randomly for a given cell-cell couple to prevent any systematic bias or history effect. Each condition (that is, same probe-target couple at same contact time) was repeated up to three times, with a resting time of 30 s between successive contacts. Each probe-cell was used to test several target-cells. No more than 40 curves were taken with any given probe-cell. Cells were observed continuously during and between the force-distance cycles to judge whether they were intact and stably associated with the cantilever/substrate. Only cells that showed characteristic 'ruffling' behavior and pseudopod formation were used. Target-cell pictures were taken to measure diameter and observe morphology. Force-distance curves were analyzed using IgorPro WAVEMETRICS and custom-made routines to extract maximum adhesion force (see Fig. 4.2, 4.3, 4.4 and Fig. 4.5) and cell deformation (see Fig. 4.4) during the contact. Data were then pooled and statistically processed as described in Sec. 3.2.14. Cadherin-dependence of cell adhesion was tested after depleting calcium by adding EGTA (5 mM, SIGMA) to the medium, or injecting embryos with E-cadherin morpholino oligonucleotides (8 ng; see Fig. 4.2). To reduce actomyosin function, cells were pre-incubated in (−)-Blebbistatin (50 µM, SIGMA). Experiments were carried out in 5 µM (−)-Blebbistatin with no more than 15-20 repeated measures taken with a single probe-cell because of mechanical fragility of the treated cells. Preparation of E-cadherin-coated substrates was carried out as described previously [155]. Approach and retract velocities were set to 4 $\mu m \cdot s^{-1}$.

3.2.9. Cell-cortex tension measurements

Preparation of colloidal force probes Cortex tension was measured by deforming the cell surface using beads as an indenter to create a large and smooth contact geometry with the cell, hence reducing the strain induced by the contact [275]. Such colloidal force probes were prepared by attaching a glass bead (5 µm diameter, KISKER BIOTECH) to a cantilever (VEECO MLCT) using a two-component ARALDIT epoxy glue. A schematic of the procedure is shown in Fig. 3.8

- modification of different cantilevers with different bead sizes
  - calibrate cantilever prior bead addition
  - spread epoxy-glue on one side of a glass slide and leave a small amount of beads on the other
  - gently approach cantilever into the glue with the very front tip by running a 'force distance cycle'
  - retract immediately after 2 seconds by moving the cantilever sideways out of the glue with the micrometer screws
    - ↪ this prevents over-deposition of the glue
  - move cantilever over a bead
  - gently touch the bead and retract the cantilever after 2 seconds using the piezo
  - leave for 1 hour to dry and check it using an optical microscope

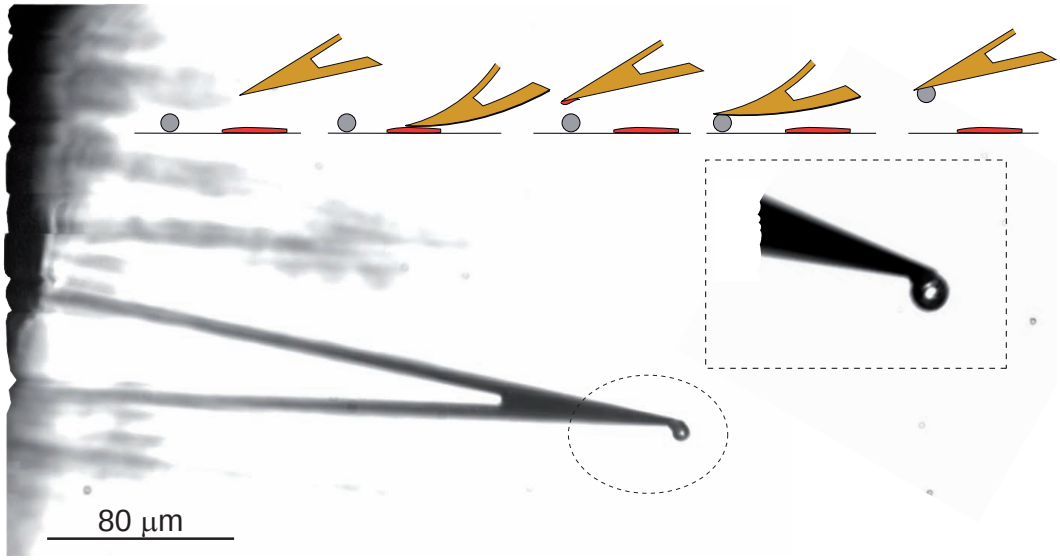

Fig. 3.8 Cantilever modification with colloidal glass beads

Schematic representation of the procedure described above. A cantilever is approached into two-component glue using the piezo of an AFM and retracted immediately. Subsequently, the cantilever is approached onto a solitary glass bead close by and retracted after two seconds. Background micrograph shows a successful modification of a cantilever.

To prevent non-specific adhesion to the cells, the modified cantilevers were either incubated with heat inactivated fetal calf serum (INVITROGEN) or silanized (1 % methyltriethoxysilane (MTES, SIGMA) in hexane (FLUKA) for 1 h) and then passivated with 1 % pluronic F127 (SIGMA) in ultrapure water.

- chemical passivation with a hydrophobic brush
  - plasma clean cantilevers for 5 min
  - immerse in 1 % methyltriethoxysilane 99 % hexane for 1 h (see Sec. 3.2.13)
  - rinse in pure hexane
  - bake for 1 hour at 373 K
  - rinse in pluronic F-127
  - wash in water

Procedure and model assumptions The cells were seeded on a glass substrate. Force-distance curves were acquired using 500 pN contact force and 1 $\mu m \cdot s^{-1}$ approach/retract velocity and indentation, δ, was calculated from tip displacement (see Fig. 4.6 B) according to Eq. 3.5. Up to three curves, with at least 15 s waiting time between successive curves, were taken per cell to prevent any history effect. To describe the mechanics of the different cell types by AFM indentation, the approach of Rosenbluth et al. [292] was chosen. The liquid droplet model [285] was applied to extract the cell-cortex tension, as previously proposed for different cell types with the micropipette technique [285, 291, 289]

using Eq. 3.13. Cell-cortex tension is influenced directly by the state of the contractile apparatus of the cell [136, 291]. The *liquid droplet model* describes the cell as a viscous cytosol surrounded by an elastic (actin-based) cortex. This is based on the following assumptions:

1. an actin cortex exists in close proximity to the cell membrane
2. the nucleus occupies only a small volume of the cell
3. cells are not adherent and spherical
4. force versus indentation curves are linear (see Eq. 3.13)
5. indentation depth is small, compared with the size of the cell [275]
6. cell-cortex tension is independent of the cantilever speed
7. cells have a large plasma-membrane reservoir.

Cell-cortex tension T_c can then be calculated using the following equation [289]:

$$f = \left[2T_c \left(\frac{1}{R_c} + \frac{1}{R_b}\right) \cdot 2\pi R_b\right] \cdot \delta \qquad \text{(Eq. 3.13)}$$

where f = force, δ = indentation, R_c = cell radius and R_b = bead radius.

The assumptions of the liquid droplet model matched with the following properties of the assay system:

1. Phalloidin staining of our progenitors showed an actin-based cortex both in dissociated cells and in embryos (see Fig. 4.6 A).
2. The ratio of cell- to nucleus- volume estimated from phase-contrast images was high (21 ± 12, mean ± SD, see Fig. 3.9).
3. Dissociated cells were roughly spherical (see Fig. 4.6 A) and weakly adherent to the substrate.
4. Force versus indentation curves were linear (70 % of all curves) for a large range of indentation values (see Fig. 4.6 B),
5. and with the deformation (max ≈ 1 µm) being at least one order of magnitude smaller than the cell diameter (approximately 18-20 µm).
6. Finally, our adhesion measurements suggest that the cells possess a large membrane reservoir as indicated by long lipid tubes extracted during the separation process using SCFS (tethers, see Fig. 4.1 and see Chap. 6 and 7).

Together, this provides experimental support for using the liquid drop model to analyze our indentation experiments and gain information about the cortex tension of the progenitor types. To determine cell-cortex tension using the equation above, we used a force versus indentation line-fit between 125 pN and 250 pN to exclude errors that could be introduced while determining the bead-to-cell contact point [321]. Bead and cell radii were determined by phase-contrast microscopy. To alter cortex tension, cells were pre-incubated in (−) - Blebbistatin (50 µM) or recombinant Activin (100 ng·ml^{-1}, Sigma) for 2 h. For Blebbistatin, cells were measured in the presence of 5 µM (−) - Blebbistatin. All experiments were performed at 25°C.

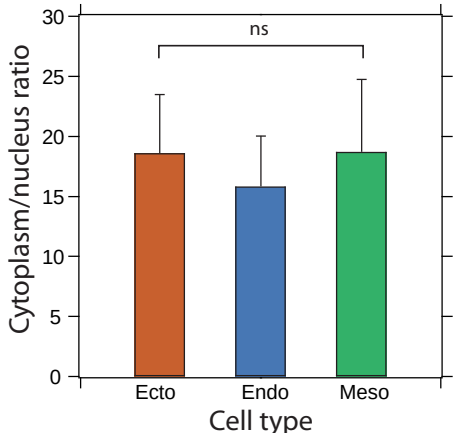

Fig. 3.9 Cell-nucleus volume ratio

The ratio of cell volume to nucleus volume is essentially unchanged between the three different germ layer progenitor cells. The volume was calculated approximating a sphere according to $V = \frac{4}{3}\pi r^3$.

3.2.10. Tether extraction using AFM

AFM cantilevers (Olympus Biolever, $6\,\mathrm{mN \cdot m^{-1}}$) were plasma-cleaned for 5 min and incubated in either $2.5\,\mathrm{mg \cdot ml^{-1}}$ Concanavalin A (Sigma) or $5\,\mathrm{mg \cdot ml^{-1}}$ BSA (Sigma) in PBS buffer for 2 hours. Prior to use, cantilevers were rinsed in PBS. Cantilevers were then mounted in an AFM (NanoWizard, JPK) that is integrated into an inverted light microscope (Axiovert 200M, Zeiss). Cantilever spring constants were determined using the thermal noise method [305]. Cells were seeded in 1 ml of culture medium onto glass surfaces (GoldSeal) in a home-built fluid chamber. Nanotubes were extracted at room temperature (25°C). To optimize the number of bonds between the cantilever and the cell, contact force was adjusted to 100 pN and the contact time was varied between 0.0 and 0.6 s. Force-distance curves showing more than one nanotubes or nanotubes shorter than 0.25 µm were omitted from the analysis. To control the nanotube extrusion force, the cantilever retraction velocity was varied between 1 and $50\,\mathrm{\mu m \cdot s^{-1}}$. Specificity was tested using cantilevers incubated with BSA ($5\,\mathrm{mg \cdot ml^{-1}}$, Sigma) at room temperature for 4 hours. Alternatively, cantilevers were incubated with Con A over night at 4°C and subsequently immersed in 20 mM 4-nitrophenyl α-D-mannopyranoside (Sigma) or pure heat-inactivated fetal calf serum (Invitrogen) for 2 hours.

Nanotube extraction forces f_t and bond lifetimes λ were determined from force-distance curves displaying a single unbinding event using an in-house IgorPro (WaveMetrics) algorithm. Lifetimes were sorted and plotted as a cumulated histogram. The number of tethers at a lifetime decayed exponentially and were fit to Eq. 7.3 to extract characteristic unbinding rate k_{off} at a certain force . Levenberg-Maquardt fitting of the lifetime*, λ, versus force, f, data to the Bell model was used (see Eq. 7.4) to determine the off-rate at zero force, k^0_{off}, and the potential width as the distance of the bond to the transition state, x_u, of the receptor-ligand pair.

The force required to extrude a tether and hold it at a constant length is dependent on the bending rigidity κ, in plane membrane tension T_{eff} and adhesion energy density W_0 according to Eq. 6.2. Additional viscous terms influence the behavior of the tether under flow, e.g. when pulled with varying extrusion velocities (see Eq. 3.14 and Eq. 6.4).

Bending rigidity κ, usually in the order of $\sim 2 - 3 \cdot 10^{-19}$ Nm for eukaryotic cell mem-

*(unbinding rate, k_{off}=$1/\lambda$)

branes (see Table 6.1 and Ref. [328, 348]), is only determined by the material property of the cell membrane and is not assumed to change upon Ezrin knockdown or cytoplasmic actin composition [349, 350, 351]. In-plane membrane tension is a weak surface tension term established by the attraction of the lipids and is assumed not to depend on the support to the actin cytoskeleton either [142, 36, 352]. Adhesion energy in contrast strongly depends on the interaction of the membrane with the cytoskeleton and is thought to be mainly responsible for the static tether force. The tether-force - extrusion velocity ($f - v$) profile is known to depend on the membrane viscosity η and has recently been modeled as a function of the density of binders ν:

$$f^3 - f f_0^2 = a \cdot dv \qquad \text{with} \qquad a = (2\pi)^3 \kappa^2 \eta \nu \ln\left(\frac{R_c}{R_t}\right) \tag{Eq. 3.14}$$

The model was fitted to the data using a home-written least squares minimization procedure to minimize the error on the force (written by Jonne Helenius in IgorPro). This yielded static tether force f_0 and the dynamics of extrusion a. This was then solved for ν relying on published data for κ=2.9·10^{-19} Nm [350, 328] and $\eta = 1.5 \cdot 10^{-7}$Pa s m [351]. The term $\ln\left(\frac{R_c}{R_t}\right)$ is nearly constant and varies only between 5.8 (wt) and 4.6 (lat A) because the tether radius R_t is almost three orders of magnitude smaller than the cell radius R_c.

3.2.11. FRAP Protocol

All FRAP experiments were carried out on a LEICA SP5 system with the FRAP-Wizard tool using a 63 × water immersion lens with a numerical aperture N_A=1.33. Cells expressing a palmitoylated GFP (gap-GFP) or a myristoylated YFP (lyn-YFP) were seeded on a Con A coated coverslip until they spread out and adhered firmly. This was necessary to prevent extensive plasma-membrane blebbing which would alter the recovery process after bleaching the defined spot. Furthermore, blebbing creates a plasma-membrane flow resulting in a recovery that is not based on brownian motion of the fluorophores. A cell was chosen and two pre-bleach images were taken. After that, a defined spot was bleached for 1.2 seconds using full laser power at 488 nm. The recovery process was followed for 110 seconds. The fluorescence intensity - time profile $I(t)$ was background (I_B) subtracted and corrected for bleaching according to:

$$I(t) = \frac{I_{Bs}(t) - I_B(t)}{I_\Sigma(t) - I_B(t)} \tag{Eq. 3.15}$$

with I_{Bs} as the intensity of the bleach spot and I_Σ the integrated density of the whole image. After correction, the FRAP curve was fit to Eq. 3.11 to extract the characteristic recovery time from which the half time of recovery was calculated. The half time and the geometry of the bleach spot was used to assess the diffusion constant of the fluorophore in the lipid-bilayer membrane.

Because the membrane was bleached parallel to the optical axis (z-extension), the determination of the 2D geometry was not straightforward. To determine the z-extension, cells adherent on a glass coverslip were fixed at 4°C over night in 8 % paraformaldehyde. The same laser settings have been used to bleach an defined area compared to the experimental conditions as described above. Recovery of the fluorophores was much slower and an image of the cell at a fixed y (x, z-scan) coordinate could be taken to measure the extension of the

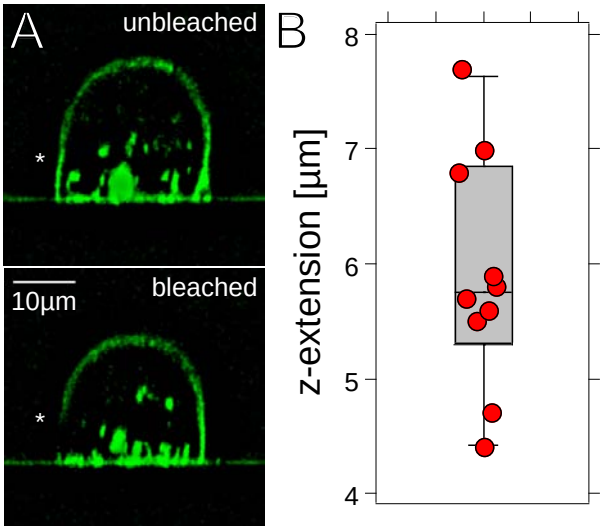

Fig. 3.10 FRAP z geometry

A: A PFA fixed cell adherent on a substrate has been bleach at full laser power. The lower panel shows the z-extension of the bleach sport which is $\sim$. 5.5 µm. **B:** Quantification of the spot size with 10 different cells.

bleach spot in z-direction (see Fig. 3.10 A). 10 cells have been bleached and the extension along z was measured to vary between 4.4 and 7.7 µm (see Fig. 3.10 B).

3.2.12. Non-covalent surface modifications

Functionalization with Cadherin ecto-domain constructs

To measure adhesion capacities of a cell to certain ligands, these molecules need to be immobilized on a solid substrate. In this work, commercial Cadherin molecules (SIGMA) fused to an antibody F_c domain were used. This has the advantage of an upright orientation of the molecules, protruding the adhesive EC1 domain into the medium.

1. clean ultra plane 'Gold Seal' glass slides for 1 min in N_2 plasma
2. incubate activated glass slide over night with 0.5 mg $\cdot$ ml^{-1} biotinylated BSA (SIGMA) in $NaHCO_3$ pH=8.6
3. wash 10 $\times$ in $NaHCO_3$ pH=8.6
4. incubate glass slide for 1 h with 0.5 mg $\cdot$ ml^{-1} Streptavidin (SIGMA) at room temperature in PBS
5. wash 10 $\times$ with PBS
6. incubate glass slide for 1 h with 0.5 mg $\cdot$ ml^{-1} SpA (*Staphylococcus* surface protein A, SIGMA) at room temperature in PBS
7. wash 10 $\times$ with PBS
8. incubate glass slide for 3-4 h with 50 µg µl^{-1} Cadherin construct (SIGMA) at room temperature in PBS + 5 mM EGTA

3.2.13. Covalent surface modification

Vapor phase silanization

- plasma-clean surfaces or cantilever
- stick cantilever on PDMS and put upside down over a petri dish filled with APTES
- put dish into an evacuation chamber and leave there for 1 hour
- bake cantilever for 30 min at 120°C

Succinimidyl 4-[N-maleimidomethyl]cyclohexane-1-carboxylat (SMCC) coupling

SMCC is a bifunctional cross-linker that presents a maleimide (MAL) and a succinimidyl (NHS) group. MAL groups preferentially react with mercapto-groups, e.g. cysteins, whereas NHS groups target preferentially primary amino groups, e.g. lysins. Therefore, SMCC offers the possibility to cross-link associated proteins or to couple a protein to a modified surface which carries a known chemical group [353].

to thiol-terminated surfaces

- silanize (3.2.13) glass slides or cantilever using mercapto-propyl-triethoxysilan (MPTES) to introduce thiol-groups on the glass
- add 3.3 mg · ml^{-1} SMCC (in DMSO) solution on the surface and incubate for 30 min
- wash in 3 × in DMSO, 3 × in ethanol, 3 × in PBS
- add protein at 1 mg · ml^{-1} for 2-3 hours
- wash surface in TBS

to amino-terminated surfaces

- silanize (3.2.13) glass-slides or cantilever using APTES to introduce NH_2 - groups on the glass
- add 3.3 mg · ml^{-1} SMCC (in PBS) solution on the surface and incubate for 30 min
- wash 3 × in PBS
- add protein at 1 mg · ml^{-1} for 2-3 hours
- wash surface in TBS

Coupling to carboxy (COOH) groups

This method was successfully used to modify AFM cantilever for the first time by the Gaub group [256]. Herein, the authors covalently coupled carboxy-groups of wheat germ agglutinin to amino-silanized cantilevers, that were used to attach living cell onto the force probe. In general it is well documented in [353]

- Aminosilanize the cantilever
- activate 10 mg · ml^{-1} carboxymethylamylose (CMA) in PBS (pH=7.4) with 4 mg · ml^{-1} NHS and 17 mg · ml^{-1} EDC for 5 min
  - use 50 mg CMA, 50 mg NHS and 280 µl EDC and add 5 ml PBS in small glass beaker
- incubate the aminosilanized tip for 10 min in the activated CMA
- rinse in PBS
- incubate with 0.5 mg · ml^{-1} Con A or WGA for 1 h
- rinse in TBS

3.2.14. Statistical data processing

After determining f_{max} for each force-distance curve, f_{max} was averaged over the experimental repetitions to determine the mean adhesion force of a given cell couple and contact time. The resulting values were then pooled to obtain the distribution of adhesion forces for a given experimental condition. The median±MAD (median absolute deviation, MAD) and percentiles were then extracted with a custom IgorPro (WaveMetrics) function and used in R for unpaired Wilcoxon based Mann-Whitney U-tests for significance with a p cut-off value of 0.05. Non-parametric tests were used on force data presented in Sec. 4, because the data are not normally distributed (see Fig. 4.2 C). Although no systematic history effect on successive force-distance curves taken with one cell was detected (data not shown), it could not be assumed that each curve is strictly independent from each other. Furthermore, adhesion force data are likely to be dependent on different properties, e.g. more than one type of adhesion molecule, which does not allow us to use parametric tests. Wilcoxon based Mann-Whitney U-tests are distribution independent and can therefore be applied on composite data-sets. Box-whisker plots are presented with the box containing 50 % of the data around the median and whiskers encompassing 80 % of the data values. Pearson's rank correlation coefficient r was computed using IgorPro or 'R' and tested for significance in 'R'. Values of T_c for each test were pooled and tested using the same procedure.

3.2.15. Single cell transplantations

Cell transplantations were done by Yohanna Arboleda Estudillo and are described in detail in her thesis. Shortly, single cells are taken from dechorionized donor embryos that have been injected with a fluorescent reporter dye (FITC-dextran, TRITC-dextran). Those cells are then transferred into the lateral side of a host embryo (MZ-*oep* or wildtype labeled with Alexa-fluor-647-dextran). Embryos were mounted in 2 % agarose and imaged until the end of gastrulation.

3.2.16. Laser scanning confocal microscopy

Single cell imaging

Blebbing cells from embryos injected with lifeact mRNA [340] and membrane bound RFP were seeded on a BSA decorated glass cover slip (thickness, 0.25 mm) and imaged using a LEICA SP5 inverted microscope for 2 min in 2 sec intervals using a 63× water immersion lens with a numerical aperture N_A=1.33.

Cell aggregate and live-embryo imaging

Aggregates and fixed embryos were imaged using a Leica SP5 upright microscope using a 20× objective lens. PFA fixed embryos were mounted in agarose wells to fix them in one position.

Live-embryo imaging of transplanted cells was done by Yohanna Arboleda and is described in detail in her thesis.

Live-embryo imaging of blebbing prechordal plate progenitor cells was done by Alba Diz Muñoz using an upright grid confocal system.

3.2.17. Image processing

Sorting dynamics To extract information about dynamic changes in boundary length or projected particle area during cell sorting (see Fig. 4.8 H), standard plug-ins for ImageJ were used. Images were first 'binarized' and 'despeckled' to remove single pixels in each frame, followed by one 'erode' and 'dilate' step. The number of particles was then counted, the area measured and normalized to the number of particles.

Western blots Western blots were quantified using ImageJ. The average intensity of each single band was measured using equal sized boxes, background was subtracted and then normalized to the intensity of intracellular α-tubulin.

Analysis of transplanted germ layer progenitor cells Confocal images of the MZ-*oep* embryos containing transplanted cells of the mesendoderm, endoderm or ectoderm were analyzed using ImageJ (see Fig. 4.15). The perimeter of the embryo was fitted to a circle and the integrated radial intensity profile was calculated (intensity as a function of the center distance). The corresponding intensity values and distances were normalized and the mean intensity at a given position was calculated.

Quantification of E-cadherin staining intensity Embryonic shield sections stained for E-cadherin were quantified using ImageJ. Cell boundaries were traced and staining intensity plotted against the distance to the germ ring margin (see Fig. 4.3).

3D motility analysis of transplanted cells For tracking transplanted cells in three dimensions (x, y, z), Imaris 6.2.0 software was used. The statistical analysis was done using IgorPro software. Tracks of transplanted cells were analyzed in 3D using home-built

IgorPro procedures to extract mean-squared displacement (MSD) $\langle \Delta x^2 \rangle$ with N = number of frames, n = number of time intervals:

$$\langle \Delta x^2 \rangle = \frac{1}{N-n+1} \sum_{i=0}^{N-n} \left[(x_{n+i} - x_i)^2 + (y_{n+i} - y_i)^2 + (z_{n+i} - z_i)^2 \right] \qquad \text{(Eq. 3.16)}$$

Cell tracks were corrected for the intrinsic curvature of the embryo according to

$$\langle \Delta x^2_{corr} \rangle = \left[2R_E \cdot \arcsin \left(\frac{\sqrt{\langle \Delta x^2 \rangle}}{2R_E} \right) \right]^2 \qquad \text{(Eq. 3.17)}$$

which would yield a lower displacement for longer time intervals. This is simply due to the fact that the cells would run in a circle and the MSD will be shorter as soon as the cells passed half the embryo. Then they get closer to the origin of migration again. Correction then yields the displacement $\langle \Delta x^2_{corr} \rangle$ of a particle on a sphere with radius R. This is similar to unfolding the curved path onto a straight line.

MSD plots were fitted to a second order polynomial [354]

$$\langle \Delta x^2_{corr} \rangle (t) = S^2 t^2 + Dt \qquad \text{(Eq. 3.18)}$$

to extract effective migration speed S and diffusion coefficient D. Instantaneous speed v_i was calculated with the distance Δd a cell traveled within two subsequent frames separated by a frame-rate:

$$v_i = \frac{\Delta d}{\Delta t} \qquad \text{(Eq. 3.19)}$$

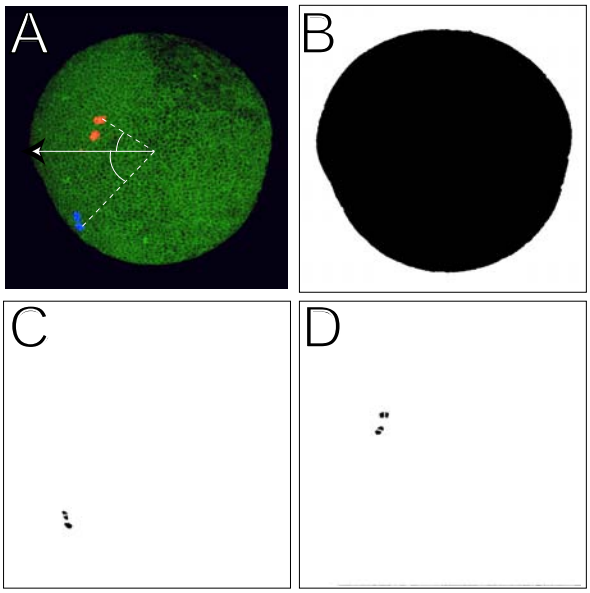

Fig. 3.11 Determining movement orientation

This procedure was applied:

- images were cropped and channels separated
- channels were binarized and 'denoised'
- center-of-mass of each particle in each image was calculated

A: The arrow represents the dorsal pointing vector, embracing an angle with a particle vector (dotted line). **B:** Binarized green channel, **C:** blue channel and **D:** red channel.

Movement orientation Migration into designated compartments was calculated from projected stacks. The last and the first picture of a time series were extracted from

the movie and separated into green, red and blue channels (Movie 3 and see Fig. 3.11). Following, each channel was binarized, despeckled, eroded and dilated. The center-of-mass $(\bar{x}, \bar{y})$ of the embryo was calculated:

$$\bar{x} = \frac{\iint xb(x,y)dxdy}{\iint b(x,y)dxdy}; \qquad \bar{y} = \frac{\iint yb(x,y)dxdy}{\iint b(x,y)dxdy} \tag{Eq. 3.20}$$

and shifted top the origin of the coordinate system. The coordinates of the cells in the other channels were calculated using the 'find particles' option in ImageJ and the vectors in respect to the center of mass of the embryo was calculated. The angle α embracing the displacement vector of the cells in the last frame and the dorsal pointing Einheitsvector was calculated:

$$\cos\alpha = \frac{\vec{x} \cdot \vec{y}}{|\vec{x}| \cdot |\vec{y}|} \tag{Eq. 3.21}$$

Area overlap DIC movies of wildtype and *e-cadherin* morphant cells were recorded during gastrulation and the thickness of the overlapping zone was measured in ImageJ. For details on the measurement see thesis by Yohanna Arboleda. Thickness was used to approximate the overlapping area. Area of overlapping cells A_o in wildtype and *e-cadherin* morphant embryos was calculated by approximating the cells with a sphere. Half the thickness of the overlapping zone corresponds to the height of a circle segment h in one cell. The area of each of the segment can be calculated by:

$$A_o = 2 \times \frac{R_c^2}{2} \cdot (\alpha - \sin\alpha) \qquad \text{with} \qquad \alpha = \arccos\left(\frac{R_c - h}{R_c}\right) \tag{Eq. 3.22}$$

where R_c is the averaged diameter of the interacting cells.

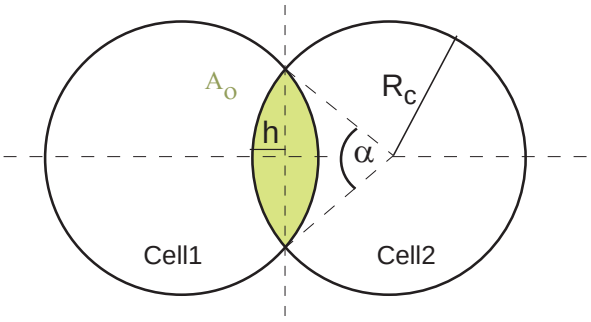

Fig. 3.12 Calculation of cell-overlapping area

Cells are approximated as a sphere and the segment area A_o is calculated using Eq. 3.22. The height of the segment h was measured as half the thickness of the overlapping zone from DIC movies.

FRAP analysis FRAP data analysis is explained in Sec. 3.2.11.

3.3. Materials

3.3.1. Cell culture

E2 Medium

- 1.0 ml Hank's Stock # 1

  - 8.0 g NaCl
  - 0.4 g KCl

    in 100 ml double distilled H_2O

- 0.1 ml Hank's Stock # 2
  - 0.358 g Na_2HPO_4 Anhydrous
  - 0.60 g KH_2PO_4

    in 100 ml ddH_2O
- 1.0 ml Hank's Stock #3
  - 0.72 g $CaCl_2$

    in 50 ml ddH_2O
- 1.0 ml Hank's Stock #4
  - 1.23 g $MgSO_4 \times 7H_2O$

    in 50 ml dd H_2O
- 1.0 ml fresh Hank's Stock #5
  - 0.35 g $NaHCO_3$
  - 10.0 ml dd H_2O
- 95.9 ml dd H2O

Use about 10 drops 1 M NaOH to pH 7.2

E3 Medium

Quantities are given for a 5 l stock of 60× concentrated E3 medium

- 5 mM NaCl 86 g
- 0.17 mM KCl 3.8 g
- 0.33 mM $CaCl_2 \cdot 2H_2O$ 14.5 g
- 0.33 mM $MgSO_4 \cdot 7H_2O$ 24.5 g

Ginzburg's fish ringer solution

- 110 mM NaCl
- 3.6 mM KCl
- 2.5 mM $NaHCO_3$

Cell culture medium

A Hanging drop cultures

- Dulbecco's modified eagle medium (DMEM, INVITROGEN)
- penicillin (100 U·ml^{-1}) and streptomycin (0.1 mg · ml^{-1})

B AFM measurements and confocal imaging

- carbonate-free DMEM/F12 1:1 supplemented with 15 mM Hepes (INVITROGEN)
- penicillin (100 U·ml^{-1}) and streptomycin (0.1 mg · ml^{-1})

C Dissociation buffer

- carbonate-free DMEM/F12 1:1 supplemented with 15 mM Hepes
- penicillin (100 U·ml^{-1}) and streptomycin (0.1 mg · ml^{-1})
- 5 mM EGTA

3.3.2. Western blotting

Blocking buffer

for 150 ml

- 15 ml 10×TBS (tris-buffered saline)
- 135 ml water
- 7.5 g milk powder
- 0.15 ml Tween (100%)

Antibodies

Antibody	Dilution	Source	Species	Ref.
anti-zf-E-cadherin	1:10 000	selfmade	rabbit	[78]
anti-pan-Cadherin	1:5 000	SIGMAALDRICH	rabbit	[355]
anti-ERM	1:2 000	CELL SIGNALLING	rabbit	[31]
anti-pERM	1:2 000	CELL SIGNALLING	rabbit	[31]
anti-α-tubulin	1:2 000	SIGMAALDRICH	mouse	
HRP-anti-rabbit	1:2 000	AMERSHAM	secondary	
HRP-anti-mouse	1:2 000	AMERSHAM	secondary	

Table 3.6 Different antibodies used in this work

Antibody buffer

for 100 ml

- 10 ml 10×TBS
- 90 ml water
- 5 g BSA
- 100 µl Tween

3.3.3. Atomic force microscopy

Cantilevers

Type	Company	k_c	ω_R	App.
MLCT	VEECO	$10\,\mathrm{mN}\cdot\mathrm{m}^{-1}$	7 kHz	T_c
MLCT	VEECO	$30\,\mathrm{mN}\cdot\mathrm{m}^{-1}$	15 kHz	f_{max}
Bio-Lever	OLYMPUS	$6\,\mathrm{mN}\cdot\mathrm{m}^{-1}$	13 kHz	Tether
NP-0	VEECO	$60\,\mathrm{mN}\cdot\mathrm{m}^{-1}$	18 kHz	f_{max}
Arrow TL	NANOWORLD	$30\,\mathrm{mN}\cdot\mathrm{m}^{-1}$	6 kHz	constant force

Table 3.7 Cantilever models

Different cantilever models used in this work to measure different cell adhesive and mechanical properties. Uncoated Arrow TL cantilevers have been used in constant height mode because they show a reduced drift. All resonance frequencies are in air.

4. Cell surface mechanics govern cell sorting and germ layer formation

4.1. Introduction

Gastrulation is the first time in vertebrate development when different progenitor cell types emerge and sort out from each other to assemble the three different primary germ layers [356]. The *Differential Adhesion Hypothesis* proposes that surface tension of the involved tissues directs positioning on the basis of differential adhesive properties (see Sec. 2.2.1 and Ref. [15, 99]). This view was challenged, mostly because of the physical terminology used to explain tissue formation and reductionistic explanation of this model [20]. In other words, morphogenetic position changes are reduced to a difference in adhesive properties among the constituent cell types, neglecting other cell properties. The outstanding question is which properties of individual cells determine the effective surface tension of a tissue [116]. Both, cell adhesion and contraction have long been implicated in germ layer formation, however, their relative contribution to these processes is still a matter of debate [4]. In this part of the thesis, specific adhesive and mechanical properties of the three different germ layer progenitor cell types at the single cell level were quantified by AFM and correlated to germ layer assembly and tissue positioning in *in-vitro* and *in-vivo*.

The importance of cell adhesion and acto-myosin based cortex tension for tissue-positioning is of central interest and will be analyzed using single cell force spectroscopy and cell re-aggregation experiments.

4.2. Results and Discussion

4.2.1. Adhesion

To measure cell adhesion at the single cell level, we used an Atomic Force Microscope (AFM) as a Single Cell Force Spectroscope (SCFS). Adhesion forces between two isolated zebrafish germ layer cells were measured by bringing the cells into contact until a pre-defined force is reached and then recording the force needed to separate them after a given dwell-time, ranging from 1 s to 1 min. Separation of the cells occurred in a sharp adhesion peak, followed by stepwise unbinding events, generally called 'jumps' and 'tethers' (see Fig. 4.1). Such 'jumps' are usually thought to represent unbinding events of single adhesion receptors or receptor clusters that are bound to the cortical cytoskeleton on the intracellular side. The unbinding event as such is characterized by a high elastic response* ultimately before bond failure. Long range interactions occur when these receptor bonds uncouple from the cortical cytoskeleton. This leads to lipid tubes that are extruded from the cell that can extend many tens of micrometers. Remarkably, when such 'tethers' are extruded almost no elastic element is observed in their force extension profile when the lipid reservoir in the plasma-membrane is large enough to ensure a constant membrane tension. Whereas 'jumps' have not been analyzed in this work, the physics of membrane tethers were utilized to determine membrane mechanics (see Chap. 6) and the lifetime of single receptor ligand bonds (see Chap. 7).

SCFS measurements reveal lower adhesion forces for ectodermal cell doublets than compared for mesodermal and endodermal cell doublets.

When maximum adhesion forces between progenitors of the same type (homotypic adhesion; 'cohesion') were measured, ectoderm progenitors showed significantly less cohesion compared to their mesoderm and endoderm counterparts for all tested contact times (see Fig. 4.2 A,B). The forces for all three germ layers are non-normally distributed and therefore the median was chosen to compare the different populations (see Fig. 4.2 C).

To test whether the progenitors display differences in Cadherin-mediated adhesion that resemble their differential cohesive properties, the adhesion of ectoderm, mesoderm and endoderm progenitors to substrates coated with E-cadherin was tested [155]. Mesoderm and endoderm progenitors adhered more to E-cadherin decorated substrates than ectoderm cells (see Fig. 4.2 D), indicating that adhesion of progenitors to Cadherins correlates with their cohesive properties†. In general the maximum adhesion force is smaller then in a typi-

*steep worm-like-chain extension before rupture

†There is no evidence in the literature that E-cadherin ectodomain constructs confer

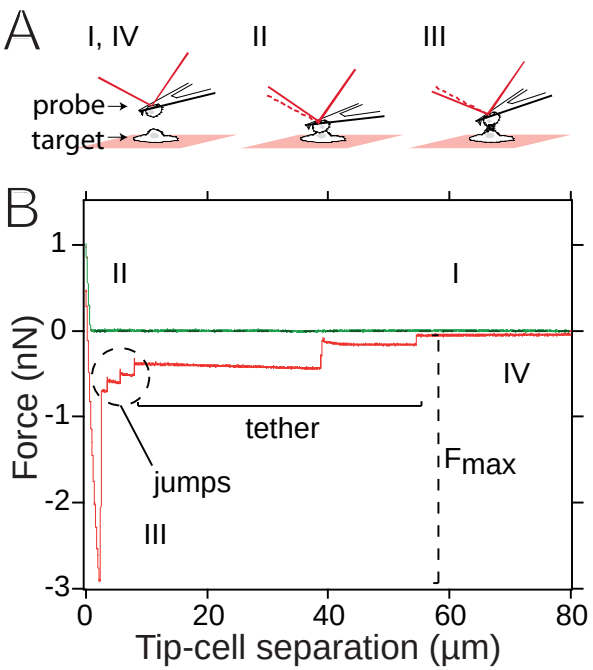

Fig. 4.1 Force-displacement curve

A: Schematics of the cell-cell separation experiment. **B:** One cell bound to an AFM cantilever (*probe*) is brought into contact (I) with a second cell adhering to a solid substrate (*target*, green curve). After contact (II), the cell is retracted and the interaction was detected by the cantilever deflection (III, red curve). The resultant force-distance curve allows quantification of the maximum adhesion (f_{max}) force and shows unbinding events termed jumps and tethers. At the end, both cells are separated again and the force on the AFM cantilever is zero (IV).

cal cell-cell adhesion experiment. This could be attributed to only one mobile species of adhesion receptors in the cell membrane. Furthermore, actual contact area between the cell and the substrate is supposed to be smaller than between two cells. Moreover, a lower force in cell-surface compared to cell-cell separation experiments can be explained by different unbinding kinetics of the zebrafish E-cadherin in the cell and the recombinant mouse E-cadherin on the surface.

Cadherin adhesion molecules - especially E-cadherin - are known to play key roles in tissue morphogenesis during vertebrate gastrulation (see Sec. 2.3.2). To test whether E-cadherin is involved in differential cohesion of germ layer progenitors, cell-cell cohesion measurements were undertaken when E-cadherin function was impaired. Cohesion of all three progenitor types was strongly reduced when Ca^{2+} was depleted from the medium and, more specifically, when E-cadherin expression was 'knocked-down' using morpholino (MO) antisense oligonucleotides (see Fig. 4.3 A), indicating that E-cadherin mediates progenitor cell cohesion. Consistent with this observation, we found that in embryos at the onset of gastrulation (6 hpf), E-cadherin density at the plasma membrane of mesendoderm (mesoderm and endoderm) progenitors was higher than in the directly adjacent ectoderm progenitors (see Fig. 4.3 B and Ref. [27]). Image quantification of the staining intensity of Fig. 4.3 C shows an up-regulation of

specificity to one of the classical Cadherins. In other words, they might bind E,N,R,C-cadherin equally efficient (unknown referee).

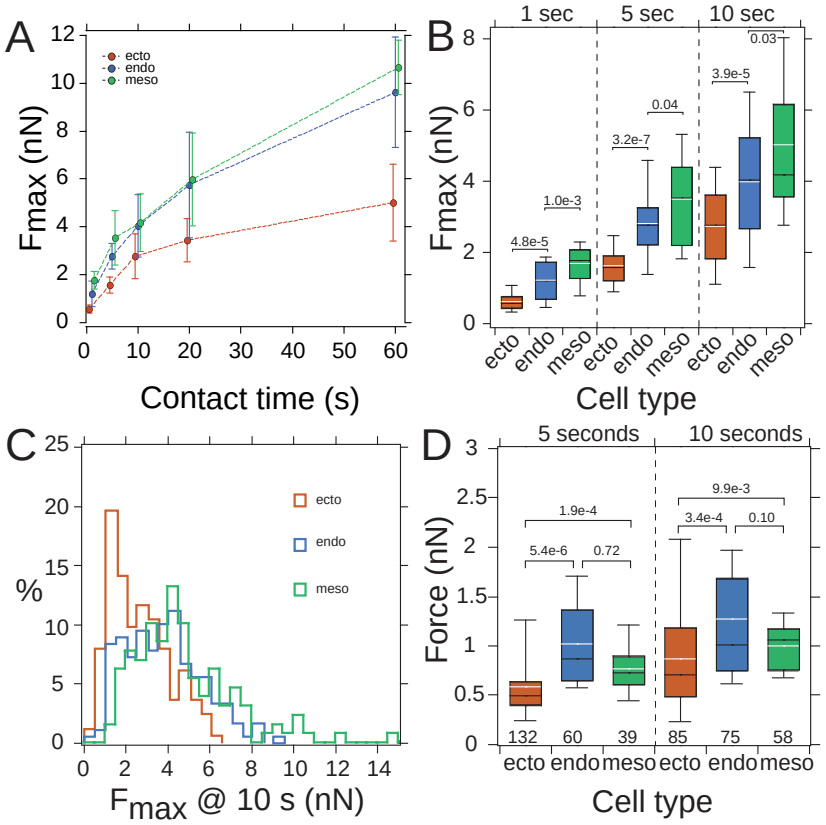

Fig. 4.2 Progenitor cell adhesion

A: Maximum adhesion forces between two cell of same genetic background and developmental stage plotted against contact time represented as median±MAD. **B:** Box-plot of maximum adhesion forces for all three germ layer cell types and three contact times. Numbers above the whiskers indicate p-value returned from Mann-Whitney U-test of statistical significance. Combinations with a p-value less than 0.01 were regarded as significantly different. **C:** Distribution of ectoderm, mesoderm and endoderm adhesion forces after 10 seconds contact time. **D:** Adhesion of progenitor cells to E-cadherin decorated substrates [155] for 5 and 10 seconds contact time. Numbers above the whiskers indicate p-value returned from Mann-Whitney U-test of statistical significance. Numbers below the boxes indicate number of individual measurements.

E-cadherin is the primary cell adhesion molecule setting up the adhesion strength, consistent with protein expression [27] and *in-situ* hybridizations [78].

E-cadherin in the developing mesendoderm during anterior migration. This result is in line with several *in-situ* hybridization studies, where mRNA levels of E-cadherin in the developing mesendoderm were increased [78]. Similarly, the amount of classical Cadherins at the plasma membrane of dissociated ectoderm progenitors detected by an anti-pan-cadherin antibody [355] on western blots was lower than in mesoderm and endoderm cells (see Fig. 4.3 B*). Together, these findings demonstrate that differential cohesion of germ layer progenitors is primarily mediated by classical Cadherins including E-cadherin.

Analogous results for homotypic adhesion forces were acquired with cells

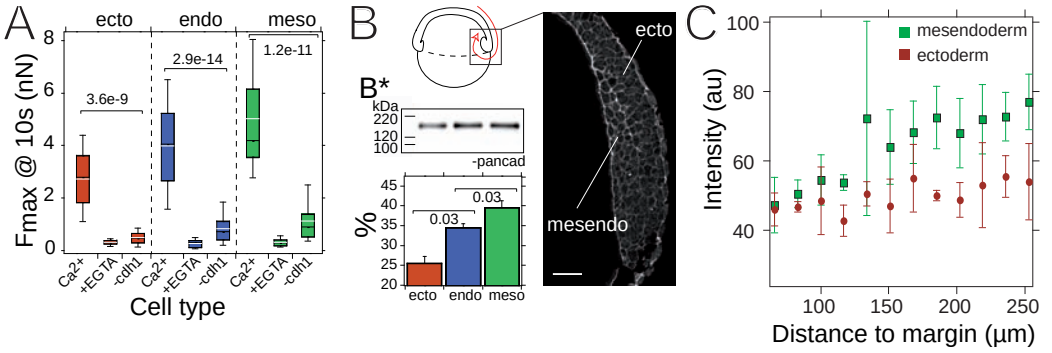

Fig. 4.3 Cell cohesion depends on E-cadherin

A: Maximum progenitor cell adhesion forces for homotypic adhesion at 10 s contact in control ($+Ca^{2+}$), EGTA (5 mM)-treated or E-cadherin-morpholino oligonucleotide injected (-cdh1; 8 ng per embryo) progenitors. **B:** Sagittal section of the dorsal germ-ring margin of a shield stage wild-type embryo (6 hpf; schematic drawing in upper left corner) fluorescently stained with an E-cadherin antibody. Picture was taken by confocal microscopy. (B*) Western blot analysis and quantification (bar chart) of the amount of biotinylated, membrane-bound classical Cadherins (pan-Cadherin antibody) in dissociated progenitors normalized to total Tubulin ($n = 4$; median $\pm$ MAD). Scale bar in (B), 50 µm. Numbers above or below square brackets indicate p values for the corresponding combinations. **C:** Quantification of the sagittal shield section shown in (B).

from different genetic background but similar developmental fate. For example, cells expressing the mesoderm-antagonizer *lefty* (see Fig. 2.2) showed similar adhesion force as cells taken from MZ-*oep* embryos. Alternatively, cells from embryos expressing constitutively active *taram-A*, which leads to endoderm formation, showed similar force compared to *casanova* over-expressing embryos (see Fig. 4.4 A).

The recorded differences in cell-cell adhesion are unlikely to be a mere consequence of dissimilar morphological and/or mechanical cell properties, as neither cell size (see Fig. 4.4 D) nor 'contact stiffness' are apparently correlated with the recorded maximum adhesion forces (see Fig. 4.4 C and see also 3.1.1). A positive correlation coefficient of r=0.14 suggests that stiffer cells can resist larger unbinding forces. This is in contrast the idea that softer cells have a larger adhesion force in SCFS measurements. This was inspired bz the Hertz model, where the contact area is related to the initial contact force which is always one nanonewton in these experiments (see Sec. 3.1.2).

Interestingly, adhesive forces between different progenitor types (heterotypic adhesion) were similar to homotypic cell contacts of ectoderm cells, the least cohesive cell type (see Fig. 4.4 B). In other words, the adhesion force recorded

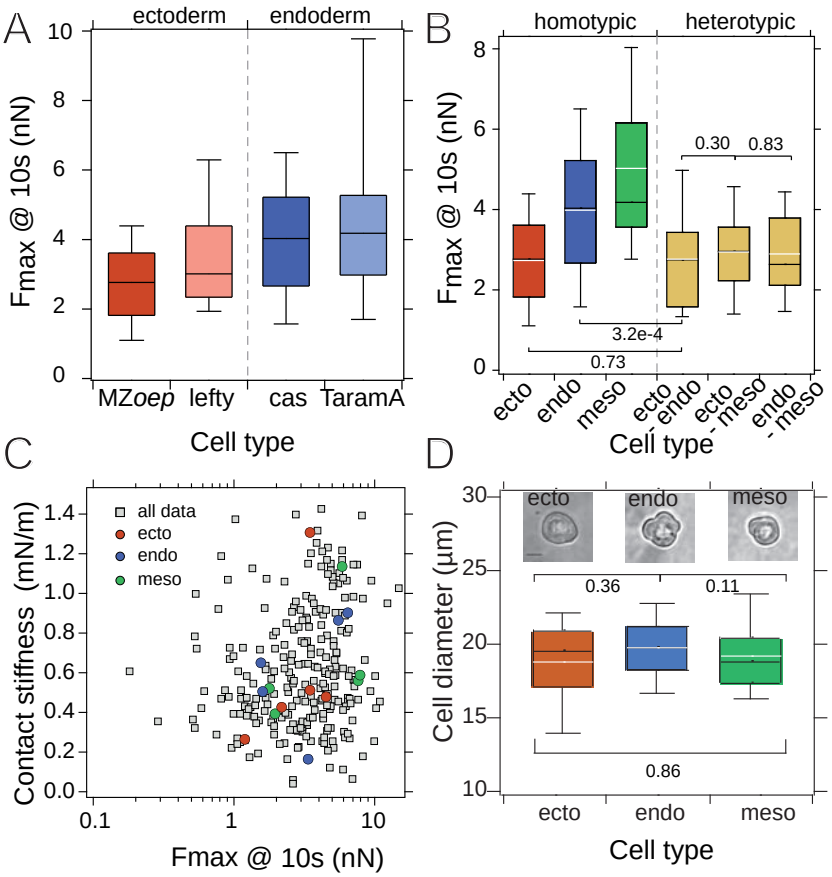

Fig. 4.4 Zebrafish cell adhesion under different conditions

A: Maximum adhesion forces between two cell of different genetic background and developmental stage plotted against contact time. Heterotypic contacts adhere less than their homotypic counterparts. **B:** Adhesion forces of cells from embryos injected with alternative Nodal-pathway components to induce ectodermal and endodermal cell fate. Over-expression of Nodal antagonist *lefty* mimics behavior of cells taken from MZ-*oep* embryos, while over-expression of *daTaramA* resembles cells from *casanova* injected embryo. **C:** Slope of contact region ('contact stiffness' green curve in Fig. 4.1) extracted from the approach trace versus f_{max} recorded for each force-distance curve. Grey squares, weak statistical correlation ($r = 0.14$); five arbitrarily chosen curves for each progenitor types are highlighted as colored circles. **D:** Three representative cells of ectoderm, mesoderm and endoderm are shown together with their distribution of cell sizes. No statistical significance was observed using a Mann-Whitney U-Test.

from a couple of a mesoderm cell and an ectoderm cell was as high as from two ectodermal cells. Moreover, heterotypic adhesion forces between an endodermal cell and a mesodermal cell were smaller than forces recorded from homotypic contacts. How can that be explained? One likely possibility is the involvement of another cell adhesion molecule participating in the contact formation. Earlier studies already showed a higher expression of N-cadherin

in the developing hypoblast (mesoderm and endoderm) as compared to the epiblast (ectoderm) [357, 341, 358]. Knocking down N-cadherin in the three germ layers showed a mild effect in the endoderm and a strong reduction in mesoderm but essentially no phenotype in the ectoderm germ layer cells (see Fig. 4.5). To further underline the role of N-cadherin in adhesion between two cells, a double knockdown of E- and N-cadherin was tested in the AFM experiment. Whereas no further decrease in f_{max} could be observed in ectoderm and endoderm cells, a slight reduction was proven in mesoderm cells. Therefore, N-cadherin probably has a role in the developing mesoderm only.

N-cadherin is has an adhesive function in mesoderm cells only.

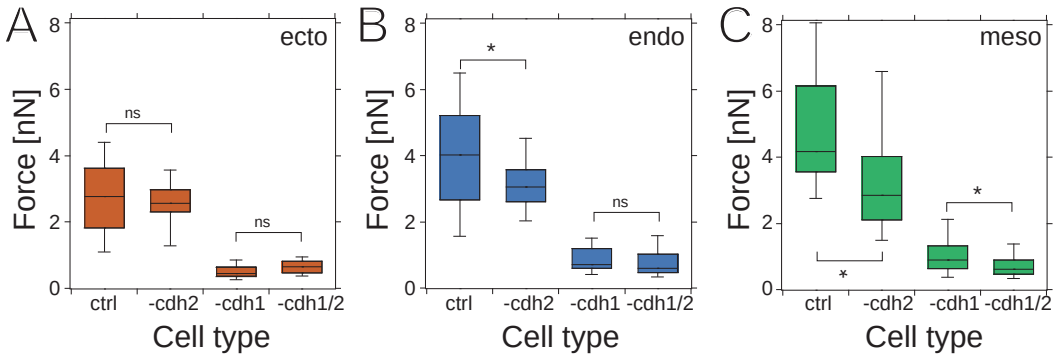

Fig. 4.5 N-cadherin dependence of adhesion force

A: Maximum adhesion force of ectodermal cells without morpholino (ctrl), with *n-cadherin* morpholino (-cdh2), *e-cadherin* morpholino (-cdh1) and with both morpholinos (-cdh1+cdh2). **B:** Adhesion forces for endodermal cells with and without E, N-cadherin. **C:** Adhesion forces for mesodermal cells with and without E, N-cadherin.

4.2.2. Cortex Tension

In addition to differential adhesion, differential cell contraction has been implicated in cell sorting and tissue self-assembly [20]. Studies using *Dictyostelium*, fibroblasts and white blood cells have shown that acto-myosin contraction and cell cortex tension T_c are directly related to each other [287]. Therefore, determination T_c of different germ layer progenitors was used as a read-out of their specific acto-myosin activity. To measure cell cortex tension, colloidal force probe microscopy was applied to deform the surface of single progenitors with a 5 µm large bead coupled to an cantilever (see Fig. 3.8) and recorded the resulting force-indentation curves with an AFM (see Fig. 4.6 A). T_c was extracted from force-indentation curves by using the Cortical Shell-Liquid Core or Liquid Droplet Model (see Sec. 2.5.2 and Ref. [285]). In the following it

Ectoderm progenitor cells have a higher cortex tension than mesodermal and endodermal counterparts. These endogenous differences in T_c depend on myosin function.

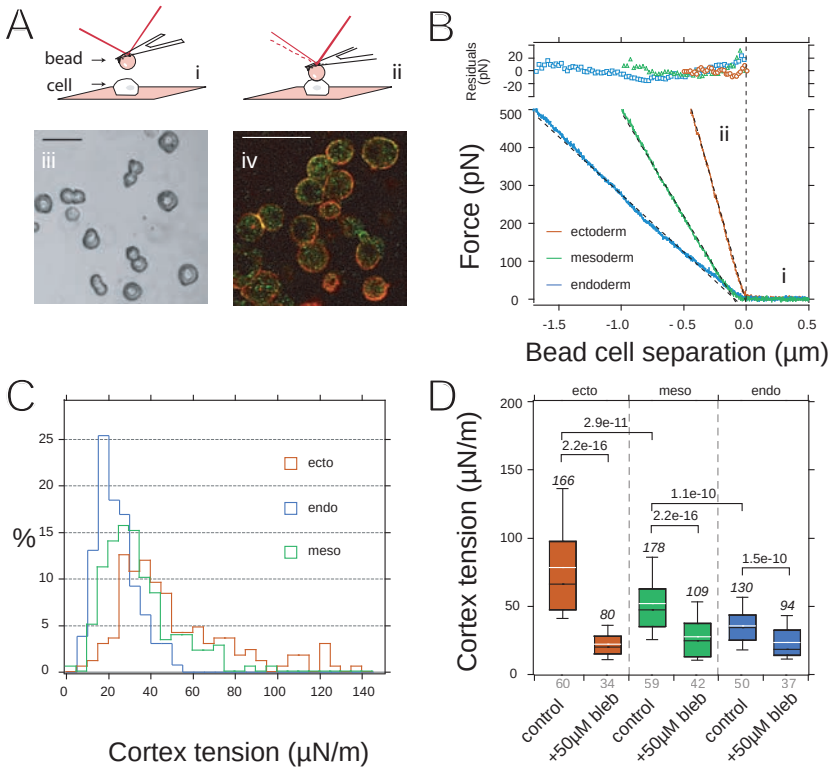

Fig. 4.6 Cell-cortex tension of germ-layer progenitor cells.

A: Principle of the indentation experiment. A passivated colloidal force probe (bead; diameter $= 5\,\mu\mathrm{m}$) is moved towards a given progenitor cell (cell) at $1\,\mu\mathrm{m}\cdot\mathrm{s}^{-1}$ (i) and the cell surface is deformed by the bead (ii). (iii) Phase-contrast micrograph of typical progenitors used for measurements. (iv) Phalloidin (actin; red) and anti-phospho-myosin antibody (green) staining of fixed mesoderm progenitors after 3 h in culture. Scale bars in iii and iv, $50\,\mu\mathrm{m}$. **B:** Representative force curves for progenitor cells are shown and fitted to Eq. 3.13 to extract the cell-cortex tension. The upper panel shows the residuals of the fit. **C:** Distribution of cell cortex tension for ectoderm, endoderm and mesoderm progenitors. **D:** Box-whisker plot of cell-cortex tension for different progenitor cell types in the presence or absence of $(-)$-Blebbistatin (bleb, $50\,\mu\mathrm{M}$). Median is black and mean is white. Sample size is indicated over each box and number of tested cells below the x axis. Numbers above brackets indicate p values for the corresponding combinations.

was found that ectoderm progenitors had the highest T_c, followed by mesoderm and then endoderm progenitors (see Fig. 4.6 B-D). To determine that the differences in T_c between the progenitor cell are not due to genetic background differences between the MZ-*oep* mutant fish and the injected wildtype fish, we used cells from embryos injected with *lefty* as ectodermal model germ layer [58, 337]. As can be seen in Fig. 4.7 A there was no significant difference among the two ectodermal model systems. Similar to this, we tested cortex tension of endodermal cells induced alternatively to *casanova* over-expression. Constitutively activating the Taram-A receptor tyrosine kinase was shown to

induce endodermal fate in zebrafish blastomeres [359]. When we tested T_c for *cas* and da*Taram-A* induced endodermal cells, we detected slight differences, that were not statistically different ($p > 0.05$; see Fig. 4.7 B).

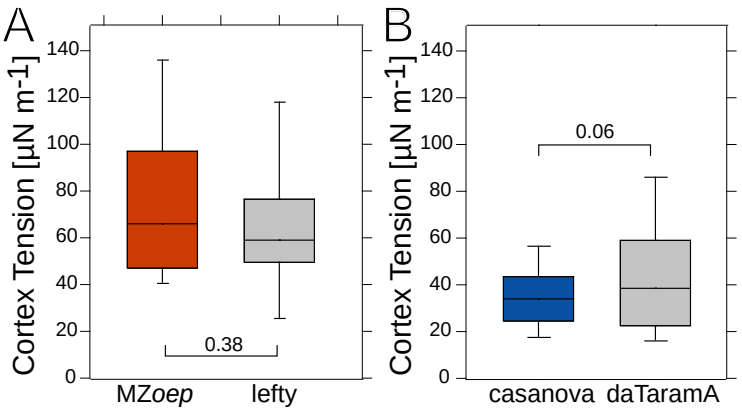

Fig. 4.7 T_c controls

A: Cortex tension of MZ-*oep* mutant and *lefty* over-expressing cells to specify ectodermal fate. **B:** T_c of casanova and da*Taram-A* over-expressing cells to induce endodermal fate.

To determine whether these differences in cell cortex tensions were due to differential acto-myosin activity, we measured T_c of germ layer progenitors in the presence of Blebbistatin, a specific inhibitor of myosin II activity. Interestingly, exposure to 50 µM (−) - Blebbistatin reduced T_c to the same level in all progenitor types (see Fig. 4.6 D). Together, these findings demonstrate that progenitors display differential acto-myosin-dependent cortex tension.

4.2.3. Cell sorting

To correlate our adhesion and cortex tension measurements with the actual sorting behavior of germ layer progenitors, we performed a series of *in-vitro* cell sorting experiments (see Fig. 4.8 A). We have previously shown that ectoderm and mesendoderm cells sort efficiently when mixed in primary culture, resulting in an ectoderm cluster surrounded by mesendoderm cells [19]. Applying the same methodology to all three germ layer progenitor types, we found that when ectoderm cells were mixed with either mesoderm or endoderm cells, ectoderm cell clusters became surrounded by mesoderm (n=56 aggregates) or endoderm cells (n=45) after 17 h in culture (see Fig. 4.8 B-F). Cell sorting also occurred in mixed mesoderm and endoderm cell populations after 17 h in culture with mesoderm clusters completely (n=27) or partially (n=29) enveloped by endoderm cells (see Fig. 4.8 G). A sorting order of germ layer progenitors thus exists *in-vitro*; ectoderm cells are surrounded by mesoderm or endoderm cells, and mesoderm cells are surrounded completely or partially by endoderm cells (see below). For an analogous experiment see Supplementary Movie 2,

where ectodermal and mesodermal progenitor cells were allowed to sort out on a glass surface. Analogous configurations and sorting orders have been reported for dissociated germ layer progenitors of *Rana pipiens* embryos [18].

The DAH explains sorting behavior of heterologous tissue combinations on the basis of cell's adhesive properties. For endoderm and mesoderm mixtures, only partial sorting was observed in 50 % of the experiments. According to Eq. 2.2, incomplete envelopment only occurs when the adhesion of the heterotypic contacts, in this combination $f_{endo,meso}$ is weaker than the adhesion between cells of similar histotype e.g. $f_{meso,meso}, f_{endo,endo}$. Surprisingly, the adhesive forces measured for heterotypic and homotypic contacts follows this prediction (see Fig. 4.4 and Tab. 4.1).

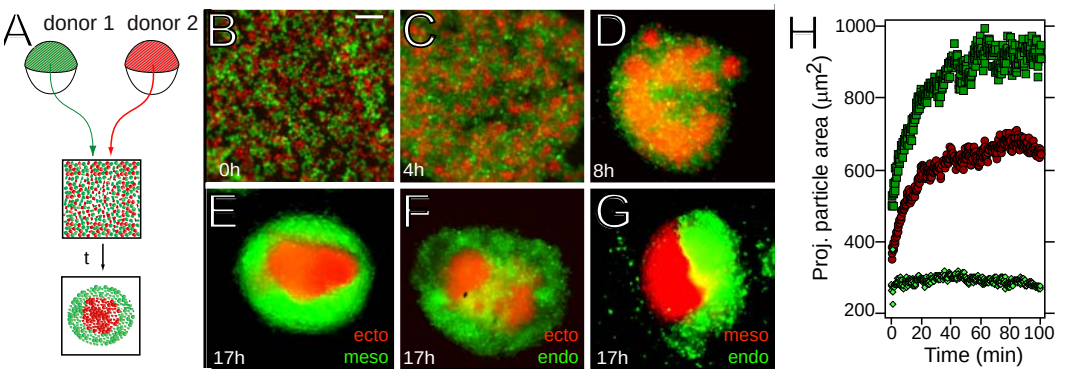

Fig. 4.8 Cell-sorting *in-vitro*

A: Schematic drawing of an *in-vitro* progenitor cell sorting assay. Two different embryos were dissociated and progenitors were mixed in a hanging drop. Cell sorting was observed after 17 h in culture. **B-E:** Sorting of mesoderm and ectoderm co-culture at different time-points. **F,G:** Sorting of ectoderm-endoderm (F) and mesoderm-endoderm (G) co-cultures after 17 h in culture. **H:** Time course of cell sorting in an ectoderm-mesoderm co-culture. The cluster size (projected particle area) increased immediately after seeding without any detectable lag-phase (ectoderm, red circles; mesoderm, green squares), whereas no increase in cluster size was observed in the presence of EDTA (blue diamonds).

Importantly, germ layer progenitor cell aggregation starts immediately after seeding and cell sorting is evident already minutes after mixing (see Fig. 4.8 H). This suggests that the cell-cell contact times used in our adhesion assay (see Fig. 4.2 A) are relevant for the actual sorting behavior of progenitors. Generally, progenitor cell aggregates after 17 h in culture did not show obvious signs of cell differentiation (as judged by marker gene expression; [19]), indicating that they retain their progenitor cell identities. To test the possible evolution of adhesion forces over the course of a hanging drop experiment, cells were incubated for 10 - 14 hours and their cell-cell adhesion was measured (see

Ectoderm envelopes mesoderm and endoderm according to their differences in surface tension.

Fig. 4.9). Whereas the absolute values of forces decreased, their relative difference was still apparent. The decrease was probably due to a smaller cell size, because the cells were continuously dividing in culture. Interestingly, endoderm cells now have a significantly higher adhesion force than their mesoderm counterparts. That they nevertheless cannot sort to the inside of the cluster supports the idea that adhesion alone cannot determine the final sorting configuration.

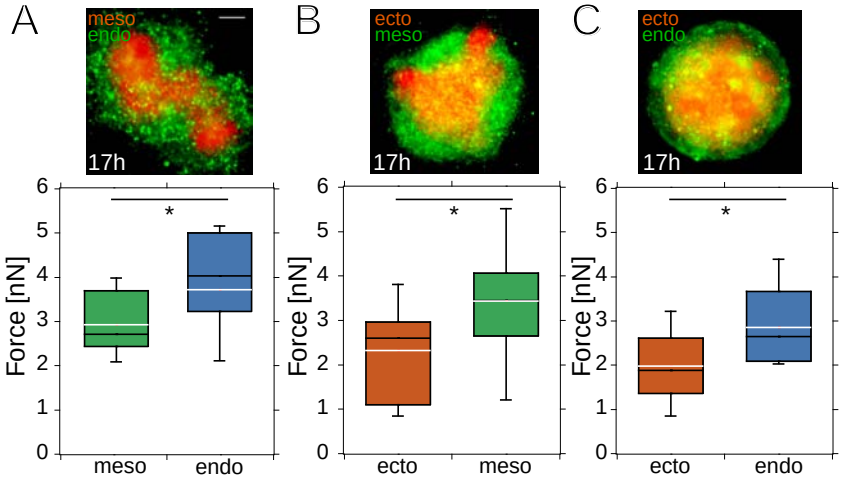

Fig. 4.9 Effect of culture time on adhesive properties

A: Sorting configuration of mesoderm and endoderm progenitors with respective detachment forces after 12 hours in culture. **B-C:** Same experiments for mesoderm-ectoderm (B) and endoderm-ectoderm co-cultures (C).

That higher acto-myosin-dependent cortex tension of ectodermal cells (see Fig. 4.6 B-D), but not cohesion (see Fig. 4.2 A), correlates with ectoderm progenitor cell sorting to the inside of a heterotypic aggregate, suggests that cortex tension rather than cohesion promotes progenitor cell sorting to the inside. To test whether acto-myosin-dependent cortex tension is required for progenitor cell sorting, we exposed mixed ectoderm and mesoderm (or endoderm) progenitors to drugs perturbing acto-myosin activity. We found that mixed ectoderm and mesoderm (as well as endoderm) progenitors failed to efficiently sort when exposed to Cytochalasin D (an actin depolymerizer) or (−)-Blebbistatin (a blocker of myosin II activity; see Fig. 4.10 A, B, D), but not to (+)-Blebbistatin (an inactive enantiomer, see Fig. 4.10 C). Similarly, no sorting occurred in the presence of BDM, another myosin ATPase inhibitor (see Fig. 4.10E and Table 3.4). Importantly, *relative* differences in homotypic cell-cell adhesion between the different progenitor types remained unchanged

in the presence of (−)-Blebbistatin (see Fig. 4.11 A), indicating that Blebbistatin functions in cell sorting by perturbing cortex tension (see Fig. 4.6 D) rather than adhesion. This was also confirmed by western blotting of cell surface biotinylated E-cadherin. An incubation of 2 hours in 50 µM Blebbistatin did not decrease the E-cadherin density at the plasma-membrane of ectodermal progenitors in comparison to the untreated counterparts. Together, these findings show that differential acto-myosin-dependent cortex tension is required for efficient progenitor cell sorting.

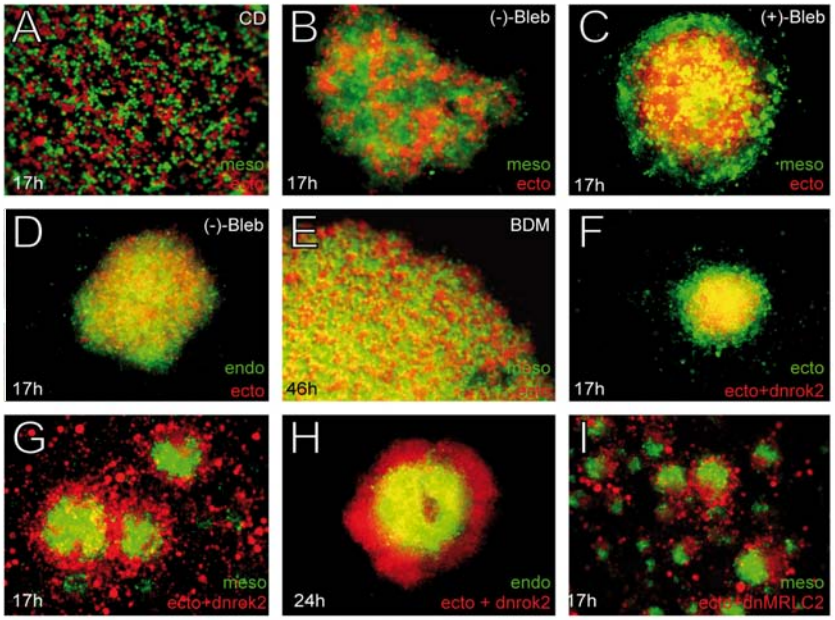

Fig. 4.10 Cell sorting and acto-myosin function

A-C: Cell sorting of mesoderm and endoderm progenitors in presence of 10 mM cytochalasin D (A), 50 µM (−)-Blebbistatin (B) and its inactive enantiomer (+)-Blebbistatin (C) 17 h after seeding into a hanging drop. **D:** Sorting of endoderm and ectoderm cells in presence of (−)-Blebbistatin. **E:** No sorting can be observed when mesoderm and ectoderm cells are co-cultured for up to 46 h in presence of BDM. **F:** Selective inhibition of myosin activity in ectodermal cells by interfering with Rho kinase activation. Untreated ectoderm cells are mixed with cell from embryos injected with 200 pg dnRok. **G-H:** Interference of myosin activation by injecting dnRok2 in ectodermal cells co-cultured with mesodermal (G) and endodermal (H) progenitors in a hanging drop. **I:** Interference of myosin activation by injecting dnMRLC in ectodermal cells co-cultured with mesodermal progenitors.

To determine whether differential acto-myosin dependent cortex tension is also sufficient to drive germ layer progenitor cell sorting, we selectively interfered with acto-myosin activation in ectoderm progenitors and then analyzed their sorting behavior when mixed with un-treated ectoderm, mesoderm or

Cell sorting in presence of Blebbistatin is impaired and ectoderm with reduced tension sorts to the inside of an heterotypic aggregate.

endoderm cells. To cell-autonomously interfere with acto-myosin activation, a dominant-negative version of Rho kinase 2 (dnRok2), an upstream regulator of acto-myosin activity [77], was expressed. DnRok2 expressing ectoderm progenitors showed reduced cortex tension while cohesion remained unchanged (see Fig. 4.6 B,C) and, when mixed with either untreated ectoderm, mesoderm or endoderm cells, sorted to the outside of heterotypic aggregates (see Fig. 4.10 F-H). Similar results were obtained by expressing a dominant-negative version of Myosin regulatory light chain 2a (dnMRLC2a), a downstream target of Rok2, to reduce cortex tension (see Fig. 4.10 I). This invokes that differential acto-myosin dependent cortex tension is sufficient to guide progenitor cell sorting.

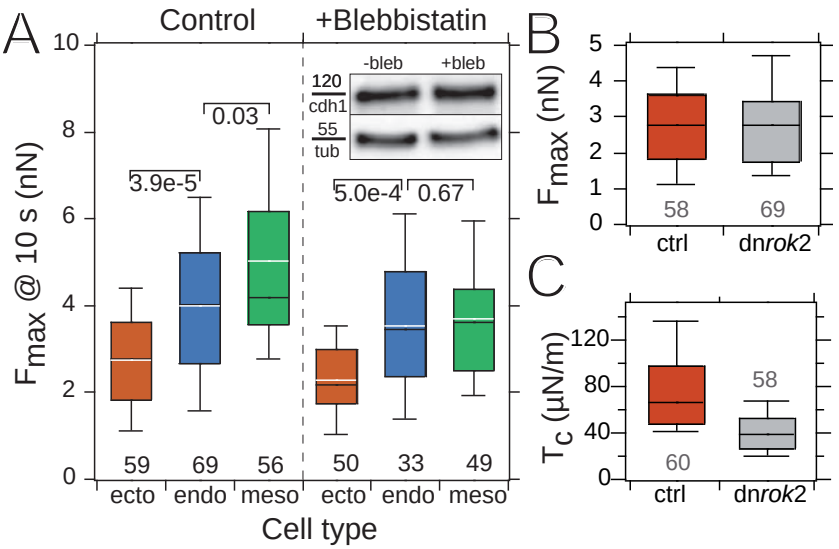

Fig. 4.11 Adhesion and cortex tension of myosin perturbed cells

A: Quantification of adhesion forces using cells incubated for 1 hour in 50 µM Blebbistatin compared to untreated cells. E-cadherin staining on western blot of Blebbistatin treated versus untreated cells. **B:** Adhesion force of ectodermal control cells and ectodermal cells from embryos injected with dn*rok2*. **C:** Cortex tension of ectodermal control cells and ectodermal cells from embryos injected with dn*rok2*.

Cell sorting does not complete when constituent cell types are treated with actin depolymerizing agents.

That adhesion differences are necessary but alone not sufficient to drive germ layer separation *in-vitro* has been observed in different experimental system and organisms before. First indications came from experiment using cytochalasin B (CCB) to inhibit actin polymerization [110, 111, 109, 112]. This apparent discrepancy was explained by an insufficiently large difference in interfacial energies between the cell types [111]. In other words, if there are large differences in adhesion among the cell types, cell sorting still takes place, but does not take place if the difference in adhesion is too small; then the interfa-

cial energy is insufficient to drive cell sorting [112, 111]. It was hypothesized that treatment of aggregates with CCB also influences cell adhesion strength [110]. More likely than that, actin dependent processes are likely to have a role in adhesion strengthening by receptor clustering on the intracellular side [146, 200] or cell motility. For example, if one cell type is more motile during the sorting process than the other the final outcome would be different in presence of CCB compared to control conditions.

Differential motility could be taken place when cells in an organism differentiate into distinct structures as in *Dictyostelium* aggregation. During this process, pre-stalk cells sort out from pres-pore cells and begin to occupy distinct areas. It has been shown that when pre-stalk and pre-spore cells are isolated from slugs, mixed together, and incubated on agar, they reconstruct slugs in which cells sort out to their original positions. Tracking the migratory behavior of single cells suggested that the pattern formation is mediated by a differential chemotaxis within the pre-stalk/pre-spore cells [8, 360]. These results were the basis for computer modeling studies that showed that sorting indeed can take place by a differential ability of the cells to handle chemotactic signals [361, 362].

The work of adhesion, what Steinberg named to be the property leading to tissue positioning, is difficult to measure [99]. Nevertheless, to prove this concept, the adhesive strength between two different cell types was measured [226] and compared to the equilibrium cell sorting configuration. To qualitatively compare the adhesive properties of aggregating cells, two aggregates were paired and interacting aggregates were counted after the application of a laminar flow. This yielded an adhesion rate of a particular combination of cell types. The hierarchy of adhesion rates did not reflect the hierarchy of final sorting configuration [363]. How can that be explained? First, in this study whole aggregates were used [226] but the surface of an aggregate does not necessarily reflect the adhesive capacity of single cells. Second, adhesion rates are not a measure of the rate of adhesion [226]. Third, adhesion does not drive cell sorting processes [20, 364]. At the end, when we probed cell adhesion strength in our system, the hierarchy of adhesive capacities measured with SCFS did not reflect the hierarchy of sorting either. In other words, the sequence in cell adhesion strength $f_{ecto} < f_{endo} \leqq f_{meso}$ cannot explain the sorting configuration *in-vitro* as observed by [226].

Another observation about cell sorting *in-vitro* communicated by Steinberg was that the ratio of the participating cells is crucial for the final sorting

pattern. If the same cell type were mixed in ration of A:B=7:3 or A:B=3:7, the position of the 'phases' was reversed [365]. For example, large liver aggregates tend to envelop smaller heart aggregates, while large heart aggregates tend to envelop smaller liver aggregates. This apparent discrepancy was explained by the time taken for cell sorting and envelopment. During this time a reversal of 'relative' tissue adhesiveness can take place and lead to the reversal of the sorting configuration. When the liver aggregate is large, a longer time will be required for the heart tissue to envelop it. If the liver aggregate has not been completely surrounded when the reversal of cohesion [365] occurs, then a reversal in the direction of envelopment will take place, and the liver tissue will proceed to surround the heart tissue.

Many studies communicated that adhesion alone is insufficient to drive cell sorting but relies on cell motility and cell cortex properties.

Further indications that cell sorting is based on more than simple adhesive-binding specificity came from studies with cells expressing different Cadherin types [188]. Although it could be shown that the amount of CAMs induced sorting *in-vitro*, the function of specificity is controversially discussed in the literature [188, 366]. In a series of experiments it was shown that cells presenting different Cadherin molecules on their surfaces are not able to separate and form distinct tissue barriers [188]. On the other hand, it was observed that cells expressing two Cadherins with the same adhesive activity clearly sorted into different aggregates. These results lead the authors to conclude that "*the lack of adhesive specificity for Cadherins may not be totally surprising in light of the fact that factors other than Cadherin subtype specificity can result in sorting of cells. ... The lack of cell sorting behavior in many instances when cells express distinct Cadherins raises the question of how generally important differential Cadherin expression is for specifying cell sorting and maintenance of tissue boundaries.*" [188]. In that respect, other molecules such as Ephrins can guide tissue positioning by regulating the repulsive interactions in the participating cells [53]. These were not the only indications, that properties of cell adhesion molecules are not the only determinants for cell sorting and tissue positioning. Recent biophysical measurements on different combinations of single Cadherin-Cadherin bonds confirmed that their specificity and kinetic properties do not predict the final sorting pattern of cells that express these molecules are combined in co-culture [189]*. Intuitively, the off-rate of a receptor-ligand interaction determines the lifetime of the bond and the higher

*A recent study communicated, that tissue separation of a mixture of N/E-cadherin expressing cells in culture can indeed be explained by kinetic properties of the involved adhesion molecules [367]. In this study, extracellular E- and N-cadherin fragments have been used to determine their K_d, which reflected the separation of a heterotypic cell culture.

the lifetime, the longer the bond should survive. In that respect, cells that express CAMs with a higher lifetime, should stay longer in contact and therefore should sort into the center when combined with cells that express CAMs with a lower bond-lifetime. This correlation could not be observed experimentally. Similar to the kinetic properties, the receptor-ligand energies measured using surface force apparatus did not correlate with the final pattern of cell sorting experiments [190]. At the end, the authors conclude that "*cell sorting in-vivo and in-vitro is likely governed by several factors, which may include but are not determined solely by subtle variations in Cadherin bonds*" [189]. In the light of these findings, cell sorting out of differentiated murine endodermal cells from primitive precursors was shown to be independent of their adhesive properties [294]. Other than that, random movement was suggested to drive the sorting process [294]. These findings, together with our quantitative measurements on single cell adhesion strength, indicate that cell sorting and germ layer separation are not solely governed by adhesion-mediated surface tension.

The factors regulating cortex tension of germ layer progenitors are poorly understood. Nodal/TGFβ signaling is known to be required and sufficient to induce mesoderm and endoderm cell fates and morphogenesis [2]. Thus to test whether Nodal/TGFβ signaling can modulate cell cortex tension of progenitors, we measured cortex tension of ectoderm progenitors exposed to recombinant Activin, a Nodal-related TGFβ signal previously shown to function as a mesendoderm inducer and dorsalizer [58]. Cell cortex tension was significantly lower in ectoderm progenitors cultured for 120 min in the presence of $100\,\mathrm{ng}\cdot\mathrm{ml}^{-1}$ Activin compared to untreated cells (untreated=$54.5\pm8.6\,\mu\mathrm{N}\cdot\mathrm{m}^{-1}$, n=32; treated= $21.7\pm8.6\,\mu\mathrm{N}\cdot\mathrm{m}^{-1}$, n=32; median±MAD). The probability that the difference between the two measurements is by chance is $p = 2.2\cdot10^{-16}$. This suggests that acto-myosin-dependent cortex tension of germ layer progenitors can be modulated by Nodal/TGFβ-related signaling.

Activin reduces cortex tension in ectodermal cells and causes tissue re-positioning.

To further address the role of Nodal TGFβ-signalling in germ layer positioning, heterotypic aggregates were allowed to sort out in presence of $100\,\mathrm{ng}\cdot\mathrm{ml}^{-1}$ Activin. As explained above, the same amount of Activin reduce cortex tension of ectodermal progenitor cells to the level endodermal cells. In contrast to the control situations (without Activin) ectodermal aggregates were found at the periphery of the heterotypic aggregate, now enveloping mesodermal ones* (see Fig. 4.12). Interestingly, when ectodermal cells (MZ-*oep*) were mixed with

*Mesodermal cells are obtained from embryos injected with *cyclops* mRNA AND *casanova* morpholino.

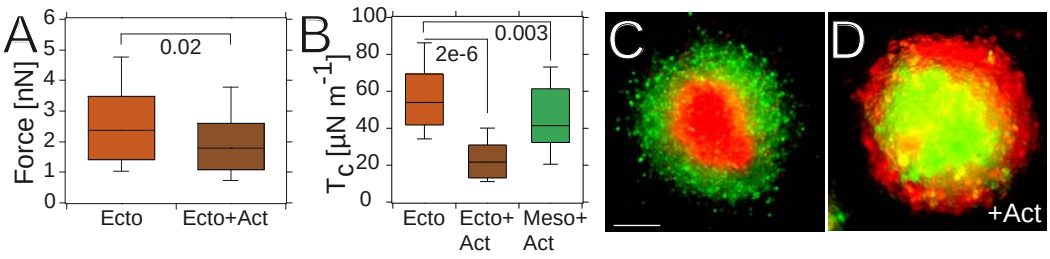

Fig. 4.12 Cell sorting in presence of Activin

A: Maximum adhesion force of Activin treated ectodermal progenitors is nearly unchanged to untreated cells. p-value indicated above the bracket. **B:** Cortex tension of Activin treated ectodermal progenitors is drastically reduced in contrast to mesodermal progenitors. p-values above the bracket. **C:** Cell sorting in a hanging drop experiment of a ectodermal (red), mesodermal (green) co-culture. **D:** Cell sorting in a hanging drop experiment of a ectodermal mesodermal co-culture in presence of Activin. Ectodermal cells now occupy the outer phase of the spherical cell aggregate. Scale bar in (C)=50 μm

mesendodermal* cell and kept in co-culture for 17 h, no sorting was observed. This is in favor with the idea of Activin as a potent endoderm inducer, which acts independently of Oep co-receptor [58]. Whereas in mesodermal cells endoderm induction is perturbed due to a lack of Casanova, both, ectodermal and mesendodermal cells could be efficiently transformed into endodermal fate and therefore are unable to sort out from each other. Together, this shows that Nodal TGFβ signaling induces germ layer separation and is sufficient to alter developmental fate *in-vitro*.

To explain the sorting behavior of germ layer progenitors in the context of our adhesion and tension measurements, collaborators of our group simulated progenitor cell sorting using the Cellular Potts Model [368, 369]. In this model, cell behavior is driven by energy minimization whereby the total energy of an aggregate depends on the interfacial tension between cell-to-cell and cell-to-medium interfaces [21, 370]. The interfacial tension between two cells is determined by the adhesion (J_{ij}) between the cell types i and j, and by the cortex elasticity and cortex tension (T_i and T_j) of the two cells [21, 120]. Relative values for adhesion reflected those measured in Fig. 4.2 A with homotypic adhesion $J_{endo} > J_{meso} > J_{ecto}$ and heterotypic adhesion $J_{ecto,meso} = J_{ecto,endo} = J_{meso,endo} = J_{ecto}$. Adhesion of cells to the medium was set to 0.

In the simulations of progenitor cell sorting two different conditions were

*Mesendodermal cells are produced from embryos injected with *cyclops* WITHOUT *casanova* morpholino - see Methods Sec. refSec:inject

Tissue self-assembly can be modeled *in-silico* only if interface specific cortex tension is assumed.

applied: in the first case, cortex tension was assumed to be homogeneous for the whole cell, independent of interactions with other cells or the medium (interface-independent tension). Relative tension values were set according to the experimental data shown in Fig. 4.6 D with $T_c^{ecto} > T_c^{meso} > T_c^{endo}$. In the second case, we regarded the tension measurements of Fig. 4.6 D as representative of only the cell-to-medium interface, as first proposed by Harris [20], with $T_c^{ecto/medium} > T_c^{meso/medium} > T_c^{endo/medium}$ (interface-specific tension). In contrast, cortex tension at cell-to-cell interfaces was set equal for all progenitor cell types.

When tissue self-assembly was simulated given the first case (interface-independent tension), ectoderm cells enveloped both mesoderm and endoderm progenitors (not shown) contrary to our experimental observations (see Fig. 4.13 A,B). In contrast, when the second case (interface-specific tension) was tested, progenitors sorted exactly as observed in the experiments, with mesoderm and endoderm progenitors surrounding ectoderm (see Fig. 4.13 B,C). This suggests that interfacial energy resulting from adhesion and cortex tension can trigger germ layer progenitor sorting if differential cortex tension exists at the cell-to-medium interface.

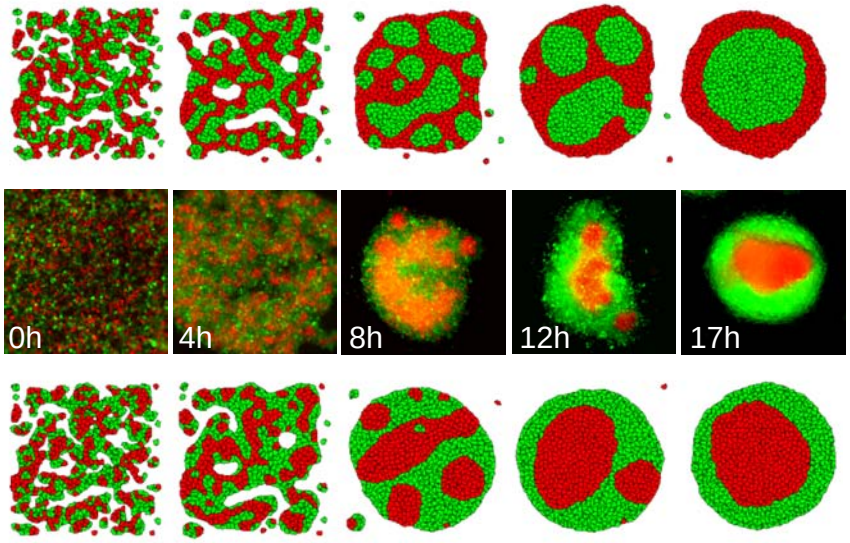

Fig. 4.13 Monte-Carlo Simulation (MCS) of progenitor cell sorting

Upper: Simulation using case I parameters with no interface specific cortex tension according to the differential adhesion hypothesis [106]. **Middle:** Actual sorting pattern of ectoderm and endoderm progenitors after indicated hours in co-culture. **Lower:** Simulation using case II parameters with interface specific cortex tension. T_c for all cell types in contact to other cells has been set to equal and to zero. MCS done by Jos Käfer, CNRS Saint Martin d'Hères.

To determine whether differences in acto-myosin-dependent cortex tension exist at the cell-to-medium interface, germ layer tissue explants were stained after 7 h in culture with the F-actin marker Phalloidin. All explants showed uniform intensity of cortical actin staining at cell-to-cell interfaces, while elevated actin staining was seen at the cell-to-medium interface (the surface of the explants; see Fig. 4.14). In addition, the surface of ectoderm explants was straighter (see Fig. 4.14 A) and displayed higher cortical actin levels than mesoderm and endoderm explants (see Fig. 4.14 B-D), suggesting higher tension at the cell-to-medium interface of ectoderm explants. Together, these findings support the prediction from our simulations that cortex tension at the cell-to-medium interface is different between ectoderm and mesoderm cells. The findings are also consistent with our previous observations that tissue surface tension is higher in ectoderm versus mesendoderm explants [19].

Differential localization of actin can be seen between different cell types and between different types of interfaces.

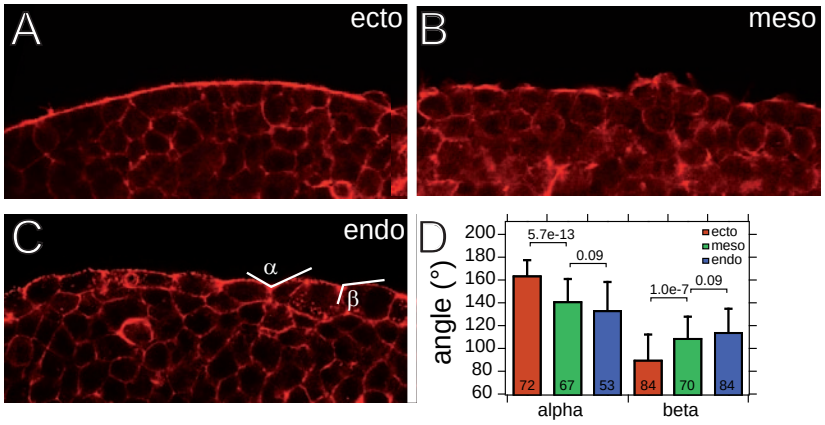

Fig. 4.14 Acto-myosin at explant interfaces

A: Phalloidin stain of fixed ectodermal cell aggregate. **B:** Phalloidin stain of fixed mesodermal cell aggregate. **C:** Phalloidin stain of fixed endodermal aggregate. Angles are highlighted that are used for quantification in D. **D:** Quantification of the two angles encompassing cell-medium interfaces. Numbers above brackets indicate p-value of Student's t-test, whereas numbers in the bar indicate number of observations. Explants were done by Yohanna Arboleda Estudillo, BioTec TU-Dresden.

Questions remain as to the relevance of progenitor sorting *in-vitro* for their actual morphogenetic behavior *in-vivo*. To compare progenitor sorting *in-vitro* and *in-vivo*, an *in-vivo* cell sorting assay system was established. Cells were transplanted from ectoderm, mesoderm or endoderm germ layers into the blastoderm margin of maternal-zygotic *one-eyed-pinhead* (MZ-*oep*) mutant embryos, which predominantly consist of ectoderm progenitors [58], and then monitored the sorting behavior between the transplanted donor cells and

the host cells of the receiving embryo (see Fig. 4.15 A). When ectoderm progenitors were transplanted into MZ-*oep* embryos at shield stage (6 hpf), they remained as a loosely coherent cluster of donor cells embedded within the epiblast of the host embryo at bud stage (10 hpf; see Fig. 4.15 B,E). In contrast, when mesoderm or endoderm progenitors were transplanted into the germ ring of a shield stage MZ-*oep* host embryo, they segregated from the host cells and either arranged into a compact cell cluster (mesoderm; see Fig. 4.15 D,G) or dispersed as single cells (endoderm; see Fig. 4.15 C,F) between the yolk cell and the overlying epiblast at bud stage. These experiments suggest that *in-vitro* and *in-vivo* sorting of germ layer progenitors retain common and divergent features. In both cases, ectoderm progenitors segregate from mesoderm and endoderm progenitors into distinct cell clusters that contact each other. However, the position of ectoderm relative to mesoderm and endoderm differs; ectoderm is on the inside of heterotypic aggregates *in-vitro*, but more superficial to mesoderm and endoderm *in-vivo*.

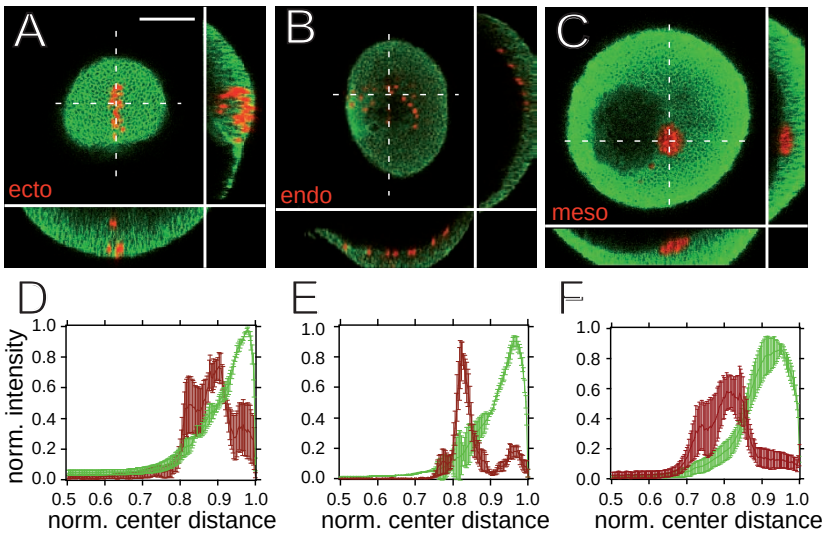

Fig. 4.15 Cell sorting *in-vivo*

A cluster of germ layer progenitor cells is transplanted into a MZ-*oep* host embryo at 50 % epiboly. **A-C:** Localization of donor ectoderm (n = 9 embryos; A), endoderm (n = 7; B) and mesoderm (n = 7; C) progenitor cells in MZ-*oep* mutant embryos at bud stage. Dorsal views. Images were constructed in LEICA SP5 LAS software. **D-F:** Analysis of the spatial configuration of transplanted donor (red) and host (green) cells depicted as normalized (norm.) intensity as a function of the distance from the center of the embryo. Ectoderm cells overlapped more strongly with host tissues compared with mesoderm and endoderm cells. Transplantations were done by Yohanna Arboleda Estudillo, BioTec TU-Dresden.

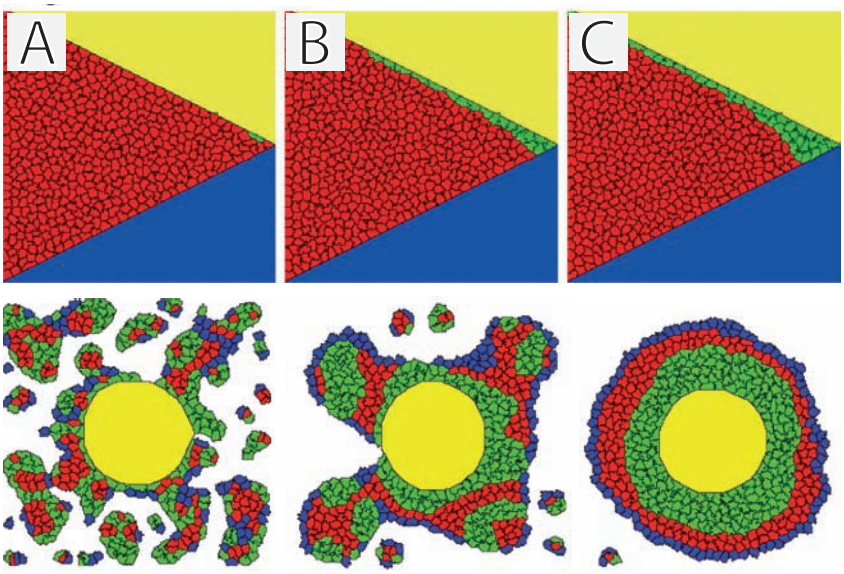

Fig. 4.16 Germ layer formation *in-silico*

Upper panel: Simulation of consecutive steps of progenitor cell sorting in the presence of extra-embryonic EVL and yolk cell. Adhesion and tension values for mesoderm and ectoderm progenitors were set as in Fig. 4.13. Same assumptions as in A, but simulation of consecutive steps of progenitor cell sorting at the *germ ring margin* with the yolk (yellow) and EVL (blue) positions fixed, the space between yolk and EVL filled with ectoderm cells (red), and the rightmost ectoderm cell differentiating into a mesoderm cell (green) at regular intervals. Similar to the situation at the germ ring margin, mesoderm progenitors disperse between the ectoderm and yolk. **Lower panel:** Alternative simulation of the same problem. Adhesion and tension values for mesoderm and ectoderm progenitors were set as in Fig. 4.13. We further assumed that EVL cells adhere preferentially to ectoderm progenitors ($J_{evl,ecto} > J_{evl,meso}$), that yolk and EVL cells have uniform contraction (not interface-specific) and that the adhesion between yolk and the germ-layer progenitors is equal to the homotypic adhesion of germ-layer progenitors ($J_{yolk,meso} = J_{meso,meso}$; $J_{yolk,ecto} = J_{ecto,ecto}$). This results in mesoderm progenitors adhering more strongly to the yolk than do ectoderm progenitors. Progenitor cell sorting was simulated with one big yolk cell (yellow) mixed with 10 % EVL cells (blue), 45 % ectoderm (red) and 45% mesoderm (green) progenitors. Similarly to the *in-vivo* situation, EVL cells were found at the outside, yolk at the center and ectoderm cells surrounding mesoderm. A-C represent snapshots after different Monte Carlo steps. Simulations were done by Jos Käfer.

The apparent discrepancy in the final positioning of germ layer progenitors is most likely due to progenitor sorting *in-vivo* being influenced by interactions with extra-embryonic tissues such as the enveloping cell layer (EVL) on the outside of the embryo and the yolk cell on the inside (initial source of Nodal signals), which are not present in our *in-vitro* preparations. To test this hypothesis, we simulated progenitor cell sorting in the presence of the yolk cell and EVL cells. Assuming both strong adhesion of ectoderm progenitors to

the EVL [371] and mesoderm to the YSL [357], progenitors sort similarly to the *in-vivo* situation (see Fig. 4.16), suggesting that our progenitor adhesion and tension measurements can predict the *in-vivo* sorting order when additional parameters, such as EVL or yolk cell adhesion are included. This view is also supported by experiments showing that when the blastoderm margin is removed from the embryo and placed in culture, endogenous mesendoderm and ectoderm, in the absence of EVL and yolk, self-assemble into an inside-out configuration similar to the *in-vitro* sorting experiments [19].

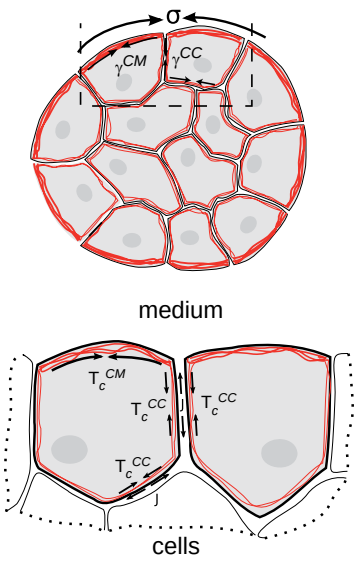

Fig. 4.17 The cellular origin of interfacial tension

At the cell-to-cell interface, the tension γ^{CC} is increased by the cortical tension T_c^{cc} of both cells, and decreased by the adhesion energy J. At the cell-to-medium interface there is no adhesion, thus the interfacial tension γ^{CM} is equal to the cortical tension T_c^{cm}. The surface tension σ is therefore increased by cell-cortex tension at the cell-to-medium interface and the adhesion between the cells within the aggregate.

The Differential Adhesion Hypothesis, one of the most prevalent hypothesis in the field, proposes that cell sorting and tissue organization result from disparate adhesiveness of the participating cells. Here we show that differential intercellular adhesion of germ layer progenitors alone is not sufficient to explain their sorting behavior and that differences in acto-myosin-dependent cortex tensions are critical. How can differences in cortex tension between progenitor cell types influence their sorting behavior? Cells sort according to their aggregate surface tension: the lower tension aggregate surrounds the higher tension one. Aggregate surface tension (σ) characterizes the tendency of the global aggregate surface area to decrease. It is therefore increased by the tension at the interface between cells and the medium (γ^{cm} ; each cell's tendency to decrease its cell-to-medium contact area) and decreased by the tension at the interface between cells (γ^{cc} ; each cell's tendency to decrease its cell-to-cell contact area; see Fig. 4.17 and Ref. [370]). Thus high tension at the cell-to-medium interface in combination with low tension at the cell-to-cell

interface results in high aggregate surface tension. Tension at the cell-to-cell interface (γ^{cc}), in turn, is the result of cortical tension minus adhesion at this interface, while tension at the cell-to-medium interface (γ^{cm}) is determined by cortical tension only (see Fig. 4.17 and Ref. [4, 120]). In order for cortex tension to increase aggregate surface tension and to influence sorting behavior, it must increase the difference between γ^{cc} and γ^{cm}; it must be higher at the cell-to-medium interface than the cell-to-cell interface. Similarly, cell-cell adhesion increases aggregate surface tension by diminishing cell-to-cell tension. It is thus important that both interface-specific cortex tension and differential adhesion should be taken into account to explain progenitor cell sorting [4].

Whether differential adhesion and tension are the only factors determining progenitor cell sorting *in-vivo*, or whether other factors such as directed cell migration, epithelialization and extracellular matrix (ECM) deposition, are also involved, remains to be determined. Notably, none of the forming germ layers in zebrafish show obvious epithelial character or clearly localized ECM depositions [27], leaving directed cell migration as the most likely process to function together with adhesion and tension in germ layer organization. Future experiments, analyzing the specific migratory behavior of germ layer progenitors, will be required to reveal the relative contribution of cell migration to germ layer formation during zebrafish gastrulation.

Adhesion and interface specific cortex tension govern tissue self-assembly and cell sorting.

condition	cell type	1sec median±mad	1sec # of curves(cells)	5sec median±mad	5sec # of curves(cells)	10sec median±mad	10sec # of curves(cells)
homo	ecto vs ecto	575±165	137(35)	1580±323	119(39)	2767±925	162(59)
	endo vs endo	1203±527	86(23)	2772±531	89(32)	4028±1310	168(69)
	meso vs meso	1778±368	91(32)	3531±1148	110(42)	4178±1199	127(56)
hetero	ecto vs meso	969±268	60(22)	2316±702	64(22)	2963±643	89(33)
	ecto vs endo	729±258	68(23)	1901±561	89(29)	2743±934	101(32)
	endo vs meso	866±251	58(20)	2436±683	53(21)	2630±731	70(28)
egta	ecto	143±40	38(10)	212±35	34(10)	284±32	50(15)
	endo	196±31	22(7)	254±50	35(9)	286±92	39(12)
	meso	175±60	43(14)	281±57	45(13)	252±93	46(14)
cdh1	ecto	254±37	37(11)	328±83	65(18)	441±126	52(16)
	endo	422±118	75(22)	592±156	86(25)	698±219	100(30)
	meso	378±100	67(20)	746±307	61(18)	892±338	75(23)

condition	cell type	20sec median±mad	20sec # of curves(cells)	60sec median±mad	60sec # of curves(cells)
homo	ecto vs ecto	3458±918	85(32)	5032±1613	34(20)
	endo vs endo	5748±2205	79(44)	9643±2290	10(7)
	meso vs meso	5979±1926	44(29)		
hetero	ecto vs meso	3575±1354	49±(18)		
	ecto vs endo	2631±893	43(14)		
	endo vs meso	2706±715	37(16)		
egta	ecto	240±51	21(8)	406±110	27(10)
	endo	279±65	29(8)	262±129	16(8)
	meso	342±106	41(14)		
cdh1	ecto	445±175	59(17)	714±354	40(14)
	endo	625±292	89(28)	1885±677	24(11)
	meso	1389±515	63(19)	1786±726	22(7)

Table 4.1 Median detachment forces in piconewton

Number of curves taken for cell-cell adhesion using different combinations and cell types are indicated outside the parenthesis, inside the number of different cell doublet.

5. Cell cohesion controls the directionality of collective cell migration

5.1. Introduction

Collective behavior has been observed in diverse biological systems, ranging from bird flocks and insect colonies to the collective migration of cells in development and disease [372, 373, 374]. A hallmark of such systems is that the collective behavior is not necessarily explained by the behavior of its individual components. Several cell properties were suggested to vary when cells undergo a transition from single cell to collective cell motility such as interaction time and force, migration speed and directionality. Movement directionality, for example, is one of the properties provoked by a community effect and constitutes a collective property of cells moving together [375]. In that context, sperm cells were shown to swim faster in a group than as single cells and displayed a unique morphological transformation, resulting in the cooperation in distinctive aggregations or trains of hundreds of cells [376]. The mean average path velocity of sperm trains was significantly greater than that of single spermatozoa. The synchronization of the sperm cells during motility was suggested to be accomplished by mechanical interaction of the single cells [377]. Because of the abundance of collective cell properties ranging from swarming of bacteria [375, 378], migration of spermatozoa [376], cell migration during vertebrate development [379] and cancer invasion [380], a comprehensive description of collective cell migration was developed. Friedl et al. define collective cell migration (CCM) according to the following characteristics [381]:

- cells remain physically connected by mechanical interactions (*adherens junctions*)

- super-cellular actin assemblies and cell-cell connections provide integrity to translocate the whole tissue mass
- migrating collectives remodel their environment

Whether all of these conditions are fulfilled depends on the context and the system of the migrating cells. For example, collective cell migration can take place in one dimension as cell strands (angiogenic sprouting), in two dimensions as cell sheets (epithelia) and of course in three dimensions as a cohesive cluster (cancer invasion) [381]. To study collective behavior *in-vitro*, confluent monolayers were used as well as many *in-vivo* model systems to understand multicellular development and cancer invasion. The most popular animals to study CCM during development are *Drosophila* and zebrafish [379]. In zebrafish the investigations on CCM up to now were restricted to the migration of the lateral line primordium, which gives rise to the sensory organ. During gastrulation, however, groups of cells undergo dramatic position changes and was suggested to undergo collective migration as well [382]. Mesendodermal cell migration strongly depends on physical integration of the single cells using E-cadherin [78, 371] as well as N-cadherin [341, 357] mediated adhesion. A mutation or down-regulation of these molecules cause severe migration defects [78, 371] although no *adherens junction* are present. Some adhesive gradient was suggested to provide traction necessary for CCM and cell move towards regions where they get more traction [382, 24, 11]. This knowledge suggests that some sort of physical coupling between the cells is necessary which is different from persistent cell junctions as seen in epithelia. Hence, the mechanism behind collective tissue behavior is not completely understood. In this chapter, we propose that zebrafish progenitor cell migration is a suitable model system to investigate different aspects of collective cell migration and argue that adhesive coupling is necessary to guide CCM during gastrulation.

5.2. Results and Discussion

5.2.1. Collective cell migration

Mesendodermal cells move in a highly coordinated manner during zebrafish gastrulation and show collective migration properties.

To investigate how movement directionality arises in collective migration *in-vivo*, we analyzed the movement of germ layer progenitor cells during zebrafish gastrulation. Specifically, we focused on mesoderm and endoderm (mesendoderm) progenitors originating from lateral domains of the early gastrula known

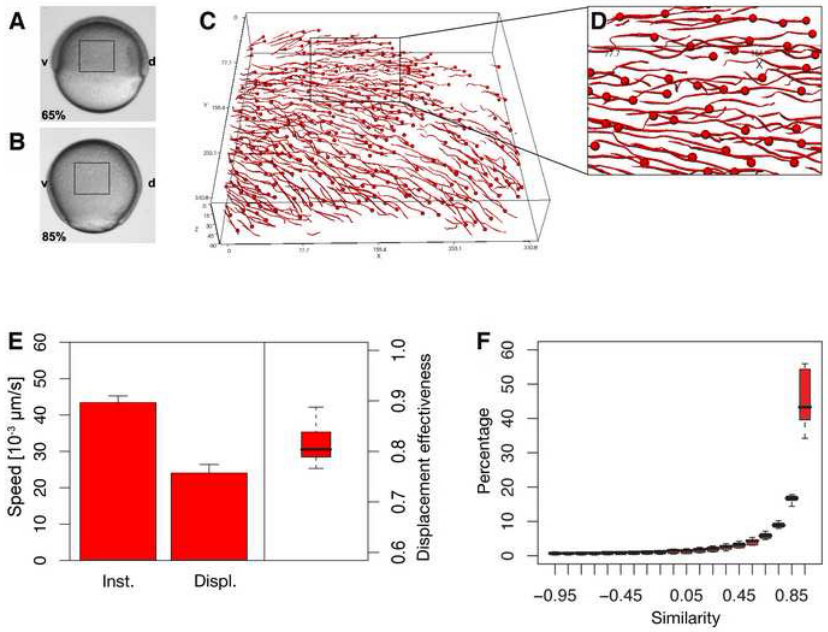

Fig. 5.1 Movement of lateral mesendoderm cells in wild-type embryos

A,**B:** Bright-field images of an embryo at the beginning of gastrulation (6.5 hpf; A) and at mid gastrulation (8.5 hpf; B). Boxes outline the imaged region in (C). **C:** Trajectories of mesendoderm progenitors during mid gastrulation stages. Nuclei were tracked with nuclei tracking software [43]. The endpoint of each track is indicated with a sphere. Dorsal is to the right. The box depicts the magnified region shown in (D). Embryos were imaged by two-photon excitation microscopy from 65% epiboly stage (6.5 hpf) until 85 % epiboly stage (8.5 hpf). Animal pole is to the top and dorsal to the right. **D:** Magnified view of the boxed region in (C). **E:** Average instantaneous speed, average displacement speed, and displacement effectiveness of mesendoderm progenitors during mid gastrulation stages. **F:** Instantaneous similarity of neighboring mesendoderm progenitor movements within a maximum distance of $20\,\mu\mathrm{m}$. Values range from -1.0 (opposite direction of movement) over 0 (movement vectors are orthogonal) to $+1$ (parallel movement). Histograms were generated separately for each embryo. Box plots show the distribution of the bin heights among the different embryos. Data acquired by Lara Carvalho and analyzed by Jan Stuehmer, MPI-CBG Dresden.

---

to display directed migration from mid to late gastrulation (7 - 9 hpf) [26]. To determine whether these mesendoderm progenitors undergo collective migration, we analyzed their movement coordination and directionality, key features of collective migration [383, 381], in two-photon excitation microscopy movies detecting nuclei. Confirming and extending previous studies [26], we found that mesendoderm progenitors during mid gastrulation stages (7-9 hpf) display highly coordinated and directed movements oriented towards the forming embryonic body axis as determined by their instantaneous speed (the speed

at a particular time point), displacement speed, and movement similarity* [43] (see Fig. 5.1), indicative for collective migration.

5.2.2. Migration in crowded and abandoned environment

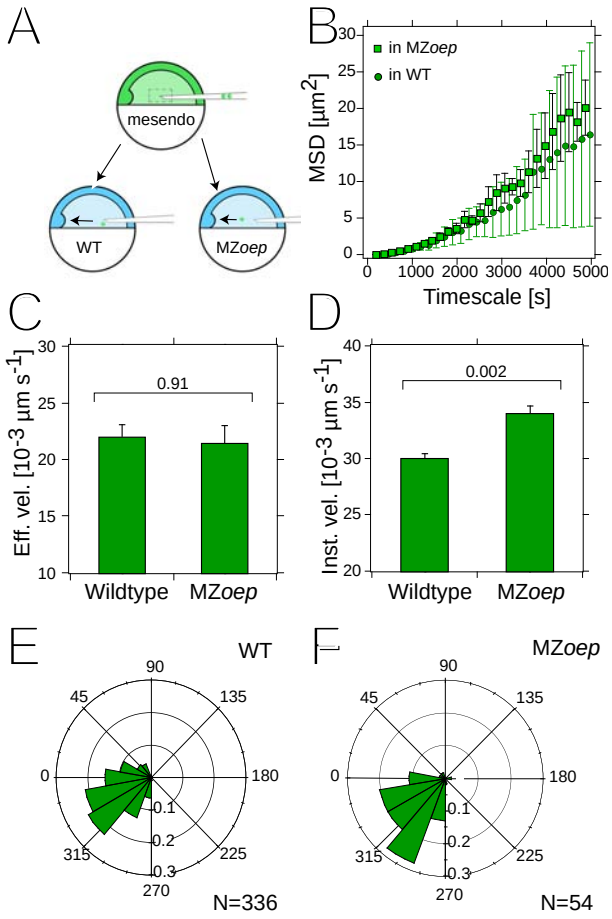

Fig. 5.2 Cell movement in wild-type and mutant embryos

A: Schematic diagram of the cell transplantation experiment. One single mesendoderm cell was transplanted from a donor embryo into either a wild-type or MZ-*oep* mutant host embryos at the onset of gastrulation (6 hpf). **B:** Mean-squared displacement (MSD) plot of individual mesendoderm donor cell movements in wildtype (circles) and MZ-*oep* (squares) host embryos. **C**,**D:** Average effective (C) and instantaneous (D) speed of individual mesendoderm donor cell movements in wildtype and MZ-*oep* host embryos. **E**,**F:** Movement orientation of individual mesendoderm donor cells in wild-type (E) and MZ-*oep* host embryos (F) calculated using Eq. 3.21. Transplantation experiments performed by Yohanna Arboleda Estudillo, MPI-CBG Dresden.

To investigate whether movement directionality is a collective property of mesendoderm cells moving together, we first asked how single mesendoderm cells migrate apart from their group. If movement directionality is a collective property, single mesendoderm progenitors are expected to exhibit poor directionality. We analyzed this by performing a series of cell transplantation experiments in which a single mesendoderm donor cell was placed into either the forming paraxial mesendoderm of a wildtype host embryo at the onset of gastrulation (6 hpf) or into an equivalent position in a maternal-zygotic *oep* (MZ-*oep*) mutant embryo, which lacks most mesendoderm [58] (see Fig. 5.2 A and Supp. Movie 3). Donor cell movements were recorded by confocal mi-

*Movement similarity is the correlation of movement direction as a function of the distance to a certain object.

croscopy throughout mid and late gastrulation stages (7 - 10 hpf), allowing us to compare the migration of individual donor cells in the presence or absence of neighboring mesendoderm cells. We found that single donor mesendoderm progenitors in MZ-*oep* mutants exhibited directed movements similar to those in wild-type embryos as determined by their instantaneous speed and effective speed (the speed of displacement; see Fig. 5.2 B-D). Moreover, single donor mesendoderm progenitors in MZ-*oep* mutants moved in a preferred dorsal-vegetal direction towards the emerging body axis, indistinguishable from single donor progenitors in wild-type embryos (see Fig. 5.2 E,F). These data shows that individual mesendoderm progenitors in the absence of neighboring cells can undergo directed migration similar to mesendoderm progenitors undergoing collective migration. It further suggests that mesendoderm movement directionality represents an intrinsic property of single mesendoderm cells, rather than a collective property of these cells moving together in collective migration.

Single mesendodermal progenitor cells in embryos without neighbors move indistinguishable from wildtype mesendodermal cells.

5.2.3. Modulation of cell adhesion properties

In addition to a cells intrinsic directionality, there might be external factors attributed to the presence of neighboring cells, particularly cell-cell adhesion, that also influence directionality. To address whether cell-cell adhesion is involved in determining movement directionality during collective mesendoderm migration, we analyzed the movement of mesendoderm cells with impaired cell-cell adhesion. We modulated cell-cell adhesion by injecting discrete quantities of a previously described morpholino antisense oligonucleotide (MO) to E-cadherin [51, 78]. The amount of E-cadherin at the plasma membrane was found to scale with the amount of *e-cadherin* MO injected (see Fig. 5.3), demonstrating a concentration-dependent effect of *e-cadherin* MO on E-cadherin expression in mesendoderm progenitors. To ascertain the effect on mesendoderm cell-cell adhesion, we correlated the amount of *e-cadherin* MO injected and E-cadherin at the plasma membrane with the cell-cell adhesion strength of mesendoderm progenitors as measured by single-cell force spectroscopy (SCFS). We found that the cell-cell adhesion force of both homotypic (morphant-to-morphant) and heterotypic (wildtype-to-morphant) cell-cell contacts scaled with the amount of *e-cadherin* MO injected (see Fig. 5.3 B-D) and the amount of E-cadherin at the plasma membrane (see Fig. 5.3 E). When high levels of *e-cadherin* MO (8 ng/embryo) were injected, both E-cadherin expression and homotypic cell-cell adhesion were strongly reduced (see Fig. 5.3 B-D), in agreement with previous findings that E-cadherin plays an important role in

mesendoderm cell-cell adhesion. We also checked the importance of other cell adhesion molecules that have been suggested to play a role during zebrafish gastrulation. The atypical Cadherin Flamingo has, apart of its signaling activity, also a functions in cell cohesion. Over-expressing a cytoplasmic truncated version of this molecules that is supposed to be retained in the Golgi apparatus [175] did not lead to a reduced adhesion force. In contrast, cortex tension of individual mesendoderm progenitors as determined by colloidal force spectroscopy remained unchanged in *e-cadherin* morphant cells (see Fig. 5.3 F), suggesting that E-cadherin does not affect the cortical cytoskeleton.

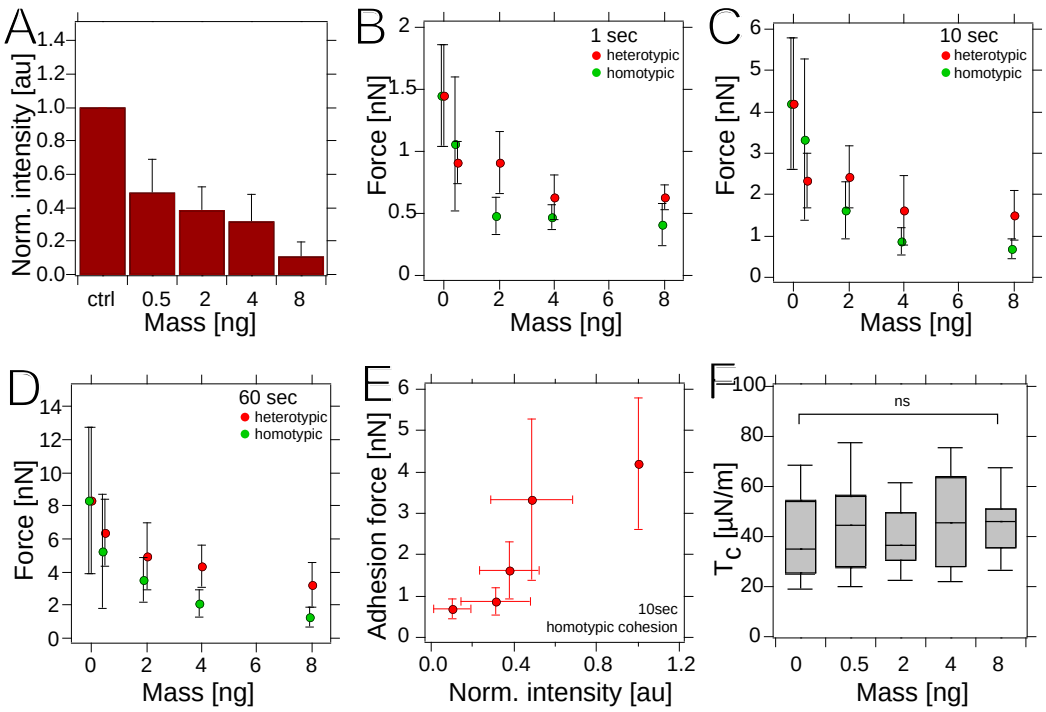

Fig. 5.3 Modulation of mesendoderm cell-cell adhesion

A: E-cadherin at the plasma membrane of mesendoderm progenitors injected with increasing amounts of *e-cadherin* morpholino (MO) as determined by *in-vitro* biotinylation. Staining intensity of biotinylated E-cadherin in *e-cadherin* morphant cells is shown relative to mesendoderm wild-type control cells (mean ± SD). **B-D:** Homotypic (green) and heterotypic (red) adhesion force of mesendoderm progenitors injected with increasing amounts of *e-cadherin* MO for 1 sec (B), 10 sec (C) and 60 sec (D) contact time measured by single-cell force spectroscopy (SCFS). **E:** Homotypic adhesion force as a function of the normalized E-cadherin staining intensity as shown in (A) of wild-type control and *e-cadherin* MO injected progenitor cells (median ± MAD). **F:** Cortex tension of mesendoderm progenitors injected with increasing amounts of *e-cadherin* MO.

5.2.4. Cell migration and cell-cell adhesion

To investigate how the demonstrated changes in cell-cell adhesion affect an individual mesendoderm progenitors movement as part of a group, we used a cell transplantation assay allowing us to simultaneously monitor the movements of mesendoderm progenitors with different adhesive strengths. Typically, a differentially labeled mix of control and experimental cells, ideally consisting of one cell each, was transplanted into the forming paraxial mesendoderm of a wild-type embryo at the onset of gastrulation (6 hpf) and the donor cell movements were recorded by confocal microscopy throughout mid and late gastrulation stages (7 - 10 hpf; see Fig. 5.4 A-C). We found that mesendoderm progenitors with lower cell-cell adhesion displayed significantly less directed movements as revealed by their mean-squared-displacement and effective movement speed (see Fig. 5.4 D,E). Moreover, mesendoderm progenitors with reduced cell adhesion failed to move in a preferred dorsal-vegetal direction towards the emerging body axis, and instead showed dorsal-directed movements with little bias along the animal-vegetal axis (see Fig. 5.4 F-J). Plotting movement directionality as a function of cell-cell adhesion force, we found that the effective movement speed of mesendoderm progenitors linearly scaled with the adhesion force of both homotypic and heterotypic cell-cell contacts (see Fig. 5.4 K). This shows that mesendoderm heterotypic cell-cell adhesion strength and effective movement speed are tightly correlated with each other (r=0.96, p=0.009), suggesting that adhesion-mediated mechanical coupling of cells is critical for directed movement of mesendoderm progenitors. In contrast, the instantaneous movement speed was hardly affected in mesendoderm progenitors with reduced cell-cell adhesion (see Fig. 5.4 E; r=0.58, p=0.31). This suggests that cell-cell adhesion predominantly affects the directionality, rather than the general motility of individual mesendoderm movements in collective migration.

Migration of mesendodermal cells in a crowded environment depends on physical coupling through E-cadherin and migration speed scales with the adhesion forces.

In our transplantation experiments, we analyzed how changes in donor cell adhesion interfere with their movement in host embryos with normal adhesion. To exclude the possibility that the observed effects in movement directionality are mere secondary consequences of cell sorting due to differential adhesion between donor and host cells, we analyzed mesendoderm movement behavior in two-photon excitation microscopy movies detecting nuclei in *e-cadherin* mutant/morphant embryos at mid gastrulation stages (7 - 9 hpf). We found that in both *e-cadherin* mutant and morphant embryos, movement directionality of mesendoderm progenitors is clearly reduced as determined by

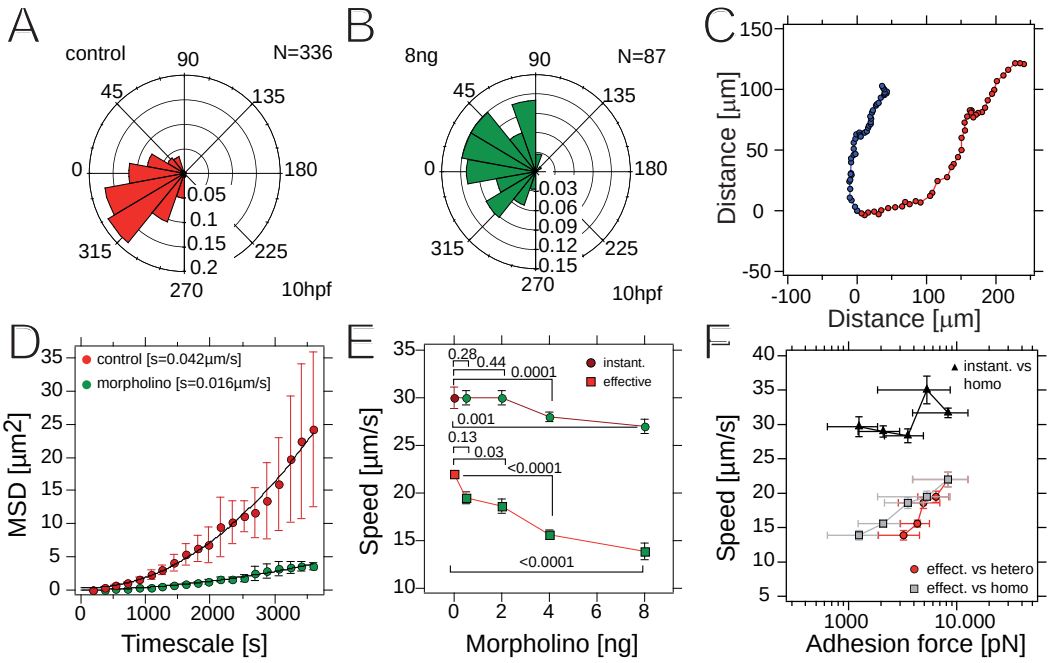

Fig. 5.4 Effect of cell-cell adhesion on individual mesendoderm cell movement

A,**B:** Movement orientation of wildtype control (red; A) and *e-cadherin* morphant cells (green) injected with 8 ng (B) *e-cadherin* morpholino per embryo during the transplantation experiment (6-9 hpf) represented as angular histograms. Angles were calculated in respect to the dorsal pointing vector originating from the embryo center. **C:** Example tracks of a mesendodermal control and E-cadherin loss-of-function cell in a wildtype embryo. **D:** Mean-squared-displacement (MSD) plot of *e-cadherin* morphant and wild-type control cells calculated from the tracks shown in (C). **E:** Average instantaneous (circles) and average effective (squares) movement speed for wild-type control (red) and *e-cadherin* morphant (green) cells. mean±sem, p values determined by t-test are shown above or below the brackets. **F:** Average effective movement speed (mean±SEM) as a function of the heterotypic and homotypic adhesion force (median±MAD) of wild-type control (red) and *e-cadherin* morphant (green) cells as measured in Fig. 5.3 D. Additionally, instantaneous speed versus homotypic adhesion force is shown as black triangles. Transplantation experiments performed by Yohanna Arboleda Estudillo, MPI-CBG Dresden.

their instantaneous and displacement speed (see Fig. 5.5 A-C), indicating that uniform reduction of cell-cell adhesion has similar consequences for individual mesendoderm movements as observed for transplanted cells with reduced adhesion. We also found that movement coordination amongst mesendoderm progenitors was strongly reduced in both *e-cadherin* mutant and morphant embryos as determined by their movement similarity (see Fig. 5.5 D-F), indicating that movement directionality and coordination are interdependent features of collective migration. Cell-cell adhesion might specifically function in collective migration or, alternatively, have additional functions in single cell migration,

e.g. regulating mesendoderm cell adhesion to the overlying ectoderm and/or underlying yolk syncytial layer. To distinguish between these possibilities, we transplanted a small number of differentially labeled control and *e-cadherin* MO cells into MZ-*oep* mutants and analyzed their migratory behavior. We found that the migration directionality of transplanted single mesendoderm progenitors remained unchanged when E-cadherin expression was reduced (see Fig. 5.6), suggesting that cell-cell adhesion is specifically required during collective migration, but is largely dispensable for single cell migration in this system.

Taken together, these findings show that individual mesendoderm progenitors must be mechanically coupled through cell-cell adhesion to participate in directed movement during collective migration. It further indicates that an intrinsic property for directed migration is not sufficient for directed movement when part of a group. Generally, collective migration has an intrinsic movement component, defined by the migratory activity of individual cells, and an extrinsic (or advective) component, describing the translocation of individual cells by the global movement of the cluster [383, 381]. Our finding that individual mesendoderm progenitors in the absence of neighboring cells migrate normally indicates that directed migration is intrinsic. It also suggests that movement directionality of the collective stems from the individual cells rather than being set *de novo* by a particular collective/group property. However, once mesendoderm progenitors move as part of a group, cell-cell adhesion mediation of movement becomes critical to their directed movement. Why do cells with similar movement directionality need cell-cell adhesion to maintain their directionality when moving together? Individual cells, although globally moving in the same direction during collective migration, exhibit some degree of variability in their individual movement paths (see Fig. 5.1 C,D). The variability of one cell can interfere with the movement of its neighbors, which is obstructive for individual cell movement when cells are in close proximity to each other, but can be overcome by mechanically coupling individual cells through cell-cell adhesion. Our observation that movement directionality linearly scales with cell-cell adhesion force supports a critical role of adhesion-mediated mechanical coupling of cells in coordinating individual cell movements during collective migration. Similar observations have been made in previous studies, showing the mechanical coupling of cells is important for movement coordination within multi-cellular aggregates [28]. However, mechanical coupling of cells is unlikely to be the only factor influencing directed movement of individ-

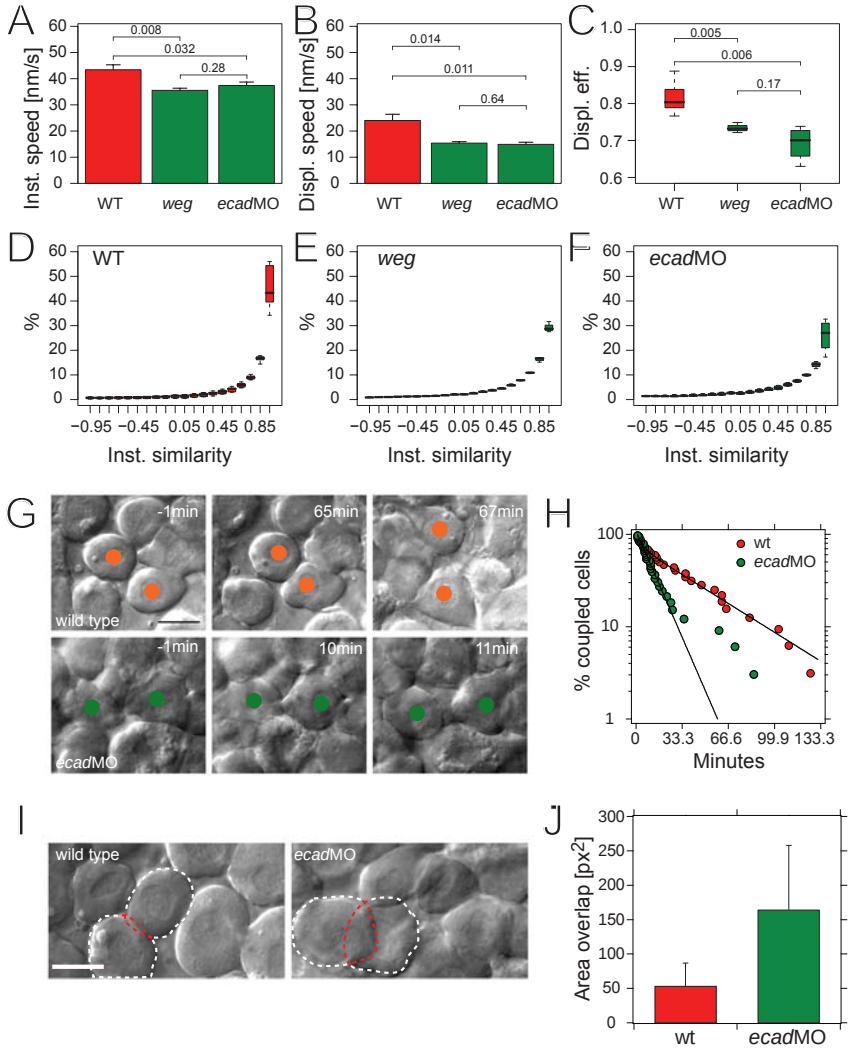

Fig. 5.5 Cell motility, cell contact and contact inhibition in *e-cadherin* mutant/morphant embryos

A-C: Average instantaneous speed (A), average displacement speed (B), and displacement effectiveness (C) of mesendoderm progenitor cell movements during mid gastrulation stages (7 - 9 hpf). p values determined by t-test are shown above the brackets. Number of tracked cells per embryo is 390 $\pm$ 169 in wild-type, 403 $\pm$ 213 in mutant, and 380 $\pm$ 121 in morphant embryos. **D**-F Instantaneous similarity of neighboring mesendoderm progenitor movements within a maximum distance of $20\,\mu\mathrm{m}$ in wildtype (D), *e-cadherin*/weg mutant (E), and *e-cadherin* morphant (F) embryos. Values range from -1.0 (opposite direction of movement) over 0 (movement vectors are orthogonal) to $+1$ (parallel movement). Data acquired by Lara Carvalho and analyzed by Jan Stuehmer, MPI-CBG Dresden. **G:** Representative images of a contact series between wildtype (upper) and *e-cadherin* morpholino (lower, 4 ng) cells are shown. **H:** Quantification of cell contact time of wildtype and *e-cadherin* morphant embryos fitted with an single exponential. **I:** Representative images of wildtype and *e-cadherin* morphant embryo showing spatial overlap between neighboring cells. **J:** Quantification of the overlapping area on the basis of the width of the overlapping zone according to Eq. 3.22.

ual cells during collective mesendoderm migration, and other cell-cell contact-mediated processes, such as contact inhibition or avoidance [84], might play equally important roles therein. Quantification of the contact area with that two cells overlap showed that cells from embryos without E-cadherin lost some sort of contact inhibition (see Fig. 5.5 J). Whereas mesendodermal wild type cells move coherently as a sheet, *e-cadherin* loss-of-function lose the ability to coordinate their movement and persistently run into each other.

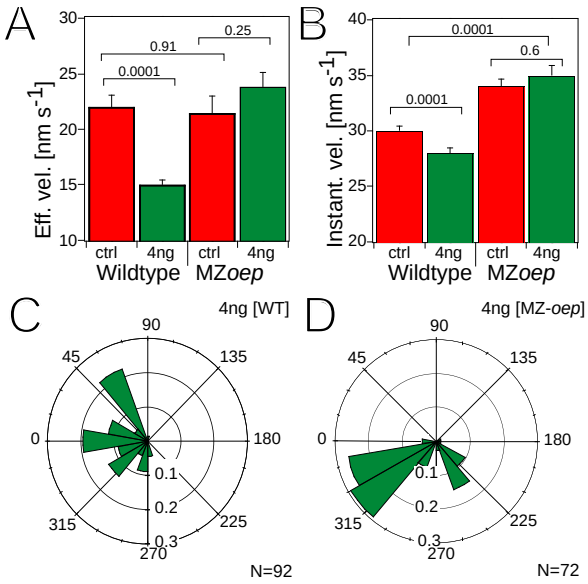

Fig. 5.6 Cell migration in MZ-*oep* embryos

A, **B:** Effective velocity (A, mean±SEM) and Instantaneous velocity (B, mean±SEM) of individual wild-type (red) and *e-cadherin* morphant (MO) donor cells (green; 4 ng) transplanted into wild-type or MZ-*oep* mutant host embryos. **C**, **D:** Angle histogram of the movement orientation of individual *e-cadherin* morphant donor cells (green; 4ng) transplanted into wild-type (C) or MZ-*oep* mutant host embryos (D). p-values determined by t-test are shown above the brackets. Transplantation experiments performed by Yohanna Arboleda Estudillo, MPI-CBG Dresden.

Adhesion-mediated cell-cell contact formation has previously been shown to be critical for collective migration of various cell types in development, including *Drosophila* border cells [384, 385], the zebrafish lateral line primordium [386, 387], and *Xenopus* mesoderm progenitors [171]. Additionally, contact inhibition has recently been shown to direct the coherent migration zebrafish neural crest cells [84], suggesting a function for cell-cell contacts in determining the direction of coherent migration. Our data confirm a critical role for adhesion-mediated cell-cell contact formation in collective cell migration and provide novel insights into the function of cell-cell adhesion in this process. Importantly, we show that adhesion-mediated mechanical coupling of cells, in contrast to contact inhibition [84], is not required to establish movement directionality de novo, but instead is important to coordinate the directed migration of individual cells undergoing collective migration. The collective behavior of cells has been hypothesized to share key features with collective animal be-

haviors such as swarming [373]. Theoretical and experimental studies have suggested that mass-migrating groups can rapidly switch from disordered individual movement to highly aligned collective motion when a specific critical group density has been reached [374]. Assuming that such group-level behavior represents a general principle underlying collective motion, independent of the actual types of individuals involved, it is conceivable that cell density is critical for mesendoderm progenitors to switch from disordered to highly aligned and directed migration. The strong likelihood that cell-cell adhesion affects mesendoderm density supports the interesting possibility that, analogous to mass-migrating animal groups, adhesion controls the directionality of individual mesendoderm movements in collective migration by determining the cellular density. Future studies addressing the functional relationship between cell-cell adhesion and cell density, and the effect of density on collective mesendoderm migration, will be needed to elucidate the common and divergent aspects of collective cell and animal motion.

5.2.5. Summary of adhesion force measurements

		1 second		10 seconds		60 seconds	
	c[MO]	curves(cells)	force	curves(cells)	force	curves(cells)	force
homotypic	cyc	144 (63)	1448	197 (100)	4213±1592	39 (28)	8338±4481
	0.5ng	97 (39)	751±354	101 (42)	3342±1940	61 (29)	6581±3436
	2ng	80 (30)	484±150	96 (34)	1622±697	74 (35)	3543±1375
	4ng	88 (38)	472±102	89 (40)	870±326	76 (35)	2085±860
	8ng	108 (32)	406±168	127 (37)	698±232	103 (35)	1251±609
heterotypic	0.5ng	61 (26)	912±171	68 (31)	2343±672	38 (25)	6400±1925
	2ng	86 (34)	957±253	89 (40)	2416±738	48 (29)	4929±2041
	4ng	127 (47)	687±177	135 (49)	1926±826	90 (36)	4859±1300
	8ng	85 (31)	674±97	105 (40)	1775±612	68 (29)	3475±1325

Table 5.1 Summary of cell adhesion measurements

Numbers of curves and cells taken measured in this chapter. Detachment forces in Median±MAD.

6. Nodal signaling controls cell migration by regulating of plasma-membrane - cytoskeleton adhesion

6.1. Introduction

6.1.1. Cell membrane architecture

Membrane structure The function of cell membrane is to selectively allow entry of wanted molecules and restrict access of unwanted molecules into the cell. This selective permeability is achieved by many different transport proteins embedded into the membrane, which float like islands in a lake of lipids. The main components of cell membranes are lipids and proteins, which form an ultrathin, amphiphatic* bilayer by non-covalent, mainly hydrophobic interactions. Most lipid molecules consist of a hydrophilic head (glycerol+phosphate) and two hydrophobic fatty acid chains. The configuration of the fatty acid chain determines the packing of the lipids into super-structures. Unsaturated fatty acids with a C=C double-bond have a kinked tail and do not pack as densely as lipids with saturated fatty acid tails. The packing thus strongly influences the fluidity of the membrane: the higher the content of unsaturated C=C bonds, the higher the fluidity at a certain temperature.

Fatty acid chains are bound to the hydrophilic head with two hydroxy-groups of a glycerol†. The remaining hydroxy-group of the glycerol is coupled with a phospho-group to a alcanol moiety. The most common phospho-

*Characteristic of being polar on one side and apolar on another side

†Glycerol is the most common. Sphingosine is more special and integrates one fatty acid chain with a phophorylcholine.

headgroup is phosphatidylcholine accounting for more than 50 % of the membrane lipids [388]. This has a choline headgroup coupled covalently to the glycerol. Many other different phospho-lipid molecules are resent in the cell and have different functions. Phosphatidylinositol is a sugar-headgroup and its hydroxy groups can carry various phosphorylations sites which are involved in signal transduction inside the cell and has a prominent function in maintaining integrity of the cell membrane with the actin cortex.

Lipid molecules and membrane shape Due to the high hydrophobicity of fatty acid chains, lipids will readily assemble into a characteristic bilayer structure in an aqueous environment. Forces that shape the bilayer and lead to self-assembly of the lipids are *van der Waals* attractive interactions of the fatty acid tails to exclude water molecules as well as electrostatic and hydrogen-bonding attractions between the hydrophilic headgroups. Depending on the types of lipids involved in the assembly either flat sheets or micelles can be obtained [389]. The decisive factor for this is the geometry of the lipid, e.g. its chain length and the headgroup-volume. Bilayer sheets are preferred over vesicles, because of the bulky fatty acid chains. The geometry of the individual lipid molecules therefore has a great impact on the shape of vesicles and hence cells, because lipids itself can create shape by spontaneously curving the membrane [390]. Micelles do form only when just one fatty acid tail is present and are limited in their sizes. Usually micelles do not form structures larger than 200 Å are formed, whereas bilayers can extend up to many millimeters. The molecules in this bilayer are mobile and therefore a cell membrane can be considered as a two-dimensional fluid. Both sheets of the bilayer are held together by non-covalent hydrophobic forces making an escape of molecules out of the membrane into the solution almost impossible [389].

A cell membrane is a disordered liquid crystal of lipid molecules held together by hydrophobic forces.

6.1.2. Cell membrane mechanics

Membrane mechanics and cell shape To create shape, membranes have to undergo deformations from its equilibrium curvature. The work to do so, is determined by the structure and the mechanical properties of the membrane. Membrane mechanics are largely influenced by its viscous, fluid-like properties, are almost not stretchable and have a very high lateral tension. A typical value for membrane stretching modulus is $200\,\mathrm{mN}\cdot\mathrm{m}^{-1}$ and membranes rupture already after 4 % elongation [352, 391]. Other than stretching, cell membranes typically deform by bending, buckling and uncoiling of a highly folded mem-

brane reservoir. But, membrane properties itself are not sufficient to determine cell shape and therefore need the support from stiffening 'agents' to maintain a deformed shape. Such structural supports can be found on the outside, diatoms and plants, or on the inside of a cell, e.g. actin cytoskeleton and Clathrin coats. Also intracellularly, membrane-compartmentalized organelles show forms from spherical (exo-, endosome) up to tubular (endoplasmatic reticulae, mitochondria) and stacked structures (chloroplasts).

The shape of organelles and shape of diatoms are usually constant, whereas animal cells change their shape dramatically *in-vivo* and a significant amount of the energy is consumed to modify and re-shape the plasma-membrane. The physical forces to actively deform membranes are typically generated within the cell and the bending resistance can be regarded to scale the effort for deformation. Many cell processes have been described to be controlled or directed by the mechanical properties of the cell-membrane. Protrusion formation, such as plasma-membrane blebbing is restricted in cells with a higher membrane tension (T_{app}) leaving the mechanics of the membrane as an important determinant for cell shape. The reason for this is that blebbing transiently increases the curvature [142], whereas membrane tension impedes excess curvature. In other words, more energy is required to bend a stiffer membrane and blebbing is temporarily suppressed. The tension in the cell membrane can be regulated by several means. If connections between the lipid bilayer and the cortex are weakened either by destroying the actin or plasma-membrane coupling molecules, increased blebbing rate can be observed [350]. This assumes a reduction in apparent tension by reducing the adhesion of plasma-membrane to the cytoskeleton and it will be shown later if this is true.

Cell shape is dependent on the mechanics of the membrane-actin cortex system.

Other than blebbing, membrane tension scales the force needed for process outgrowth in neuronal growth cones [329, 328]. A low T_{app} in the membrane favors axon outgrowth by locally reducing the resistance to membrane extension into lamellipodia [329]. During process outgrowth, a tension gradient is created which pulls lipids into the process, due to a low of lipids from low to high tension. Cell migration and process formation has long been explained by the so-called elastic brownian ratchet model [392], in which addition of actin monomers at the leading edge of a migrating cell generates a force to drive the cell forward. Thereby, actin polymerization has to do work against the bending resistance of the plasma-membrane and stalls if the tension is the membrane is too high. Normally, small amplitude thermal bilayer undulations allow actin monomers to be added at membrane proximal pointed

ends [393]. These undulations are scaled by the tension in the plane of the plasma-membrane. Adhesion sites of the membrane to the substrates adjacent to the leading edge can create local tension differentials in the membrane and balances propulsive forces [394].

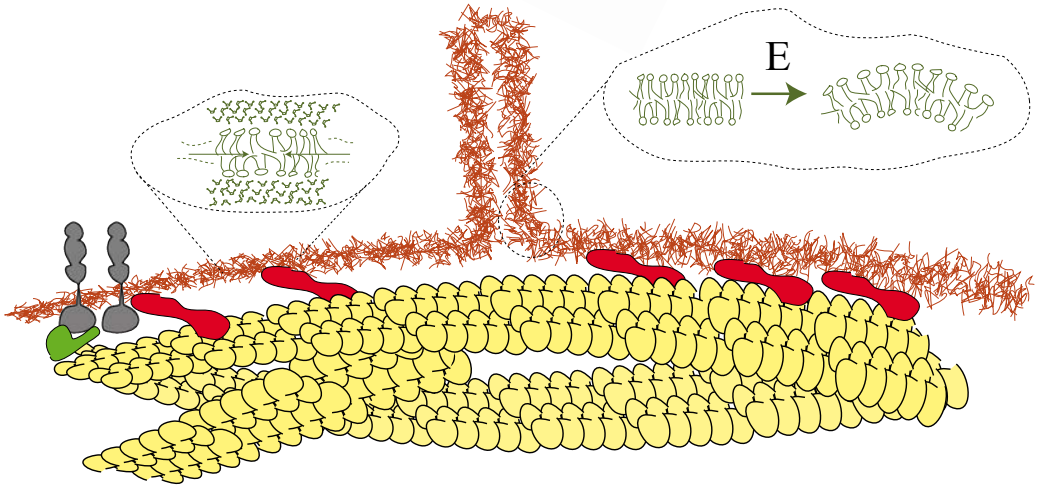

Fig. 6.1 Cell membrane mechanics

Different physical properties determine the resistance to deformation in lipid bilayers that are coupled to the cytoskeleton. Membrane is shown in red, actin in yellow, transmembrane protein in grey, bilayer-cytoskeleton linkers in red and green. In-plane membrane tension (T_{eff}) can be defined as the attraction of individual lipid molecules in parts imposed by the hydrophobic effect and the exclusion of water molecules (left inset, [390]). The adhesion of the bilayer to the cytoskeleton maintains an continuous interaction with the cortical actin network [36]. This interactions is set-up by specialized linker molecules (red) or by integrating cell adhesion molecules to the actin network (green). Bending elasticity is the resistance of the bilayer to be bend out of its equilibrium shape [395] and requires an energy scaled by the bending modulus κ (right inset).

Cell migration and shape are not the only properties that are strongly influenced by plasma-membrane mechanics. The tension in the plane of the membrane has been proposed to account for exocytosis/endocytosis cycles. Logically, high membrane tensions inhibit endocytosis because removal of further lipid material from the membrane would increase the T_{app} even further. Concomitantly, exocytosis is favored because it 'relaxes' the tension [396]. It has been shown that there is an increase in the rate of endocytosis after the stimulation of secretion and that an increase in endocytosis is caused by a decrease in membrane tension. Furthermore, increasing the membrane tension by stretching the membrane with microneedles induced the release of contents from endosomes [396] possibly as a mechanism to reduce tension. The question

Cell membrane mechanics influence cellular behavior such as endocytosis or migration.

here arises about the machinery sensing the tension differential in the plane of the membrane.

One of the most interesting phenomena is the involvement of membrane tension in volume homeostasis. Several hypothesis have been put forward that stretch sensitive ion channels are activated upon osmotic shock. The increase in cell volume results in a higher membrane tension which concomitantly leads to a conformational change that activates ion pumps* to increase the cellular osmolarity preventing further water flow into the cell [397]. Taken together, the cell membrane is an important sub-compartment which is involved in many different physiological function. To fully understand these functions, the biophysical properties need to be examined.

Membrane bending and membrane tension The energy required to bend a piece of membrane from its equilibrium to a new shape [390] is scaled by the membrane bending rigidity and explained in the seminal work of Helfrich [395]. The bending of the bilayer requires the input of energy and leads to the compression of one leaflet and extension of the other (see Fig. 6.1). In general it is the resistance to any deviation from the spontaneous curvature of a piece of membrane. The intrinsic or equilibrium shape depends on the geometry of the lipid molecules, e.g. the head-group and fatty acid tail geometry. For certain lipid molecules, membranes can already be curved. In such a case, an considerable amount of energy is needed to force the membrane in a flat configuration. Because membranes as a two-dimensional liquid crystal are very soft structures, large deformations have to be applied to be able to measure such low forces involved in re-shaping. Therefore, bending rigidities of membranes are very low and are usually in the order of the thermal energy†. As a consequence, isolated membranes readily start to undulate at room temperature, if the geometry is not constrained and no tension is imposed. Analysis of these thermal undulations is the heart of many experimental approaches to estimated bending elasticity of lipid bilayers [399, 350, 400, 401].

$$\langle |u(q)|^2 \rangle = \frac{k_B T}{\kappa q^4 + T_{eff} q^2} \qquad \text{(Eq. 6.1)}$$

Herein, $\langle |u(q)|^2 \rangle$ is the mean square fluctuation amplitude, q the wave number and $k_B \cdot T$ the thermal energy term and T_{eff} the tension of the lipid vesicle. As

*so called mechanosensitive transmembrane proteins

†The bending rigidity κ is a material constant of $\approx 2 \cdot 10^{-19}$N·m [398] or $20 k_B T$

one can see in Eq. 6.1, the amplitude decreases with higher tension and higher bending rigidity. The impact of both properties on the amplitude is scaled by the thermal energy input k_BT. Recently, the membrane tension and the bending modulus of living cells have been measured using flicker spectroscopy [350, 400], but is in general technically very challenging.

System	$\kappa \cdot 10^{-19}$J	Technique	Ref.	+csk
Walker cells	2.87	FS	[350]	bleb
Macrophage	41	RICM	[148]	yes
Neutrophil	≈20	MPM	[286]	yes
SOPC	1.26	CA	[400]	vesicle
SOPC	1.15	MPM	[402]	vesicle
SOPC	1.2	tether	[403]	vesicle
SOPC+cholesterol	2.96	CA	[400]	vesicle
SOPC+cholesterol	3.3	tether	[404]	vesicle
ER membrane	3.3	tether	[405]	no

Table 6.1 Published values for lipid-bilayer bending rigidity

Collection of literature data for bending rigidity (curvature elasticity) of different lipid bilayer compositions or different cell types. Various techniques have been used to date such as micropipette manipulation (MPM), flicker spectroscopy (FS), contour analysis (CA), tether pulling.

The thermal undulations have an interesting consequence on the mechanical properties of membranes under strain. Due to out-of-plane undulations the projected area of free bilayers is always lower than the contour area. Small tensions tend to reduce such fluctuations, leading to a larger projected area. Therefore, when applying a longitudinal stress on the bilayer, the membrane will grow transversely, yielding a negative Poisson ratio [390].

An elegant and theoretically less demanding approach to measure κ was performed by tether extraction of pre-tensed lipid vesicles [406, 348, 403]. In such experiments, a lipid vesicle was aspirated into a micropipette with varying suction pressures , hence varying membrane tensions. Using these structures, the force to extrude a lipid-nanotube was measured with optical tweezers. The slope of the correlative properties yields the bending rigidity κ of the vesicle membrane. Up to now, many more techniques have been presented to estimate the curvature elasticity of various lipid mixtures and membranes [406, 407] although the correct measurement in cells is still a challenge.

Cell membrane mechanics is characterized by membrane curvature elasticity, surface tension and adhesion to the cytoskeleton.

Next to the bending rigidity, in-plane (or effective when speaking about

cells) membrane tension T_{eff} acts against the deformation of a lipid bilayer. This tension acts as a force to minimize the surface area of the bilayer and can be regarded as a classical surface tension. Therefore, the membrane tension is the energy required to expand the surface area of a lipid bilayer by one unit area. The molecular origin lies within the individual lipid molecules and is dependent on several features [390]:

- compression caused by the Van der Waals attraction of the acyl chains [408]
- separation caused by the entropic motions of the acyl chains to occupy all available configurations and thus push each other out of the way
- close packing at the level of the carbonyl groups that form the junction between the head group and the hydrocarbon tail to avoid water incursion
- and generally expansive interactions of the head groups with each other and solvent components due to their hydration, ion binding, and endogenous electrostatics.

Overall, the hydrophobic effect is the dominating force that creates membrane shape and surface tension of the bilayer. It is energetically very unfavorable to present acyl chains to water, therefore, any edges of the membrane are prevented and self-organization into spheres or vesicles occurs spontaneously [389, 390]. This is also the reason why the probability that a lipid molecule spontaneously changes a bilayer is very low. In order to facilitate such processes, specific enzymes, called flippases have been evolved to catalyze this reaction.

6.1.3. Biophysics of membrane-nanotube extrusion

Membranes of living cells have an additional component influencing the tension of the bilayer, to be precise, its adhesion to the cytoskeleton. Many proteins have evolved to confer specific binding of the membrane with the underlying cytoskeleton. Such proteins are either incorporated into the plane of the membrane* or specifically bind to modified lipid molecules†. Estimation of the cell-membrane to cytoskeleton adhesion energy (W_0) is conceptually much

*transmembrane proteins
†peripheral membrane proteins, such as Ezrin, Radixin, Moesin

easier and has been applied to many cell biological problems [36]. Physically, W_0 is the free energy that is released when a unit area of membrane comes into contact with the cytoskeleton. Next to the interaction energy of specific receptor-ligand bonds, it is postulated that an important contribution to the energy of association between bilayer and skeleton comes from the increase in chemical potential due to the lateral segregation of lipids and integral proteins [409]. To estimate W_0, the force needed to disrupt this interaction was measured by peeling off the membrane from the actin cortex. This can be done in various ways. In first experimental evaluation, a cell, accelerated by a laminar flow, was allowed to roll over a ligand coated glass slide. Once in a while, an interaction of the cell with the substrate slows down the speed with which the cell rolls over the surface [410]. The speed difference is a measure of the force that is exerted on this particular interaction. When the flow was turned off, surprisingly the cell jumped back to its anchoring position immediately [411]. So-called lipid nanotubes or membrane tethers were hypothesized to facilitate the binding between the cell and the surface [412], which was proven much later [413]. Since back then in 1973, tethers were widely used to measure mechanical properties of cell membranes (see Tab. 6.1, Tab. 6.2 and Tab. 6.3). For a tether to form, a threshold force is needed bend the membrane and to detach it from the cytoskeleton. This force is a measure of the plasma-membrane mechanics.

Statics of extrusion Force measurements with flow chambers are tedious to perform and difficult to analyze. A much simpler assay to measure membrane mechanics is to take a membrane at some handles, e.g. adherent beads and pull them away to extrude a tether. The restoring force on the handles is the force needed to extrude a membrane nanotube. Optical and magnetic tweezers as well as AFM are widely used to manipulate membranes in that way [36, 414, 415]. Therein, a bead is manipulated in a optical trap and brought into contact with a cell (see Fig. 6.2). Upon retraction, a single tether is extruded. When the bead is held at a constant length, the restoring force on the bead is then dependent on the (apparent) tension of the plasma membrane T_{app},

$$f_0 = 2\pi\sqrt{2\kappa \cdot T_{app}} = \frac{2\pi\kappa}{R_t} \qquad \text{(Eq. 6.2)}$$

W_0 can be measured with the force needed to extrude lipid nanotubes out of living cells.

and the bending rigidity κ. An important feature of this relation is that the force does not change after the tether has been extracted, but stays constant until the lipid reservoir of the cell is exceeded [416]. On the right hand side

of Eq. 6.2 one can see that with constant bending modulus the radius of the tether R_t get smaller when the force on the tether is increased. This suggests, that a higher membrane tension leads to a smaller tether radius [35, 417].

It is useful to relate tether force f_0 to other membrane parameters such as the adhesion energy per unit area W_0, and the in-plane tension T_{eff}. Measurements of membrane tension in living cells is more complex due to a existing adhesion term of the membrane to the underlying cytoskeleton. In intact cells one cannot readily distinguish between the far-field in plane membrane tension T_{eff} and the work of adhesion to the underlying cytoskeleton W_0 so that these two terms are generally expressed together as the apparent membrane tension T_{app}:

$$T_{app} = T_{eff} + W_0 = \frac{f_0^2}{8\pi^2\kappa} \qquad \text{(Eq. 6.3)}$$

To separate adhesion and in-plane tension, one can measure the tether force on cells lacking membrane support by the actin cytoskeleton [36, 351, 250]. This can be achieved for example by treating the cell with actin depolymerizing agents or extrusion of tethers from fresh plasma membrane blebs [142].

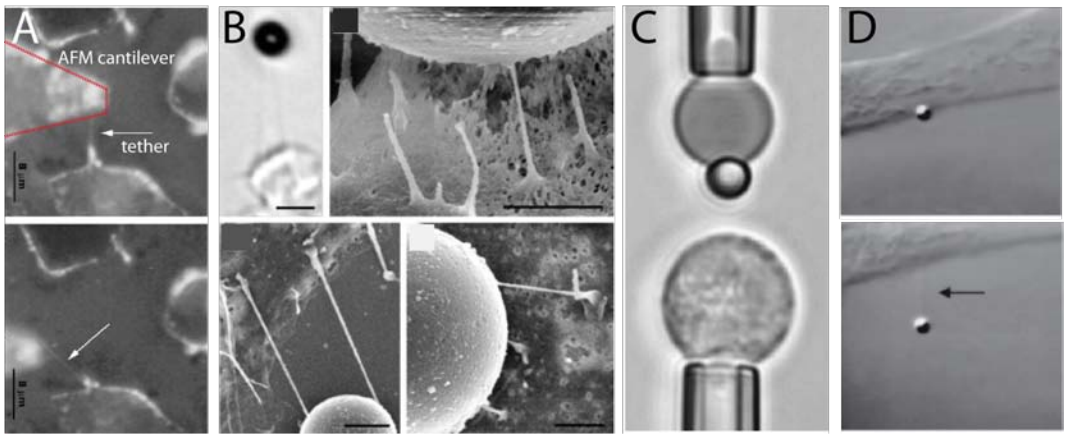

Fig. 6.2 Tether extrusion using different techniques

A: Tether extraction using AFM [414]. Cells have been labeled with quantum dots to visualize the membrane. **B:** Tether extraction using magnetic tweezers [414]. **C:** Biomembrane-force-probe technique to extract single tethers using an antibody coated bead [418, 419, 420]. Several modifications of this techniques have been presented in the literature [421, 35] were a tether is extruded with a bead and the change in geometry of the cell is recorded. **D:** Tether extraction using optical tweezers. Initially used by Sheetz group, it represents one of the main techniques to extrude tethers from cells [422, 423, 142, 416, 29, 424] and vesicles [425, 426]

Up to now, the mechanics of the membrane-cytoskeleton was tested experimentally using a variety of different techniques. First experimental evidence of

tether formation was achieved accidently in flow chamber analysis of red blood cells [411]. Herein, the detachment of the cells during the flow was incomplete, resulting in long, filamentous nanotubes extruded from the cell body. Flow techniques have been used further to characterize the rolling of neutrophils on substrate which mimics intravenous flow of blood-cells [413]. Many micromanipulation techniques have been used that offer a force transduction in the piconewton range and the positional accuracy to stretch small membrane segments for several micrometers. Using these different approaches with different cells, a variety of problems were solved by measuring the membrane properties of cells in different aspects. The Sheetz group was one of the main contributors of our understanding how membrane mechanics and cytoskeleton adhesion influences the behavior of cells during endocytosis [427], cell spreading [29], process extension of nerve cells [329], second messenger action of PIP_2 [428] and cell blebbing [142].

Dynamics of extrusion Apart from holding a tether at a constant length after extrusion to measure the static tether force, another way to estimate equilibrium membrane mechanics is possible. Tethers are extruded at various velocities and the force is recorded as a function of the extrusion velocity. Now, the force f_t is different from the tether force, f_0, when the bead is hold a a constant length. During extrusion, lipid flow occurs and energy dissipates due to membrane internal friction or other viscous effects (η) which add to the static components of the force (see Eq. 6.4). Therefore, the tether force is in general higher, the faster the tether is extruded from a cell. Following the trend to zero velocity by fitting the $f_t(v)$ data to one of the following models, one can yield the static tether force to calculate membrane apparent tension according to Eq. 6.2.

One of the first models treating force-velocity data of extruded nanotubes suggests a linear correlation between f_t and v. Originally developed for vesicles which have no interaction of the membrane to the cytoskeleton [429, 35] it was shown to be valid for many cell types [328]:

$$f(v) = f_0 + 2\pi\eta v \qquad \text{(Eq. 6.4)}$$

In this model, the viscosity is defined as the slope of the graph. Ergo, when two cells have different slopes, this model thus assumes changes in cell membrane viscosity η. This might be true for vesicles, but when working with cell this assumption is not necessarily valid anymore because additional components of

System	$\eta[Pa\,s\,m]$	Technique	Ref.
EPC	$13{\cdot}10^{-9}$	Flow field	[429]
EPC	$0.53{\cdot}10^{-9}$	Diffusion	[430]
RBC	$9\text{-}13{\cdot}10^{-6}$	MPA	[431]
RBC	$0.13{\cdot}10^{-6}$	SSTT	[432]
RBC	$4.8{\cdot}10^{-5}$	Flow field	[433]
RBC	$\sim 3 \cdot 10^{-6}$	MPA	[35]
Fibroblast	$6{\cdot}10^{-6}$	AFM	[434]
NGC	$0.2{\cdot}10^{-6}$	OT	[142]
CHO	$0.33{\cdot}10^{-6}$	MT	[414]
Neutrophil	$0.57{\cdot}10^{-6}$	MPM	[32]
OHC	$5.5{\cdot}10^{-6}$	OT	[435]

Table 6.2 Literature values for cell surface viscosity

Published values for η acquired using different techniques and cell types. Values measured with vesicles are usually lower compared to values acquired from diffusion measurements [429]. Viscosity was calculated from diffusion measurements using Saffman-Delbrück Relation [327].
Abbreviations used in this table: EPC, egg phosphatidylcholine; RBC, red blood cell; NGC, neuronal growth cone; MPA, Micropipette aspiration; SSTT, steady-state-tank-treading; MPM, Micropipette manipulation; AFM, Atomic Force Microscopy

the membrane restrain the flow of the lipid bilayer into the tether. Considering that adhesion of the lipid bilayer to the underlying cytoskeleton can impeded membrane flow, a more complicated model was communicated recently and was shown to fit tether force - extrusion velocity data equally well (see Eq. 3.14 and Ref. [34]). In this model, the force increase with speed not only comes from the internal friction (viscosity, η) of the lipid molecules, but also of the drag of the lipids around integral membrane proteins (density of binders, ν) and the underlying cortical cytoskeleton.

$$f_t^3 - f_t f_0^2 = \left[(2\pi)^3 \kappa^2 \eta \nu \ln\left(\frac{R_c}{R_t}\right)\right] \cdot v \qquad \text{(Eq. 6.5)}$$

This model is only valid for limited extrusion velocities. For speeds larger than $100\,\mu\text{m} \cdot \text{s}^{-1}$ forces get too large and result in an unbinding of the transmembrane proteins from the cytoskeleton. Nevertheless, one is able to estimate the numbers of cross-linking molecules by knowing the viscosity of the lipid phase of the bilayer. Which molecules cross link the membrane with the cytoskeleton, will be introduced in the following section.

6.1.4. Molecular strategy of membrane-cytoskeleton adhesion

Most animal cells have complex morphologies because the membrane adheres strongly to the cytoskeleton, fitting like a glove to a hand. Despite the con-

tinuous adhesion, anchoring of the plasma-membrane to the underlying actin cytoskeleton is very dynamic and changes occur rapidly. This can be explained by many weak bonds between membrane lipids and cytoskeletal proteins [36]. Above all, phosphoinositides (PtdIns(4,5)P_2, PIP_2) are one of the major lipid component involved in maintaining the interaction to the cell cortex. Strong bonds mainly occur in adherent parts of the cell, were cell-adhesion receptors are clustered and bound to the cytoskeleton. The highest estimates of strong-bond density are about 200-300 nm between two different attachments. In contrast, there are up to 10.000 PtdIns(4,5)P_2 molecules per μm^2 of cell membrane. This means that there is an average distance of about 1 Ångstrøm between two potential cytoskeleton binding sites. Such a high density of interacting components and their localization in two dimensions along the surface of the membrane assure that the effective concentrations are high, and so the bilayer and cytoskeleton adhere seemingly continuous [36]. Proteins recognizing PIP_2 lipids typically contain so called pleckstring homology (PH) domains, named after a main kinase target in platelets, and C2 domains. Both are among the largest domain families in the human proteome [436]. Not all of the PH domains bind PIP_2 lipids strongly although some exhibit remarkable affinity and specificity for other kinds of phosphatidylinositols such as phosphatidylinositol-tri-phosphate (PIP_3). For example, PH domains of protein kinase B binds PIP_3 lipids in membranes that contain a 30folds excess of PIP_2.

The membrane adheres seemingly continuously to the cytoskeleton by many weak bonds, such as lipid-protein interactions [36].

One of the proteins which contains a PH domain and binds PIP_2 is Ezrin (see Fig. 6.3 A). Ezrin belongs to the band 4.1 protein family together with Radixin and Moesin [30] and the tumor suppressor Merlin. Ezrin is highly enriched in microvilli of epithelial cells and cell surface structures containing an actin cytoskeleton such as membrane ruffles. It provides a regulated linkage of membrane proteins to the cytoskeleton, which pull the membrane over the filaments like a glove over fingers. ERM proteins are essential for many fundamental processes like cell migration [439], adhesion [440], cytokinesis [144] and cell protrusion formation (see Fig. 6.3 C).

ERM proteins usually reside in the cytoplasm in an inactive, dormant form and are only capable of binding the membrane after specific activation. In the dormant form, an intramolecular association of the N-terminal with the C-terminal domains masks actin binding site [30]. The N-terminal FERM* domain contains 300 aminoacid residues and is composed of three sub-domains

*Four-point-one, Ezrin, Radixin, Moesin

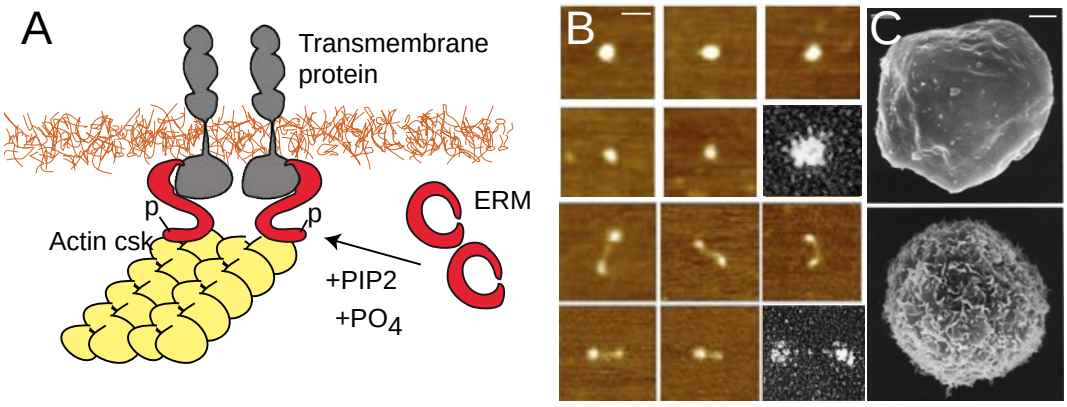

Fig. 6.3 Function of ERM proteins

Schematic representation of the ERM activation scenario. ERM proteins reside in the cytoplasm in an inactive state by an intramolecular association which masked the actin binding site. Activation occurs via phosphorylation at a conserved threonine residue as a response to a signaling cascade. After activation, ERM proteins are able to bind both, membrane lipids or proteins and actin cytoskeleton simultaneously. **B:** AFM scanning topograph of dormant (upper) and activated Ezrin molecules (lower) [437]. The lower right corner shows the same pattern in electron micrographs [438]. **C:** Cell morphology of cell over-expressing an constitutively dormant Ezrin molecule (upper) and a constitutively active Ezrin version [153].

Members of Ezrin, Radixin, Moesin family (ERM) participate in membrane csk adhesion by binding both, membrane and actin.

which arrange into a globular, cloverleaf-like structure. These sub-domains are involved in binding lipid ligands like PIP_2 and have high similarity to the previously mentioned PH domains. The C-terminal actin binding domain (C-ERMAD) adopts an extended structure containing several β-strands and six α-helical regions. In crystal structures, this domain is very flexible and adopts very different conformations depending on whether it is free or actin bound. Actin binding probably occurs at some acidic residues in the very C-terminal part of this domain and is deeply buried in the dormant proteins via FERM - C-ERMAD interaction [441]. The switch from dormant to active elongated conformation occurs upon phosphorylation of a conserved threonine residue T567 in Ezrin* and T558 in Moesin (see Fig. 6.3 B). This residue is buried in the interface. The addition of a highly negatively charged group is unfavorable next to the negative charged FERM domain surface and results in a weakened FERM - C-ERMAD association. Since this residue is buried in the interface between the two domains, conformational flexibility is necessary to accommodate phosphorylation. Probably, the binding of ERM proteins to PIP_2 lipids is necessary to facilitate activation by phosphorylation [442]. Several other studies favor the idea that phospholipid binding is necessary to unmask the

*Threonine residue 567 in mouse and 564 in zebrafish

F-actin binding site [443]. The conserved threonine residue seems to be necessary but not sufficient to completely activate the protein [444]. Mutating this threonine to a non-phosphorylatable residue, e.g. alanine T567A, leads to a loss-of-function of isolated molecules [442] as well as in living cells [338]. In contrast, the phospho-mimetic mutant T564D did not show activation in biochemical assays [444] although it has been argued in AFM and EM studies [437, 438]. At the end the exact function of ERM proteins in the cell are remained to be determined. Its function has never been shown unambiguously due to lack of rigorous control experiments [424], transient activation [445] or the redundancy of plasma-membrane to cytoskeleton integrating proteins. ERM family members are not the only proteins that mediate the interaction of the membrane with the cytoskeleton. Cell adhesion molecules, for example, bind directly or indirectly to the cytoskeleton with their intracellular domains while being anchored within the membrane. Recently it has been shown that E-cadherin has a profound role in determining the coupling of actin with the membrane [410]. It seems that cells have evolved various mechanisms to ensure a persistent coupling of the cell membrane to the cytoskeleton and do rarely rely on one molecule only. Next to the redundant nature of membrane-cytoskeleton adhesion, the study of Ezrin function in tissue culture cells was humbled, because of the transient activation of ERM proteins in certain cell functions, such as mitosis. We believe that zebrafish is a good model system to study ERM function because Ezrin2 is constitutively activated during zebrafish gastrulation [31].

Nodal signaling constitutes a key regulator of mesoderm cell specification and morphogenesis. While Nodal function in cell specification has been intensively analyzed, much less is known about its function in morphogenesis. Recently it has been shown that Nodal signaling is sufficient to phosphorylate and hence activate Ezrin, Radixin, Moesin (ERM) family proteins [31], potential modulators of cell shape changes during progenitor cell motility. Using single tether extraction experiments with AFM we aim to investigate that ERM proteins indeed facilitate the interaction of the membrane with the cortical actin network and direct plasma membrane blebbing in mesendodermal progenitor cells both, *in-vivo* and *in-vitro*.

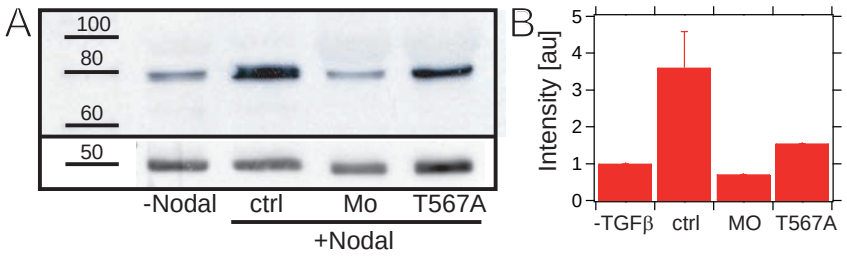

Fig. 6.4 Nodal signaling and ERM expression.

A: Western blot of Nodal-activated and blocked cells using a phosphospecific antibody against ERM (pERM) proteins. **B:** pERM intensity normalized by intracellular tubulin staining.

6.2. Results

Nodal/TGFβ signaling has a dual function during germ layer formation in zebrafish and specifies mesendodermal cell fate at the onset of gastrulation [2]. Next to its role of cell fate determination, Nodal also has a role in germ layer morphogenesis [446]. Whereas the signaling pathway from the ligand-receptor binding down to its transcriptional targets have been analyzed in great detail [447] much less is known how Nodal signaling controls morphogenesis of mesendodermal progenitor cells [448]. Gastrulating zebrafish cells change their gene expression and cell properties when induced to form mesendoderm, invade the embryo at the organizer and get highly motile. How motility is regulated specifically by Nodal signaling and how this affects behavior within a tissue is not completely understood yet.

6.2.1. Activation of Ezrin by Nodal signaling

On the search for the activation of potential regulators of mesendodermal motility as a response to Nodal signaling we recently identified several promising candidates [31]. Among those, a member of ERM domain family proteins, namely Ezrin2, is ubiquitously expressed throughout the embryo but specifically activated in the developing mesendoderm during gastrulation. Ezrin is hypothesized to bind both, plasma-membrane and cortical actin cytoskeleton after activation by phosphorylation, but usually resides inactively in the cytoplasm with the actin binding site masked by an intramolecular association [30].

We first asked whether Nodal signaling is sufficient to induces the activation

of Ezrin by phosphorylation at the conserved threonine residue T564. Cells from zebrafish embryos injected with components known to activate Nodal signaling pathway showed significantly higher intensity of activated Ezrin on western blots with a phosphospecific antibody as compared to cells taken from Nodal deficient embryos. Blocking the transcription with a morpholino previously characterized to inhibit translation and germ layer morphogenesis yielded a manyfold reduction of phosphorylated ERMs (see Fig. 6.4). When we overexpressed a non-phosphorylatable, dominant negative version of Ezrin (T564A, dnEZR) in the cells, we observed a small reduction on normal western blots, but an almost complete reduction of the phosphorylation on phos-tag gels which delays the migration of phosphorylated proteins in an SDS-gel*. This shows that Nodal signaling is sufficient to induce the phosphorylation of Ezrin at the conserved threonine residue and confirms previously observed findings [31].

Nodal signaling is sufficient to phosphorylate ERM proteins at the conserved T564.

6.2.2. Ezrin and plasma-membrane blebbing

Activated ERM family member proteins are supposed to bind membrane and actin filaments to regulate cell behavior including process formation [338] and migration [439]. To understand what is the contribution of Ezrin in process formation in zebrafish progenitor cells, we brought single cells into culture that were stained for membrane and filamentous actin. Only few cells show filopodia and lammelipodia but all cells show clear signs of blebbing by a decoupling of the membrane from the cytoskeleton (see [150] and see Fig. 6.5 A). Blebs usually expand isotropically and retract as soon as a new actin cortex is build up and supports the free membrane (see Suppl. Movie 4 and Fig. 6.7). Zebrafish blastomeres brought into culture showed a behavior which was previously called circus movement [150, 449]. Herein, a part of the membrane detaches from the cortical actin belt and propagates asymmetrically around the cell circumference. The leading bleb edge is devoid of actin which re-assembles on the backside of the bleb (see Fig. 6.7).

Zebrafish cells do blebbing *in-vitro* and *in-vivo*. Blebbing activity is partially controlled by the activity of ERM proteins.

How is a circular bleb-wave created? During circus movement, the leading edge bleb has the weakest actin deposition and is more prone to break than an older bleb. The older 'bleb' clearly shows a stronger deposition of actin at the periphery (see Fig. 6.6), suggesting a stronger mechanical stability. Therefore, new blebs have a higher probability to nucleate on the side of the

*Data acquired by Alba Diz

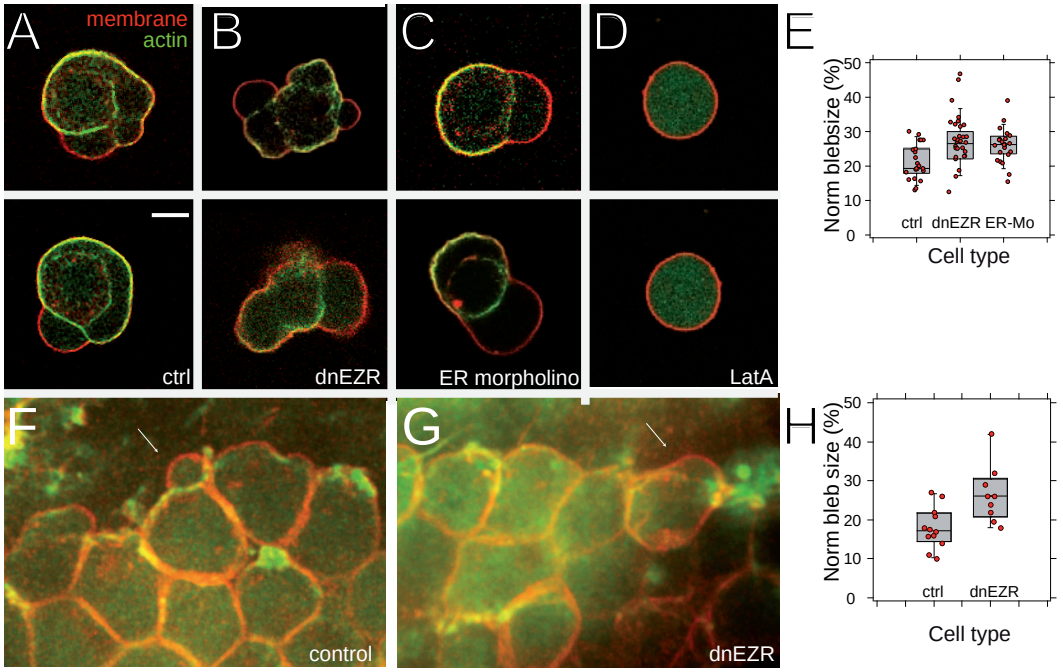

Fig. 6.5 Blebbing of mesendodermal cells *in-vitro* and *in-vivo*.

A: Cell shape of mesendodermal cells in culture stained for filamentous actin (green) and membrane (red). A hemispherical protrusion is projected from the cell and eventually translocates around the cell circumference. **B**-**C:** Cell-shape of a mesendodermal progenitor injected with a dominant negative version of Ezrin (B; dnEZR, T564A) and Ezrin/Radixin morpholino (C; MO). **D:** Latrunculin A (1 µM) treated cell. **E:** Quantification of the *in-vitro* bleb size as a projected area normalized by the total area of the cell. **F:** Cell morphology in pre-chordal-plate progenitor cells during zebrafish gastrulation movements stained for actin (green) and membrane (red). Leading edge cells frequently engage in blebs (arrow). **G:** Cell morphology of the prechordal plate in embryos injected with dnEZR. **H:** Quantification of the projected area of plasma-membrane blebs from control and Ezrin loss-of-function cells. *In-vivo* data provided by Alba Diz.

thinner cortex. Furthermore, the myosin contraction in the back of the bleb is supposed to be stronger, creating a forward directed pressure. This gives rise to a circumferential bleb-wave with several compartments (older blebs) that are separated by a thin, radial actin fiber (see Fig. 6.6). These radial actin fibers shrink when the bleb retracts, which suggests that such fibers assist in re-incorporation of the concentric bleb by a radial contraction and if lost, aberrant bleb growth is observed. By supporting the cortical actin layer with radial spokes, a larger stability might be created.

To understand if blebbing also occurs *in-vivo*, we stained gastrulating zebrafish embryos for membrane and actin and observed their behavior with spinning disk confocal microscopy. Leading edge cells which do not engage in adhesive interactions form different types of protrusions like lamellipodia, filopodia

and also undergo extensive plasma-membrane blebbing (see Fig. 6.5 F).

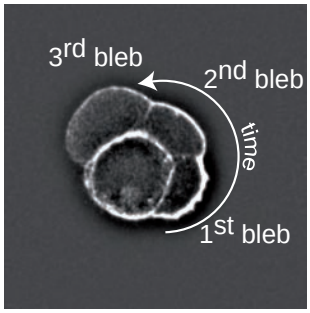

Fig. 6.6 Radial actin fibers

Fluorescently labeled actin localization within a blebbing cell that undergoes circus movement. The oldest bleb has the highest cortical actin density whereas the youngest bleb (3^{rd}) has almost no actin deposition near the cortex.

Having learned that blebbing constitutes a common mode of migration we set out to learn if ERM proteins participate in the process of progenitor cell blebbing. We analyzed loss-of-function by over-expressing a dominant negative form Ezrin (T564A [338]) in the cells which cannot be phosphorylated and therefore is unable to bind filamentous actin [30]. Alternatively, we used cells from embryos injected with a combination of Ezrin and Radixin morpholino [31]. Still, cell membrane decouples from the cortex and is infiltrated with cytosol like in wildtype cells but now leading to significantly larger blebs when single cells were brought into culture (see Fig. 6.5 B, C and Supp. Movie 5 & 6). Importantly, if we inhibit actin polymerization after incubating the cells in 1 µM Latrunculin A (or Cytochalasin D) all filamentous actin structures collapse and we did not observe any cell surface protrusive activity (see Fig. 6.5 D and Supp. Movie 7).

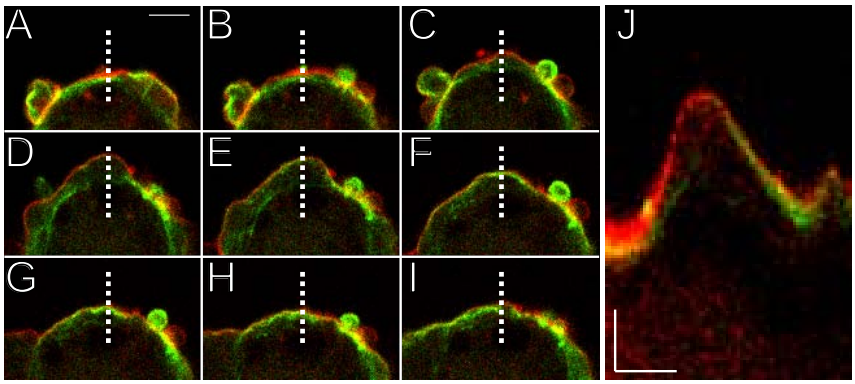

Fig. 6.7 Blebbing and actin polymerization

A-I: Sequential images of a blebbing mesendodermal zebrafish cell. **J:** Kymograph of a bleb taken at the indicated position in (A). Actin in green, membrane in red.

Similar to the *in-vitro* results, plasma-membrane blebs increased *in-vivo* when loss-of-function of Ezrin was tested. In addition to that, cells developed

less filopodia and an increased number of blebs in a given period of time (see Fig. 6.5 G,H).

6.2.3. Cortex mechanics

Plasma-membrane blebs have been proposed to arise by contraction of the cortical acto-myosin belt and a therefore created intracellular pressure [143], leading to plasma-membrane cytoskeleton disruption and blebbing [152]. To evaluate if this increases in blebbing activity and bleb size in *ezrin* T564A mutated or morphant cells are due to a increased hydrostatic pressure, we measured cell cortex tension T_c of progenitor cells using colloidal force microscopy [51, 292]. We could not observe a significant increase in T_c after Ezrin depletion which would be responsible for a higher blebbing activity. The small but insignificant reduction of T_c that we observed is probably due to an increased probability of testing a un-supported bleb and suggests that Ezrin modulates the interaction of the membrane with the cytoskeleton rather than the contractility of the cortical system (see Fig. 6.8). When we treat mesendodermal progenitor cells with Latrunculin A, they become very soft and show a strongly reduced resistance upon deformation. Moreover, AFM force curves deviate substantially from the model and are not linear anymore. Rather than that, these curves show a highly non-linear behavior, resulting from a breakdown of the force-resisting cell-cortex and a loss of cortical tension. At the same time, cells stop any blebbing motility and round-up.

Differences in blebbing activity between control and experimental cell cannot be explained by a difference in intracellular pressure.

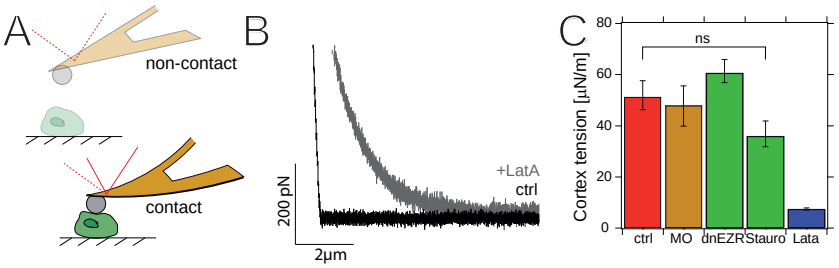

Fig. 6.8 Cortex tension of cells ± Ezrin

A: Schematic representation of the cortex tension experiment. Time between two images: 10 seconds. **B:** Representative curves of an AFM - deformation experiment. Control cells in black and Latrunculin A cells in grey. **C:** Quantification of T_c for mesendodermal cells tested in different condition.

Increased plasma-membrane-blebbing can arise when the hydrostatic pressure within the cells imposed by cortical acto-myosin contraction exceeds the

resistance of the cytosol-embracing actin cortex, leading to cortex rupture [139]. With the use of colloidal force spectroscopy we measured cortex tension of the cells and estimated the intracellular pressure to be ≈5.2±2 Pa according to the Laplace law ($P = R \cdot T$). The value is not significantly different between control and *ezrin* loss-of-function cells. In conclusion, another mechanism is responsible for an increased blebbing behavior in the treated cell types.

6.2.4. Membrane mechanics

A cortical tension is necessary for any blebbing activity [139, 350] and is drastically reduced upon destruction of the cell cortex with Latrunculin A but not sufficient to explain the differences in bleb size we observe in Ezrin loss-of-function cells (see Fig. 6.5 D and Fig. 6.8 C). Alternatively, ERM proteins coordinate cell shape changes by a interaction of the membrane with the cell cortex. To directly proof that Ezrin suppresses and restrict catastrophical bleb growths by coupling the membrane to the cortical actin meshwork, we sought to experimentally asses the mechanics of the plasma-membrane - cortex system by measuring the interaction of the lipid-bilayer with the cytoskeleton.

Extrusion of lipid-membrane nanotubes (tethers) are frequently used to estimate the mechanical properties of the plasma-membrane in living cells [142, 328, 35, 36, 351] (see Fig. 6.9 A,B). We therefore artificially pulled single lipid nanotubes from living zebrafish cells at different velocities from 1 to 50 $\mu m \cdot s^{-1}$ using AFM [51, 351, 434] to measure the static tether force f_0 and the viscous properties of the membrane (for details on the method and model assumption see Sec. 3.2.10). To do so, cantilevers were approached to a cell sitting on a substrate and contact time was adjusted so that only 30-40% of all contacts established a interaction and single tethers were pulled.

The force to extrude a membrane tether is strongly reduced in ERM loss-of-function cells.

As predicted by the physics of membrane tubes, membrane tether extraction shows a constant force plateau after the tether has been extruded (see Fig. 6.9 B). Reason for this is a buffering membrane reservoir which supplies sufficient lipid material to ensure a constant tension upon pulling for several micrometers [416]. The length of each tether is therefore independent on the mechanical properties and only depends on the lifetime of the coupling bonds [415]. As anticipated by Eq. 3.14, the tether force increased non-linearly with faster extrusion velocity for all tested cell types [34] due to a viscous drag of the membrane movement into the tube (see below). When we compared the mean force we found that Ezrin loss-of-function cells have a significantly lower tether force for each extrusion velocity tested. Recent studies suggested

that sequential tether pulls show a history effect and deviate from the first extrusions [410]. Importantly, the tether force was not affected by sequential pulls and tethers extruded first are not different to tethers from subsequent extrusions (see Fig. 6.10).

To specifically deduce equilibrium membrane properties we extrapolated the force to zero pulling velocity [328, 351]. Fitting the data in Fig. 6.9 C to Eq. 3.14 yields the static tether force, f_0 (see Fig. 6.9 D) and the dynamics of extrusion a (see below). Importantly, Ezrin/Radixin loss-of-function cells have a strongly reduced f_0 compared to control cells suggesting a lower apparent membrane tension of the lipid-bilayer (T_{app} according to Eq. 6.3; see Fig. 6.9 D,E and Ref. [141, 34, 328]). T_{app} is the sum of its components, effective tension T_{eff} and (membrane-cytoskeleton) adhesion energy density W_0 which

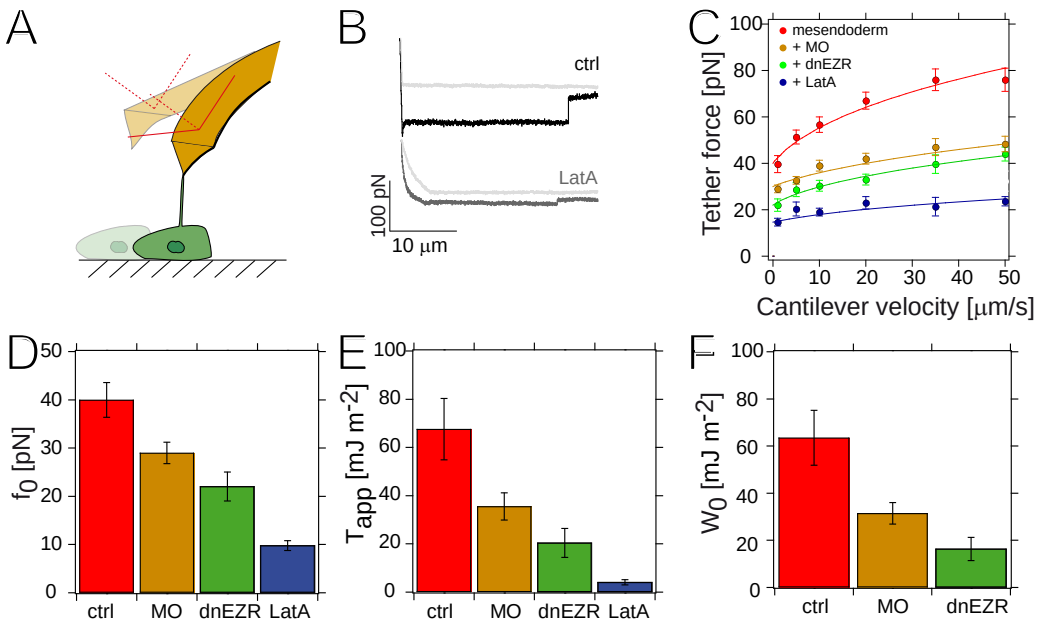

Fig. 6.9 Tether extraction to probe physical membrane properties

A: Schematic drawing of a single cell force spectroscopy experiment probing the mechanics of single membrane nanotubes. A cantilever coated with a sugar-binding protein is brought into contact with a cell sitting on the surface. Upon retraction, eventually a tether is extruded. **B:** Representative force curve taken under different conditions. Black curve was taken using control mesendodermal cell, grey curve represents a measurement with a latA treated cell. Approach curve is shown in light grey. **C:** Tether force as a function of the pulling speed. Data for mesendodermal, dnEZR and latA treated cells is shown and fitted to Eq. 3.14. **D:** Static tether-force estimated from the fit of Eq. 3.14 to the data in F. **E:** Apparent membrane tension for the different experimental as well as control conditions calculated using Eq. 6.3. **F:** Adhesion energy density for control, Ezrin morphant and dnEZR cells.

was previously used to estimate the interaction strength of the membrane with the cytoskeleton [141, 29, 33, 450, 409]. W_0 is a measure for the energy which is released when an unit area of membrane is coupled to the cytoskeleton. Because ERM proteins are supposed to built-up the interaction between the membrane and the cell cortex we set out to determine an approximate calculation W_0 in our experimental cells. To decouple the T_{app} into its components, we measured the force needed to extrude tethers from cells pre-treated with 1 µM Latrunculin A for 10 minutes. Because these cells lack any filamentous actin and do not have a cytoskeleton supported membrane anymore, we measured a restoring force on the cantilever while pulling nanotubes, which is due to in-plane membrane tension T_{eff} [329, 142, 351], which is manyfold lower than the tension of a cytoskeleton supported bilayer [141]. To calculate the adhesion energy density W_0 for the three cell types, we subtracted T_{eff} (as measured for latA treated cell, see Fig. 6.9 E) from T_{app} (see Eq. 6.3). We find that control cells have a significantly higher adhesion energy of the plasma membrane to the cortical cytoskeleton compared with Ezrin morpholino treated cells and cells expressing a dominant negative version of Ezrin. The values we get for membrane tension and adhesion energy density are in good agreement with values previously reported in the literature (see Tab. 6.3). This is the first experimental indication for this interaction provided with an *in-vivo* system [442]. These results suggest, with all the included assumption, that Ezrin molecules cross-link plasma-membrane with the actin cortex and suppresses blebbing activity (see Fig. 6.9 F).

Membrane-csk adhesion energy density is reduced in experimental compared to control cells.

Fig. 6.10 Extrusion force of the first tether

Extrusion force of the first tether that has been extruded from a cell is compared to the tether force of all measurements to show that the presented data is not influenced by the pulling history. The fit parameters for all curves are $a = 7939$ & $f_0 = 28$pN and for the first curves $a = 7636$ & $f_0 = 40$pN.

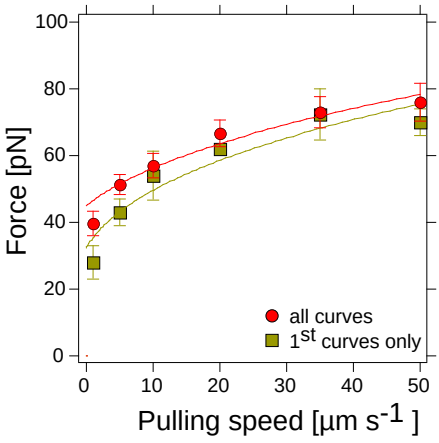

In addition to the role of Ezrin in maintaining the adhesion of the membrane with the cortex, a change in the forces during tether extraction at higher velocities can be due to a change in the cell surface viscosity. To evaluate whether an anchoring of the plasma-membrane influences the diffusion of lipids in the

bilayer and hence the viscosity η, we performed a series of *Fluorescence Recovery After Photobleaching (FRAP)* experiments ([451, 452], see Supp. Movie 8). FRAP is a widely used technique to measure the mobility of a fluorophor in the plane of a bilayer and has been extensively applied to living cells [330, 351] to estimate the fluidity and hence the viscosity of the lipid bilayer. We expressed palmitoyl-anchored GFP in mesendodermal cells with and without Ezrin and observed the rate of recovery after photobleaching in a defined area (see Fig. 6.11 A-E). Whereas we could not observe any changes in the mobility of the fluorophores in the plasma-membrane in dnEZR expressing cells compared to control mesendodermal progenitors, recovery rate was significantly faster in Latrunculin A treated cells (see Fig. 6.11 F). The mobility of molecules in the bilayer is hindered by the friction of the lipids past each other or embedded membrane proteins as well as past the cortical cytoskeleton [329, 452]. These results suggest that the fluidity of the lipid bilayer of mesendodermal cells is unaffected by Ezrin loss-of-function and that the viscosity does not change when the interaction of the bilayer to the cortex is reduced.

Only actin depolymerization influenced the mobility of fluorophores in the membrane as measured by FRAP

Force measurements of single tether extrusion experiments [35] was extensively used to estimate the adhesion energy of the plasma-membrane to the cytoskeleton [33] and a theoretical framework was developed to guide interpretation of physical measurements [328, 34]. A classical model proposed by Hochmuth and Sheetz [328, 36] proposed a linear relation between tether force and extrusion velocity. The slope of the line is is proportional to the viscosity of the lipid bilayer. Our AFM data clearly shows a non-linear $f - v$ relationship (see Fig. 6.9 C). The Hochmuth-model assumes a change in the viscosity of the cell membrane when the slope of the f_t-v relation changes. Our FRAP data does not suggest any changes in cell surface viscosity upon ERM knockdown [330, 327] suggesting that this linear model is not applicable to our data. Fitting the model of Brochard-Wyart [34] to our data yields values for f_0 close to values obtained by others and does not assume changes in the viscosity per se. We conclude that changes in the f_t vs. v dependency between control and Ezrin loss-of-function cells are more likely to be due to an altered coupling of the lipid-bilayer to the cytoskeleton rather than affecting the viscosity of the membrane.

ERM proteins function in the cell to couple the membrane to the actin cortex and control bleb growth by increasing lipid-bilayer to cytoskeleton adhesion energy density (see Fig. 6.5 and Fig. 6.9 F). This can be a consequence of a reduced affinity of each interaction or a lower density of plasma-membrane-

System	W_0	T_{eff}	Technique	Ref.
DOPC	–	$1.4\,\mu N \cdot m^{-1}$	CA	[453]
hMSC	$1.5\,\mu N \cdot m^{-1}$	–	OT	[422]
Renal cells	$19\,\mu N \cdot m^{-1}$	$3\,\mu N \cdot m^{-1}$	OT	[142]
M2 cells	$20\,\mu N \cdot m^{-1}$	$11\,\mu N \cdot m^{-1}$	OT	[142]
RBC	$60\,\mu N \cdot m^{-1}$	–	MPM	[33]
RBC	$60\,\mu N \cdot m^{-1}$	–	MPM	[407]
NGC	$2\,\mu N \cdot m^{-1}$	$1\,\mu N \cdot m^{-1}$	OT	[328]
Neutrophil	$130\,\mu N \cdot m^{-1}$	–	MPM	[33]
Neutrophil	$128\,\mu N \cdot m^{-1\star}$	–	Flow chamber	[413]
Neutrophil	$131\,\mu N \cdot m^{-1\star}$	$9\,\mu N \cdot m^{-1\star}$	MPM	[32]
HL60	$31.22\,\mu N \cdot m^{-1\star}$	$2.3\,\mu N \cdot m^{-1\star}$	MPM	[32]
Fibroblast	$9.1\,\mu N \cdot m^{-1}$	–	OT	[29]
MEC	$90\,\mu N \cdot m^{-1\star}$	$68\,\mu N \cdot m^{-1\star}$	MPM	[421]
bAEC	$24\,\mu N \cdot m^{-1\star}$	$12\,\mu N \cdot m^{-1\star}$	AFM	[351]
ER	-	$13\,\mu N \cdot m^{-1}$	OT	[405]
Golgi	-	$5\,\mu N \cdot m^{-1}$	OT	[405]

Table 6.3 Published values for membrane tensions

Different techniques and cells that have been used to estimate membrane to cytoskeleton adhesion and effective in-plane membrane tension T_{eff}. When no T_{eff} is indicated, the measured W_0 is the sum of adhesion energy and T_{eff}. Abbreviations used in this table: DOPC, 1,2-dioleoyl-sn-glycero-3-phosphocholine; CA, contour analysis; hMSC, human mesenchymal stem cell; OT, optical tweezer; M2 cell, melanoma cell; RBC, red blood cell; NGC, neuronal growth cone; MPM, micropipette manipulation; MEC, microvascular endothelial cells; bAEC, bovine aortic endothelial cells; AFM, atomic force microscopy; ER, endoplasmatic reticulum. Values denoted with a '$\star$' have been calculated from static tether forces according to Eq. 6.2 using κ=2·10^{-19}.

cortex coupling molecules. To judge whether the density and concomitantly the lateral spacing of the binders changes between control and experimental cells, we analyzed the dynamics of extrusion [34]. To do so, we used published parameters for κ and η and resolved Eq. 3.14 for ν. R_c was measured by light microscopy (see Fig. 6.7 F) and R_t was calculated according to $R_t = \frac{2\pi\kappa}{f_0}$ [328] yielding a radius of ≈45 nm, 82 nm and 110 nm for control, ERM depleted and latA treated cells respectively. We find that ERM loss-of-function cells have a dramatically reduced density of binders when compared to control cells (see Fig. 6.12 A). The membrane of control cells interacts on ≈ 600 sites per μm^2

Next to a decrease in W_0, the number of membrane-cytoskeleton cross-linkers is strongly reduced from 600 to $100\,\mu m^{-2}$ in experimental cells.

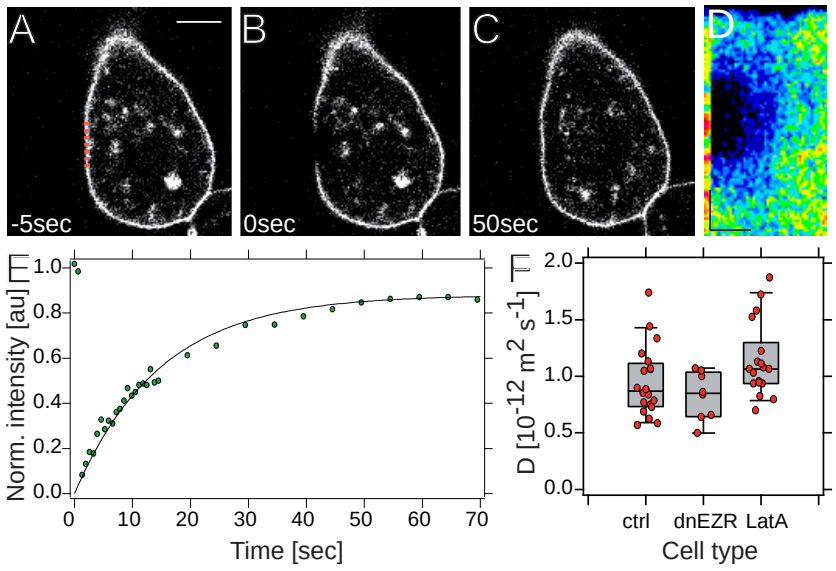

Fig. 6.11 Determination of membrane bilayer fluidity

Fluorescence recovery after photobleaching. **A**-**C:** Sequential images of a typical frap experiment before bleaching (A), directly after (B) and after complete recovery (C). Cells adherent to a substrate were used for determination of the diffusion coefficient. Adhesion reduces blebbing activity and therefore suppresses active recovery after bleaching. **D:** Kymograph of the bleached region. Recovery occurs entirely from the rims of the bleached area. **E:** Exemplarily recovery curve for a mesendodermal cell stained with membrane bound GFP. **F:** Diffusion coefficient as measured by FRAP for mesendodermal control cells, cells from embryos expressing dnEZR and Latrunculin A treated cells.

---

with the cytoskeleton in contrast to Ezrin depleted expressing cells which interact on 100 sites per square micrometer. This value suggests a mesh size for the cortical cytoskeleton of around 40 nm according to $\zeta = \frac{1}{\sqrt{\nu}}$ for control cell (see Fig. 6.12 B). Theoretical calculations have found that the critical mesh-size to impede bleb-nucleation is around 30 nm. Scanning electron micrographic studies of blebbing cells have found a value for the cortical mesh size close to 30 nm [350]. Our value found by tether extraction is surprisingly close to this value but sufficiently higher to explain a probabilistic nucleation frequency for control cells. It also suggests why ERM depleted cells bleb more than control cell, because the average distance between the membrane-actin cortex connectors increases threefold which is not sufficient to couple the bilayer continuously to the cortex.

Nevertheless it is surprising that ≈70 % of the membrane-cytoskeleton cross-linkers are Ezrin molecules, although there are several other proteins in the cell membrane which bind to the cortical actin cytoskeleton (see Fig.

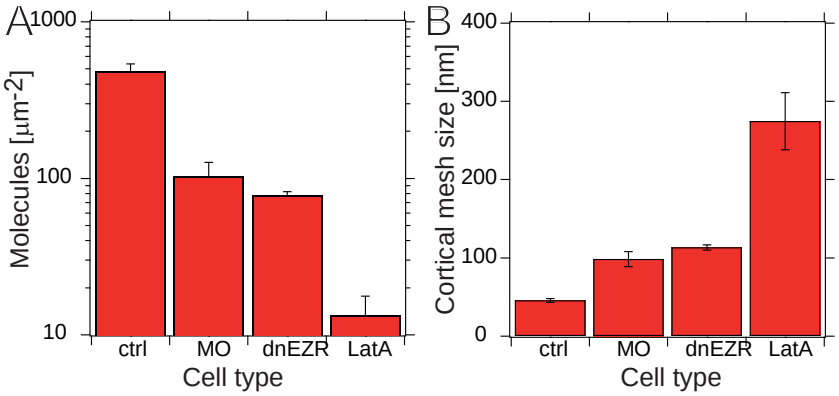

Fig. 6.12 Discrete membrane-cortex interactions

A: Density of membrane cortex interaction molecules in mesendodermal cells treated with Ezrin morpholino, dnEZR or latA. **B:** Average separation of the cross-linkers as determined from the density according to $\zeta = \frac{1}{\sqrt{\nu}}$.

6.12 A). Among them, E-cadherin has been shown to substantially contribute to the linkage [410] as well as other cross-linking proteins such as filamin [350], myosin [454], MARCKS [141] or other ERM family members [144].

Recent studies suggested that the density of available PIP_2 molecules in a cell is around $10.000\,\mu m^{-1}$ [36]. This is sufficiently high to seal the entire inner leaflet, providing a resistance against the outward hydrostatic pressure given that sufficiently PIP_2 molecules are occupied by Ezrin linkers ensuring a continuous adhesion of the membrane to the cytoskeleton. We estimate a density of cross-linking molecules of ca 600 attachments per square micrometer, which is in good agreement for the density of membrane proteins in the plasma-membrane. Ezrin is known to bind weak and reversible to the membrane and this reversibility seems to be necessary for the rapid dynamic processes occurring at the membrane interface [36]. Intuitively, a drop in the number of cross-linking molecules has dramatic consequences on the adhesion energy density of the membrane and the cytoskeleton. A drop in the number of ERM molecules has the similar effect as reducing the number of PIP_2 molecules, the central ligand for ERMs on the membrane [455]. Therefore, if the adhesion of the membrane to the cortex is discontinuous, blebbing might occur. How this connection is regulated by external cues and how blebbing can be canalized for efficient migration of the cells is still under debate [149], but an excess of PIP_2 molecules over cytoskeleton linker proteins such as Ezrin ensures a dynamic regulation of the attachment.

A question remains as to the importance of bilayer-cytoskeleton interactions

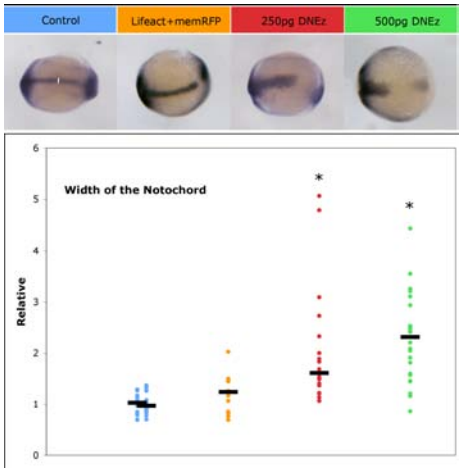

Fig. 6.13 Morphogenesis of ERM depleted embryos

In-situ staining of *goosecoid* mRNA expression in wildtype and ERM depleted embryos as an indicator for mesendodermal germ layer progenitor migration. The upper panel shows pictures of representative embryos fixed and stained at the end of gastrulation. Lower graph shows the quantification of the notochord width. Experiments done by Alba Diz.

specifically for zebrafish germ layer development. Nodal induced phosphorylation of Ezrin2 has a great effect in regulating individual cell shape changes by a regulation of plasma-membrane to cortex adhesion, but we were not aware of the consequences for germ layer morphogenesis. Recent studies suggested that ERM proteins are involved during migration of tissue cells and cancer [456]. To specifically address the morphogenetic role of Ezrin function, we observed the migratory behavior of axial hypoblast cells during the first hours of zebrafish gastrulation. Using the length of the notochord as a read-out for efficient convergent extension, we can show that the ERM loss-of-function cells have a defect in migration. Injection of Ezrin2 morpholinos or dnEZR into wildtype embryos reduced significantly the length of the notochord – a derivative of mesendodermal structures. Taken together, these data suggest that ERM proteins have a crucial role in during zebrafish germ layer migration.

Generally, cells are thought to migrate using actin polymerization dependent lammellipodia formation [393] on two dimensional flat substrates [457]. But what is the functional importance of blebbing for migrating cells in three dimensional environments? Because the cortex is under isometric contraction which pressurizes the cytosol [142, 143] regulated decoupling of the membrane from the cytoskeleton in direction of designated migration could represent a fairly easy and conservative mechanism to translocate. Similar to the classical ratchet model during 2D migration [392], a three step cycle can explain blebbing type motility. First, cells are aligned and guided by an extracellular signal gradient whereas the membrane decouples from the cytoskeleton where the signaling molecule is the largest. For *Dictyostelium* cells it has been shown that they can perceive small difference in the concentration of cAMP between the leading and the trailing edge. After decoupling the acto-myosin powered

cytoplasm flows into the bleb, in direction of presumptive migration. The trailing edge of the cell, also contracting, is drawn afterwards, while a new actin cortex is assembled in the new bleb. This new bleb has the thinnest actin cortex and is the weakest boundary (see Fig. 6.6) working against the intracellular pressure. Therefore the probability of decoupling or cortex breakage [139] in this part is higher than in the trailing edge, which could initiate a new cycle (bleb within a bleb). We propose therefore, once blebbing was initiated by an extracellular signaling gradient, blebbing constitutes a self-propelled motility mechanism.

Whether there is a signal gradient performing the proposed function is not known yet but several candidates have been proposed. Among one of them SDF-1 has been shown to induce directed blebbing in germ cells during zebrafish [130] and mouse [458] development. During zebrafish gastrulation, SDF-1 was shown to guide cells of the mesendoderm [10, 459] by modulating Integrin adhesive function. Future studies have to address the exact function of this signal within the cell and whether SDF1 acts independently to regulating cell-cell adhesion.

	$1\,\mu m \cdot s^{-1}$		$5\,\mu m \cdot s^{-1}$		$10\,\mu m \cdot s^{-1}$	
cell type	average	number (cells)	average	number (cells)	average	number (cells)
mesendo	39.8pN	89(38)	51.2pN	101(40)	56.7pN	137(38)
+dnEZR	22pN	38(22)	28.8pN	50(26)	30.3pN	70(30)
+Ezrin MO	29.1pN	77(37)	32.8pN	112(37)	39pN	130(37)
+latA	14.6pN	58(28)	20.5pN	72(29)	19pN	81(34)
+dnEZR+latA	12pN	28(13)	16.6pN	29(15)	19.3pN	31(15)
+caEZR	30pN	43(25)	39pN	61(27)	43pN	64(36)
+U73122	82pN	17(6)	89pN	22(6)	94pN	18(9)

	$20\,\mu m \cdot s^{-1}$		$35\,\mu m \cdot s^{-1}$		$50\,\mu m \cdot s^{-1}$	
cell type	average	number (cells)	average	number (cells)	average	number (cells)
mesendo	67pN	116(39)	76pN	26(13)	76pN	63(25)
+dnEZR	33pN	50(26)	39.6pN	14(6)	44pN	66(27)
+Ezrin MO	42pN	142(40)	47pN	40(16)	48.5pN	55(20)
+latA	22.9pN	71(24)	21.4pN	24(12)	23.7pN	47(20)
+dnEZR+latA	23pN	28(12)	28pN	21(10)	32.5pN	15(10)
+caEZR	46pN	77(33)			65pN	87(43)
+U73122	95pN	22(7)			151pN	34(8)

Table 6.4 Number of measurement and average tether forces for cells used in this chapter

7. Extrusion of single membrane nanotubes to determine receptor ligand kinetics

7.1. Introduction

Cell adhesion molecules have to integrate cells into tissues and are subjected to external forces. Each bond has an equilibrium lifetime.

One of the major functions of cell adhesion molecules is to withstand external forces. How do such forces arise? A cell in a tissue can migrate and generate a traction-force using intracellular acto-myosin contractility to translate itself forward. In another scenario, a cell is associated within an epithelium, which by nature experiences high stresses due to environmental factors. There are for example deformations that stretch or bend the tissue. In an epithelium, the stresses are shared amongst the individual cells and the forces transmitted from cell to cell by the connecting adhesion molecules and their intracellular anchorages. Latest since the work of Bell [460] it is known that a force alters the kinetics of a bi-molecular interaction. The interaction of two molecular species of specific receptor ligand bond is expected to follow a simple relation:

$$A + B \rightleftarrows AB \tag{Eq. 7.1}$$

with a forward reaction rate k_{on} and a reverse reaction rate k_{off}. Therefore, the concentration of product AB evolves over time as a function of initial concentrations of the educt and the forward and reverse reaction rates:

$$\frac{d[AB]}{dt} = k_{on} \cdot [A] \cdot [B] - k_{off} \cdot [AB] \tag{Eq. 7.2}$$

The product AB is separated by the educts A and B by an energy barrier. Without an external force, little time is sufficient that thermal energy dissociates the bond AB. Application of an external force accelerates the unbinding

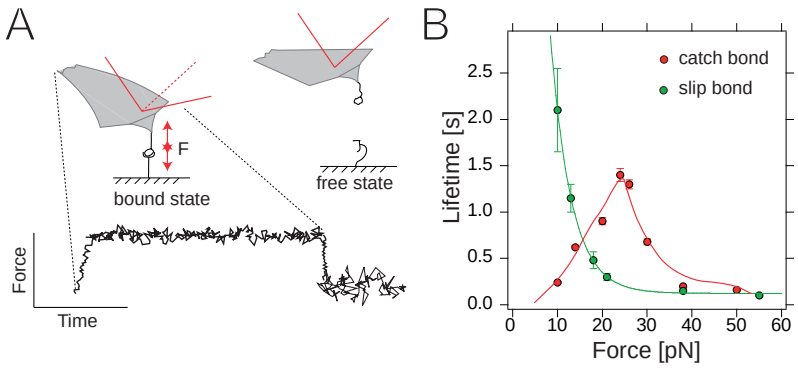

Fig. 7.1 Measurement of force-induced receptor-ligand kinetics

A: Principle of the technique. An receptor-ligand interaction is tensed with a given force imposed by an AFM cantilever. The time is recorded until the interaction breaks, which can be seen as a sudden force drop in the force-time curve. **B:** Increasing forces concomitantly lead to a decrease in lifetime of a specific receptor-ligand interaction for a slip bond (green curve) whereas a biphasic behavior is observed with a catch bond (red curve). Data adapted from [263].

of receptor ligand pair by lowering the activation energy of the particular interaction [461]. Now, less thermal energy is sufficient to cause unbinding which is a stochastic process. For single receptor-ligand interaction, the probability of bond survival $P(t)$ decreases exponentially with time due to the stochastic nature of the thermal agitations*:

$$P(t) = e^{-\lambda \cdot t} \qquad \text{(Eq. 7.3)}$$

The off-rate is reciprocal to the lifetime λ of the bond. If cells now interact by a single bond only, they would fall apart after a lifetime inherent to the receptor ligand system. Fortunately, cells adhere with more than one bond to each other and the probability that many bonds fail at the same time is very low. If many bonds connect two cells, a larger force is required to separate the cells on a reasonable time scale, because all bonds need to traverse the energy barrier for unbinding. It is very unlikely that under equilibrium conditions all bonds traverse the energy barrier at the same time so that two cells do not fall apart spontaneously.

Several theories have emerged which describe receptor ligand kinetics in the aspect of cell adhesion where a force acts on the system [461, 460, 462]. A classical and still widely used model it the one developed by Bell [460]. Inspired

*It is totally by chance when a next wave of thermal energy is sufficient to induce crossing of the potential barrier in a receptor-ligand energy landscape.

by fracture theories of solid materials [463], Kramers theory of a diffusion over a potential barrier [464] and Arrhenius theory for activation energies of chemical reactions, Bell elaborated a theoretical framework to account for receptor mediated cell adhesion. A keypoint in his model was the emphasis that the rate of bond dissociation was dependent on the applied force:

$$k_{off}(f) = k_{off}^{0} \exp\left(\frac{x_u \cdot f}{k_B \cdot T}\right) \qquad \text{(Eq. 7.4)}$$

The lifetime of a bond is dependent on the force acting on it. The lifetime can increase (catch bond) or decrease (slip bond) with higher forces.

with f as the distractive force, $k_B \cdot T$ is the thermal energy term and x_u is the distance of bound and un-bound state of the receptor-ligand pair. As one can see, the k_{off} increases exponentially with the applied force and leads to decrease in lifetime of the complex (see also Fig. 7.1). A variation of the Bell model is a theory developed by Dembo and coworkers [465, 466]. In their work, they treated receptor-ligand complexes as linear springs whose k_{off} a function of the transition state spring constant. As hypothesized in their theory, there is no thermodynamic need implying that a force increases the off-rate of a molecular complex. With this statement, the concept of a so-called catch bond was introduced. A catch-bond is characterized by the fact that its lifetime is prolonged by an applied force in contrast to the ordinary slip bond, whose lifetime decreases according to Eq. 7.4. This idea is interesting and although counterintuitive was proven at various examples already. First direct evidence came lifetime measurements on isolated adhesion molecules P-selectin and its ligand (P-selectin-glycoprotein-ligand, PSGL-1, [263, 230]). In this type of experiments the AFM cantilever is coated with either the cognate ligand or with a specific antibody against the receptor. The surface was coated with the receptor and both are brought into contact. After that the cantilever was retracted a prescribed distance to stress the bonds with a constant tensile force. The time until the interaction failed was recorded and quantified for different loading forces. Loading this interaction with forces up to 20 pN surprisingly increased the lifetime of the receptor-ligand bond (see Fig. 7.1). Above a certain threshold, the bond switches into a 'canonical' slip bond pathway where the lifetime decreases exponentially with force. Interestingly, when a receptor dimer was probed, the lifetime and the force increased twofold, suggesting that each molecule shared the load imposed by the cantilever. In contrast to that, when the interaction of the antibody with P-selectin was probed, a monotonous decrease in lifetime for all tested forces was observed according to Eq. 7.4. Other examples of receptor-ligand systems as a catch bonds involve

actin-myosin [467], van-Willebrand factor [468] and $\alpha_5\beta_1$ Integrin-fibronectin interactions [469].

The force-lifetime relation ship of Con A - mannose bond will be tested using nanotubes extruded from living cells.

The subject of this chapter is to analyze the force-lifetime behavior of a well-caharcterized ligand-receptor interacrion under a constant force. Thereby it is of interest, whether it is possible to exploit the physics of membrane nanotubes as a constant force actuator and the lifetime of an particular interaction could be measured within a living cell.

7.2. Results

Single-molecule force spectroscopy (SMFS) approaches can probe these adhesive forces at different loading rates (applied force versus time) to reveal insights into the kinetics of isolated receptor-ligand pairs [470]. Although such *in-vitro* measurements provide insights into the behavior of receptor-ligand interactions, they have limitations. For example, ligands and receptors must be purified, which means removing them from their cellular environment, so one cannot be certain of their functional state. This is of particular concern for cell adhesion molecules (CAMs) which *in-vivo* are functionally modulated by the cell [171]. Therefore such biomolecular interaction need to be studied in the cellular context.

The relation between unbinding rate and force for various CAMs has been studied by different single-molecule methods including atomic force microscopy (AFM), laser traps, biological membrane force probes and flow assays [471, 244, 472, 473]. Here we implement an AFM to characterize the unbinding rate of a molecular interaction at physiological relevant conditions. This novel AFM method uses membrane nanotubes formed by the living cell (also referred to as tethers) to excerpt a constant force on a specific biological bond. The benefit of using a cell is that it allows the strength and lifetime of fully functional receptor-ligand interactions to be studied at forces that are determined by plasma membrane properties. To validate this method we set out to study the binding of Concanavalin A (Con A) to N-linked oligosaccharides attached to extracellular domains of membrane receptor proteins [474].

To measure specific binding forces in the piconewton (pN) range, AFM cantilevers were functionalized with Con A. In repeated cycles, the AFM cantilever was lowered onto single mesendoderm zebrafish embryo cells at a contact force of 100 pN for short contact times (< 0.2 s, see Fig. 7.2 A, B). Upon separating the Con A functionalized AFM stylus, adhesive interactions with the cell

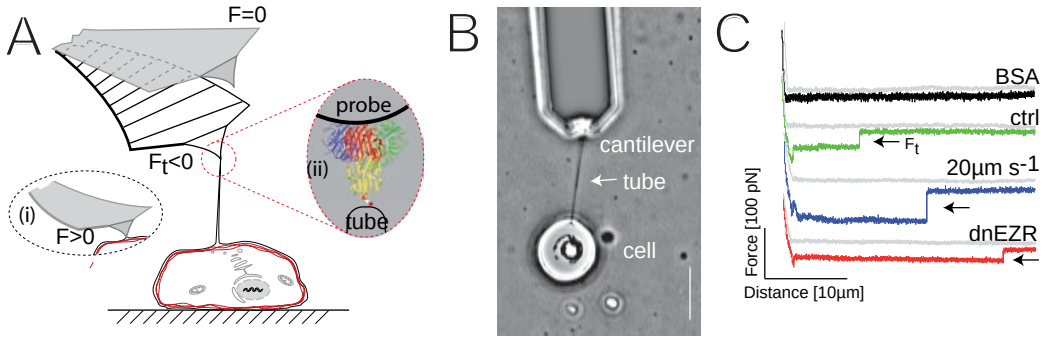

Fig. 7.2 Tether-force measurements using AFM

A: Schematics of the experimental principle. An AFM cantilever is coated with a sugar-binding protein and brought into contact with a cell resting on a surface. Subsequent retraction will eventually extrude a lipid tube from the cell. **B:** Optical micrograph of an AFM cantilever and a cell connected with a membrane tether. **C:** Force-distance curves acquired using a BSA-coated cantilever (no bond failure is observed; black), and Con A coated cantilevers at retraction velocities of $10\,\mu\mathrm{m}\cdot\mathrm{s}^{-1}$ (green) and $20\,\mu\mathrm{m}\cdot\mathrm{s}^{-1}$ (blue). A force curve (red) obtained with a cell expressing dominant negative version of Ezrin (dnEzr) at a retraction speed of $10\,\mu\mathrm{m}\cdot\mathrm{s}^{-1}$ is shown. The rupture of the bond between Con A and its ligand results in a force step (indicated by arrows) equal to the nanotube extraction force (f_t). Approach traces are shown in light gray. The bond lifetime equals the tether length at bond rupture divided by the velocity of cantilever retraction.

surface will bend the cantilever. As soon as these interactions ruptures the cantilever deflection relaxes to zero force. This force drop is seen as a step in the force-distance curve (see Fig. 7.2 C). The contact conditions were adjusted such that connective bonds formed ≈40% of the time.

To demonstrate binding specificity, the interaction between Con A and N-linked oligosaccharides was inhibited. Both the substitution of Con A with bovine serum albumin (BSA) on the cantilever and the incubation of Con A coated cantilevers in heat inactivated fetal calf serum (HiFCS) nearly abolished binding between cantilever and cell (see Fig. 7.4). Cantilever incubation with 4-Nitrophenyl α-D-mannopyranoside (NPM), a low affinity competitive inhibitor of Con A binding, also reduced the binding rate. We conclude that $\geqslant$80% of the interactions are between Con A and cell surface exposed oligosaccharides (see Fig. 7.4). By retracting the cantilever an outward force was applied to the bonds formed between the Con A and the cell. Either the bond breaks or the protein to which the oligosaccharide is covalently attached is pulled away from the cell surface at the tip of a membrane nanotube (see Fig. 7.2 A-C). Once the membrane nanotube is initiated, the force required to pull the nanotube stays essentially constant. Upon the unbinding of Con A the force on the

Pulling membrane nanotubes with higher speeds increased the force on the specific interaction.

cantilever is instantly reduced. The four representative force-distance curves in Fig. 7.2 C show clearly recognizable constant force plateaus. The physical model of lipid membranes predicts this force versus nanotube length behavior. The force required to pull the nanotube, f_t , is given by Eq. 3.14, which implies that without changes in plasma membrane properties, the force changes only with nanotube extension velocity v. Thus, adjusting the extension velocities of the membrane nanotube allowed tuning the constant force applied to the receptor-ligand bond (see Fig. 7.2). To characterize interaction between Con A and N-linked oligosaccharides, the length at the time of unbinding and the pulling force were determined for nanotubes longer than 0.25 µm. At a given nanotube extension velocity the forces clamped by the membrane were normally distributed (see Fig. 7.3).

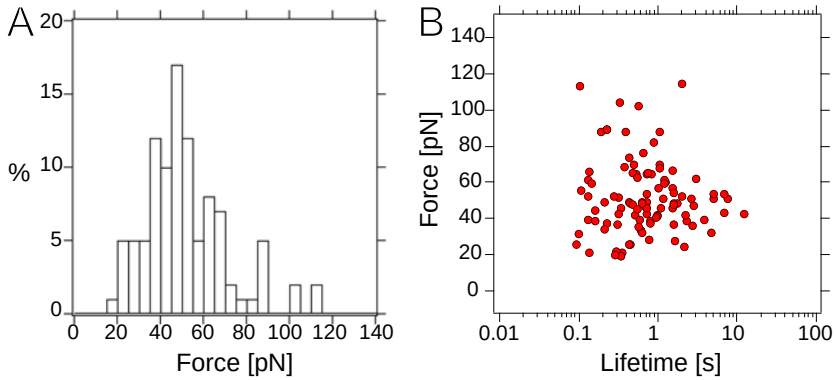

Fig. 7.3 Probability distributions of tether forces and lifetimes

A: Distribution of tether forces for $10\,\mu m \cdot s^{-1}$ extrusion velocity. **B:** Plot of the lifetime versus the force on a Con A - mannose bond at a pulling velocity of $10\,\mu m \cdot s^{-1}$.

As expected, the restoring force was independent of the length of the membrane nanotube (see Fig. 7.2 C). Therefore, it can be concluded that the length of a nanotube divided by the cantilever speed represents the lifetime of the anchoring bond at a given applied force. Figure 7.5 shows the lifetimes of the Con A−N-linked oligosaccharide bond measured for different extension velocities of membrane nanotubes. In agreement with Eq. 3.14, different pulling velocities of membrane nanotubes adjusted different constant forces that were applied to the receptor-ligand bond. Variation of nanotube extension velocities from 1 to $20\,\mu m \cdot s^{-1}$ allowed force-clamp experiments ranging from 15 to 75 pN (see Fig. 7.5). In addition to normal mesendoderm cells, cells expressing a dominant negative form of ezrin (dnEzr) were used [338]. The disruption of Ezrin activity likely decreased membrane-cortex adhesion and, thereby, lowered the

The force-lifetime relation of the Con A - mannose interaction follows a simple exponential according to the Bell model.

apparent membrane tension, T_{app} (see Eq. 6.2 and Ref. [35]). As predicted, the expression of dn*Ezr* reduced the mean nanotube forces for all extension velocities (see Fig. 6.9 C). Indicative of the stochastic unbinding of a common ligand-receptor interaction, simple exponential decays characterized the nanotube lifetime distribution at all pulling forces (see Fig. 7.5 A,B) according to Eq. 7.3.

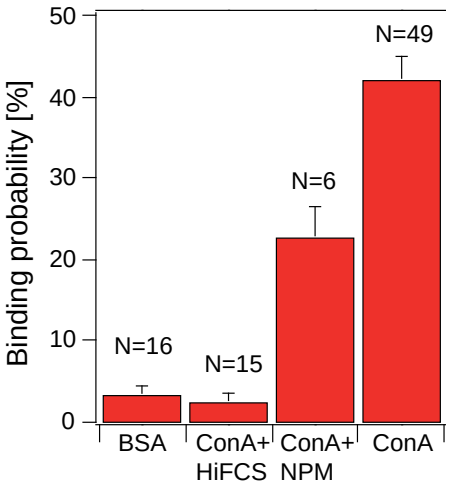

Fig. 7.4 Specificity of tether-extrusion

Cantilevers incubated with BSA as well as Con A-coated cantilever incubated in heat-inactivated fetal calf serum show a strongly reduced binding probability compared with control cells. Con A-coated cantilevers with a mannose-analog show reduced but not complete blocking of the interactions.

The calculated Con A unbinding (or decay) rate increased with the restoring force of the nanotube (see Fig. 7.5 C). In the assayed range of forces clamped by the membrane nanotubes of living cells the Bell model with a k^0_{off} of $0.053\,\mathrm{s}^{-1}$ and an x_u of 2.9 Ådescribes the observed rates well. The bond between Con A and single mannose residues has been examined using dynamic force spectroscopy and was found to have a considerably higher k^0_{off} of $0.17\,\mathrm{s}^{-1}$ and an x_u of 2.7 Å[475]. However, because N-linked oligosaccharides of the cell surface bind Con A with a much higher ($\approx$50$\times$) affinity (k_a) than single mannose residues [476], a significantly higher dissociation rate (k_{off}) is expected in the latter case.

Averaging the data not only reduces noise but also removes data points available for analysis. The importance of single molecule experiments is, that the properties of *single* receptor-ligand interaction can be investigated. This advantage is sometimes discarded when the data are averaged and an mean unbinding force or lifetime is presented. Rather than that, information acquired from each unbinding event carries the same if not more information about the particular interaction of interest. Rather than fitting the mean lifetimes and the median forces to the Bell model (see Eq. 7.4), each individual unbinding event can be considered. In Figure 7.6 A each data point acquired from tether extrusion experiments is plotted. We observed an intense scatter of the data,

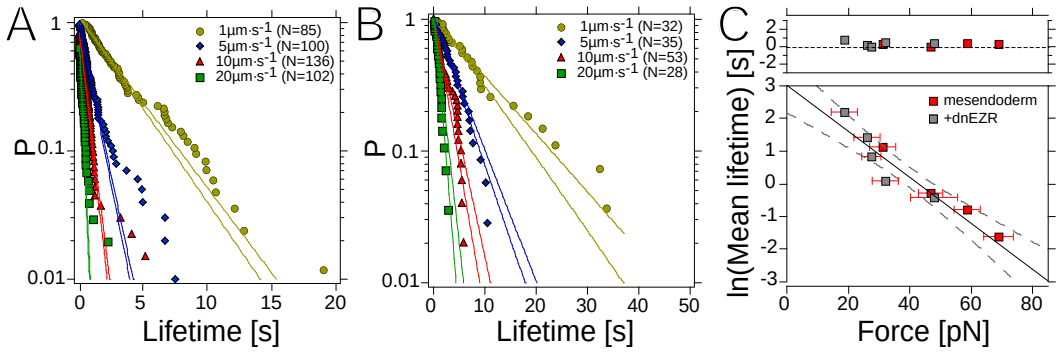

Fig. 7.5 Receptor-ligand lifetime

A: Lifetimes of Con A−N-linked oligosaccharide bonds plotted for different pulling velocities. P is the number of nanotubes having a lifetime greater than or equal to the lifetime of the data point, divided by the total number of nanotubes analyzed for the condition (n). The mean bond lifetime, λ, was fitted at each velocity by using Eq. 7.3. Paired lines represent the 99% confidence interval of the fit. Deviations at very long lifetimes may result from nanotubes bound by more than one interaction. N is the number of nanotubes analyzed. **B:** Data from dn*Ezr* cells represented in the same manner as in A. **C:** Mean lifetimes of the Con A-oligosaccharide bond plotted with respect to the median tether force. Data points stem from A and B. The solid line represents the fit calculated by using the Bell model (see Eq. 7.4), dashed lines represent the 99% confidence interval of the fit. For fitting, data points were weighted by the inverse of the error in the lifetime. Horizontal bars denote standard error of the median force while the errors of the lifetimes were smaller than the data points. The residuals of the fit are shown in the upper section.

---

but we will show that this is intrinsic to the stochastic nature of single molecule unbinding events and not attributed to any experimental errors. We fitted the Bell model to the raw data in Fig. 7.6 A and used the values for k^0_{off} and x_u to simulate unbinding lifetimes and forces. We find that the large scatter of the AFM data comes from the probabilistic nature of such unbinding events as indicated by Monte Carlos simulations (see Fig. 7.6 B) of unbinding events which look similar compared to the 'real' data. The parameters for unbinding rate and potential width are k^0_{off}=0.64 s^{-1} and x_u=1.4 Å. These are in the same range compared with the unbinding rate and potential width acquired with the averaged data. This is important to note and shows that the averaging does not bias the data acquired from single molecule experiments.

There are other methods that use membranes to measure the lifetime of a molecular interaction including biological membrane force probes and flow assays. However, the atomic force microscope enables the most accurate spatial control and the least complicated means to measure the nanotube extraction force. Furthermore, our use of nanotubes extracted from living cells has several

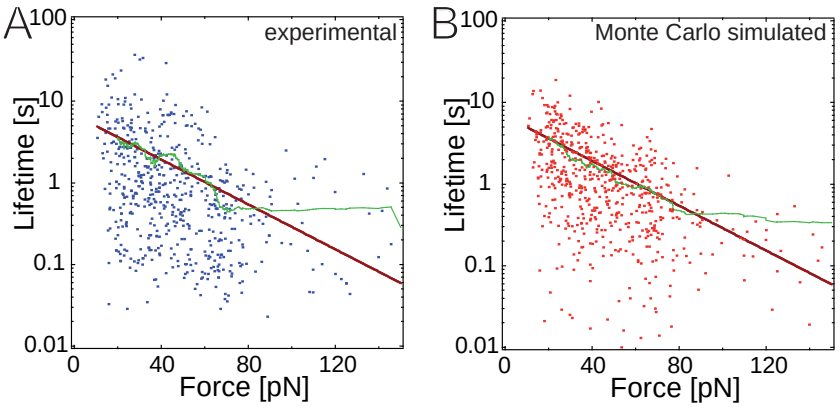

Fig. 7.6 Lifetimes and forces for individual tethers

A: Lifetimes vs. force plot of all individual tether data. The large scatter is due to the probabilistic unbinding of the receptor from its ligand. **B:** Monte Carlo Simulation of Con A mannose unbinding lifetimes using values for k_{off} and x_u determined from the fit of Eq. 7.4 to the data in (A). Note that the scatter appears, although the simulation was computed without noise and the data follow strictly the Bell model. The solid green line represents an average of the data points. Simulation performed by Jonne Helenius.

---

advantages. Unlike dynamic force spectroscopy measurements that use artificially high forces to accelerate unbinding, the presented method examines unbinding at forces that are innate to cells. Moreover, the binding of *in-situ* cell surface proteins that are neither manipulated, modified, purified nor artificially immobilized are studied. In the future, this simple assay should allow characterizing the functional regulation of CAMs by the cell or the cellular environment. The method is not limited to the study of CAMs because normally soluble signaling molecules, i.e. growth factors, can be bound to AFM cantilever to probe their interaction kinetics with receptors on live cells. In summary, the presented method is an easy approach to study fully native receptor-ligand interactions at the single molecule level.

8. Final observations

A lot of understanding about cell structure and cell physiology has come from experiments with tissue culture cells. Tissue culture cells, however, are removed from their natural environment and, therefore, represent only a snapshot of a given cellular process [477]. Developmental biologists will doubt how reliable these findings are for the 'real' *in-vivo* situation. With these snap-shots, however, cell biology elevated classical developmental biology into a new era. Morphogenesis explained by molecules. Developmental defects, long characterized by the appearance and behavior of an animal, can now be described by the lack or de-regulation of specific molecules. Especially, the origin of positional information within an developing tissue has attracted a lot of interest. Spatiotemporal gradients of secreted signaling molecules were shown to switch gene expression patterns and precisely define tissue boundaries [478, 479]. But this is not enough to explain morphogenesis!

Phenotypes into forces, mutants into numbers. Quantitative developmental biology provides further understanding into the complex self-organizing phenomena underlying developmental morphogenesis [135]. Physical measurements on various cell properties are now possible after the emergence of various techniques to study different cell properties. First, diffusion of a protein within an embryo can easily be studied using FCS, FRAP or SPT to estimate cellular environment of the molecule. The formation of extracellular signaling gradients were deciphered and positional information decoded with the help of quantitative mobility measurements [135]. Seconds, electrophysiology has enabled researchers to correlate motor neuron activity with neuronal development in zebrafish larvae [480]. And at last, forces on different levels can easily be measured with a diverse set of techniques: optical tweezers to characterize single molecules [481], atomic force microscopy to characterize single cells [267] and parallel plate compression to characterize tissue or whole embryos [7].

25 years after the advent of *Atomic Force Microscopy*, numerous applications that measure cellular forces have been communicated. Among them,

Single Cell Force Spectroscopy is an extremely powerful mode and can be used to measure single molecule unbinding kinetics on the surface of living cells, cell mechanical and acto-myosin contractile properties and cell adhesion strength to various kind of substrates, cells and ligand molecules. The AFM set-up is commercially available and a lot was done to simplify technical difficulties [347].

In this thesis, four different approaches of AFM were applied. In Chapter 4 single cell elastography was implemented to measure acto-myosin dependent cortex tension and the adhesion force of a cell doublet as a function of the contact time. It could be shown that, in contrast to a prevalent view in the field, adhesion alone is not sufficient to explain cell re-arrangements in cell aggregation experiments. Importantly, this is not restricted to zebrafish germ layer morphogenesis and these results were confirmed with cell sorting experiments using mouse germ layer progenitors [294].

In Chapter 5, cell adhesion forces were shown to correlate with the amount of antisense oligonucleotide injection and hence the expression of E-cadherin molecules on the cell surface of mesendodermal progenitors. Mesendodermal control wildtype as well as cells with reduced expression of E-cadherin were transplanted into gastrulating zebrafish embryos and the directionality of migration scaled linearly with the adhesion force. Whereas wildtype cells were able to 'join-the-crowd' of endogenous mesendodermal cells, *e-cadherin* loss-of-function cells were not able to move as a collective but moved more or less independent of each other. This is the first experimental verification of a recent hypothesis that mesodermal cells during gastrulation undergo collective cell migration [382].

Single Cell Force Spectroscopy is also capable to measure membrane mechanical properties such as bilayer-cytoskeleton interaction energies. In Chapter 6, SCFS was applied for the first time to measure the membrane tension and adhesion energy by extruding single lipid-nanotubes out of gastrulating cells. The adhesion energy was dramatically reduced when cells expressed a dominant negative version of Ezrin2, a protein previously shown to interact simultaneously with lipids and membranes [442]. The reduction in membrane tension lead to a perturbed cell behavior and, concomitantly, to a disordered embryonic development.

Finally, in Chapter 7, SCFS was used to determine the lifetime of single receptor ligand bonds. Single lipid nanotubes were extruded at different forces by the means of Con A – mannoside interactions. The force was adjusted

by pulling the tube as defined speeds and the lifetime of each nanotube was measured. It could be shown that the interaction time decreases exponentially as predicted by the Bell model.

Taken together, cell mechanical properties have a great influence on cell behavior as previously recognized. This thesis extend the findings of previous studies and suggest that adhesion and mechanics in different scales — cell compartments, whole cells and embryos — is critical for the correct development of multicellular animals. Further studies have to elucidate how signaling activity affects mechanical properties in particular and how the mechanical properties — membrane tension, cortex tension and adhesion — affect each other.

At the very end it remains thrilling, whether quantitative developmental biology is the holy grail for elucidating the common principles of organismal development.

Acknowledgments

This work of the thesis would not have been possible without the help of many people. At first I would like to thank my supervisors Prof. Daniel J. Müller and Prof. Dr. Carl-Philipp Heisenberg and all their lab members in general for the excellent scientific environment and continuous help with scientific problems. Carl-Philipp is acknowledged for his help on data interpretation all over the different subjects and supporting me during the last four years. Of course also lab-members that are not members of the lab anymore are acknowledged ... how can I forget about Clemens and Alexej!

Many thanks go as well to Boehringer Ingelheim Fonds for giving me the opportunity to work financially independent and to give support during my PhD work. Thanks to you, I could gain a lot of experience on many different international conferences.

Next I thank Yohanna Arboleda Estudillo for excellent co-work (not only transplantations, transplantations and transplantations) and spanish lessons. Without her help, this thesis would not been possible in this dimension.

Hearty thanks go to Pierre-Henri Puech (PHP), this time not for making coffee, but for advices in everyday life situation and of course suggestions on specific working hypothesis. I hope we can go another time climbing in the Calanque de Sugiton. Un paradis de escalade trés jolie. I am still lacking some orchids that are growing in the fields close by Lumini :) btw, the code for the iro is `\PHPlumedhead`

Similarly, I want to convey many thanks to Alba Diz Muñoz an Ewa Paluch

for collaboration with the blebbing cells and brilliant imaging of zebrafish prechordal plate progenitor cell migration. I also want to thank Jos Käfer and François Graner for their excellent collaboration and computer simulations on tissue self assembly.

Isabel Richter is gratefully acknowledged for her help on western blotting, agarose gel preparations, lab handling, volley ball organization, shaping wonderful lab-retreats in the Czech Republic, preventing all of us eating too much sweets, elevating the mood of the lab with her refreshing spirit. The same is actually true for Anna (Annaliese) Taubenberger, although she did not prevent me from eating chocolate, bananas, pickles, crisps, nuts ... what more? Apart of that, thanks for holidays in Italy, Manchester, Marseille, Prebischtor and Australia! Also more thanks to her for serious help on reading and giving critical comments and suggestions which guided me through the last years. Also Anna, das haben wir zwei wirklich gut gemacht!

I like to thank Itziar Ibarlucea Benítez (Ixi) for help on cortex tension measurements on ezrin depleted cells. ¿Que puedo decir? Mir faellt nixt ein. Chica, has hecho un tajo muy bien, pero mas hace falta aun. Y mi español se mejoró mucho! Muchas Gracias!

Furthermore I would like to thank Jonne Hendrik (Dr.) Helenius for his thoughtful scientific discussions on many topics, be it data analysis, interpretation or conduction. Nobody can program like you, Jonne. Thanks for finnish liquorice — that's the best!

Many thanks are delivered to Erik Schäffer (Scheppi) for reading manuscripts, correcting errors and especially pushing the limits to the far far far top. No matter which weather – ☼ ⇝ 🌡 ⇝ 🌤 ⇝ 🌧 ⇝ 🌪 I just say 8b ... (yes i know, it's sächsisch, but i say it again: 8b)

Thank you very much, Jenny, for correcting and proof-reading the wordings of this thesis. (now it makes perfect sense and sounds super good)! Thanks a lot, you're the best!

I would also like to thank the Fish Facility in the MPI-CBG as well as the Fish Facility in the BioTec for excellent fish-care. Special thanks go to Jean-Christoph Olaya from the BioTec Imaging Team for his help on wide field and confocal microscopy. Thanks a lot JC, also for supporting me while bouldering through Dresden.

Torsten Müller. I would also like to thank you for encouraging discussions and a very nice trip to Woods Hole. I hope we stay in contact even if I do not work with AFM anymore. Thank you very much. And your company JPK.

This leads me to Susanne (Suzette) Wegmann. ⌂⌂⌂↗ ◣↬ ⌂Thanks for the nice time we had in the lab.

Most importantly, I want to thank my family, especially my mother and my father for continuous support; my sisters and my brothers-in-law, first and foremost Katrin for many helpful advices during this time of my life.

Lastly, I would like to thank my friends who were not mentioned before yet, above all Annika for supporting me a very long time.

Appendix

List of Figures

1.1 Vertebrate development 4
1.2 Cell adhesion, cortex tension and membrane mechanics influence cell behavior 6

2.1 Early zebrafish development 12
2.2 Nodal signaling 15
2.3 Epithelial mesenchymal transition in development 17
2.4 Fluid phase separation and cell sorting 22
2.5 Differential adhesion determines tissue positioning 24
2.6 Cell surface mechanics in development 28
2.7 Apical constriction and cortex tension 30
2.8 Cortex tension in the cell 33
2.9 Integrins structure and function 36
2.10 Overall architecture of classical Cadherins 38
2.11 Molecular basis of cell adhesion 39
2.12 Cadherins in development 41
2.13 Tissue surface tensiometry 44
2.14 Flow chamber and spinning disc 47
2.15 Micropipette aspiration 49
2.16 Optical tweezers 50
2.17 Single cell force spectroscopy 52
2.18 Cell adhesion strengthening with time 54
2.19 Single cell elastography using AFM 56
2.20 Micropipettes to measure T_c 60

3.1 Atomic force microscopy 63
3.2 Schematics of force curves taken on different surfaces 66
3.3 mRNA transcription 73
3.4 Zebrafish egg microinjection 73

3.5 Hanging drop culture . . . 75
3.6 Assembly of an electro-blot . . . 78
3.7 AFM Set-up . . . 80
3.8 AFM Cantilever modification . . . 82
3.9 Cell-nucleus volume ratio . . . 84
3.10 FRAP z geometry . . . 86
3.11 Procedure to determine movement orientation . . . 90
3.12 Calculation of cell-overlap . . . 91

4.1 Force-displacement curve . . . 97
4.2 Progenitor cell adhesion . . . 98
4.3 Cell cohesion depends on E-cadherin . . . 99
4.4 Controls . . . 100
4.5 N-cadherin dependence of adhesion force . . . 101
4.6 Cell-cortex tension of germ-layer progenitor cells. . . . 102
4.7 T_c of control cells . . . 103
4.8 Cell-sorting *in-vitro* . . . 104
4.9 SCFS after cell culture . . . 105
4.10 Cell sorting and acto-myosin function . . . 106
4.11 Adhesion and cortex tension of myosin perturbed cells . . . 107
4.12 Cell sorting in presence of Activin . . . 111
4.13 Monte-Carlo Simulation (MCS) of progenitor cell sorting . . . 112
4.14 Acto-myosin at explant interfaces . . . 113
4.15 Cell sorting *in-vivo* . . . 114
4.16 Germ layer formation *in-silico* . . . 115
4.17 The cellular origin of interfacial tension . . . 116

5.1 Movement of lateral mesendoderm cells in wild-type embryos . . . 121
5.2 Cell movement in wild-type and mutant embryos . . . 122
5.3 Modulation of mesendoderm cell-cell adhesion . . . 124
5.4 Effect of cell-cell adhesion on individual mesendoderm cell movement . . . 126
5.5 Cell motility, cell contact and contact inhibition in *e-cadherin* mutant/morphant embryos . . . 128
5.6 Cell migration in MZ-*oep* embryos . . . 129

6.1 Cell membrane mechanics . . . 134
6.2 Tether extrusion using different techniques . . . 139

6.3 Function of ERM proteins . . . 143
6.4 Nodal signaling and ERM expression. . . . 145
6.5 Blebbing of mesendodermal cells *in-vitro* and *in-vivo*. . . . 147
6.6 Radial actin fibers . . . 148
6.7 Blebbing and actin polymerization . . . 148
6.8 Cortex tension and blebbing . . . 150
6.9 Tether extrusion . . . 151
6.10 Extrusion force of the first tether . . . 153
6.11 Fluorescence recovery after photobleaching . . . 155
6.12 Membrane-cortex interactions . . . 156
6.13 Migration & ERM loss-of-function . . . 157

7.1 Measurement of force-induced receptor-ligand kinetics . . . 162
7.2 Tether-force measurements using AFM . . . 165
7.3 Probability distribution . . . 166
7.4 Specificity . . . 167
7.5 Receptor-ligand lifetime . . . 168
7.6 Lifetimes and forces for individual tethers . . . 169

List of Tables

2.1 Published values for cortex tension 61

3.1 Diffusion coefficients 72
3.2 mRNA injections 74
3.3 Antisense morpholino injections 75
3.4 List of used inhibitors 76
3.5 Recipes to prepare a SDS-PAGE gel 78
3.6 Different antibodies used in this work 93
3.7 Cantilever models 94

4.1 Median detachment forces in piconewton 118

5.1 Summary of cell adhesion measurements 130

6.1 Published values for lipid-bilayer bending rigidity 136
6.2 Published values for membrane viscosity 141
6.3 Published values for membrane tensions 154
6.4 Number of measurement and average tether forces for cells used in this chapter 159

Movie legends

Movie1.mov

Zebrafish embryogenesis from two-cell stage until the end of somitogenesis [1]. The most important features of early development are captured, like cleavage period, epiboly, gastrulation.

Movie2.avi

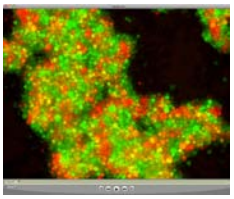

Sorting of mesoderm (green) and ectoderm (red) progenitor cell on a non-adherent substrate monitored by epifluorescence microscopy. Frame rate=5min, field of view is 1.2 mm.

Movie3.avi

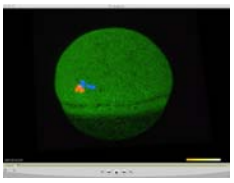

Movie of wildtype mesendodermal (red) and *e-cadherin* morphant (blue) cells transplanted into a wildtype host (green). Cells were transplanted into the lateral mesendoderm at 50 % epiboly and monitored by confocal microscopy during gastrulation (kindly provided by Yohanna Arboleda Estudillo). Both cell types separate from each other and end up in different 'compartments'. Scalebar=200 µm

Movie4.avi

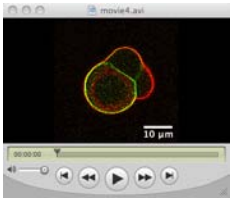

Mesendodermal wildtype cell injected with membrane bound RFP and gfp-lifeact to visualize the plasma-membrane and cortical actin cytoskeleton simultaneously. Framerate=2seconds. Cell undergoes circus movement as well as de-novo bleb nucleation events are visible. Scale bar=10 µm

Movie5.avi

Movie of a mesendodermal cell injected with 300 pg dominant negative Ezrin, membrane bound RFP and gfp-lifeact. Frame rate=2seconds. Cell shape integrity is messed up. Scale bar=10 µm

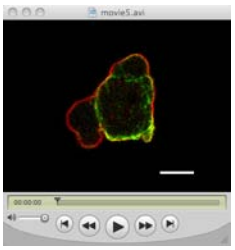

Movie6.avi

Movie of a mesendodermal cell injected with 4 ng *ezrin* and 4 ng *radixin* morpholino, membrane bound RFP and gfp-lifeact. Frame rate=2seconds. Scale bar=10 µm

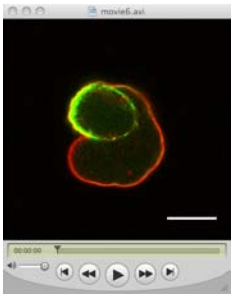

Movie7.avi

Movie of a mesendodermal cell injected with membrane bound RFP and gfp-lifeact subjected to 1 µM latA. Frame rate=2seconds. Filamentous actin is depolymerized and the cell rounds up immediately, loosing any surface protrusion. Scale bar=10 µm

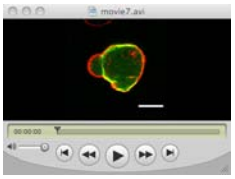

Movie8.avi

FRAP experiment. A mesendodermal cell expressing a gap-gfp is bleached at a part of its plasma-membrane. The recovery process is monitored for 2 min every 0.7 s. Scalebar=10 µm

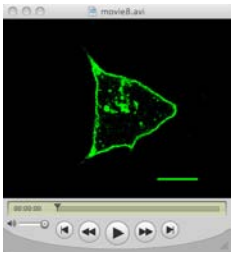

Curriculum vitae

Personal information

Name:	Michael Krieg
Adress:	Bürgerstrasse 33 01127 Dresden, Germany
Phone:	[redacted] – +49 351 463 40 306 (lab)
E mail:	krieg@biotec.tu-dresden.de
Date of birth:	25. 04. 1981
Place of birth:	Weimar, Germany
Nationality:	German
Marital status:	Single
Parents:	Peter Krieg, [redacted] Karla Krieg, [redacted]

Education

08/1991–05/1999	Secondary school in Weimar Final examinations: Abitur, [redacted]

Civil Service

10/1999–08/2000	Support of senior citizen, surveillance of security installation in a home for retired people, Weimar

Studies

10/2000–09/2002	Intermediate examinations in "Biology" at the University of Kassel [redacted]
07/2004–10/2004	Wissenschaftliche Hilfskraft at the Department of Biochemistry
10/2002–12/2004	Diploma studies at the University of Kassel in Nanobiology
12/2004	Diploma exams in Genetics (Prof. Dr. W. Nellen, [redacted]), Cell Biology (Prof. Dr. M. Maniak, [redacted]) and Physics (Prof. Dr. Th. Baumert, [redacted])
01/2005–09/2005	Diploma thesis at the Department of Cellular Machines (Prof. Dr. D. J. Müller, TU-Dresden)

Training

02/2003	Cytogenetics course at IPK Gatersleben Supervisor: Prof. I. Schubert & Dr. A. Houben
03/2003–04/2003	Institute for Microtechnology and Analysis (IMA) Kassel (Prof. R. Kassing) "Microfabrication of Si_3N_4 AFM cantilevers" Supervisor: Dr. E. Oesterschulze
09/2003–11/2003	MPI-FKF Stuttgart, Nanoscale Science Department (Prof. K. Kern) "Spatially selective electroless deposition of noble metals in/on tobacco mosaic viruses" Supervisor: Dr. A. Bittner (Chemical Nanostructuring and Self-Assembly)

11/2003–12/2003	MPI-CBG Dresden, Cellular Machines (Prof. D.J. Müller) "Locating ligand binding and activation of a single antiporter" Supervisor: A. Kedrov
03/2004	MPI-Biophysics Frankfurt, Department of Structural Biology (Prof. W. Kuehlbrandt) "Structure and function of osmoregulatory secondary transporters" Supervisor: Dr. Ch. Ziegler

Language

German:	mother tongue
English:	negotiation skills (usual language in the lab)
Spanish:	fluent
French:	basic

Teaching

Lecture "New Methods in Nano-Biotechnology" — Cell Force spectroscopy

Supervision of Labcourse "Biochemie für Chemieingenieure"

Supervision of two diploma theses

Conference Participation - oral

Feb. 2008	Linz Winter Workshop, invited lecture Tensile forces govern germ layer organization in zebrafish
June 2008	IUTAM meeting Woods Hole, Mass. Deciphering molecular forces that govern germ layer morphogenesis during gastrulation

January 4, 2010

List of Publications

- Kedrov, A. **Krieg, M.** Ziegler, C. Kühlbrandt, W. Müller, D.J; Locating ligand binding and activation of a single antiporter, *EMBO Reports* **6**, 668-674 (2005).

- Puech, P-H. Taubenberger, A. Ulrich, F. **Krieg, M.** Müller, D. J; Heisenberg, C-P. Measuring cell adhesion forces of primary gastrulating cells from zebrafish using atomic force microscopy, *Journal of Cell Science* **118**, 4199-4206 (2005)

- Ulrich, F.♭ **Krieg, M.**♭ Schötz, E-M.♭ Link, V. Castanon, I. Schanbel, V. Taubenberger, A. Müller, D.J. Puech, P-H. Heisenberg, C-P; Wnt11 functions in gastrulation by controlling cell cohesion through Rab5c and E-cadherin, *Developmental Cell* **9** 555-564 (2005) ♭ . . .equal contribution

- **Krieg, M.** Arboleda-Estudillo, Y. Puech, P. H. Kafer, J. Graner, F. Müller, D. J. Heisenberg, C. P; Tensile forces govern germ-layer organization in zebrafish, *Nature Cell Biology* **10** 429-436 (2008)

- **Krieg, M.** Helenius, J. Heisenberg, C. P. Müller, D. J; A bond for a lifetime: employing membrane nanotubes from living cells to determine receptor-ligand kinetics, *Angewandte Chemie International Edition* **47** 9775-9777 (2008)

- Müller, D. J. **Krieg, M.** Alsteens, D. Dufrêne, Y. F; New frontiers in atomic force microscopy: analyzing interactions from single-molecules to cells, Current Opinion Biotechnology **20** 4-13 (2009)

- Arboleda-Estudillo, Y. **Krieg, M.** Stühmer, J. Müller, D.J. Heisenberg, C. P; Movement directionality in collective germ layer progenitor migration, *submitted*

Versicherung

Hiermit versichere ich, dass ich die vorliegende Arbeit ohne unzulässige Hilfe Dritter und ohne Benutzung anderer als der angegebenen Hilfsmittel angefertigt habe; die aus fremden Quellen direkt oder indirekt übernommenen Gedanken sind als solche kenntlich gemacht. Die Arbeit wurde bisher weder im Inland noch im Ausland in gleicher oder ähnlicher Form einer anderen Prüfungsbehörde vorgelegt. Die Arbeit wurde im Biotechnologischen Zentrum der Technischen Universität Dresden unter der Leitung von Professor Daniel J. Müller angefertigt. Sie erfolgte in enger Kollaboration und Betreuung durch Dr. Carl-Philipp Heisenberg, Gruppenleiter am Max-Planck-Institut für Zellbiologie und Genetic, Dresden.

Glossary

A_c	contact area, 66
A_o	Area of two overlapping cells, 90
D	Diffusion coefficient, 70
D_{pzt}	Piezo travel distance, 65
E	Young's modulus, 57
$I(t)$	Fluorescence intensity profile over time, 85
I_0	Fluorescence intensity directly after bleaching, 70
I_B	Background intensity, 85
I_i	Fluorescence intensity before bleaching, 70
I_{Bs}	Fluorescence intensity of the bleach spot, 85
I_Σ	Fluorescence intensity of the whole image, 85
I_{inf}	Fluorescence intensity after full recovery, 70
J_{ij}	Cell-cell adhesion between cell i and cell j, 111
L	Length of the aspirated tongue in MPA experiments, 59
L_0	Equilibrium dimension of a material under zero load, 66
L_c	Length of the AFM cantilever, 64
M	Saturation magnetization of a micro-particle used for Magnetic Tweezers, 49
M_f	Mobile fraction of the fluorophor, 70
N_A	Numerical aperture of a microscope lens, 88

N_c	Number of bound cells after application of a force, 47
P	Pressure in the pipette, 59
P_n	Critical pressure of the last cycle needed to separate two cells in MPA experiments, 48
P_{crit}	threshold pressure in micropipette aspiration experiments, 57
R_E	Radius of a zebrafish embryo, 89
R_H	Hydrodynamic radius of the labeled species, 71
R_b	bead radius, 68
R_c	Cell radius, 59, 60, 83
R_p	Pipette radius, 59
R_t	Tether radius, 84
$R_{contact}$	Contact radius of the aggregate during compression in a PPC apparatus, 45
R_{con}	Contact radius of a indenting bead with a cell, 59
R_{equat}	Radius of the equatorial region of the aggregate during compression, 45
R_{height}	Height of the aggregate during compression in a PPC, 45
S	Effective migration speed, 89
T	Translational momentum, 49
T_c	Cell cortex tension, 57
T_{app}	Apparent membrane tension of a cell as the sum of lipid bilayer surface tension and membrane-cytoskeleton adhesion, 133
T_{eff}	Effective surface tension of a lipid bilayer, 84
V	Volume of a cell or bead, 49
W	Power of a focussed laser beam, 50

W_0	Lipid-bilayer - cytoskeleton adhesion energy, 84
ΔL	dimension change of the material under stress, 66
ΔV	Potential difference on the photodiode after deflection of the cantilever from the equilibrium position, 64
Δ_{PSD}	Displacement of the lasers pot on the photodiode, 64
Θ	Stress within a material upon an external load, 66
α_c	opening angle of the AFM cantilever pyramidal tip, 68
$\urcorner$	Characteristic bond attachment time, 51
δ	AFM cantilever probe - surface separation, 65
η	Viscosity of the membrane, 71
γ^{cc}	interfacial tension at the cell-cell interface, 116
γ^{cm}	interfacial tension at the cell-medium interface, 116
κ	Bending elasticity of a lipid bilayer, 84
λ	Receptor ligand lifetime, 84
$\langle \Delta x^2 \rangle$	Mean squared displacement, 89
$\langle \Delta x^2_{corr} \rangle$	Mean squared displacement corrected for embryo curvature, 89
$\langle \Delta z_c^2 \rangle$	mean squared cantilever deflection, 64
$\nabla \vec{H}$	Magnetic field gradient, 49
ν	Density of membrane cytoskeleton binding molecules, 84
ν_p	Poisson ratio, 68
ω	Spinning velocity of a spinning disc device, 46
ϕ	Shear stress, 46

ρ	Density of the medium, 47
σ	Aggregate surface tension, 44
ε	strain in an material upon a stress, 66
ζ	Average cortical mesh size, 154
c	Speed of light, 50
d	distance between AFM cantilever and the photo-diode, 64
d_p	Inner diameter of the pipette in MPA experiments, 48
f_0	Tether force at zero velocity; static tether force, 84
f_t	Tether-force at a certain velocity, 165
k	Stiffness of a material, spring constant in general, 67
k_{off}^0	natural receptor ligand unbinding rate under zero force, 84
k_bT	Boltzmann term = temperature×Boltzmann constant= 300K× $1.4{\cdot}10^{-23}$J/K, 64
k_c	AFM cantilever spring constant, 64
k_{off}	Receptor ligand unbinding rate under external force, 84
q	wavenumber, 135
s	deflection sensitivity of the cantilever on the PSD, 65
t_c	thickness of the AFM cantilever, 64
$t_{1/2}$	Half time of the recovery process in a FRAP experiment, 70
v	Piezo velocity, 84
w	Width of the bleach spot in a FRAP experiment, 71
w_c	width of the AFM cantilever, 64

x_u	width of the potential barrier of a receptor ligand bond, 84
z	Depth of the bleach spot along the optical axis, 71
z_c	deflection of the cantilever due to a external force, 64

Bibliography

[1] R. O. Karlstrom and D. A. Kane. A flipbook of zebrafish embryogenesis. *Development*, 123:461, 1996. 1, VIII

[2] A. F. Schier and W. S. Talbot. Molecular genetics of axis formation in zebrafish. *Annu Rev Genet*, 39:561–613, 2005. 3, 4, 10, 13, 14, 110, 145

[3] U. Tepass, D. Godt, and R. Winklbauer. Cell sorting in animal development: signalling and adhesive mechanisms in the formation of tissue boundaries. *Curr Opin Genet Dev*, 12(5):572–82, 2002. 3, 36, 40, 42

[4] T. Lecuit and P. F. Lenne. Cell surface mechanics and the control of cell shape, tissue patterns and morphogenesis. *Nat Rev Mol Cell Biol*, 8(8):633–44, 2007. 3, 95, 117

[5] P. W. Atkins and Julio De Paula. *Physical chemistry*. Oxford University Press, Oxford ; New York, 8th edition, 2006. 3

[6] N.K. Adam. *Physics and Chemistry of surfaces*. Dover Publications, 1969. 3

[7] R. A. Foty, G. Forgacs, C. M. Pfleger, and M. S. Steinberg. Liquid properties of embryonic tissues: Measurement of interfacial tensions. *Physical Review Letters*, 72(14):2298–2301, 1994. 3, 44, 171

[8] I. Takeuchi, T. Kakutani, and M. Tasaka. Cell behavior during formation of prestalk/prespore pattern in submerged agglomerates of dictyostelium discoideum. *Dev Genet*, 9(4-5):607–14, 1988. 3, 108

[9] G. Pezeron, P. Mourrain, S. Courty, J. Ghislain, T. S. Becker, F. M. Rosa, and N. B. David. Live analysis of endodermal layer formation identifies random walk as a novel gastrulation movement. *Curr Biol*, 18(4):276–81, 2008. 3, 11, 15

[10] S. Nair and T. F. Schilling. Chemokine signaling controls endodermal migration during zebrafish gastrulation. *Science*, 322(5898):89–92, 2008. 3, 158

[11] M. Arnold, V. C. Hirschfeld-Warneken, T. Lohmuller, P. Heil, J. Blummel, E. A. Cavalcanti-Adam, M. Lopez-Garcia, P. Walther, H. Kessler, B. Geiger, and J. P. Spatz. Induction of cell polarization and migration by a gradient of nanoscale variations in adhesive ligand spacing. *Nano Lett*, 8(7):2063–9, 2008. 3, 120

[12] C. B. Kimmel, W. W. Ballard, S. R. Kimmel, B. Ullmann, and T. F. Schilling. Stages of embryonic development of the zebrafish. *Dev Dyn*, 203(3):253–310, 1995. 4, 10, 11, 12, 13

[13] Florian Ulrich, Miguel L. Concha, Paul J. Heid, Ed Voss, Sabine Witzel, Henry Roehl, Masazumi Tada, Stephen W. Wilson, Richard J. Adams, David R. Soll, and Carl-Philipp Heisenberg. Slb/wnt11 controls hypoblast cell migration and morphogenesis at the onset of zebrafish gastrulation. *Development*, 130(22):5375–5384, 2003. 4, 9

[14] L. Solnica-Krezel. Gastrulation in zebrafish – all just about adhesion? *Curr Opin Genet Dev*, 16(4):433–41, 2006. 4, 5, 11, 15, 42

[15] P. L. Townes and Holtfreter. J. Directed movements and selective adhesion of embryonic amphibian cells. *Journal of Experimental Zoology*, 128(1):53–120, 1955. 4, 21, 62, 95

[16] M. S. Steinberg. On the mechanism of tissue reconstruction by dissociated cells. i. population kinetics, differential adhesiveness. and the absence of directed migration. *Proc Natl Acad Sci U S A*, 48:1577–82, 1962. 4, 5, 21, 24, 25, 34, 41

[17] D. A. Beysens, G. Forgacs, and J. A. Glazier. Cell sorting is analogous to phase ordering in fluids. *Proc Natl Acad Sci U S A*, 97(17):9467–71, 2000. 4, 22, 44

[18] G. S. Davis, H. M. Phillips, and M. S. Steinberg. Germ-layer surface tensions and "tissue affinities" in rana pipiens gastrulae: quantitative measurements. *Dev Biol*, 192(2):630–44, 1997. 4, 25, 44, 104

[19] E. M. Schotz, R. D. Burdine, F. Julicher, M. S. Steinberg, C. P. Heisenberg, and R. A. Foty. Quantitative differences in tissue surface tension influence zebrafish germ layer positioning. *HFSP J*, 2(1):42–56, 2008. 4, 5, 15, 25, 34, 42, 43, 44, 103, 104, 113, 116

[20] A. K. Harris. Is cell sorting caused by differences in the work of intercellular adhesion? a critique of the steinberg hypothesis. *J Theor Biol*, 61(2):267–85, 1976. 5, 26, 62, 95, 101, 108, 112

[21] G. W. Brodland. The differential interfacial tension hypothesis (dith): a comprehensive theory for the self-rearrangement of embryonic cells and tissues. *J Biomech Eng*, 124(2):188–97, 2002. 5, 62, 111

[22] T. Lecuit. Cell adhesion: sorting out cell mixing with echinoid? *Curr Biol*, 15(13):R505–7, 2005. 5, 26, 27

[23] T. Lammermann, B. L. Bader, S. J. Monkley, T. Worbs, R. Wedlich-Soldner, K. Hirsch, M. Keller, R. Forster, D. R. Critchley, R. Fassler, and M. Sixt. Rapid leukocyte migration by integrin-independent flowing and squeezing. *Nature*, 453(7191):51–5, 2008. 5, 18

[24] S. P. Palecek, J. C. Loftus, M. H. Ginsberg, D. A. Lauffenburger, and A. F. Horwitz. Integrin-ligand binding properties govern cell migration speed through cell-substratum adhesiveness. *Nature*, 385(6616):537–40, 1997. 5, 120

[25] E. Sahai and C. J. Marshall. Differing modes of tumour cell invasion have distinct requirements for rho/rock signalling and extracellular proteolysis. *Nat Cell Biol*, 5(8):711–9, 2003. 5, 33, 34

[26] D. S. Sepich, C. Calmelet, M. Kiskowski, and L. Solnica-Krezel. Initiation of convergence and extension movements of lateral mesoderm during zebrafish gastrulation. *Dev Dyn*, 234(2):279–92, 2005. 5, 13, 121

[27] J. A. Montero, L. Carvalho, M. Wilsch-Brauninger, B. Kilian, C. Mustafa, and C. P. Heisenberg. Shield formation at the onset of zebrafish gastrulation. *Development*, 132(6):1187–98, 2005. 6, 18, 43, 74, 97, 98, 117

[28] S. Huang, C. P. Brangwynne, K. K. Parker, and D. E. Ingber. Symmetry-breaking in mammalian cell cohort migration during tissue pattern formation: role of random-walk persistence. *Cell Motil Cytoskeleton*, 61(4):201–13, 2005. 6, 127

[29] D. Raucher and M. P. Sheetz. Cell spreading and lamellipodial extension rate is regulated by membrane tension. *J Cell Biol*, 148(1):127–36, 2000. 7, 76, 139, 140, 152, 154

[30] A. Bretscher, K. Edwards, and R. G. Fehon. Erm proteins and merlin: integrators at the cell cortex. *Nat Rev Mol Cell Biol*, 3(8):586–99, 2002. 7, 142, 145, 148

[31] V. Link, L. Carvalho, I. Castanon, P. Stockinger, A. Shevchenko, and C. P. Heisenberg. Identification of regulators of germ layer morphogenesis using proteomics in zebrafish. *J Cell Sci*, 119(Pt 10):2073–83, 2006. 7, 75, 93, 144, 145, 146, 148

[32] W. D. Marcus, R. P. McEver, and C. Zhu. Forces required to initiate membrane tether extrusion from cell surface depend on cell type but not on the surface molecule. *Mech Chem Biosyst*, 1(4):245–51, 2004. 7, 141, 154

[33] R. M. Hochmuth and W. D. Marcus. Membrane tethers formed from blood cells with available area and determination of their adhesion energy. *Biophys J*, 82(6):2964–9, 2002. 7, 152, 153, 154

[34] F. Brochard-Wyart, N. Borghi, D. Cuvelier, and P. Nassoy. Hydrodynamic narrowing of tubes extruded from cells. *Proc Natl Acad Sci U S A*, 103(20):7660–3, 2006. 7, 141, 151, 152, 153, 154, 155

[35] R. M. Hochmuth and E. A. Evans. Extensional flow of erythrocyte membrane from cell body to elastic tether. i. analysis. *Biophys J*, 39(1):71–81, 1982. 7, 71, 139, 140, 141, 150, 153, 167

[36] M. P. Sheetz. Cell control by membrane-cytoskeleton adhesion. *Nat Rev Mol Cell Biol*, 2(5):392–6, 2001. 7, 50, 85, 134, 138, 139, 142, 150, 153, 156, 157

[37] G. Streisinger, C. Walker, N. Dower, D. Knauber, and F. Singer. Production of clones of homozygous diploid zebra fish (brachydanio rerio). *Nature*, 291(5813):293–6, 1981. 9

[38] A. Carmany-Rampey and A. F. Schier. Single-cell internalization during zebrafish gastrulation. *Curr Biol*, 11(16):1261–5, 2001. 9

[39] A. Amsterdam and N. Hopkins. Mutagenesis strategies in zebrafish for identifying genes involved in development and disease. *Trends Genet*, 22(9):473–8, 2006. 9

[40] S. von der Hardt, J. Bakkers, A. Inbal, L. Carvalho, L. Solnica-Krezel, C. P. Heisenberg, and M. Hammerschmidt. The bmp gradient of the zebrafish gastrula guides migrating lateral cells by regulating cell-cell adhesion. *Curr Biol*, 17(6):475–87, 2007. 9, 43

[41] D. Sharma and W. H. Kinsey. Regionalized calcium signaling in zebrafish fertilization. *Int J Dev Biol*, 52(5-6):561–70, 2008. 10

[42] Lilianna Solnica-Krezel. *Pattern formation in zebrafish*. Results and problems in cell differentiation 40. Springer, Berlin ; New York, 2002. 10

[43] L. Carvalho, J. Stuhmer, J. S. Bois, Y. Kalaidzidis, V. Lecaudey, and C. P. Heisenberg. Control of convergent yolk syncytial layer nuclear movement in zebrafish. *Development*, 136(8):1305–15, 2009. 10, 121, 122

[44] C. Y. Ho, C. Houart, S. W. Wilson, and D. Y. Stainier. A role for the extraembryonic yolk syncytial layer in patterning the zebrafish embryo suggested by properties of the hex gene. *Curr Biol*, 9(19):1131–4, 1999. 10

[45] J. P. Trinkaus. Mechanism of fundulus epiboly–a current view. *Amer. Zool.*, 24(3):673–688, 1984. 11

[46] L. A. Rohde and C. P. Heisenberg. Zebrafish gastrulation: cell movements, signals, and mechanisms. *Int Rev Cytol*, 261:159–92, 2007. 11

[47] L. Solnica-Krezel and W. Driever. Microtubule arrays of the zebrafish yolk cell: organization and function during epiboly. *Development*, 120(9):2443–55, 1994. 11

[48] P. Oteiza, M. Koppen, M. L. Concha, and C. P. Heisenberg. Origin and shaping of the laterality organ in zebrafish. *Development*, 135(16):2807–13, 2008. 11

[49] R. M. Warga and C. B. Kimmel. Cell movements during epiboly and gastrulation in zebrafish. *Development*, 108(4):569–80, 1990. 11, 12, 13

[50] N. S. Glickman, C. B. Kimmel, M. A. Jones, and R. J. Adams. Shaping the zebrafish notochord. *Development*, 130(5):873–87, 2003. 13

[51] M. Krieg, Y. Arboleda-Estudillo, P. H. Puech, J. Kafer, F. Graner, D. J. Muller, and C. P. Heisenberg. Tensile forces govern germ-layer organization in zebrafish. *Nat Cell Biol*, 10(4):429–36, 2008. 13, 123, 149, 150

[52] D. S. Sepich and L. Solnica-Krezel. Analysis of cell movements in zebrafish embryos: morphometrics and measuring movement of labeled cell populations in vivo. *Methods Mol Biol*, 294:211–33, 2005. 13

[53] S. Wacker, K. Grimm, T. Joos, and R. Winklbauer. Development and control of tissue separation at gastrulation in xenopus. *Dev Biol*, 224(2):428–39, 2000. 13, 109

[54] B. Feldman, M. A. Gates, E. S. Egan, S. T. Dougan, G. Rennebeck, H. I. Sirotkin, A. F. Schier, and W. S. Talbot. Zebrafish organizer development and germ-layer formation require nodal-related signals. *Nature*, 395(6698):181–5, 1998. 14

[55] S. K. Cheng, F. Olale, J. T. Bennett, A. H. Brivanlou, and A. F. Schier. Egf-cfc proteins are essential coreceptors for the tgf-beta signals vg1 and gdf1. *Genes Dev*, 17(1):31–6, 2003. 14

[56] T. O. Aoki, J. Mathieu, L. Saint-Etienne, M. R. Rebagliati, N. Peyrieras, and F. M. Rosa. Regulation of nodal signalling and mesendoderm formation by taram-a, a tgfbeta-related type i receptor. *Dev Biol*, 241(2):273–88, 2002. 14, 74

[57] A. F. Schier and M. M. Shen. Nodal signalling in vertebrate development. *Nature*, 403(6768):385–9, 2000. 14

[58] K. Gritsman, J. Zhang, S. Cheng, E. Heckscher, W. S. Talbot, and A. F. Schier. The egf-cfc protein one-eyed pinhead is essential for nodal signaling. *Cell*, 97(1):121–32, 1999. 14, 76, 102, 110, 111, 113, 122

[59] S. Schulte-Merker, M. Hammerschmidt, D. Beuchle, K. W. Cho, E. M. De Robertis, and C. Nusslein-Volhard. Expression of zebrafish goosecoid and no tail gene products in wild-type and mutant no tail embryos. *Development*, 120(4):843–52, 1994. 15

[60] Y. Kikuchi, L. A. Trinh, J. F. Reiter, J. Alexander, D. Yelon, and D. Y. Stainier. The zebrafish bonnie and clyde gene encodes a mix family homeodomain protein that regulates the generation of endodermal precursors. *Genes Dev*, 14(10):1279–89, 2000. 15

[61] Y. Kikuchi, A. Agathon, J. Alexander, C. Thisse, S. Waldron, D. Yelon, B. Thisse, and D. Y. Stainier. casanova encodes a novel sox-related protein necessary and sufficient for early endoderm formation in zebrafish. *Genes Dev*, 15(12):1493–505, 2001. 15, 74

[62] J. E. Cooke, H. A. Kemp, and C. B. Moens. Epha4 is required for cell adhesion and rhombomere-boundary formation in the zebrafish. *Curr Biol*, 15(6):536–42, 2005. 15

[63] M. Koppen, B. G. Fernandez, L. Carvalho, A. Jacinto, and C. P. Heisenberg. Coordinated cell-shape changes control epithelial movement in zebrafish and drosophila. *Development*, 133(14):2671–81, 2006. 15, 29

[64] C. D. Stern. *Gastrulation : from cells to embryo*. Cold Spring Harbor Laboratory Press, Cold Spring Harbor, N.Y., 2004. 16

[65] A. M. Arias. Epithelial mesenchymal interactions in cancer and development. *Cell*, 105(4):425–31, 2001. 16, 17

[66] J. L. Duband, F. Monier, M. Delannet, and D. Newgreen. Epithelium-mesenchyme transition during neural crest development. *Acta Anat (Basel)*, 154(1):63–78, 1995. 16, 17

[67] J. R. Miller and D. R. McClay. Characterization of the role of cadherin in regulating cell adhesion during sea urchin development. *Dev Biol*, 192(2):323–39, 1997. 16, 17

[68] J. P. Thiery and J. P. Sleeman. Complex networks orchestrate epithelial-mesenchymal transitions. *Nat Rev Mol Cell Biol*, 7(2):131–42, 2006. 16

[69] D. R. Shook and R. Keller. Epithelial type, ingression, blastopore architecture and the evolution of chordate mesoderm morphogenesis. *J Exp Zoolog B Mol Dev Evol*, 310(1):85–110, 2008. 16

[70] M. A. Nieto. Epithelial-mesenchymal transitions in development and disease: old views and new perspectives. *Int J Dev Biol*, 2008. 17

[71] S. Yamashita, C. Miyagi, T. Fukada, N. Kagara, Y. S. Che, and T. Hirano. Zinc transporter livi controls epithelial-mesenchymal transition in zebrafish gastrula organizer. *Nature*, 429(6989):298–302, 2004. 17, 42

[72] C. Thisse, B. Thisse, T. F. Schilling, and J. H. Postlethwait. Structure of the zebrafish snail1 gene and its expression in wild-type, spadetail and no tail mutant embryos. *Development*, 119(4):1203–15, 1993. 17, 18

[73] R. Suriben, S. Kivimae, D. A. Fisher, R. T. Moon, and B. N. Cheyette. Posterior malformations in dact1 mutant mice arise through misregulated vangl2 at the primitive streak. *Nat Genet*, 41(9):977–85, 2009. 18

[74] A. F. Safina, A. E. Varga, A. Bianchi, Q. Zheng, D. Kunnev, P. Liang, and A. V. Bakin. Ras alters epithelial-mesenchymal transition in response to tgfbeta by reducing actin fibers and cell-matrix adhesion. *Cell Cycle*, 8(2):284–98, 2009. 18

[75] R. Keller, D. Shook, and P. Skoglund. The forces that shape embryos: physical aspects of convergent extension by cell intercalation. *Phys Biol*, 5(1):15007, 2008. 18, 29

[76] O. Voiculescu, F. Bertocchini, L. Wolpert, R. E. Keller, and C. D. Stern. The amniote primitive streak is defined by epithelial cell intercalation before gastrulation. *Nature*, 449(7165):1049–52, 2007. 18, 29

[77] F. Marlow, J. Topczewski, D. Sepich, and L. Solnica-Krezel. Zebrafish rho kinase 2 acts downstream of wnt11 to mediate cell polarity and effective convergence and extension movements. *Curr Biol*, 12(11):876–84, 2002. 18, 74, 107

[78] S. G. Babb and J. A. Marrs. E-cadherin regulates cell movements and tissue formation in early zebrafish embryos. *Dev Dyn*, 230(2):263–77, 2004. 18, 42, 75, 93, 98, 120, 123

[79] S. G. Babb, J. Barnett, A. L. Doedens, N. Cobb, Q. Liu, B. C. Sorkin, P. C. Yelick, P. A. Raymond, and J. A. Marrs. Zebrafish e-cadherin: expression during early embryogenesis and regulation during brain development. *Dev Dyn*, 221(2):231–7, 2001. 18

[80] C. M. Franz, G. E. Jones, and A. J. Ridley. Cell migration in development and disease. *Dev Cell*, 2(2):153–8, 2002. 18

[81] N. Desprat, W. Supatto, P. A. Pouille, E. Beaurepaire, and E. Farge. Tissue deformation modulates twist expression to determine anterior midgut differentiation in drosophila embryos. *Dev Cell*, 15(3):470–7, 2008. 19

[82] E. Farge. Mechanical induction of twist in the drosophila foregut/stomodeal primordium. *Curr Biol*, 13(16):1365–77, 2003. 19

[83] A. J. Engler, S. Sen, H. L. Sweeney, and D. E. Discher. Matrix elasticity directs stem cell lineage specification. *Cell*, 126(4):677–89, 2006. 19, 20

[84] C. Carmona-Fontaine, H. K. Matthews, S. Kuriyama, M. Moreno, G. A. Dunn, M. Parsons, C. D. Stern, and R. Mayor. Contact inhibition of locomotion in vivo controls neural crest directional migration. *Nature*, 456(7224):957–61, 2008. 19, 129

[85] R. B. Martin. Determinants of the mechanical properties of bones. *J Biomech*, 24 Suppl 1:79–88, 1991. 19

[86] P. Kazmierczak, H. Sakaguchi, J. Tokita, E. M. Wilson-Kubalek, R. A. Milligan, U. Muller, and B. Kachar. Cadherin 23 and protocadherin 15 interact to form tip-link filaments in sensory hair cells. *Nature*, 449(7158):87–91, 2007. 19, 20, 37, 42

[87] Y. Sawada, M. Tamada, B. J. Dubin-Thaler, O. Cherniavskaya, R. Sakai, S. Tanaka, and M. P. Sheetz. Force sensing by mechanical extension of the src family kinase substrate p130cas. *Cell*, 127(5):1015–26, 2006. 19

[88] V. Vogel and M. P. Sheetz. Cell fate regulation by coupling mechanical cycles to biochemical signaling pathways. *Curr Opin Cell Biol*, 21(1):38–46, 2009. 19

[89] D. E. Discher, P. Janmey, and Y. L. Wang. Tissue cells feel and respond to the stiffness of their substrate. *Science*, 310(5751):1139–43, 2005. 19

[90] A. Kostic, C. D. Lynch, and M. P. Sheetz. Differential matrix rigidity response in breast cancer cell lines correlates with the tissue tropism. *PLoS ONE*, 4(7):e6361, 2009. 19

[91] C. J. Meyer, F. J. Alenghat, P. Rim, J. H. Fong, B. Fabry, and D. E. Ingber. Mechanical control of cyclic amp signalling and gene transcription through integrins. *Nat Cell Biol*, 2(9):666–8, 2000. 19

[92] C. S. Chen, M. Mrksich, S. Huang, G. M. Whitesides, and D. E. Ingber. Geometric control of cell life and death. *Science*, 276(5317):1425–8, 1997. 19

[93] K. Saha, A. J. Keung, E. F. Irwin, Y. Li, L. Little, D. V. Schaffer, and K. E. Healy. Substrate modulus directs neural stem cell behavior. *Biophys J*, 95(9):4426–38, 2008. 19

[94] R. McBeath, D. M. Pirone, C. M. Nelson, K. Bhadriraju, and C. S. Chen. Cell shape, cytoskeletal tension, and rhoa regulate stem cell lineage commitment. *Dev Cell*, 6(4):483–95, 2004. 19, 20

[95] B. M. Chen and A. D. Grinnell. Kinetics, ca2+ dependence, and biophysical properties of integrin-mediated mechanical modulation of transmitter release from frog motor nerve terminals. *J Neurosci*, 17(3):904–16, 1997. 20

[96] S. Lehoux and A. Tedgui. Signal transduction of mechanical stresses in the vascular wall. *Hypertension*, 32(2):338–45, 1998. 20

[97] W. Roux. Uber den cytotropismns der furchungszellen des grasfrosches (rana fusca). *Archiv der Entwicklungsmechanik*, 1:43–68, 1894. 21

[98] W.H. Lewis. Mechanics of invagination. *Anatomical Records*, 97:139–156, 1947. 21

[99] M. S. Steinberg. On the mechanism of tissue reconstruction by dissociated cells, iii. free energy relations and the reorganization of fused, heteronomic tissue fragments. *Proc Natl Acad Sci U S A*, 48(10):1769–76, 1962. 21, 22, 23, 43, 95, 108

[100] M. S. Steinberg and M. Takeichi. Experimental specification of cell sorting, tissue spreading, and specific spatial patterning by quantitative differences in cadherin expression. *Proc Natl Acad Sci U S A*, 91(1):206–9, 1994. 21

[101] M. S. Steinberg. Adhesion-guided multicellular assembly: a commentary upon the postulates, real and imagined, of the differential adhesion hypothesis, with special attention to computer simulations of cell sorting. *J Theor Biol*, 55(2):431–43, 1975. 21, 23

[102] P.G. de Gennes. Wetting: statics and dynamics. *Reviews in modern physics*, 57(3):827–863, 1985. 22

[103] H. M. Phillips and M. S. Steinberg. Equilibrium measurements of embryonic chick cell adhesiveness. i. shape equilibrium in centrifugal fields. *Proc Natl Acad Sci U S A*, 64(1):121–7, 1969. 23, 44

[104] M. S. Steinberg. Does differential adhesion govern self-assembly processes in histogenesis? equilibrium configurations and the emergence of a hierarchy among populations of embryonic cells. *J Exp Zool*, 173(4):395–433, 1970. 23

[105] R. A. Foty, C. M. Pfleger, G. Forgacs, and M. S. Steinberg. Surface tensions of embryonic tissues predict their mutual envelopment behavior. *Development*, 122(5):1611–20, 1996. 23, 44

[106] J. A. Glazier and F. Graner. Simulation of the differential adhesion driven rearrangement of biological cells. *Physical Review. E. Statistical Physics, Plasmas, Fluids, and Related Interdisciplinary Topics*, 47(3):2128–2154, 1993. 23, 112

[107] M. S. Steinberg and S. F. Gilbert. Townes and holtfreter (1955): directed movements and selective adhesion of embryonic amphibian cells. *J Exp Zoolog A Comp Exp Biol*, 301(9):701–6, 2004. 24

[108] D. Godt and U. Tepass. Drosophila oocyte localization is mediated by differential cadherin-based adhesion. *Nature*, 395(6700):387–91, 1998. 24, 25

[109] D. E. Maslow and E. Mayhew. Cytochalasin b prevents specific sorting of reaggregating embryonic cells. *Science*, 177(45):281–2, 1972. 25, 76, 107

[110] J. W. Sanger and H. Holtzer. Cytochalasin b: effects on cell morphology, cell adhesion, and mucopolysaccharide synthesis (cultured cells-contractile microfilaments-glycoproteins-embryonic cells-sorting-out). *Proc Natl Acad Sci U S A*, 69(1):253–7, 1972. 25, 107, 108

[111] M. S. Steinberg and L. L. Wiseman. Do morphogenetic tissue rearrangements require active cell movements? the reversible inhibition of cell sorting and tissue spreading by cytochalasin b. *J Cell Biol*, 55(3):606–15, 1972. 25, 45, 62, 107, 108

[112] P. B. Armstrong and D. Parenti. Cell sorting in the presence of cytochalasin b. *J Cell Biol*, 55(3):542–53, 1972. 25, 107, 108

[113] R. A. Foty and M. S. Steinberg. The differential adhesion hypothesis: a direct evaluation. *Dev Biol*, 278(1):255–63, 2005. 25, 41, 44

[114] P. B. Armstrong and M. T. Armstrong. A role for fibronectin in cell sorting. *J Cell Sci*, 69:179–97, 1984. 25

[115] J. Overton and Kapmarski. Hybrid desmosomes in aggregated chick and mouse cells. *J Exp Zool*, 192(1):33–41, 1975. 25, 62

[116] A. J. Ewald and J. B. Wallingford. Vertebrate gastrulation: separation is sticky and tense. *Curr Biol*, 18(14):R615–7, 2008. 25, 56, 95

[117] S. Bao and R. Cagan. Preferential adhesion mediated by hibris and roughest regulates morphogenesis and patterning in the drosophila eye. *Dev Cell*, 8(6):925–35, 2005. 25

[118] T. Lecuit and L. Le Goff. Orchestrating size and shape during morphogenesis. *Nature*, 450(7167):189–92, 2007. 25, 27, 30, 31, 32, 33

[119] H. Ninomiya and R. Winklbauer. Epithelial coating controls mesenchymal shape change through tissue-positioning effects and reduction of surface-minimizing tension. *Nat Cell Biol*, 10(1):61–9, 2008. 25, 26, 44

[120] Jos Kafer, Takashi Hayashi, Athanasius F. M. Maree, Richard W. Carthew, and Francois Graner. Cell adhesion and cortex contractility determine cell patterning in the drosophilaretina. *Proceedings of the National Academy of Sciences*, 104(47):18549–18554, 2007. 25, 27, 29, 31, 32, 62, 111, 117

[121] B. Burnside. Microtubules and microfilaments in amphibian neurulation. *American Zoologist*, 13:989–1006, 1973. 27

[122] G. M. Odell, G. Oster, P. Alberch, and B. Burnside. The mechanical basis of morphogenesis. i. epithelial folding and invagination. *Dev Biol*, 85(2):446–62, 1981. 27

[123] T. Lecuit. "developmental mechanics": cellular patterns controlled by adhesion, cortical tension and cell division. *HFSP J*, 2(2):72–8, 2008. 27

[124] R. Farhadifar, J. C. Roper, B. Aigouy, S. Eaton, and F. Julicher. The influence of cell mechanics, cell-cell interactions, and proliferation on epithelial packing. *Curr Biol*, 17(24):2095–104, 2007. 27

[125] C. M. Nelson, R. P. Jean, J. L. Tan, W. F. Liu, N. J. Sniadecki, A. A. Spector, and C. S. Chen. Emergent patterns of growth controlled by multicellular form and mechanics. *Proc Natl Acad Sci U S A*, 102(33):11594–9, 2005. 27

[126] D. E. Ingber. Mechanical control of tissue growth: function follows form. *Proc Natl Acad Sci U S A*, 102(33):11571–2, 2005. 27

[127] T. Hayashi and R. W. Carthew. Surface mechanics mediate pattern formation in the developing retina. *Nature*, 431(7009):647–52, 2004. 27, 28, 29, 31, 32, 62

[128] J.A.F. Plateau. *Statique experimentale et théorique des liquides soumis aux seules forces moleculaires*. Gauthiers-Villars, Paris, 1873. 28

[129] R. W. Carthew. Pattern formation in the drosophila eye. *Curr Opin Genet Dev*, 17(4):309–13, 2007. 28

[130] Heiko Blaser, Michal Reichman-Fried, Irinka Castanon, Karin Dumstrei, Florence L. Marlow, Koichi Kawakami, Lilianna Solnica-Krezel, Carl-Philipp Heisenberg, and Erez Raz. Migration of zebrafish primordial germ cells: A role for myosin contraction and cytoplasmic flow. *Developmental Cell*, 11(5):613–627, 2006. 29, 31, 158

[131] A. C. Martin, M. Kaschube, and E. F. Wieschaus. Pulsed contractions of an actin-myosin network drive apical constriction. *Nature*, 457(7228):495–9, 2009. 29, 31

[132] A. Rolo, P. Skoglund, and R. Keller. Morphogenetic movements driving neural tube closure in xenopus require myosin iib. *Dev Biol*, 327(2):327–38, 2009. 29

[133] R. Keller, L. A. Davidson, and D. R. Shook. How we are shaped: the biomechanics of gastrulation. *Differentiation*, 71(3):171–205, 2003. 29, 31, 56

[134] L. Wolpert. *Principles of development*. Oxford University Press, Oxford ; New York, 3rd edition, 2007. 29

[135] A. C. Oates, N. Gorfinkiel, M. Gonzalez-Gaitan, and C. P. Heisenberg. Quantitative approaches in developmental biology. *Nat Rev Genet*, 10(8):517–30, 2009. 31, 171

[136] J. Dai, H. P. Ting-Beall, R. M. Hochmuth, M. P. Sheetz, and M. A. Titus. Myosin i contributes to the generation of resting cortical tension. *Biophys J*, 77(2):1168–76, 1999. 31, 58, 61, 83

[137] T. T. Egelhoff, T. V. Naismith, and F. V. Brozovich. Myosin-based cortical tension in dictyostelium resolved into heavy and light chain-regulated components. *J Muscle Res Cell Motil*, 17(2):269–74, 1996. 31

[138] J. Bereiter-Hahn. Mechanics of crawling cells. *Med Eng Phys*, 27(9):743–53, 2005. 31

[139] E. Paluch, M. Piel, J. Prost, M. Bornens, and C. Sykes. Cortical actomyosin breakage triggers shape oscillations in cells and cell fragments. *Biophys J*, 89(1):724–33, 2005. 31, 149, 158

[140] M. Herant, V. Heinrich, and M. Dembo. Mechanics of neutrophil phagocytosis: behavior of the cortical tension. *J Cell Sci*, 118(Pt 9):1789–97, 2005. 31, 61

[141] M. P. Sheetz, J. E. Sable, and H. G. Dobereiner. Continuous membrane-cytoskeleton adhesion requires continuous accommodation to lipid and cytoskeleton dynamics. *Annu Rev Biophys Biomol Struct*, 35:417–34, 2006. 31, 152, 156

[142] J. Dai and M. P. Sheetz. Membrane tether formation from blebbing cells. *Biophys J*, 77(6):3363–70, 1999. 31, 33, 67, 85, 133, 139, 140, 141, 150, 152, 154, 158

[143] G. T. Charras, J. C. Yarrow, M. A. Horton, L. Mahadevan, and T. J. Mitchison. Non-equilibration of hydrostatic pressure in blebbing cells. *Nature*, 435(7040):365–9, 2005. 31, 33, 58, 149, 158

[144] P. Kunda, A. E. Pelling, T. Liu, and B. Baum. Moesin controls cortical rigidity, cell rounding, and spindle morphogenesis during mitosis. *Curr Biol*, 18(2):91–101, 2008. 31, 142, 156

[145] F. Drees, A. Reilein, and W. J. Nelson. Cell-adhesion assays: fabrication of an e-cadherin substratum and isolation of lateral and basal membrane patches. *Methods Mol Biol*, 294:303–20, 2005. 32, 38, 40

[146] W. J. Nelson. Regulation of cell-cell adhesion by the cadherin-catenin complex. *Biochem Soc Trans*, 36(Pt 2):149–55, 2008. 32, 40, 108

[147] S. Yamada and W. J. Nelson. Localized zones of rho and rac activities drive initiation and expansion of epithelial cell-cell adhesion. *J Cell Biol*, 178(3):517–27, 2007. 32

[148] A. Zidovska and E. Sackmann. Brownian motion of nucleated cell envelopes impedes adhesion. *Phys Rev Lett*, 96(4):048103, 2006. 32, 61, 136

[149] O. T. Fackler and R. Grosse. Cell motility through plasma membrane blebbing. *J Cell Biol*, 181(6):879–84, 2008. 33, 157

[150] G. T. Charras, M. Coughlin, T. J. Mitchison, and L. Mahadevan. Life and times of a cellular bleb. *Biophys J*, 94(5):1836–53, 2008. 33, 146

[151] J. C. Mills, N. L. Stone, J. Erhardt, and R. N. Pittman. Apoptotic membrane blebbing is regulated by myosin light chain phosphorylation. *J Cell Biol*, 140(3):627–36, 1998. 33

[152] E. Paluch, J. van der Gucht, and C. Sykes. Cracking up: symmetry breaking in cellular systems. *J Cell Biol*, 175(5):687–92, 2006. 33, 34, 149

[153] Bruce Alberts. *Molecular biology of the cell*. Garland Science, New York, 5th edition, 2008. 34, 37, 40, 143

[154] R. S. Fischer, M. Gardel, X. Ma, R. S. Adelstein, and C. M. Waterman. Local cortical tension by myosin ii guides 3d endothelial cell branching. *Curr Biol*, 19(3):260–5, 2009. 34

[155] F. Ulrich, M. Krieg, E. M. Schotz, V. Link, I. Castanon, V. Schnabel, A. Taubenberger, D. Mueller, P. H. Puech, and C. P. Heisenberg. Wnt11 functions in gastrulation by controlling cell cohesion through rab5c and e-cadherin. *Dev Cell*, 9(4):555–64, 2005. 34, 39, 54, 76, 81, 96, 98

[156] L. Langbein and J. Schweizer. Keratins of the human hair follicle. *Int Rev Cytol*, 243:1–78, 2005. 35

[157] V. Petit and J. P. Thiery. Focal adhesions: structure and dynamics. *Biol Cell*, 92(7):477–94, 2000. 35

[158] E. Ruoslahti. Rgd and other recognition sequences for integrins. *Annu Rev Cell Dev Biol*, 12:697–715, 1996. 35

[159] J. A. Askari, P. A. Buckley, A. P. Mould, and M. J. Humphries. Linking integrin conformation to function. *J Cell Sci*, 122(Pt 2):165–70, 2009. 35

[160] R. Zaidel-Bar, S. Itzkovitz, A. Ma'ayan, R. Iyengar, and B. Geiger. Functional atlas of the integrin adhesome. *Nat Cell Biol*, 9(8):858–67, 2007. 35

[161] T. Ludwig, R. Kirmse, K. Poole, and U. S. Schwarz. Probing cellular microenvironments and tissue remodeling by atomic force microscopy. *Pflugers Arch*, 456(1):29–49, 2008. 35

[162] J. P. Xiong, B. Mahalingham, J. L. Alonso, L. A. Borrelli, X. Rui, S. Anand, B. T. Hyman, T. Rysiok, D. Muller-Pompalla, S. L. Goodman, and M. A. Arnaout. Crystal structure of the complete integrin alphavbeta3 ectodomain plus an alpha/beta transmembrane fragment. *J Cell Biol*, 186(4):589–600, 2009. 36

[163] J. D. Humphries, P. Wang, C. Streuli, B. Geiger, M. J. Humphries, and C. Ballestrem. Vinculin controls focal adhesion formation by direct interactions with talin and actin. *J Cell Biol*, 179(5):1043–57, 2007. 36

[164] R. Winklbauer and R. E. Keller. Fibronectin, mesoderm migration, and gastrulation in xenopus. *Dev Biol*, 177(2):413–26, 1996. 35

[165] S. K. Sastry and A. F. Horwitz. Adhesion-growth factor interactions during differentiation: an integrated biological response. *Dev Biol*, 180(2):455–67, 1996. 36

[166] M. Takeichi. Functional correlation between cell adhesive properties and some cell surface proteins. *J Cell Biol*, 75(2 Pt 1):464–74, 1977. 36

[167] L. Shapiro, A. M. Fannon, P. D. Kwong, A. Thompson, M. S. Lehmann, G. Grubel, J. F. Legrand, J. Als-Nielsen, D. R. Colman, and W. A. Hendrickson. Structural basis of cell-cell adhesion by cadherins. *Nature*, 374(6520):327–37, 1995. 36

[168] B. M. Gumbiner. Regulation of cadherin-mediated adhesion in morphogenesis. *Nat Rev Mol Cell Biol*, 6(8):622–34, 2005. 37, 39

[169] C. Redies, K. Vanhalst, and F. Roy. delta-protocadherins: unique structures and functions. *Cell Mol Life Sci*, 62(23):2840–52, 2005. 37

[170] S. Hirano, Q. Yan, and S. T. Suzuki. Expression of a novel protocadherin, ol-protocadherin, in a subset of functional systems of the developing mouse brain. *J Neurosci*, 19(3):995–1005, 1999. 37

[171] X. Chen and B. M. Gumbiner. Paraxial protocadherin mediates cell sorting and tissue morphogenesis by regulating c-cadherin adhesion activity. *J Cell Biol*, 174(2):301–13, 2006. 37, 129, 164

[172] E. Fukuda, S. Hamada, S. Hasegawa, S. Katori, M. Sanbo, T. Miyakawa, T. Yamamoto, H. Yamamoto, T. Hirabayashi, and T. Yagi. Down-regulation of protocadherin-alpha a isoforms in mice changes contextual fear conditioning and spatial working memory. *Eur J Neurosci*, 28(7):1362–76, 2008. 37

[173] J. M. Halbleib and W. J. Nelson. Cadherins in development: cell adhesion, sorting, and tissue morphogenesis. *Genes Dev*, 20(23):3199–214, 2006. 37

[174] M. T. Veeman, J. D. Axelrod, and R. T. Moon. A second canon. functions and mechanisms of beta-catenin-independent wnt signaling. *Dev Cell*, 5(3):367–77, 2003. 37

[175] F. Carreira-Barbosa, M. Kajita, V. Morel, H. Wada, H. Okamoto, A. Martinez Arias, Y. Fujita, S. W. Wilson, and M. Tada. Flamingo regulates epiboly and convergence/extension movements through cell cohesive and signalling functions during zebrafish gastrulation. *Development*, 136(3):383–92, 2009. 37, 43, 124

[176] M. Frank and R. Kemler. Protocadherins. *Curr Opin Cell Biol*, 14(5):557–62, 2002. 37

[177] S. D. Patel, C. P. Chen, F. Bahna, B. Honig, and L. Shapiro. Cadherin-mediated cell-cell adhesion: sticking together as a family. *Curr Opin Struct Biol*, 13(6):690–8, 2003. 37, 39, 40

[178] M. J. Moeller, A. Soofi, G. S. Braun, X. Li, C. Watzl, W. Kriz, and L. B. Holzman. Protocadherin fat1 binds ena/vasp proteins and is necessary for actin dynamics and cell polarization. *EMBO J*, 23(19):3769–79, 2004. 37

[179] M. Overduin, T. S. Harvey, S. Bagby, K. I. Tong, P. Yau, M. Takeichi, and M. Ikura. Solution structure of the epithelial cadherin domain responsible for selective cell adhesion. *Science*, 267(5196):386–9, 1995. 38

[180] O. Pertz, D. Bozic, A. W. Koch, C. Fauser, A. Brancaccio, and J. Engel. A new crystal structure, ca2+ dependence and mutational analysis reveal molecular details of e-cadherin homoassociation. *Embo J*, 18(7):1738–47, 1999. 38

[181] T. J. Boggon, J. Murray, S. Chappuis-Flament, E. Wong, B. M. Gumbiner, and L. Shapiro. C-cadherin ectodomain structure and implications for cell adhesion mechanisms. *Science*, 296(5571):1308–13, 2002. 38

[182] C. P. Chen, S. Posy, A. Ben-Shaul, L. Shapiro, and B. H. Honig. Specificity of cell-cell adhesion by classical cadherins: Critical role for low-affinity dimerization through beta-strand swapping. *Proc Natl Acad Sci U S A*, 102(24):8531–6, 2005. 38, 39, 41

[183] W. He, P. Cowin, and D. L. Stokes. Untangling desmosomal knots with electron tomography. *Science*, 302(5642):109–13, 2003. 38

[184] O. Huber, R. Kemler, and D. Langosch. Mutations affecting transmembrane segment interactions impair adhesiveness of e-cadherin. *J Cell Sci*, 112 (Pt 23):4415–23, 1999. 38

[185] A. Nose, A. Nagafuchi, and M. Takeichi. Expressed recombinant cadherins mediate cell sorting in model systems. *Cell*, 54(7):993–1001, 1988. 39

[186] P. Panorchan, M. S. Thompson, K. J. Davis, Y. Tseng, K. Konstantopoulos, and D. Wirtz. Single-molecule analysis of cadherin-mediated cell-cell adhesion. *J Cell Sci*, 119(Pt 1):66–74, 2006. 39, 51

[187] Y. S. Chu, W. A. Thomas, O. Eder, F. Pincet, E. Perez, J. P. Thiery, and S. Dufour. Force measurements in e-cadherin-mediated cell doublets reveal rapid adhesion strengthened by actin cytoskeleton remodeling through rac and cdc42. *J Cell Biol*, 167(6):1183–94, 2004. 39, 48, 49

[188] C. M. Niessen and B. M. Gumbiner. Cadherin-mediated cell sorting not determined by binding or adhesion specificity. *J Cell Biol*, 156(2):389–399, 2002. 39, 109

[189] Q. Shi, Y. H. Chien, and D. Leckband. Biophysical properties of cadherin bonds do not predict cell sorting. *J Biol Chem*, 283(42):28454–63, 2008. 39, 109, 110

[190] A. K. Prakasam, V. Maruthamuthu, and D. E. Leckband. Similarities between heterophilic and homophilic cadherin adhesion. *Proc Natl Acad Sci U S A*, 103(42):15434–9, 2006. 39, 110

[191] S. Chappuis-Flament, E. Wong, L. D. Hicks, C. M. Kay, and B. M. Gumbiner. Multiple cadherin extracellular repeats mediate homophilic binding and adhesion. *J Cell Biol*, 154(1):231–43, 2001. 39

[192] K. Tamura, W. S. Shan, W. A. Hendrickson, D. R. Colman, and L. Shapiro. Structure-function analysis of cell adhesion by neural (n-) cadherin. *Neuron*, 20(6):1153–63, 1998. 39

[193] E. Perret, A. M. Benoliel, P. Nassoy, A. Pierres, V. Delmas, J. P. Thiery, P. Bongrand, and H. Feracci. Fast dissociation kinetics between individual e-cadherin fragments revealed by flow chamber analysis. *Embo J*, 21(11):2537–46, 2002. 39, 46

[194] Q. Meng, M. Qi, D. Z. Chen, R. Yuan, I. D. Goldberg, E. M. Rosen, K. Auborn, and S. Fan. Suppression of breast cancer invasion and migration by indole-3-carbinol: associated with up-regulation of brca1 and e-cadherin/catenin complexes. *J Mol Med*, 78(3):155–65, 2000. 39

[195] MP. de Melo, TM. Lima, TC. Pithon-Curi, and R. Curi. The mechanism of indole acetic acid cytotoxicity. *Toxicology letters*, 148:103–111, 2004. 39

[196] E. J. Williams, G. Williams, B. Gour, O. Blaschuk, and P. Doherty. Inp, a novel n-cadherin antagonist targeted to the amino acids that flank the hav motif. *Mol Cell Neurosci*, 15(5):456–64, 2000. 39

[197] D. Leckband. Beyond structure: mechanism and dynamics of intercellular adhesion. *Biochem Soc Trans*, 36(Pt 2):213–20, 2008. 39

[198] R. Winklbauer, A. Medina, R. K. Swain, and H. Steinbeisser. Frizzled-7 signalling controls tissue separation during xenopus gastrulation. *Nature*, 413(6858):856–60, 2001. 40

[199] J. Heasman, A. Crawford, K. Goldstone, P. Garner-Hamrick, B. Gumbiner, P. McCrea, C. Kintner, C. Y. Noro, and C. Wylie. Overexpression of cadherins and underexpression of beta-catenin inhibit dorsal mesoderm induction in early xenopus embryos. *Cell*, 79(5):791–803, 1994. 40

[200] A. Hartsock and W. J. Nelson. Adherens and tight junctions: structure, function and connections to the actin cytoskeleton. *Biochim Biophys Acta*, 1778(3):660–9, 2008. 40, 108

[201] A. B. Reynolds and A. Roczniak-Ferguson. Emerging roles for p120-catenin in cell adhesion and cancer. *Oncogene*, 23(48):7947–56, 2004. 40

[202] W. Meng, Y. Mushika, T. Ichii, and M. Takeichi. Anchorage of microtubule minus ends to adherens junctions regulates epithelial cell-cell contacts. *Cell*, 135(5):948–59, 2008. 40

[203] X. Chen, S. Kojima, G. G. Borisy, and K. J. Green. p120 catenin associates with kinesin and facilitates the transport of cadherin-catenin complexes to intercellular junctions. *J Cell Biol*, 163(3):547–57, 2003. 40

[204] S. W. Kim, J. I. Park, C. M. Spring, A. K. Sater, H. Ji, A. A. Otchere, J. M. Daniel, and P. D. McCrea. Non-canonical wnt signals are modulated by the kaiso transcriptional repressor and p120-catenin. *Nat Cell Biol*, 6(12):1212–20, 2004. 40

[205] M. Takeichi, S. Nakagawa, S. Aono, T. Usui, and T. Uemura. Patterning of cell assemblies regulated by adhesion receptors of the cadherin superfamily. *Philos Trans R Soc Lond B Biol Sci*, 355(1399):885–90, 2000. 40

[206] H. Posthaus, C. M. Dubois, M. H. Laprise, F. Grondin, M. M. Suter, and E. Muller. Proprotein cleavage of e-cadherin by furin in baculovirus over-expression system: potential role of other convertases in mammalian cells. *FEBS Lett*, 438(3):306–10, 1998. 41

[207] M. Ozawa, M. Ringwald, and R. Kemler. Uvomorulin-catenin complex formation is regulated by a specific domain in the cytoplasmic region of the cell adhesion molecule. *Proc Natl Acad Sci U S A*, 87(11):4246–50, 1990. 41

[208] R. Pey, C. Vial, G. Schatten, and M. Hafner. Increase of intracellular ca2+ and relocation of e-cadherin during experimental decompaction of mouse embryos. *Proc Natl Acad Sci U S A*, 95(22):12977–82, 1998. 41

[209] L. A. Taneyhill. To adhere or not to adhere: the role of cadherins in neural crest development. *Cell Adh Migr*, 2(4):223–30, 2008. 41

[210] C. A. Cowan and M. Henkemeyer. Ephrins in reverse, park and drive. *Trends Cell Biol*, 12(7):339–46, 2002. 41

[211] D. J. Muller, M. Krieg, D. Alsteens, and Y. F. Dufrene. New frontiers in atomic force microscopy: analyzing interactions from single-molecules to cells. *Curr Opin Biotechnol*, 20(1):4–13, 2009. 42, 53

[212] M. S. Steinberg. Differential adhesion in morphogenesis: a modern view. *Curr Opin Genet Dev*, 17(4):281–6, 2007. 42

[213] F. Ahimou, L. P. Mok, B. Bardot, and C. Wesley. The adhesion force of notch with delta and the rate of notch signaling. *J Cell Biol*, 167(6):1217–29, 2004. 42, 54, 55

[214] R. P. McEver and C. Zhu. Rolling adhesion. *Annu Rev Cell Dev Biol*, 2009. 42, 46

[215] U. Cavallaro and G. Christofori. Cell adhesion and signalling by cadherins and ig-cams in cancer. *Nat Rev Cancer*, 4(2):118–32, 2004. 42

[216] J. Helenius, C. P. Heisenberg, H. E. Gaub, and D. J. Muller. Single-cell force spectroscopy. *J Cell Sci*, 121(Pt 11):1785–91, 2008. 42

[217] Jr. Enmon, R. M., K. C. O'Connor, D. J. Lacks, D. K. Schwartz, and R. S. Dotson. Dynamics of spheroid self-assembly in liquid-overlay culture of du 145 human prostate cancer cells. *Biotechnol Bioeng*, 72(6):579–91, 2001. 43

[218] Jr. Enmon, R. M., K. C. O'Connor, H. Song, D. J. Lacks, and D. K. Schwartz. Aggregation kinetics of well and poorly differentiated human prostate cancer cells. *Biotechnol Bioeng*, 80(5):580–8, 2002. 43

[219] G. Pearce, V. Angeli, G. J. Randolph, T. Junt, U. von Andrian, H. J. Schnittler, and R. Jessberger. Signaling protein swap-70 is required for efficient b cell homing to lymphoid organs. *Nat Immunol*, 7(8):827–34, 2006. 43

[220] H. M. Phillips, L. L. Wiseman, and M. S. Steinburg. Self vs nonself in tissue assembly. correlated changes in recognition behavior and tissue cohesiveness. *Dev Biol*, 57(1):150–9, 1977. 43

[221] M. S. Steinberg. "ecm": its nature, origin and function in cell aggregation. *Exp Cell Res*, 30:257–79, 1963. 44

[222] H. M. Phillips and M. S. Steinberg. Embryonic tissues as elasticoviscous liquids. i. rapid and slow shape changes in centrifuged cell aggregates. *J Cell Sci*, 30:1–20, 1978. 44

[223] R. David, H. Ninomiya, R. Winklbauer, and A. W. Neumann. Tissue surface tension measurement by rigorous axisymmetric drop shape analysis. *Colloids Surf B Biointerfaces*, 2009. 44

[224] A. Kalantarian, H. Ninomiya, S. M. Saad, R. David, R. Winklbauer, and A. W. Neumann. Axisymmetric drop shape analysis for estimating the surface tension of cell aggregates by centrifugation. *Biophys J*, 96(4):1606–16, 2009. 44, 45

[225] H. M. Phillips and G. Davis. Liquid-tissue mechanics in amphibian gastrulation: Germ-layer assembly in rana pipiens. *American Zoologist*, 18:81–93, 1978. 44

[226] W. A. Moyer and M. S. Steinberg. Do rates of intercellular adhesion measure the cell affinities reflected in cell-sorting and tissue-spreading configurations? *Dev Biol*, 52(2):246–62, 1976. 45, 108

[227] R. J. Klebe. Isolation of a collagen-dependent cell attachment factor. *Nature*, 250(463):248–51, 1974. 45

[228] F. A. Fierro, A. Taubenberger, P. H. Puech, G. Ehninger, M. Bornhauser, D. J. Muller, and T. Illmer. Bcr/abl expression of myeloid progenitors increases beta1-integrin mediated adhesion to stromal cells. *J Mol Biol*, 377(4):1082–93, 2008. 45, 54

[229] O. Tissot, A. Pierres, C. Foa, M. Delaage, and P. Bongrand. Motion of cells sedimenting on a solid surface in a laminar shear flow. *Biophys J*, 61(1):204–15, 1992. 46

[230] J. Lou, T. Yago, A. G. Klopocki, P. Mehta, W. Chen, V. I. Zarnitsyna, N. V. Bovin, C. Zhu, and R. P. McEver. Flow-enhanced adhesion regulated by a selectin interdomain hinge. *J Cell Biol*, 174(7):1107–17, 2006. 46, 47, 163

[231] A. M. Benoliel, N. Pirro, V. Marin, B. Consentino, A. Pierres, J. Vitte, P. Bongrand, I. Sielezneff, and B. Sastre. Correlation between invasiveness of colorectal tumor cells and adhesive potential under flow. *Anticancer Res*, 23(6C):4891–6, 2003. 46

[232] A. Pierres, D. Touchard, A. M. Benoliel, and P. Bongrand. Dissecting streptavidin-biotin interaction with a laminar flow chamber. *Biophys J*, 82(6):3214–23, 2002. 46

[233] A. J. Garcia, F. Huber, and D. Boettiger. Force required to break alpha5beta1 integrin-fibronectin bonds in intact adherent cells is sensitive to integrin activation state. *J Biol Chem*, 273(18):10988–93, 1998. 46, 47

[234] A. J. Garcia and N. D. Gallant. Stick and grip: measurement systems and quantitative analyses of integrin-mediated cell adhesion strength. *Cell Biochem Biophys*, 39(1):61–73, 2003. 46, 47

[235] O. Thoumine, A. Ott, and D. Louvard. Critical centrifugal forces induce adhesion rupture or structural reorganization in cultured cells. *Cell Motil Cytoskeleton*, 33(4):276–87, 1996. 46

[236] Y. S. Chu, O. Eder, W. A. Thomas, I. Simcha, F. Pincet, A. Ben-Ze'ev, E. Perez, J. P. Thiery, and S. Dufour. Prototypical type i e-cadherin and type ii cadherin-7 mediate very distinct adhesiveness through their extracellular domains. *J Biol Chem*, 281(5):2901–10, 2006. 48

[237] A. R. Bausch, W. Moller, and E. Sackmann. Measurement of local viscoelasticity and forces in living cells by magnetic tweezers. *Biophys J*, 76(1 Pt 1):573–9, 1999. 49, 67

[238] N. Walter, C. Selhuber, H. Kessler, and J. P. Spatz. Cellular unbinding forces of initial adhesion processes on nanopatterned surfaces probed with magnetic tweezers. *Nano Lett*, 6(3):398–402, 2006. 49

[239] F. J. Alenghat, B. Fabry, K. Y. Tsai, W. H. Goldmann, and D. E. Ingber. Analysis of cell mechanics in single vinculin-deficient cells using a magnetic tweezer. *Biochem Biophys Res Commun*, 277(1):93–9, 2000. 49

[240] G. Massiera, K. M. Van Citters, P. L. Biancaniello, and J. C. Crocker. Mechanics of single cells: rheology, time dependence, and fluctuations. *Biophys J*, 93(10):3703–13, 2007. 49

[241] J. R. Moffitt, Y. R. Chemla, S. B. Smith, and C. Bustamante. Recent advances in optical tweezers. *Annu Rev Biochem*, 77:205–28, 2008. 50

[242] E. Schaffer, S. F. Norrelykke, and J. Howard. Surface forces and drag coefficients of microspheres near a plane surface measured with optical tweezers. *Langmuir*, 23(7):3654–65, 2007. 50

[243] N. Schlegel and J. Waschke. Impaired integrin-mediated adhesion contributes to reduced barrier properties in vasp-deficient microvascular endothelium. *J Cell Physiol*, 220(2):357–66, 2009. 50

[244] W. Baumgartner, N. Golenhofen, N. Grundhofer, J. Wiegand, and D. Drenckhahn. Ca2+ dependency of n-cadherin function probed by laser tweezer and atomic force microscopy. *J Neurosci*, 23(35):11008–14, 2003. 50, 164

[245] V. Bormuth, A. Jannasch, M. Ander, C. M. van Kats, A. van Blaaderen, J. Howard, and E. Schaffer. Optical trapping of coated microspheres. *Opt Express*, 16(18):13831–44, 2008. 50

[246] E. J. Peterman, F. Gittes, and C. F. Schmidt. Laser-induced heating in optical traps. *Biophys J*, 84(2 Pt 1):1308–16, 2003. 50

[247] Y. Liu, D. K. Cheng, G. J. Sonek, M. W. Berns, C. F. Chapman, and B. J. Tromberg. Evidence for localized cell heating induced by infrared optical tweezers. *Biophys J*, 68(5):2137–44, 1995. 50

[248] G. Sagvolden. Protein adhesion force dynamics and single adhesion events. *Biophys J*, 77(1):526–32, 1999. 51

[249] G. Sagvolden, I. Giaever, E. O. Pettersen, and J. Feder. Cell adhesion force microscopy. *Proc Natl Acad Sci U S A*, 96(2):471–6, 1999. 51

[250] M. Sun, J. S. Graham, B. Hegedus, F. Marga, Y. Zhang, G. Forgacs, and M. Grandbois. Multiple membrane tethers probed by atomic force microscopy. *Biophys J*, 89(6):4320–9, 2005. 51, 139

[251] G. Ng, K. Sharma, S. M. Ward, M. D. Desrosiers, L. A. Stephens, W. M. Schoel, T. Li, C. A. Lowell, C. C. Ling, M. W. Amrein, and Y. Shi. Receptor-independent, direct membrane binding leads to cell-surface lipid sorting and syk kinase activation in dendritic cells. *Immunity*, 29(5):807–18, 2008. 51

[252] X. Zhang, E. Wojcikiewicz, and V. T. Moy. Force spectroscopy of the leukocyte function-associated antigen-1/intercellular adhesion molecule-1 interaction. *Biophys J*, 83(4):2270–9, 2002. 51

[253] A. Taubenberger, D. A. Cisneros, J. Friedrichs, P. H. Puech, D. J. Muller, and C. M. Franz. Revealing early steps of alpha2beta1 integrin-mediated adhesion to collagen type i by using single-cell force spectroscopy. *Mol Biol Cell*, 18(5):1634–44, 2007. 51, 54, 55

[254] M. Benoit and H. E. Gaub. Measuring cell adhesion forces with the atomic force microscope at the molecular level. *Cells Tissues Organs*, 172(3):174–89, 2002. 51, 52, 53

[255] C. Selhuber-Unkel, M. Lopez-Garcia, H. Kessler, and J. P. Spatz. Cooperativity in adhesion cluster formation during initial cell adhesion. *Biophys J*, 95(11):5424–31, 2008. 52

[256] M. Benoit, D. Gabriel, G. Gerisch, and H. E. Gaub. Discrete interactions in cell adhesion measured by single-molecule force spectroscopy. *Nat Cell Biol*, 2(6):313–7, 2000. 52, 53, 87

[257] G. Shaulsky and R. H. Kessin. The cold war of the social amoebae. *Curr Biol*, 17(16):R684–92, 2007. 52

[258] M. Benoit. *Kraftspektroskopie an lebenden Zellen*. Phd, 2000. 53

[259] O. Chaudhuri, S. H. Parekh, W. A. Lam, and D. A. Fletcher. Combined atomic force microscopy and side-view optical imaging for mechanical studies of cells. *Nat Methods*, 6(5):383–7, 2009. 53

[260] D. A. Cisneros, L. Oberbarnscheidt, A. Pannier, J. P. Klare, J. Helenius, M. Engelhard, F. Oesterhelt, and D. J. Muller. Transducer binding establishes localized interactions to tune sensory rhodopsin ii. *Structure*, 16(8):1206–13, 2008. 53

[261] A. Kedrov, M. Krieg, C. Ziegler, W. Kuhlbrandt, and D. J. Muller. Locating ligand binding and activation of a single antiporter. *EMBO Rep*, 6(7):668–74, 2005. 53

[262] D. J. Muller and Y. F. Dufrene. Atomic force microscopy as a multifunctional molecular toolbox in nanobiotechnology. *Nat Nanotechnol*, 3(5):261–9, 2008. 53

[263] B. T. Marshall, M. Long, J. W. Piper, T. Yago, R. P. McEver, and C. Zhu. Direct observation of catch bonds involving cell-adhesion molecules. *Nature*, 423(6936):190–3, 2003. 53, 162, 163

[264] A. Kedrov, M. Appel, H. Baumann, C. Ziegler, and D. J. Muller. Examining the dynamic energy landscape of an antiporter upon inhibitor binding. *J Mol Biol*, 375(5):1258–66, 2008. 53

[265] J. Friedrichs, A. Manninen, D. J. Muller, and J. Helenius. Galectin-3 regulates integrin alpha2beta1-mediated adhesion to collagen-i and -iv. *J Biol Chem*, 283(47):32264–72, 2008. 54

[266] M. Tulla, J. Helenius, J. Jokinen, A. Taubenberger, D. J. Muller, and J. Heino. Tpa primes alpha2beta1 integrins for cell adhesion. *FEBS Lett*, 582(23-24):3520–4, 2008. 54

[267] P. H. Puech, A. Taubenberger, F. Ulrich, M. Krieg, D. J. Muller, and C. P. Heisenberg. Measuring cell adhesion forces of primary gastrulating cells from zebrafish using atomic force microscopy. *J Cell Sci*, 118(Pt 18):4199–206, 2005. 54, 171

[268] S. Bajpai, J. Correia, Y. Feng, J. Figueiredo, S. X. Sun, G. D. Longmore, G. Suriano, and D. Wirtz. alpha-catenin mediates initial e-cadherin-dependent cell-cell recognition and subsequent bond strengthening. *Proc Natl Acad Sci U S A*, 105(47):18331–6, 2008. 54, 55

[269] R. G. Fehon, P. J. Kooh, I. Rebay, C. L. Regan, T. Xu, M. A. Muskavitch, and S. Artavanis-Tsakonas. Molecular interactions between the protein products of the neurogenic loci notch and delta, two egf-homologous genes in drosophila. *Cell*, 61(3):523–34, 1990. 55

[270] M. Hu, J. Wang, J. Cai, Y. Wu, and X. Wang. Nanostructure and force spectroscopy analysis of human peripheral blood cd4+ t cells using atomic force microscopy. *Biochem Biophys Res Commun*, 374(1):90–4, 2008. 55

[271] C. M. Cuerrier, M. Benoit, G. Guillemette, Jr. Gobeil, F., and M. Grandbois. Real-time monitoring of angiotensin ii-induced contractile response and cytoskeleton remodeling in individual cells by atomic force microscopy. *Pflugers Arch*, 457(6):1361–72, 2009. 55

[272] R. E. Mahaffy, S. Park, E. Gerde, J. Kas, and C. K. Shih. Quantitative analysis of the viscoelastic properties of thin regions of fibroblasts using atomic force microscopy. *Biophys J*, 86(3):1777–93, 2004. 56

[273] E A-Hassan, W. F. Heinz, M. D. Antonik, N. P. D'Costa, S. Nageswaran, C. A. Schoenenberger, and J. H. Hoh. Relative microelastic mapping of living cells by atomic force microscopy. *Biophys J*, 74(3):1564–78, 1998. 56, 67, 69

[274] J. C. Martens and M. Radmacher. Softening of the actin cytoskeleton by inhibition of myosin ii. *Pflugers Arch*, 456(1):95–100, 2008. 56, 67

[275] E. K. Dimitriadis, F. Horkay, J. Maresca, B. Kachar, and R. S. Chadwick. Determination of elastic moduli of thin layers of soft material using the atomic force microscope. *Biophys J*, 82(5):2798–810, 2002. 57, 68, 81, 83

[276] M. Sato, K. Suzuki, Y. Ueki, and T. Ohashi. Microelastic mapping of living endothelial cells exposed to shear stress in relation to three-dimensional distribution of actin filaments. *Acta Biomater*, 3(3):311–9, 2007. 57

[277] M. Radmacher, M. Fritz, C. M. Kacher, J. P. Cleveland, and P. K. Hansma. Measuring the viscoelastic properties of human platelets with the atomic force microscope. *Biophys J*, 70(1):556–67, 1996. 57, 67, 68

[278] Y. F. Dufrene. Towards nanomicrobiology using atomic force microscopy. *Nat Rev Microbiol*, 6(9):674–80, 2008. 57

[279] N. Caille, O. Thoumine, Y. Tardy, and J. J. Meister. Contribution of the nucleus to the mechanical properties of endothelial cells. *J Biomech*, 35(2):177–87, 2002. 57, 67

[280] Y. R. Silberberg, A. E. Pelling, G. E. Yakubov, W. R. Crum, D. J. Hawkes, and M. A. Horton. Mitochondrial displacements in response to nanomechanical forces. *J Mol Recognit*, 21(1):30–6, 2008. 57

[281] A. E. Pelling, D. W. Dawson, D. M. Carreon, J. J. Christiansen, R. R. Shen, M. A. Teitell, and J. K. Gimzewski. Distinct contributions of microtubule subtypes to cell membrane shape and stability. *Nanomedicine*, 3(1):43–52, 2007. 57

[282] J. Guck, S. Schinkinger, B. Lincoln, F. Wottawah, S. Ebert, M. Romeyke, D. Lenz, H. M. Erickson, R. Ananthakrishnan, D. Mitchell, J. Kas, S. Ulvick, and C. Bilby. Optical deformability as an inherent cell marker for testing malignant transformation and metastatic competence. *Biophys J*, 88(5):3689–98, 2005. 57

[283] S. E. Cross, Y. S. Jin, J. Rao, and J. K. Gimzewski. Nanomechanical analysis of cells from cancer patients. *Nat Nanotechnol*, 2(12):780–3, 2007. 57

[284] O. Thoumine and A. Ott. Comparison of the mechanical properties of normal and transformed fibroblasts. *Biorheology*, 34(4-5):309–26, 1997. 57

[285] E. Evans and A. Yeung. Apparent viscosity and cortical tension of blood granulocytes determined by micropipet aspiration. *Biophys J*, 56(1):151–60, 1989. 58, 60, 61, 82, 101

[286] D. V. Zhelev, D. Needham, and R. M. Hochmuth. Role of the membrane cortex in neutrophil deformation in small pipets. *Biophys J*, 67(2):696–705, 1994. 58, 59, 136

[287] Carmela Pasternak, James A. Spudich, and Elliot L. Elson. Capping of surface receptors and concomitant cortical tension are generated by conventional myosin. *Nature*, 341(6242):549–551, 1989. 58, 61, 101

[288] D. Needham and R. M. Hochmuth. A sensitive measure of surface stress in the resting neutrophil. *Biophys J*, 61(6):1664–70, 1992. 59, 60, 61

[289] E. B. Lomakina, C. M. Spillmann, M. R. King, and R. E. Waugh. Rheological analysis and measurement of neutrophil indentation. *Biophys J*, 87(6):4246–58, 2004. 59, 60, 61, 82, 83

[290] C. Pasternak and E. L. Elson. Lymphocyte mechanical response triggered by cross-linking surface receptors. *J Cell Biol*, 100(3):860–72, 1985. 61

[291] O. Thoumine, O. Cardoso, and J. J. Meister. Changes in the mechanical properties of fibroblasts during spreading: a micromanipulation study. *Eur Biophys J*, 28(3):222–34, 1999. 61, 82, 83

[292] M. J. Rosenbluth, W. A. Lam, and D. A. Fletcher. Force microscopy of nonadherent cells: a comparison of leukemia cell deformability. *Biophys J*, 90(8):2994–3003, 2006. 60, 61, 67, 82, 149

[293] J. Lam, M. Herant, M. Dembo, and V. Heinrich. Baseline mechanical characterization of j774 macrophages. *Biophys J*, 2008. 61

[294] R. Moore, K. Q. Cai, D. O. Escudero, and X. X. Xu. Cell adhesive affinity does not dictate primitive endoderm segregation and positioning during murine embryoid body formation. *Genesis*, 47(9):579–589, 2009. 61, 110, 172

[295] G. W. Brodland and H. H. Chen. The mechanics of heterotypic cell aggregates: insights from computer simulations. *J Biomech Eng*, 122(4):402–7, 2000. 62

[296] G. W. Brodland, D. Viens, and J. H. Veldhuis. A new cell-based fe model for the mechanics of embryonic epithelia. *Comput Methods Biomech Biomed Engin*, 10(2):121–8, 2007. 62

[297] J. C. Mombach, J. A. Glazier, R. C. Raphael, and M. Zajac. Quantitative comparison between differential adhesion models and cell sorting in the presence and absence of fluctuations. *Physical Review Letters*, 75(11):2244–2247, 1995. 62

[298] G. Binnig, C. F. Quate, and C. Gerber. Atomic force microscope. *Physical Review Letters*, 56(9):930–933, 1986. 63

[299] Jacob N. Israelachvili. *Intermolecular and surface forces : with applications to colloidal and biological systems*. Academic Press, London ; Orlando, [Fla]., 1985. 64

[300] Hans-Jürgen Butt, Brunero Cappella, and Michael Kappl. Force measurements with the atomic force microscope: Technique, interpretation and applications. *Surface Science Reports*, 59(1-6):1–152, 2005. 64

[301] R. Sonnenfeld and P. K. Hansma. Atomic-resolution microscopy in water. *Science*, 232(4747):211–213, 1986. 64

[302] M. Tortonese. Cantilevers and tips for atomic force microscopy. *IEEE Eng Med Biol Mag*, 16(2):28–33, 1997. 64

[303] G. M. King, A. R. Carter, A. B. Churnside, L. S. Eberle, and T. T. Perkins. Ultrastable atomic force microscopy: atomic-scale stability and registration in ambient conditions. *Nano Lett*, 9(4):1451–6, 2009. 64

[304] J. Alcaraz, L. Buscemi, M. Puig-De-Morales, A. Colchero, M. Baro, and D. Navajas. Correction of microrheological measurements of soft samples with atomic force microscopy for the hydrodynamic drag on the cantilever. *Langmuir*, 18:716–721, 2002. 64, 65

[305] J. L. Hutter and J. Bechhoefer. Calibration of atomic force microscope tips. *Review Scientific Instruments*, 64(7):1868–1873, 1993. 65, 84

[306] J. D. Pajerowski, K. N. Dahl, F. L. Zhong, P. J. Sammak, and D. E. Discher. Physical plasticity of the nucleus in stem cell differentiation. *Proc Natl Acad Sci U S A*, 104(40):15619–24, 2007. 67

[307] E. Henderson, P. G. Haydon, and D. S. Sakaguchi. Actin filament dynamics in living glial cells imaged by atomic force microscopy. *Science*, 257(5078):1944–6, 1992. 67

[308] M. Radmacher. Measuring the elastic properties of living cells by the atomic force microscope. *Methods Cell Biol*, 68:67–90, 2002. 67

[309] W. B. McConnaughey and N. O. Petersen. Cell poker: an apparatus for stress-strain measurements on living cells. *Rev Sci Instrum*, 51(5):575–80, 1980. 67

[310] W. H. Goldmann, R. Galneder, M. Ludwig, A. Kromm, and R. M. Ezzell. Differences in f9 and 5.51 cell elasticity determined by cell poking and atomic force microscopy. *FEBS Lett*, 424(3):139–42, 1998. 67

[311] K. D. Costa. Single-cell elastography: probing for disease with the atomic force microscope. *Dis Markers*, 19(2-3):139–54, 2003. 67

[312] E. C. Faria, N. Ma, E. Gazi, P. Gardner, M. Brown, N. W. Clarke, and R. D. Snook. Measurement of elastic properties of prostate cancer cells using afm. *Analyst*, 133(11):1498–500, 2008. 67

[313] J. Alcaraz, L. Buscemi, M. Grabulosa, X. Trepat, B. Fabry, R. Farre, and D. Navajas. Microrheology of human lung epithelial cells measured by atomic force microscopy. *Biophys J*, 84(3):2071–9, 2003. 67

[314] M. Radmacher. Measuring the elastic properties of biological samples with the afm. *IEEE Eng Med Biol Mag*, 16(2):47–57, 1997. 67

[315] C. Rotsch, F. Braet, E. Wisse, and M. Radmacher. Afm imaging and elasticity measurements on living rat liver macrophages. *Cell Biol Int*, 21(11):685–96, 1997. 67

[316] J. Guck, R. Ananthakrishnan, H. Mahmood, T. J. Moon, C. C. Cunningham, and J. Kas. The optical stretcher: a novel laser tool to micromanipulate cells. *Biophys J*, 81(2):767–84, 2001. 67

[317] W. H. Goldmann, R. Galneder, M. Ludwig, W. Xu, E. D. Adamson, N. Wang, and R. M. Ezzell. Differences in elasticity of vinculin-deficient f9 cells measured by magnetometry and atomic force microscopy. *Exp Cell Res*, 239(2):235–42, 1998. 67

[318] O. Thoumine and A. Ott. Time scale dependent viscoelastic and contractile regimes in fibroblasts probed by microplate manipulation. *J Cell Sci*, 110 (Pt 17):2109–16, 1997. 67

[319] H. Miyazaki, Y. Hasegawa, and K. Hayashi. A newly designed tensile tester for cells and its application to fibroblasts. *J Biomech*, 33(1):97–104, 2000. 67

[320] J. H. Hoh and C. A. Schoenenberger. Surface morphology and mechanical properties of mdck monolayers by atomic force microscopy. *J Cell Sci*, 107 (Pt 5):1105–14, 1994. 67

[321] S. L. Crick and F. C. Yin. Assessing micromechanical properties of cells with atomic force microscopy: importance of the contact point. *Biomech Model Mechanobiol*, 6(3):199–210, 2007. 69, 83

[322] C. Rotsch, K. Jacobson, and M. Radmacher. Dimensional and mechanical dynamics of active and stable edges in motile fibroblasts investigated by using atomic force microscopy. *Proc Natl Acad Sci U S A*, 96(3):921–6, 1999. 69

[323] Y. S. Chu, S. Dufour, J. P. Thiery, E. Perez, and F. Pincet. Johnson-kendall-roberts theory applied to living cells. *Phys Rev Lett*, 94(2):028102, 2005. 70

[324] J. Lippincott-Schwartz, E. Snapp, and A. Kenworthy. Studying protein dynamics in living cells. *Nat Rev Mol Cell Biol*, 2(6):444–56, 2001. 70

[325] B. L. Sprague and J. G. McNally. Frap analysis of binding: proper and fitting. *Trends Cell Biol*, 15(2):84–91, 2005. 70

[326] E. A. Reits and J. J. Neefjes. From fixed to frap: measuring protein mobility and activity in living cells. *Nat Cell Biol*, 3(6):E145–7, 2001. 70, 71

[327] P. G. Saffman and M. Delbruck. Brownian motion in biological membranes. *Proc Natl Acad Sci U S A*, 72(8):3111–3, 1975. 71, 141, 154

[328] F. M. Hochmuth, J. Y. Shao, J. Dai, and M. P. Sheetz. Deformation and flow of membrane into tethers extracted from neuronal growth cones. *Biophys J*, 70(1):358–69, 1996. 71, 85, 133, 140, 150, 152, 153, 154, 155

[329] J. Dai and M. P. Sheetz. Axon membrane flows from the growth cone to the cell body. *Cell*, 83(5):693–701, 1995. 71, 133, 140, 152, 153

[330] J. S. Goodwin, K. R. Drake, C. L. Remmert, and A. K. Kenworthy. Ras diffusion is sensitive to plasma membrane viscosity. *Biophys J*, 89(2):1398–410, 2005. 72, 153, 154

[331] P. F. Lenne, L. Wawrezinieck, F. Conchonaud, O. Wurtz, A. Boned, X. J. Guo, H. Rigneault, H. T. He, and D. Marguet. Dynamic molecular confinement in the plasma membrane by microdomains and the cytoskeleton meshwork. *EMBO J*, 25(14):3245–56, 2006. 72

[332] K. Jacobson, Y. Hou, Z. Derzko, J. Wojcieszyn, and D. Organisciak. Lipid lateral diffusion in the surface membrane of cells and in multibilayers formed from plasma membrane lipids. *Biochemistry*, 20(18):5268–75, 1981. 72

[333] T. Fujiwara, K. Ritchie, H. Murakoshi, K. Jacobson, and A. Kusumi. Phospholipids undergo hop diffusion in compartmentalized cell membrane. *J Cell Biol*, 157(6):1071–81, 2002. 72

[334] J. N. Rosen, M. F. Sweeney, and J. D. Mably. Microinjection of zebrafish embryos to analyze gene function. *J Vis Exp*, (25), 2009. 73

[335] S. Yuan and Z. Sun. Microinjection of mrna and morpholino antisense oligonucleotides in zebrafish embryos. *J Vis Exp*, (27), 2009. 73

[336] M. R. Rebagliati, R. Toyama, P. Haffter, and I. B. Dawid. cyclops encodes a nodal-related factor involved in midline signaling. *Proc Natl Acad Sci U S A*, 95(17):9932–7, 1998. 74

[337] Y. Chen and A. F. Schier. Lefty proteins are long-range inhibitors of squint-mediated nodal signaling. *Curr Biol*, 12(24):2124–8, 2002. 74, 102

[338] G. T. Charras, C. K. Hu, M. Coughlin, and T. J. Mitchison. Reassembly of contractile actin cortex in cell blebs. *J Cell Biol*, 175(3):477–90, 2006. 74, 76, 144, 146, 148, 166

[339] S. Witzel, V. Zimyanin, F. Carreira-Barbosa, M. Tada, and C. P. Heisenberg. Wnt11 controls cell contact persistence by local accumulation of frizzled 7 at the plasma membrane. *J Cell Biol*, 175(5):791–802, 2006. 74

[340] J. Riedl, A. H. Crevenna, K. Kessenbrock, J. H. Yu, D. Neukirchen, M. Bista, F. Bradke, D. Jenne, T. A. Holak, Z. Werb, M. Sixt, and R. Wedlich-Soldner. Lifeact: a versatile marker to visualize f-actin. *Nat Methods*, 5(7):605–7, 2008. 74, 89

[341] Z. Lele, A. Folchert, M. Concha, G. J. Rauch, R. Geisler, F. Rosa, S. W. Wilson, M. Hammerschmidt, and L. Bally-Cuif. parachute/n-cadherin is required for morphogenesis and maintained integrity of the zebrafish neural tube. *Development*, 129(14):3281–94, 2002. 75, 101, 120

[342] M. Poulain and T. Lepage. Mezzo, a paired-like homeobox protein is an immediate target of nodal signalling and regulates endoderm specification in zebrafish. *Development*, 129(21):4901–14, 2002. 75

[343] M. Kovacs, J. Toth, C. Hetenyi, A. Malnasi-Csizmadia, and J. R. Sellers. Mechanism of blebbistatin inhibition of myosin ii. *J Biol Chem*, 279(34):35557–63, 2004. 76

[344] E. M. Ostap. 2,3-butanedione monoxime (bdm) as a myosin inhibitor. *J Muscle Res Cell Motil*, 23(4):305–8, 2002. 76

[345] C. A. de Oliveira and B. Mantovani. Latrunculin a is a potent inhibitor of phagocytosis by macrophages. *Life Sci*, 43(22):1825–30, 1988. 76

[346] P. N. Kanellopoulos, K. Pavlou, A. Perrakis, B. Agianian, C. E. Vorgias, C. Mavrommatis, M. Soufi, P. A. Tucker, and S. J. Hamodrakas. The crystal structure of the complexes of concanavalin a with 4'-nitrophenyl-alpha-d-mannopyranoside and 4'-nitrophenyl-alpha-d-glucopyranoside. *J Struct Biol*, 116(3):345–55, 1996. 76

[347] P. H. Puech, K. Poole, D. Knebel, and D. J. Muller. A new technical approach to quantify cell-cell adhesion forces by afm. *Ultramicroscopy*, 106(8-9):637–44, 2006. 79, 172

[348] L. Bo and R. E. Waugh. Determination of bilayer membrane bending stiffness by tether formation from giant, thin-walled vesicles. *Biophys J*, 55(3):509–17, 1989. 85, 136

[349] J. Dai and M. P. Sheetz. Mechanical properties of neuronal growth cone membranes studied by tether formation with laser optical tweezers. *Biophys J*, 68(3):988–96, 1995. 85

[350] G. Charras and E. Paluch. Blebs lead the way: how to migrate without lamellipodia. *Nat Rev Mol Cell Biol*, 9(9):730–6, 2008. 85, 133, 135, 136, 149, 156

[351] M. Sun, N. Northup, F. Marga, T. Huber, F. J. Byfield, I. Levitan, and G. Forgacs. The effect of cellular cholesterol on membrane-cytoskeleton adhesion. *J Cell Sci*, 120(Pt 13):2223–31, 2007. 85, 139, 150, 152, 153, 154

[352] E. A. Evans and R. Skalak. Mechanics and thermodynamics of biomembranes: part 2. *CRC Crit Rev Bioeng*, 3(4):331–418, 1979. 85, 132

[353] G.T. Hermanson. *Bioconjugate Techniques*. Academic Press, 1996. 87

[354] H. Qian, M. P. Sheetz, and E. L. Elson. Single particle tracking. analysis of diffusion and flow in two-dimensional systems. *Biophys J*, 60(4):910–21, 1991. 90

[355] B. Geiger, T. Volberg, D. Ginsberg, S. Bitzur, I. Sabanay, and R. O. Hynes. Broad spectrum pan-cadherin antibodies, reactive with the c-terminal 24 amino acid residues of n-cadherin. *J Cell Sci*, 97 (Pt 4):607–14, 1990. 93, 98

[356] J. A. Montero and C. P. Heisenberg. Gastrulation dynamics: cells move into focus. *Trends Cell Biol*, 14(11):620–7, 2004. 95

[357] R. M. Warga and D. A. Kane. A role for n-cadherin in mesodermal morphogenesis during gastrulation. *Dev Biol*, 310(2):211–25, 2007. 101, 116, 120

[358] S. Bitzur, Z. Kam, and B. Geiger. Structure and distribution of n-cadherin in developing zebrafish embryos: morphogenetic effects of ectopic over-expression. *Dev Dyn*, 201(2):121–36, 1994. 101

[359] N. B. David and F. M. Rosa. Cell autonomous commitment to an endodermal fate and behaviour by activation of nodal signalling. *Development*, 128(20):3937–47, 2001. 103

[360] D. Dormann, B. Vasiev, and C. J. Weijer. The control of chemotactic cell movement during dictyostelium morphogenesis. *Philos Trans R Soc Lond B Biol Sci*, 355(1399):983–91, 2000. 108

[361] J. Kafer, P. Hogeweg, and A. F. Maree. Moving forward moving backward: directional sorting of chemotactic cells due to size and adhesion differences. *PLoS Comput Biol*, 2(6):e56, 2006. 108

[362] K. J. Painter. Continuous models for cell migration in tissues and applications to cell sorting via differential chemotaxis. *Bull Math Biol*, 71(5):1117–47, 2009. 108

[363] L. N. Nejsum and W. J. Nelson. Epithelial cell surface polarity: the early steps. *Front Biosci*, 14:1088–98, 2009. 108

[364] AK Harris. A dozen questions about how tissue cells crawl. *Biochemical Society Symposia*, 65:315–41, 1999. 108

[365] L. L. Wiseman, M. S. Steinberg, and H. M. Phillips. Experimental modulation of intercellular cohesiveness: reversal of tissue assembly patterns. *Dev Biol*, 28(3):498–517, 1972. 109

[366] D. R. Friedlander, R. M. Mege, B. A. Cunningham, and G. M. Edelman. Cell sorting-out is modulated by both the specificity and amount of different cell adhesion molecules (cams) expressed on cell surfaces. *Proc Natl Acad Sci U S A*, 86(18):7043–7, 1989. 109

[367] P. Katsamba, K. Carroll, G. Ahlsen, F. Bahna, J. Vendome, S. Posy, M. Rajebhosale, S. Price, T. M. Jessell, A. Ben-Shaul, L. Shapiro, and B. H. Honig. Linking molecular affinity and cellular specificity in cadherin-mediated adhesion. *Proc Natl Acad Sci U S A*, 2009. 109

[368] A. F. M. Maree, V. A. Grieneisen, and P. Hogeweg. *The Cellular Potts Model and biophysical properties of cells, tissues and morphogenesis.* Single Cell Based Models in Biology and Medicine. Birkhäuser Verlag, Basel, 2007. 111

[369] Noriyuki Bob Ouchi, James A. Glazier, Jean-Paul Rieu, Arpita Upadhyaya, and Yasuji Sawada. Improving the realism of the cellular potts model in simulations of biological cells. *Physica A: Statistical Mechanics and its Applications*, 329(3-4):451–458, 2003. 111

[370] Francois Graner. Can surface adhesion drive cell-rearrangement? part i: Biological cell-sorting. *Journal of Theoretical Biology*, 164(4):455–476, 1993. 111, 116

[371] T. Shimizu, T. Yabe, O. Muraoka, S. Yonemura, S. Aramaki, K. Hatta, Y. K. Bae, H. Nojima, and M. Hibi. E-cadherin is required for gastrulation cell movements in zebrafish. *Mech Dev*, 122(6):747–63, 2005. 116, 120

[372] R. H. Insall and G. E. Jones. Moving matters: signals and mechanisms in directed cell migration. *Nat Cell Biol*, 8(8):776–9, 2006. 119

[373] T. S. Deisboeck and I. D. Couzin. Collective behavior in cancer cell populations. *Bioessays*, 31(2):190–7, 2009. 119, 130

[374] J. Buhl, D. J. Sumpter, I. D. Couzin, J. J. Hale, E. Despland, E. R. Miller, and S. J. Simpson. From disorder to order in marching locusts. *Science*, 312(5778):1402–6, 2006. 119, 130

[375] T. Ishikawa. Suspension biomechanics of swimming microbes. *J R Soc Interface*, 6(39):815–34, 2009. 119

[376] H. Moore, K. Dvorakova, N. Jenkins, and W. Breed. Exceptional sperm cooperation in the wood mouse. *Nature*, 418(6894):174–7, 2002. 119

[377] Y. Yang, J. Elgeti, and G. Gompper. Cooperation of sperm in two dimensions: synchronization, attraction, and aggregation through hydrodynamic interactions. *Phys Rev E Stat Nonlin Soft Matter Phys*, 78(6 Pt 1):061903, 2008. 119

[378] M. Bees and N. Hill. Wavelengths of bioconvection patterns. *J Exp Biol*, 200(Pt 10):1515–26, 1997. 119

[379] P. Haas and D. Gilmour. Chemokine signaling mediates self-organizing tissue migration in the zebrafish lateral line. *Dev Cell*, 10(5):673–80, 2006. 119, 120

[380] T. Tsuji, S. Ibaragi, and G. F. Hu. Epithelial-mesenchymal transition and cell cooperativity in metastasis. *Cancer Res*, 2009. 119

[381] P. Friedl and D. Gilmour. Collective cell migration in morphogenesis, regeneration and cancer. *Nat Rev Mol Cell Biol*, 10(7):445–57, 2009. 119, 120, 121, 127

[382] C. J. Weijer. Collective cell migration in development. *J Cell Sci*, 122(Pt 18):3215–23, 2009. 120, 172

[383] D. J. Montell. Morphogenetic cell movements: diversity from modular mechanical properties. *Science*, 322(5907):1502–5, 2008. 121, 127

[384] M. Melani, K. J. Simpson, J. S. Brugge, and D. Montell. Regulation of cell adhesion and collective cell migration by hindsight and its human homolog rreb1. *Curr Biol*, 18(7):532–7, 2008. 129

[385] P. Niewiadomska, D. Godt, and U. Tepass. De-cadherin is required for intercellular motility during drosophila oogenesis. *J Cell Biol*, 144(3):533–47, 1999. 129

[386] A. E. Kerstetter, E. Azodi, J. A. Marrs, and Q. Liu. Cadherin-2 function in the cranial ganglia and lateral line system of developing zebrafish. *Dev Dyn*, 230(1):137–43, 2004. 129

[387] A. L. Wilson, Y. C. Shen, S. G. Babb-Clendenon, J. Rostedt, B. Liu, K. F. Barald, J. A. Marrs, and Q. Liu. Cadherin-4 plays a role in the development of zebrafish cranial ganglia and lateral line system. *Dev Dyn*, 236(3):893–902, 2007. 129

[388] G. van Meer, D. R. Voelker, and G. W. Feigenson. Membrane lipids: where they are and how they behave. *Nat Rev Mol Cell Biol*, 9(2):112–24, 2008. 132

[389] D. Leckband and J. Israelachvili. Intermolecular forces in biology. *Q Rev Biophys*, 34(2):105–267, 2001. 132, 137

[390] J. Zimmerberg. Membrane biophysics. *Curr Biol*, 16(8):R272–6, 2006. 132, 134, 135, 136, 137

[391] E. A. Evans and R. Skalak. Mechanics and thermodynamics of biomembranes: part 1. *CRC Crit Rev Bioeng*, 3(3):181–330, 1979. 132

[392] T. D. Pollard and G. G. Borisy. Cellular motility driven by assembly and disassembly of actin filaments. *Cell*, 112(4):453–65, 2003. 133, 158

[393] G. Giannone, B. J. Dubin-Thaler, O. Rossier, Y. Cai, O. Chaga, G. Jiang, W. Beaver, H. G. Dobereiner, Y. Freund, G. Borisy, and M. P. Sheetz. Lamellipodial actin mechanically links myosin activity with adhesion-site formation. *Cell*, 128(3):561–75, 2007. 134, 158

[394] L. Ji, J. Lim, and G. Danuser. Fluctuations of intracellular forces during cell protrusion. *Nat Cell Biol*, 10(12):1393–400, 2008. 134

[395] W. Helfrich. Elastic properties of lipid bilayers: theory and possible experiments. *Z Naturforsch C*, 28(11):693–703, 1973. 134, 135

[396] M. P. Sheetz and J. Dai. Modulation of membrane dynamics and cell motility by membrane tension. *Trends Cell Biol*, 6(3):85–9, 1996. 134

[397] C. E. Morris and U. Homann. Cell surface area regulation and membrane tension. *J Membr Biol*, 179(2):79–102, 2001. 135

[398] V. Heinrich and C. Ounkomol. Force versus axial deflection of pipette-aspirated closed membranes. *Biophys J*, 93(2):363–72, 2007. 135

[399] E. Evans and W. Rawicz. Entropy-driven tension and bending elasticity in condensed-fluid membranes. *Phys Rev Lett*, 64(17):2094–2097, 1990. 135

[400] J. Pecreaux, H. G. Dobereiner, J. Prost, J. F. Joanny, and P. Bassereau. Refined contour analysis of giant unilamellar vesicles. *Eur Phys J E Soft Matter*, 13(3):277–90, 2004. 135, 136

[401] V. Vitkova, P. Meleard, T. Pott, and I. Bivas. Alamethicin influence on the membrane bending elasticity. *Eur Biophys J*, 35(3):281–6, 2006. 135

[402] D. V. Zhelev, D. Needham, and R. M. Hochmuth. A novel micropipet method for measuring the bending modulus of vesicle membranes. *Biophys J*, 67(2):720–7, 1994. 136

[403] J. Song and R. E. Waugh. Bilayer membrane bending stiffness by tether formation from mixed pc-ps lipid vesicles. *J Biomech Eng*, 112(3):235–40, 1990. 136

[404] J. Song and R. E. Waugh. Bending rigidity of sopc membranes containing cholesterol. *Biophys J*, 64(6):1967–70, 1993. 136

[405] A. Upadhyaya and M. P. Sheetz. Tension in tubulovesicular networks of golgi and endoplasmic reticulum membranes. *Biophys J*, 86(5):2923–8, 2004. 136, 154

[406] V. Heinrich and R. E. Waugh. A piconewton force transducer and its application to measurement of the bending stiffness of phospholipid membranes. *Ann Biomed Eng*, 24(5):595–605, 1996. 136

[407] W. C. Hwang and R. E. Waugh. Energy of dissociation of lipid bilayer from the membrane skeleton of red blood cells. *Biophys J*, 72(6):2669–78, 1997. 136, 154

[408] H. I. Petrache, S. W. Dodd, and M. F. Brown. Area per lipid and acyl length distributions in fluid phosphatidylcholines determined by (2)h nmr spectroscopy. *Biophys J*, 79(6):3172–92, 2000. 137

[409] R. E. Waugh and R. G. Bauserman. Physical measurements of bilayer-skeletal separation forces. *Ann Biomed Eng*, 23(3):308–21, 1995. 138, 152

[410] E. Tabdanov, N. Borghi, F. Brochard-Wyart, S. Dufour, and J. P. Thiery. Role of e-cadherin in membrane-cortex interaction probed by nanotube extrusion. *Biophys J*, 96(6):2457–65, 2009. 138, 144, 152, 156

[411] R. M. Hochmuth, N. Mohandas, E. E. Spaeth, J. R. Williamson, Jr. Blackshear, P. L., and D. W. Johnson. Surface adhesion, deformation and detachment at low shear of red cells and white cells. *Trans Am Soc Artif Intern Organs*, 18(0):325–34, 1972. 138, 140

[412] R. M. Hochmuth, N. Mohandas, and Jr. Blackshear, P. L. Measurement of the elastic modulus for red cell membrane using a fluid mechanical technique. *Biophys J*, 13(8):747–62, 1973. 138

[413] D. W. Schmidtke and S. L. Diamond. Direct observation of membrane tethers formed during neutrophil attachment to platelets or p-selectin under physiological flow. *J Cell Biol*, 149(3):719–30, 2000. 138, 140, 154

[414] B. G. Hosu, M. Sun, F. Marga, M. Grandbois, and G. Forgacs. Eukaryotic membrane tethers revisited using magnetic tweezers. *Phys Biol*, 4(2):67–78, 2007. 138, 139, 141

[415] M. Krieg, J. Helenius, C. P. Heisenberg, and D. J. Muller. A bond for a lifetime: employing membrane nanotubes from living cells to determine receptor-ligand kinetics. *Angew Chem Int Ed Engl*, 47(50):9775–7, 2008. 138, 151

[416] D. Raucher and M. P. Sheetz. Characteristics of a membrane reservoir buffering membrane tension. *Biophys J*, 77(4):1992–2002, 1999. 138, 139, 151

[417] R. E. Waugh and R. M. Hochmuth. Mechanical equilibrium of thick, hollow, liquid membrane cylinders. *Biophys J*, 52(3):391–400, 1987. 139

[418] E. Evans, V. Heinrich, A. Leung, and K. Kinoshita. Nano- to microscale dynamics of p-selectin detachment from leukocyte interfaces. i. membrane separation from the cytoskeleton. *Biophys J*, 88(3):2288–98, 2005. 139

[419] V. Heinrich, A. Leung, and E. Evans. Nano- to microscale dynamics of p-selectin detachment from leukocyte interfaces. ii. tether flow terminated by p-selectin dissociation from psgl-1. *Biophys J*, 88(3):2299–308, 2005. 139

[420] M. R. King, V. Heinrich, E. Evans, and D. A. Hammer. Nano-to-micro scale dynamics of p-selectin detachment from leukocyte interfaces. iii. numerical simulation of tethering under flow. *Biophys J*, 88(3):1676–83, 2005. 139

[421] Y. Chen, G. Girdhar, and J. Y. Shao. Single membrane tether extraction from adult and neonatal dermal microvascular endothelial cells. *Am J Physiol Cell Physiol*, 292(4):C1272–9, 2007. 139, 154

[422] I. Titushkin and M. Cho. Distinct membrane mechanical properties of human mesenchymal stem cells determined using laser optical tweezers. *Biophys J*, 90(7):2582–91, 2006. 139, 154

[423] L. Jauffred, T. H. Callisen, and L. B. Oddershede. Visco-elastic membrane tethers extracted from escherichia coli by optical tweezers. *Biophys J*, 93(11):4068–75, 2007. 139

[424] J. Chen and M. C. Wagner. Altered membrane-cytoskeleton linkage and membrane blebbing in energy-depleted renal proximal tubular cells. *Am J Physiol Renal Physiol*, 280(4):F619–27, 2001. 139, 144

[425] G. Koster, A. Cacciuto, I. Derenyi, D. Frenkel, and M. Dogterom. Force barriers for membrane tube formation. *Phys Rev Lett*, 94(6):068101, 2005. 139

[426] D. Cuvelier, I. Derenyi, P. Bassereau, and P. Nassoy. Coalescence of membrane tethers: experiments, theory, and applications. *Biophys J*, 88(4):2714–26, 2005. 139

[427] D. Raucher and M. P. Sheetz. Membrane expansion increases endocytosis rate during mitosis. *J Cell Biol*, 144(3):497–506, 1999. 140

[428] D. Raucher, T. Stauffer, W. Chen, K. Shen, S. Guo, J. D. York, M. P. Sheetz, and T. Meyer. Phosphatidylinositol 4,5-bisphosphate functions as a second messenger that regulates cytoskeleton-plasma membrane adhesion. *Cell*, 100(2):221–8, 2000. 140

[429] R. E. Waugh. Surface viscosity measurements from large bilayer vesicle tether formation. ii. experiments. *Biophys J*, 38(1):29–37, 1982. 140, 141

[430] E. S. Wu, K. Jacobson, F. Szoka, and Jr. Portis, A. Lateral diffusion of a hydrophobic peptide, n-4-nitrobenz-2-oxa-1,3-diazole gramicidin s, in phospholipid multibilayers. *Biochemistry*, 17(25):5543–50, 1978. 141

[431] G. B. Nash and H. J. Meiselman. Red cell and ghost viscoelasticity. effects of hemoglobin concentration and in vivo aging. *Biophys J*, 43(1):63–73, 1983. 141

[432] R. Tran-Son-Tay, S. P. Sutera, and P. R. Rao. Determination of red blood cell membrane viscosity from rheoscopic observations of tank-treading motion. *Biophys J*, 46(1):65–72, 1984. 141

[433] N. Borghi and F. Brochard-Wyart. Tether extrusion from red blood cells: integral proteins unbinding from cytoskeleton. *Biophys J*, 93(4):1369–79, 2007. 141

[434] J. Schmitz, M. Benoit, and K. E. Gottschalk. The viscoelasticity of membrane tethers and its importance for cell adhesion. *Biophys J*, 95(3):1448–59, 2008. 141, 150

[435] Z. Li, B. Anvari, M. Takashima, P. Brecht, J. H. Torres, and W. E. Brownell. Membrane tether formation from outer hair cells with optical tweezers. *Biophys J*, 82(3):1386–95, 2002. 141

[436] M. A. Lemmon. Membrane recognition by phospholipid-binding domains. *Nat Rev Mol Cell Biol*, 9(2):99–111, 2008. 142

[437] D. Liu, L. Ge, F. Wang, H. Takahashi, D. Wang, Z. Guo, S. H. Yoshimura, T. Ward, X. Ding, K. Takeyasu, and X. Yao. Single-molecule detection of phosphorylation-induced plasticity changes during ezrin activation. *FEBS Lett*, 581(18):3563–71, 2007. 143, 144

[438] H. Ishikawa, A. Tamura, T. Matsui, H. Sasaki, T. Hakoshima, and S. Tsukita. Structural conversion between open and closed forms of radixin: low-angle shadowing electron microscopy. *J Mol Biol*, 310(5):973–8, 2001. 143, 144

[439] M. N. Knowlton, B. M. Chan, and G. M. Kelly. The zebrafish band 4.1 member mir is involved in cell movements associated with gastrulation. *Dev Biol*, 264(2):407–29, 2003. 142, 146

[440] P. Pujuguet, L. Del Maestro, A. Gautreau, D. Louvard, and M. Arpin. Ezrin regulates e-cadherin-dependent adherens junction assembly through rac1 activation. *Mol Biol Cell*, 14(5):2181–91, 2003. 142

[441] S. D. Edwards and N. H. Keep. The 2.7 a crystal structure of the activated ferm domain of moesin: an analysis of structural changes on activation. *Biochemistry*, 40(24):7061–8, 2001. 143

[442] M. Janke, A. Herrig, J. Austermann, V. Gerke, C. Steinem, and A. Janshoff. Actin binding of ezrin is activated by specific recognition of pip2-functionalized lipid bilayers. *Biochemistry*, 47(12):3762–9, 2008. 143, 144, 152, 172

[443] S. Coscoy, F. Waharte, A. Gautreau, M. Martin, D. Louvard, P. Mangeat, M. Arpin, and F. Amblard. Molecular analysis of microscopic ezrin dynamics by two-photon frap. *Proc Natl Acad Sci U S A*, 99(20):12813–8, 2002. 144

[444] D. N. Chambers and A. Bretscher. Ezrin mutants affecting dimerization and activation. *Biochemistry*, 44(10):3926–32, 2005. 144

[445] S. Carreno, I. Kouranti, E. S. Glusman, M. T. Fuller, A. Echard, and F. Payre. Moesin and its activating kinase slik are required for cortical stability and microtubule organization in mitotic cells. *J Cell Biol*, 180(4):739–46, 2008. 144

[446] C. P. Heisenberg and L. Solnica-Krezel. Back and forth between cell fate specification and movement during vertebrate gastrulation. *Curr Opin Genet Dev*, 18(4):311–6, 2008. 145

[447] Y. Shi and J. Massague. Mechanisms of tgf-beta signaling from cell membrane to the nucleus. *Cell*, 113(6):685–700, 2003. 145

[448] J. Ng. Tgf-beta signals regulate axonal development through distinct smad-independent mechanisms. *Development*, 135(24):4025–35, 2008. 145

[449] N. Fujinami. Studies on the mechanism of circus movement in dissociated embryonic cells of a teleost, oryzias latipes: fine-structural observations. *J Cell Sci*, 22(1):133–47, 1976. 146

[450] G. J. Doherty and H. T. McMahon. Mediation, modulation, and consequences of membrane-cytoskeleton interactions. *Annu Rev Biophys*, 37:65–95, 2008. 152

[451] D. Axelrod, D. E. Koppel, J. Schlessinger, E. Elson, and W. W. Webb. Mobility measurement by analysis of fluorescence photobleaching recovery kinetics. *Biophys J*, 16(9):1055–69, 1976. 153

[452] C. A. Day and A. K. Kenworthy. Tracking microdomain dynamics in cell membranes. *Biochim Biophys Acta*, 1788(1):245–53, 2009. 153

[453] J. Solon, J. Pecreaux, P. Girard, M. C. Faure, J. Prost, and P. Bassereau. Negative tension induced by lipid uptake. *Phys Rev Lett*, 97(9):098103, 2006. 154

[454] R. Nambiar, R. E. McConnell, and M. J. Tyska. Control of cell membrane tension by myosin-i. *Proc Natl Acad Sci U S A*, 106(29):11972–7, 2009. 156

[455] T. Nebl, S. W. Oh, and E. J. Luna. Membrane cytoskeleton: Pip(2) pulls the strings. *Curr Biol*, 10(9):R351–4, 2000. 157

[456] K. Endo, S. Kondo, J. Shackleford, T. Horikawa, N. Kitagawa, T. Yoshizaki, M. Furukawa, Y. Zen, and J. S. Pagano. Phosphorylated ezrin is associated with ebv latent membrane protein 1 in nasopharyngeal carcinoma and induces cell migration. *Oncogene*, 28(14):1725–35, 2009. 157

[457] K. Poole, K. Khairy, J. Friedrichs, C. Franz, D. A. Cisneros, J. Howard, and D. Mueller. Molecular-scale topographic cues induce the orientation and directional movement of fibroblasts on two-dimensional collagen surfaces. *J Mol Biol*, 349(2):380–6, 2005. 158

[458] K. A. Molyneaux, H. Zinszner, P. S. Kunwar, K. Schaible, J. Stebler, M. J. Sunshine, W. O'Brien, E. Raz, D. Littman, C. Wylie, and R. Lehmann. The chemokine sdf1/cxcl12 and its receptor cxcr4 regulate mouse germ cell migration and survival. *Development*, 130(18):4279–86, 2003. 158

[459] T. Mizoguchi, H. Verkade, J. K. Heath, A. Kuroiwa, and Y. Kikuchi. Sdf1/cxcr4 signaling controls the dorsal migration of endodermal cells during zebrafish gastrulation. *Development*, 135(15):2521–9, 2008. 158

[460] G. I. Bell. Models for the specific adhesion of cells to cells. *Science*, 200(4342):618–27, 1978. 161, 162

[461] R. Merkel, P. Nassoy, A. Leung, K. Ritchie, and E. Evans. Energy landscapes of receptor-ligand bonds explored with dynamic force spectroscopy. *Nature*, 397(6714):50–3, 1999. 162

[462] E. Evans and K. Ritchie. Dynamic strength of molecular adhesion bonds. *Biophys J*, 72(4):1541–55, 1997. 162

[463] S.N. Zhurkov. *International Journal Fracture Mechanics*, 1:311, 1965. 163

[464] H.A. Kramers. Brownian motion in a field of force and the diffusion model of chemical reactions. *Physica 7*, 4:284–304, 1940. 163

[465] M. Dembo, D. C. Torney, K. Saxman, and D. Hammer. The reaction-limited kinetics of membrane-to-surface adhesion and detachment. *Proc R Soc Lond B Biol Sci*, 234(1274):55–83, 1988. 163

[466] D.A. Hammer and M. Tirrell. Biological adhesion at interfaces. *Annual Reviews Material Sciences*, 26:651–691, 1996. 163

[467] B. Guo and W. H. Guilford. Mechanics of actomyosin bonds in different nucleotide states are tuned to muscle contraction. *Proc Natl Acad Sci U S A*, 103(26):9844–9, 2006. 164

[468] T. Yago, J. Lou, T. Wu, J. Yang, J. J. Miner, L. Coburn, J. A. Lopez, M. A. Cruz, J. F. Dong, L. V. McIntire, R. P. McEver, and C. Zhu. Platelet glycoprotein ibalpha forms catch bonds with human wt vwf but not with type 2b von willebrand disease vwf. *J Clin Invest*, 118(9):3195–207, 2008. 164

[469] F. Kong, A. J. Garcia, A. P. Mould, M. J. Humphries, and C. Zhu. Demonstration of catch bonds between an integrin and its ligand. *J Cell Biol*, 185(7):1275–84, 2009. 164

[470] E. A. Evans and D. A. Calderwood. Forces and bond dynamics in cell adhesion. *Science*, 316(5828):1148–53, 2007. 164

[471] W. Baumgartner, P. Hinterdorfer, W. Ness, A. Raab, D. Vestweber, H. Schindler, and D. Drenckhahn. Cadherin interaction probed by atomic force microscopy. *Proc Natl Acad Sci U S A*, 97(8):4005–10, 2000. 164

[472] K. E. Edmondson, W. S. Denney, and S. L. Diamond. Neutrophil-bead collision assay: pharmacologically induced changes in membrane mechanics regulate the psgl-1/p-selectin adhesion lifetime. *Biophys J*, 89(5):3603–14, 2005. 164

[473] M. V. Bayas, A. Leung, E. Evans, and D. Leckband. Lifetime measurements reveal kinetic differences between homophilic cadherin bonds. *Biophys J*, 90(4):1385–95, 2006. 164

[474] I. J. Goldstein and R. N. Iyer. Interaction of concanavalin a, a phytohemagglutinin, with model substrates. *Biochim Biophys Acta*, 121(1):197–200, 1966. 164

[475] A. Chen and V. T. Moy. Cross-linking of cell surface receptors enhances cooperativity of molecular adhesion. *Biophys J*, 78(6):2814–20, 2000. 167

[476] D. K. Mandal, N. Kishore, and C. F. Brewer. Thermodynamics of lectin-carbohydrate interactions. titration microcalorimetry measurements of the binding of n-linked carbohydrates and ovalbumin to concanavalin a. *Biochemistry*, 33(5):1149–56, 1994. 167

[477] R. E. Dawes-Hoang and E. F. Wieschaus. Cell and developmental biology–a shared past, an intertwined future. *Dev Cell*, 1(1):27–36, 2001. 171

[478] T. Gregor, E. F. Wieschaus, A. P. McGregor, W. Bialek, and D. W. Tank. Stability and nuclear dynamics of the bicoid morphogen gradient. *Cell*, 130(1):141–52, 2007. 171

[479] T. Gregor, A. P. McGregor, and E. F. Wieschaus. Shape and function of the bicoid morphogen gradient in dipteran species with different sized embryos. *Dev Biol*, 316(2):350–8, 2008. 171

[480] D. L. McLean, M. A. Masino, I. Y. Koh, W. B. Lindquist, and J. R. Fetcho. Continuous shifts in the active set of spinal interneurons during changes in locomotor speed. *Nat Neurosci*, 11(12):1419–29, 2008. 171

[481] M. A. Welte, S. P. Gross, M. Postner, S. M. Block, and E. F. Wieschaus. Developmental regulation of vesicle transport in drosophila embryos: forces and kinetics. *Cell*, 92(4):547–57, 1998. 171